



UNIVERSITAT POLITÈCNICA DE CATALUNYA
BARCELONATECH

Departament d'Enginyeria Electrònica

“CONTRIBUTION TO ADVANCED HOT WIRE WIND SENSING”

Tesi doctoral presentada per a l'obtenció del títol de Doctor per la Universitat Politècnica de Catalunya, dins el Programa de Doctorat en Enginyeria Electrònica

Lukasz Kowalski

Director: *Vicente Jiménez Serres*

Enero 2016

... to Gabriela my daughter

Acknowledgment

There are a number of people without whom this thesis and many other contributions [1–12] might not have happen in the form they are, and to whom I am immeasurably appreciate.

I am grateful to my supervisor, Dr. Vicente Jiménez, whose expertise, generous guidance, and support made possible for me to contribute to thermal anemometry topic in this dissertation form.

I am hugely indebted to the Prof. Luis Castañer and Dr. Manuel Domínguez who are the persons who have recognized my possible role in the ongoing project for the development of the wind sensor for Mars. Without your support, counsel and valuable comments my paperwork contribution along the Ph. D. course would not be possible.

I would like to acknowledge institutions like: Center of Astrobiology (CAB), Instituto Nacional de Técnica Aeroespacial (INTA), Centro Nacional de Microelectrónica (CNM), Aarhus University and Oxford University, with whom the collaboration was always kind and fruitful.

I would like to express my gratitude to the Miguel Garcia the boss of the clean room facility and Santiago Perez an administrator of the software servers and computer network. Without your professional skills and dedication, many from the work I have done would not be possible.

I would like to thank my colleagues Jordi Ricart, Gema Lopez, Vito de Virgilio, Arnau Coll, Sergi Gorreta and Teresa Atienza without whom my written contribution would not be as valuable as they are. You enriched not only my paperwork but also me day by day life, so a big thank you for that.

Thanks also go to my fellows from the Electronic Engineering Department who made me feel like at home when I have appeared at UPC and trough all these years of investigation when you provide me with energy and friendship.

I would like to recognize the generous support of the Catalan Agency for Administration of University and Research Grants (AGAUR) for the 2006FI00302 scholarship.

Finally, I would like to thank my wife, parents, and sister for their unconditional love and support. Your encouragement and continuous love are making me stronger also when it goes about finishing this very important milestone in my educational career.

Contents

1	Introduction	1
2	Mars We Know	3
2.1	Orbit of Mars	3
2.2	Planet Mars	4
2.3	Atmosphere of Mars	6
3	Thesis Background	11
3.1	Wind definition	11
3.2	Physical mechanism of heat transfer	13
3.2.1	Knudsen number	14
3.2.2	Reynolds number	15
3.2.3	Nusselt number	16
3.2.4	Mach number	16
3.2.5	Grashof number	17
3.2.6	Velocity boundary layer	18
3.2.7	Thermal boundary layer	18
3.2.8	Prandtl number	19
3.2.9	Mars atmosphere gas properties	19
3.3	Thermal flow sensors	21
3.3.1	Thermal anemometers	21
3.3.2	Calorimetric sensors	22
3.4	Operating modes	22
4	Thermal Anemometry in Mars Missions	25
4.1	Viking mission	26
4.1.1	Viking wind sensor unit	27
4.2	Mars Pathfinder mission	28
4.2.1	Mars Pathfinder wind sensor unit	29
4.3	Mars Science Laboratory mission	30
5	REMS 2-D Wind Transducer	33
5.1	Rover Environmental Monitoring Station (REMS) project . .	33
5.1.1	REMS objectives	34

CONTENTS

5.1.2	REMS instruments	34
5.2	Concept of the REMS 2-D wind transducer	39
5.2.1	REMS wind sensor unit	41
5.2.2	Constant temperature overhear anemometer	43
5.3	Numerical experimentation	43
5.3.1	Simulations parameters	43
5.3.2	Different geometries	45
5.4	Fluidical-thermal simulation	46
5.4.1	Single unit simulation	47
5.4.2	Four hot dice array	50
5.4.3	Angular sensitivity	52
5.5	Fabrication and assembly	54
5.5.1	Chip mask layout	55
5.5.2	Silicon chip fabrication	56
5.5.3	Fabrication process	58
5.5.4	Resistance measurements	66
5.5.5	Resistance distribution	68
5.5.6	Alpha coefficient	68
5.6	2-D wind sensor assembly	71
5.6.1	Printed Circuit Board (PCB) base	72
5.6.2	Pyrex support	72
5.6.3	Wire bonding process	74
5.7	Measurement circuit	74
5.7.1	Electro-thermal sigma-delta modulator	75
5.7.2	Electronic circuit	76
5.7.3	Overheat value	79
5.8	Convection heat model	81
5.8.1	Algebraic equation model	82
5.8.2	Finite Element Method (FEM) model	87
5.9	Measurement campaign	89
5.9.1	Wind tunnel facilities	90
5.9.2	Re-circulating wind tunnel in Aarhus	92
5.9.3	Sensitivity to the wind speed	92
5.9.4	Sensitivity to the wind direction	93
5.9.5	Sensitivity to the atmospheric pressure	95
5.9.6	Time response experiment	97
5.9.7	Open circuit wind tunnel in Oxford	98
5.10	REMS wind sensor in comparison to Viking and Pathfinder	99
5.10.1	First order model	100
5.10.2	Power efficiency	107
5.11	REMS 2-D wind transducer summary	109

6	3-D Hot Sphere Anemometer	115
6.1	Mars Environmental Instrumentation for Ground and Atmosphere (MEIGA) project	115
6.1.1	MEIGA wind sensor	116
6.2	Hot sphere anemometer concept	117
6.2.1	Hot sphere transducer	119
6.2.2	Hot sphere diameter	120
6.3	Hot sphere convection model	121
6.3.1	Algebraic solution for sphere	122
6.3.2	Fluidic-thermal simulations	124
6.3.3	Local heat flux modelling	126
6.3.4	Convection model verification	129
6.4	Wind magnitude and temperature issue	129
6.5	Wind direction issue	131
6.5.1	Simple yaw rotation	134
6.5.2	Angular sensitivity	135
6.5.3	Angle inverse algorithm	138
6.6	Tetrahedral 3-D sensor prototype	140
6.7	Preliminary measurements	143
6.7.1	Measurements set-up	143
6.7.2	Measurements sequence	143
6.7.3	Yaw rotation experiment	145
6.7.4	Wind velocity steps	147
6.7.5	3-D wind angle discrimination	148
6.8	3-D hot sphere anemometer summary	149
7	Conclusions	151
7.1	Discussion	151
7.1.1	2-D Wind Transducer	151
7.1.2	3-D Hot Sphere Anemometer	154
7.2	Suggestion for further research	157
Appendix A		169
	Metodo para la medida de la velocidad del aire y de su dirección en dos dimensiones para aplicaciones aeroespaciales	169
Appendix B		185
	A hot film anemometer for the Martian atmosphere	185
Appendix C		199
	Applications of hot film anemometry to space missions	199
Appendix D		207
	Sensitivity analysis of the chip for REMS wind sensor	207

CONTENTS

Appendix E	211
Contribution to advanced hot wire wind sensing	211
Appendix F	215
Chip UPC para la medida del viento en Marte	215
Appendix G	227
Thermal modelling of the chip for the REMS wind sensor	227
Appendix H	243
Multiphysics Simulation of REMS hot-film Anemometer Under Typical Martian Atmosphere Conditions	243
Appendix I	249
Hypobaric chamber for wind sensor testing in Martian conditions .	249
Appendix J	257
Congratulations & Exhibitions	257
Appendix K	261
NASA Group Achievement Award	261
Appendix L	265
Low pressure spherical thermal anemometer for space mission . . .	265

List of Figures

2.1	Our Solar System	4
2.2	Earth, Mars and Moon in the same scale, [13].	5
2.3	Comparison of mean free path for Mars and Earth atmosphere according to the typical pressure and temperature variation.	8
2.4	Surface atmospheric pressure over a Martian year, recorded by the Viking landers and showing seasonal fluctuation. The two landers recorded different absolute pressures because they were sited at different altitudes. Image courtesy of Annual Reviews [14].	9
3.1	Example of how humans harness the energy of the wind a) windmill, b) wind power plant.	12
3.2	Four different flow regimes according to the Knudsen number value.	14
3.3	Character of different flow regimes: a) laminar, b) turbulent.	15
3.4	Velocity boundary layer for flow medium continuum regime.	18
4.1	Mars landing sites for planetary missions: a) Viking 1, b) Viking 2, c) Mars Pathfinder, d) Spirit, e) Opportunity, f) Phoenix, g) Mars Science Laboratory (MSL), superimposed on the topography map of the Red Planet. Courtesy NASA/JPL-Caltech.	26
4.2	First panoramic image of <i>Chryse Planitia</i> taken by camera 1 on the Viking 1 Lander. The image was taken on 23 July 1976, three days after Viking 1 landed. The meteorology boom is at the center of the image and to the left is the support for the high-gain dish antenna, [15]. Courtesy NASA/JPL-Caltech.	27
4.3	Viking wind speed sensor unit.	28

LIST OF FIGURES

4.4	Mars Pathfinder wind sensor unit composed of platinum-iridium wire wound 7 times fold and attached to the insulating formers around circumference cone. Entire 2-D wind sensor was made out of 6 sensor units equally distributed with 60° radial step and 3 mm of separation from cylindrical cone shown here.	30
4.5	a) Concept of the three 2-D Wind Transducer (WT) boards located in 120° orientation around the boom to form 3-D wind sensor and enable reconstruction wind magnitude and direction, b) Universitat Politècnica de Catalunya (UPC) prototype, c) CAB engineering model.	31
5.1	The logos of cooperative institutions: a) CAB, b) National Aeronautics and Space Administration (NASA), c) UPC, d) Finnish Meteorological Institute (FMI), e) for REMS project.	34
5.2	Curiosity rover mast with two booms pointed horizontally in two different direction with Wind Transducer (WT) position (three for each boom). Image credit: NASA/JPL-Caltech/INTA (Instituto Nacional de Técnica Aeroespacial).	35
5.3	Concept of the wind sensor unit with its cold point and hot point elements.	39
5.4	Sigma-delta closed loop diagram of the REMS wind transducer. Only the blocks associated with one of the hot points (namely hot point C) are shown.	40
5.5	MSL - REMS wind sensor unit concept	41
5.6	Front view of silicon die with three resistances: R_{sens} , R_{heat} , R_{delta} and six PADs.	42
5.7	Sound of speed and incompressible flow speed limit ($0.3 Ma$) for Martian (CO_2) atmosphere.	44
5.8	Typical Martian atmosphere (CO_2) parameters variation as a function of temperature: a) thermal conductivity, b) dynamic viscosity and, c) specific heat, d) Prandtl number with reference to the same Earth AIR atmosphere parameters.	45
5.9	Several sets of geometry candidates for wind sensor to Mars surface under Finite Element Method (FEM) simulation.	46
5.10	Concept of the REMS wind sensor geometry of four silicon dice array fixed on the Pyrex inverted table in Analysis System (ANSYS) finite element method simulation software.	47
5.11	Knudsen number calculation	48
5.12	REMS wind sensor unit a) boundary conditions: temperature $T_{hot} = 201$ K for ANSYS static FEM simulation under the CO_2 wind of 10 m/s from southwest direction and ambient temperature $T_{amb.} = 200$ K, b) temperature cross section graph for non-compressible flow solution.	48

5.13	a) The symmetry of the wind incidence angle in reference to the square die geometry b) simulation of the hot die convection as a function of the wind direction ϕ for the range of $\langle 270^\circ \dots 360^\circ \rangle$. Convection power has been measured for 600 Pa CO ₂ flow where die temperature was set for 201 K, whereas gas temperature was set for 200 K.	49
5.14	a) Power convection in function of the wind flow velocity U , b) example for wind incidence angle $\phi = 315^\circ$, CO ₂ pressure 600 Pa where die temperature was set for 201 K and gas temperature was set for 200 K.	49
5.15	FEM simulation results of: a) thermal conductance of the die A as a function of incidence angle and wind speed, b) four silicon dice array orientation according to the wind incidence angle directions.	50
5.16	Thermal conductance for the four hot dice array as a function of rotation angle for the same wind speed of 10 m/s.	51
5.17	Average thermal conductivity for the four dice array, a) as a function of wind incidence angle for different wind speeds, b) as a function of wind speed, having its variation for full range of the rotation angles.	51
5.18	Combination of thermal conductances a) for terms: <i>North-South</i> and <i>East-West</i> b) and what is their position in function of the wind incidence angle.	52
5.19	Angular sensitivity for the hot dice array: A, B, C, D a) as a function of the wind direction (α), b) as a function of the wind velocity (U)	53
5.20	Angular sensitivity for the the diffential terms <i>North-South</i> and <i>East-West</i> a) in the function of the wind direction (α), b) in function of the wind velocity (U)	54
5.21	View of UPC-REMS wind sensor prototype, a) from the top where square array dimension is depicted, b) from the perspective where dice thickness can be see.	54
5.22	Microscope photography of the silicon die of wind transducer after fabrication: a) <i>type L</i> , b) <i>type N</i>	55
5.23	Set of photolithograpy masks for UPC-REMS wind sensor chip: a) Mask A - Contact Windows, b) Mask B - Titanium/Platinum Paths c) Mask C - Pads	57
5.24	Superposition of the three layouts: A, B and C with its perfect alignment a) mask design b) photograph of the real wafer.	58
5.25	Silicon Wafer N-Cz 1-10 Ω -cm, thickness 400 μ m.	59
5.26	Silicon oxide, thickness 120 nm.	59
5.27	Thin resin spinning RPM profile.	60
5.28	Resin SPR-220 1.2, thickness 1 μ m.	60
5.29	First photolithography	61

LIST OF FIGURES

5.30	Contact window opening.	61
5.31	Second resin lift-off.	61
5.32	Temperature profile of doping.	62
5.33	Bulk doping with impurities type N.	62
5.34	Silicon wafer after second resin step.	62
5.35	Second photolithography.	62
5.36	Pattern engrave in silicon dioxide.	63
5.37	Titanium sputtering, thickness 10 nm.	63
5.38	Platinum sputtering, thickness 70 nm.	64
5.39	Second resin lift-off.	64
5.40	Thick resin spinning RPM profile.	65
5.41	Resin SPR-220 7.0, thickness 7 μm	65
5.42	Third photolithography.	65
5.43	Platinum sputtering for PADs, thickness 100 nm.	66
5.44	Third resin lift-off.	66
5.45	New fabricated wind sensor chips on a silicon wafer. Image Courtesy: Dr. Jordi Ricart.	67
5.46	Geometry and position of the resistances R_{sens} , R_{heat} and ΔR according to the type of the dice.	68
5.47	Example of R_{heat} distribution along the silicon wafer. Re- sistance has been measured in laboratory temperature con- ditions $\sim 25^\circ\text{C}$. Circular pattern results from rotatory base equipment during platinum raw material sputtering process.	69
5.48	Measurement of temperature-dependent titanium/platinum thin film resistance as a function of temperature, with its perfect match by lineal approximation function.	70
5.49	Square dice after cutting procedure with nominal size of $1675 \mu\text{m}$ $\pm 10 \mu\text{m}$	70
5.50	Photography of the 2-D wind sensor.	71
5.51	Difference in numbers of dice wire-bonding according to the a) hot point b) cold point.	71
5.52	Basic diagram of the assembled sensor with PCB, pyrex sup- port, oxidized silicon chip with Titanium/Platinum resistances on it and gold wire bonding.	72
5.53	Custom desind PCB base a) front view with visible pin-out, b) rear view.	73
5.54	Pyrex support <i>inverted table</i> shape a) lateral view, b) dimen- sions.	73
5.55	Schematic of the 4x7 wire bonding for the hot element array plus 2 wires for the reference die at the bottom of the figure.	74
5.56	Block diagram of the electro-thermal sigma-delta converter for ther REMS wind sensor die.	75

5.57	Close loop mode circuit to maintain constant temperature overheat of the hot element in reference to the ambient tem- perature, where reference die is located.	78
5.58	Electronic circuit board implemented electro-thermal sigma- delta control.	80
5.59	Overheat as a function of ambient temperature for particular resistance set.	81
5.60	Schematic diagram of hot volume convection model.	82
5.61	Isothermal conductance curves in the 2-D graph as a function of air temperature and mass flow product.	85
5.62	Numerical simulation of four hot dice structure for $P_{amb.} = 600$ Pa, $T_{amb.} = 220$ K and $U = 10$ m/s.	86
5.63	Static FEM simulation of the REMS wind sensor unit under constant heat convection cooling, a) Temperature solution, b) Heat flow channels.	88
5.64	Close look for the FEM simulation of the REMS chip under constant heat convection cooling, a) up the surface , b) down the surface.	89
5.65	Wind tunnel facilities: a) rotating arm, b) re-circulating, c) open circuit, d) linear. Wind sensor under test has been sym- bolised by the red hot ball on the green support, where arrows represent either movement of the flow or wind sensor unit. . .	90
5.66	REMS wind 2-D transducer set up inside Aarhus AWSTI wind tunnel facility.	92
5.67	Averaged power dissipated per silicon die to the ambient tem- perature CO ₂ at 6 mBar a) raw data as sampled with fre- quency of 1 Hz b) as a function of the wind velocity and incidence angle (ϕ).	93
5.68	Visual interpretation of the data from Table 5.5.	95
5.69	Averaged power delivered to the four dice structure as a func- tion of a) velocity, b) velocity by pressure product.	96
5.70	Power delivered to the four dice A, B, C, D as a function of velocity by pressure product.	96
5.71	Thermal conductance in result of the steep change in direction of the wind yaw angle (from -20 degree to +20 degree and then back to the -20 degree). Measurement conditions: carbon dioxide pressure 6 mBar, ambient temperature -50°C , hot point overheat 23°C, wind speed 10 m/s.	97
5.72	Prototype of the REMS wind sensor boom set-up for experi- ments inside Oxford open circuit wind tunnel chamber	98
5.73	Orientation of the REMS boom and its three Wind Trans- ducer (WT) boards for the $Yaw = 0^\circ$ and $Pitch = 0^\circ$	99

LIST OF FIGURES

5.74	Longitude thermal conductance (G_{th}) differential term: $North-South=(A+D)-(B+C)$ for three WT board of REMS boom prototype as a function of a) wind velocity b) wind velocity and pressure product. Experiment was run for three ambient pressure 5, 6 and 7 mBar and same temperature and overheat conditions	100
5.75	1-D model of wind sensors from different Mars planetary missions: a) Viking, b) Pathfinder, c) MSL-REMS.	101
5.76	Temperature profile for 1-D thermal model solution for anemometers at Mars conditions ($h = 80 \text{ W}/(\text{m}^2\text{K})$ and $T_{amb} = 300 \text{ K}$). The typical overheat values for Viking 100 K, for Pathfinder 10 K and for REMS 30 K can also be deduced from this plot.	104
5.77	Temperature profile for the 1-D thermal model of hot silicon REMS die according to the die boundary conditions (bc) considered.	105
5.78	Comparison of the three wind sensor: Viking, Pathfinder and REMS in a) total power and b) overheat for whole wind velocity range specified for each sensor and at given atmospheric conditions ($P = 670 \text{ Pa}$, $T = 220 \text{ K}$).	107
5.79	Comparison of the three wind sensor: Viking, Pathfinder and REMS in total power to overheat ratio as a function of the Reynolds number for whole wind velocity range specified for each sensor and at given atmospheric conditions.	108
5.80	Space design of the three thermal anemometers used in Mars planetary mission in comparison of the Kn regime and $P\Delta T$ ratio for any possible variation of Martian conditions: pressure, temperature and flow velocity. Single unit and global wind sensor are shown for clarification.	109
5.81	Viking, Pathfinder and REMS wind sensor units in comparison for velocity range from 2 to 50 m/s for Martian atmosphere conditions adjust to: pressure 600 Pa and temperature 300 K. Different working behaviour for these three thermal anemometers have been reflected in a) power demand, b) temperature overheat, c) power to overheat ratio.	110
6.1	Spherical thermal anemometer concept of the hot point working with overheat to the wind ambient temperature.	117
6.2	Heat convection proportional to the root square of the wind speed and to the overheat value.	118
6.3	Heat delivered to the sensor surface split into three component of convection, conduction and radiation.	119
6.4	Reynolds Number as a function of flow velocity for given sphere diameter (D).	120

6.5	Measurement maximal and minimal wind velocity limit on Mars as a function of ambient temperature for hot sphere anemometer ($D = 9$ mm) working with constant overheat $\Delta T = 20$ K.	122
6.6	Thermal conductance of the overheated sphere as function of flow velocity for Mars-like atmospheric condition.	123
6.7	Mesh geometry of the sphere skin and the cylindrical volume.	125
6.8	Local heat flux, H [W/m^2K] over the 20 K overheated sphere surface with regard to the CO_2 wind flow velocity of 7 m/s incoming from $-\vec{Z}$ direction.	125
6.9	Spherical coordinates system.	126
6.10	a) Local heat flux, H approximation for sphere position as a function of ϕ angle; b) function of Z coordinate for $D = 15$ mm $P_{CO_2} = 650$ Pa, $T_{amb} = 220$ K, $T_{surf} = 240$ K, $U_f = 7$ m/s	127
6.11	Euler Rotation Angles	128
6.12	Thermal conductance G_{th} [mW/K] for different sector shapes and possible 3-D wind direction angle for wind flow $U_{flow} = 7$ m/s of $P_{CO_2} = 650$ K and $T_{amb} = 220$ K, $T_{surf} = 240$ K; a) two hemispheres, b) the eighth of the sphere.	130
6.13	Total convection heat for sphere as a function of wind magnitude for three ambient temperatures	131
6.14	Thermal conductance for the whole sphere as a function of the wind speed. Empirical model based on Feng&Michaelides (F&M) compared to FEM simulation results	132
6.15	Local heat flux at any point of a sphere as a function of angle Θ for wind incidence angle to be from $-\vec{Z}$ direction	133
6.16	a) Physical model of spherical shell division based on tetrahedron geometry into separated from each other four triangular sectors, b) real model has been made out in 3D printing technology from ABS material with upscale 5:1 (1 cent coin added for size reference). Sectors: #1, #3, #4 can be seen from the picture, whereas sector #2 is in the rear of the plot. Sectors orientation, according to the Cartesian coordinate system, is shown as well as theoretical wind incidence point (represented by black dot) described with polar angles Θ and Φ	134
6.17	Percentage of the total sphere convection heat rate transferred to the ambient by the triangular sector #1 as function of the wind direction angles (Θ , Φ). Values produced from the simulation data presented in Figure 6.15 according to the sector #1 orientation shown in Fig. 6.16.	135
6.18	Percentage of the total sphere convection heat rate which goes to the each of the four sectors as a function of wind angle Φ , for $\Theta=90^\circ$	135

LIST OF FIGURES

6.19 Angular sensitivity plots for two type of spherical geometries division into four equal sectors. Traditional biangle tessellation has been contrasted with a tetrahedral division. S_{Θ} and S_{Φ} for both geometries and wind speed of 5m/s can be observed for Φ rotation range 0° to 90° and for $\Theta=90^{\circ}$ 136

6.20 Angular sensitivity plots for tetrahedral sphere division a) S_{Θ} b) S_{Φ} . Analysis was done for particular ambient conditions: $T_{amb} = 220$ K, $U_{flow} = 5$ m/s, $\Delta T = 20$ K 137

6.21 Minimum angular sensitivity analysis of tetrahedral sphere structure working in CO₂ 600Pa atmosphere as a function of wind speed and for different ambient temperatures scenario at constant overheat $20^{\circ}C$ 138

6.22 Percentage heat rate solution for 3-D incidence angel example (Θ_{Ex} , Φ_{Ex}) together with other wind angle possibility that satisfies this particular share of each from the tetrahedral sectors. 139

6.23 Wind incidence angle discrimination from Computational Fluid Dynamics (CFD) simulation model of the power delivered to four triangular sectors, a) the Iso-percentage curves were superposed in order appoint cross section zone, b) the final wind incidence angle point ($\hat{\Theta}$, $\hat{\Phi}$), was determined by minimizing an error function. 139

6.24 Models of the spherical wind sensor components, a) triangular sector with its interior heat resistor mold, b) PCB with electrical layout and central core resistor, c) union of the two PCB's were mechanical support and electrical wiring are provided for each sector, d) four triangular sectors assembly. . . 141

6.25 Pictures of wind sensor triangular sectors, a) made out of Silver Sterling material (alloy Au 92.5%, Cu 7.5%) in a stereolithography 3-D printing commercial process, b) after tumbler polishing operations with progressive grit, c) after gold thin film (100 nm) deposition on the outer surface. 142

6.26 Picture of the spherical 'tetrahedral' wind sensor prototype, a) in the upside-down position for the wind tunnel chamber, b) in a perspective view after measurements in a Mars-like conditions. 143

6.27 a) Aarhus Mars wind tunnel facility AWTSI when opened b) 3-D hot sphere wind sensor setup with yaw rotation angle degree of freedom 144

6.28	Power delivered to the sectors, a) for different wind velocities and for wind direction angle Φ sequence [45°, 75°, 90°, 105°, 135°], b) zoom on the section where the wind velocity was 7m/s and only wind direction sequence is on display. CO ₂ atmosphere at $P = 10$ mBar and $T_{amb} = -18^\circ\text{C}$ conditions, for $\Theta = 90^\circ$ and overheat $\Delta T = 40^\circ\text{C}$	144
6.29	Polar plot of the average power delivered to the four sectors: a) sector #1, b) sector #2, c) sector #3, d) sector #4 as function of the wind speed and wind direction angle Φ , for $\Theta = 90^\circ$	145
6.30	Raw measurements of total power delivered to the sphere for different wind speed blowing from direction $\Phi = 45^\circ$ and $\Theta = 90^\circ$ together with mean power value calculated for each wind direction slot.	146
6.31	Mean power delivered to each sector and total sphere demand as a function of the wind speed for wind direction $\Theta = 90^\circ$ and $\Phi = 45^\circ$. Data selected from the Figure 6.28, whereas CFD curve was added from multi-physic numerical simulation for the same ambient parameters	147
6.32	Wind incidence angle discrimination from the real measurement of the power delivered to four triangular sectors. Iso-percentage curves were superposed in order appoint cross section zone. Final wind incidence angle point (Θ, Φ) was determined by minimizing an error function.	149

List of Tables

2.1	Orbital information about Mars and Earth, [16].	5
2.2	Planetary information about Mars in comparison to Earth, [16].	6
2.3	Atmosphere's parameters of Mars and Earth, [16]	7
2.4	Atmospheric composition of Mars and Earth, [16, 17].	7
5.1	Scientific requests for the REMS instruments, [18]	36
5.2	Measurement table of resistances R_{sens} , R_{heat} and ΔR resistances for several dice <i>type L</i> and <i>type N</i> at ambient temperature $\sim 25^\circ\text{C}$	67
5.3	Table of overheat value for ambient temperature at 0°C , where chip resistance parameters are as follow: $R_{ref0} = 7000 \Omega$, $\Delta R_{A,B,C,D} = 700 \Omega$ and $\alpha = 0.003 / ^\circ\text{C}$	81
5.4	Domains and equations	88
5.5	Averaged power of each from four hot dice array: P_A , P_B , P_C , P_D with its differential therms: <i>North-South (N-S)</i> and <i>East-West (E-W)</i> for different wind flow velocity (U_{flow}) and yaw (ϕ) incidence angle.	94
5.6	Main parameters of thermal unit elements (NA - Not Applicable).	102
5.7	Comparison of the wind sensor system for Viking [19, 20], Pathfinder [21, 22] and MSL-REMS [9]. *Power consumption data has been calculated according to the first order model proposed in Section (5.10.1) for CO_2 atmosphere: 300K, 600Pa, 50m/s.	112
6.1	FEM simulation conditions and geometry parameters.	124
6.2	FEM simulation boundary conditions	124
6.3	Percentage heat rate share	138
6.4	Measurement conditions.	144
6.5	Percentage power share from measurements.	148

Glossary

- ANSYS** Analysis System. xiv, 43, 44, 46
- ASI/MET** Atmospheric Structure Instrument/Meteorology Packaged. 28
- ASIC** Application Specific Integrated Circuit. 79, 146, 157
- ATS** Air Temperature Sensor. 37
- CAB** Center of Astrobiology. vii, xiv, 1, 30, 33, 34, 90, 157
- CCA** Constant Current Anemometry. 22, 29, 87, 103, 112
- CFD** Computational Fluid Dynamics. xx, xxi, 33, 43, 46, 84, 85, 128, 132, 137, 138, 139, 140, 147, 148, 150, 151, 153, 155, 158
- CNM** Centro Nacional de Microelectrónica. vii, 73
- COMSOL** Computers and Solutions. 87, 147
- CPA** Constant Power Anemometry. 22, 29, 154
- CRISA** Computadoras, Redes e Ingeniería , S.A.U.. 72, 90
- CSIC** Consejo Superior de Investigaciones Cientificas. 33, 90
- CTA** Constant Temperature Anemometry. 22, 23, 27, 43, 45, 103, 112, 118, 146, 151, 153, 154
- CTDA** Constant Temperature Difference Anemometry. 23, 43, 79, 103, 109, 112, 153, 154
- CVA** Constant Voltage Anemometry. 22
- DS** Dust Sensor. 115
- DSMC** Direct Simulation Monte Carlo. 14
- FEM** Finite Element Method. x, xiv, xv, xvii, xix, xxiii, 43, 44, 45, 46, 50, 80, 85, 86, 87, 88, 89, 92, 118, 123, 124, 132, 152

- FMI** Finnish Meteorological Institute. xiv, 33, 37, 115
- GTS** Ground Temperature Sensor. 36
- HS** Humidity Sensor. 37
- ICU** Instrument Control Unit. 35, 37
- IKI** Russian Space Research Institute. 115
- INTA** Instituto Nacional de Técnica Aeroespacial. vii, 2, 33, 90, 115, 157
- JPL** Jet Propulsion Laboratory. 1, 33, 34, 35
- LA** Lavochkin Association. 115
- LDA** Laser Doppler Anemometry. 92
- MEDA** Mars Environmental Dynamics Analyzer. 1, 157
- MEIGA** Mars Environmental Instrumentation for Ground and Atmosphere.
x, xi, 2, 115, 116, 117, 149, 154
- MetNet** Meteorological Network. 2, 115, 154
- MMPM** Mars MetNet Precursor Mission. 149
- MNL** MetNet Lander. 115
- MNT** Micro and Nanotechnology. 38, 45, 55, 68, 110, 111, 115, 149, 150,
151, 154, 157
- MSL** Mars Science Laboratory. xiii, xiv, xviii, xxiii, 1, 25, 29, 30, 33, 41,
45, 68, 100, 111, 112, 151, 157
- NASA** National Aeronautics and Space Administration. xiv, 1, 25, 33, 38,
111
- PCB** Printed Circuit Board. x, 37, 41, 54, 72, 73, 74, 79, 93, 146, 153, 154,
157, 158
- PS** Pressure Sensor. 37
- REMS** Rover Environmental Monitoring Station. ix, x, xiv, xv, xvi, xvii,
xviii, xxiii, 1, 2, 30, 33, 34, 35, 36, 37, 38, 39, 40, 41, 43, 46, 55, 56,
68, 75, 76, 79, 88, 89, 90, 92, 96, 97, 98, 99, 100, 102, 103, 104, 106,
107, 108, 109, 111, 112, 116, 117, 149, 151, 154, 156, 157

RSM Remote Sensing Mast. 35

SIS Solar Irradiance Sensor. 115

SWS Spherical Wind Sensor. 115

UPC Universitat Politècnica de Catalunya. xiv, xv, 30, 33, 34, 38, 45, 54, 55, 56, 68, 72, 111, 112, 149, 150, 152, 157

USA United States of America. 25

USSR Union of Soviet Socialist Republics. 25

UVS Ultraviolet Sensor. 37

WS Wind Sensor. 30, 37

WT Wind Transducer. xiv, xvii, 30, 34, 37, 38, 39, 40, 72, 98, 99

Chapter 1

Introduction

The thermal anemometry is a method which allows to estimate wind magnitude by the mean of measuring heat transfer to the ambient in a forced convection process. For Earth's atmosphere condition, this method is typically applied to the hot wires made of temperature dependent electrical conductor, typically platinum or tungsten, which working with overheat in reference to the ambient temperature estimate wind velocity. In the case of the low-pressure atmospheres, like this on Mars, the mean free path for molecules, due to the rarefied ambient conditions, is much bigger. Using hot wires designed for Earth in this conditions gives that heat exchange at a macroscopic scale which does not obey medium continuum model but rather reveals ballistic behavior. Thus, instead of using hot wire, a structure of bigger dimension like hot films are usually proposed for such a kind of application. The work included in this thesis is the contribution of the author Lukasz Kowalski to the goal of developing a new generation of wind sensors for the atmosphere of Mars. The work consists in the conception, design, simulation, manufacture and measurement of two novel types wind sensors based on thermal anemometers. Some aspects of the work during the development of this thesis has been reflected in author's paperwork like patent, articles and conference proceedings shown in references [1–12].

The first kind of concept has been developed in this thesis by using hot silicon die made out of silicon wafer of approximate size: 1.5 x 1.5 x 0.5 mm with platinum resistances deposited on top in order to heat it and sense its temperature. These work was been a part of the bigger undertaking under the project CYCYT: "*Colaboración en el desarrollo de la estación medioambiental denominada REMS*" (Ref. C05855). Inside the project REMS author of the thesis was responsible for sensor shape development and concept validation of proposed geometry. Thermal-fluidical model of the device, as well as characterization and behavior, were analyzed for a simplified 2-D wind model for typical Martian atmospheric conditions. The leader of the project Center of Astrobiology (CAB) was in charge of extrap-

olated 2-D model results into a full 3-D model by placing six 2-D sensors on two supporting booms. The use of six independent 2-D measurements provides enough redundancy for the use of an inverse algorithm to estimate 3-D wind parameters. REMS was a Spanish contribution to the NASA mission MSL which has been a great success since rover Curiosity has landed on Mars on 6th August 2012 (1:32 a.m. Eastern Standard Time) at the foot of a layered mountain inside Gale Crater. Since then has been constantly running experiments on the *Red Planet* sending data to Earth for interpretation. Currently, author of the thesis is participating in similar Jet Propulsion Laboratory (JPL) mission Mars 2020, where aboard of the new Rover will be Spanish instrument Mars Environmental Dynamics Analyzer (MEDA) incorporating new improved in performance and efficiency wind sensor build out of similar silicon hot die units as it was in the case of REMS. This project is in its beginning phase and won't be addressed in this document.

From the experience and knowledge gained during REMS project, the author came out with an idea of the novel spherical sensor structure overcoming some fragility problems detected in the REMS wind sensor. The new 3-D wind sensor concept, besides this advantage, also provided a radical simplification of data post-processing providing the comprehensive thermal model based on numerical simulation for any possible wind occurrence. This new device has been developed under Spanish Ministry of the Science and Innovation project: "*Sensor de viento para la superficie de Marte para la misión Metnet (fase inicial)*" (Ref. AYA-2010-20847) and "*Sensor de viento para la superficie de Marte para la misión Meteorological Network (MetNet) (Modelo de Ingenieria)*" (Ref. AYA-2011-29967-C05-04). This project, denominated as MEIGA, was a join effort of many Spanish institutions under the leadership of INTA for the development of space technology for Mars-oriented application in a framework of an upcoming space mission.

To sum up, author's work include contributions to the development of two wind sensor concepts:

- REMS wind sensor on board of the rover Curiosity in the surface of Mars since August 6th 2012, that is described in paperwork [1–9] (Appendix A, Appendix B, Appendix C, Appendix D, Appendix E, Appendix F, Appendix G, Appendix H).
- Spherical wind sensor concept developed in a course of MEIGA project and described in paperwork [10–12] (Appendix I, Appendix L).

Chapter 2

Mars We Know

The main objective of this chapter is to present information about planet Mars, so the reader will understand the need of further in-situ exploration of the Red Planet. Up to date, knowledge of this land is wide and comprehensive, extensively published, [23–25]. Some chosen facts, related to this thesis will be presented. In the first section I will describe Mars position inside the Solar System. In the second section I will present the most important details about geology and Mars landscape. Finally in the third section I will give information about Martian climate. Although Mars is one of the closer celestial body in our terrestrial neighborhood is different to our natural environment we human live in, so it is logical that in many occasions it's parameters will be contrasted with the Earth's ones.

2.1 Orbit of Mars

Mars is the fourth planet of our Solar System situated in between the Earth and the much bigger Jupiter, see figure 2.1.

We were aware of it existence from the prehistoric times. Ancient Greeks called the red-bloody spot on the sky *Ares*, as their god of war, whereas for Romans it was *Mars* also named after the god of war. Status of planet comes from Greek word *planetes* which means *wanderer*. Mars together with Mercury, Jupiter and Saturn gained their migrant status as observed from the ground the trajectories of these shinny points on the sky were not in shape with the fixed stars on the firmament. What's more, the disordered movement of Mars was identified with a chaos during times of war, [27]. The other thing that has been noticed for Mars, as seen from Earth, was that his brightness is not at the constant level. These two intriguing question of Mars behavior have been resolved not sooner as his orbit had been revealed. What in the past geocentric theories was believed to have mysterious character and be assign to the over-natural phenomena today is well known and thanks to the modern heliocentric solar system model it is easy to calculate relative

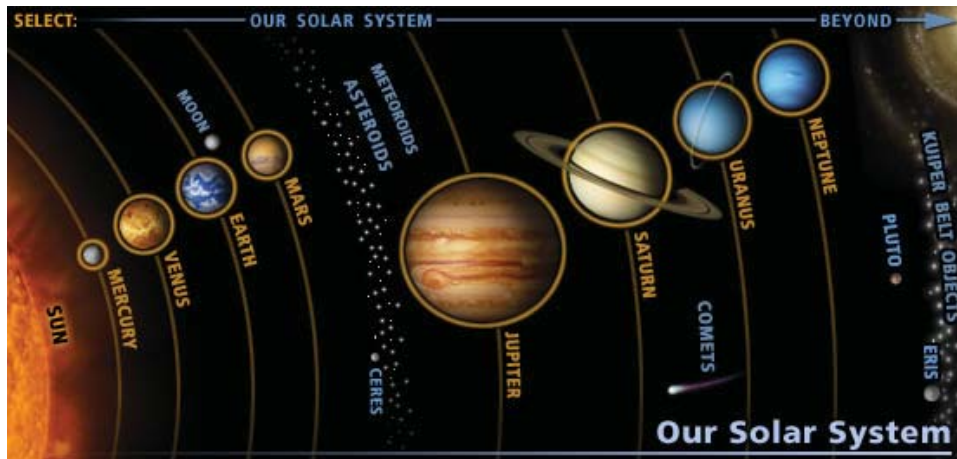


Figure 2.1: Our Solar System [26]

position of Mars according to its sister planet Earth. Nowadays, modern astronomy resolving equations of perpetual movement of the planets against the gravity force of the Sun on their orbits says, that on 26 August 2003 Mars was just 55.8 million kilometers from the Earth - the closer distance between these two planets from almost 60,000 years.

Whereas Earth orbit is more or less circular maximum and minimum distance from the Sun are about 150 million kilometers, the Perihelion and Aphelion for Mars vary more than 20%. However elliptical orbit for Mars doesn't change the fact that average distance from the Sun is more than one and half times greater than for Earth. For Mars semi-major axis is 230 million kilometers what will result in weakest solar radiation onto its surface. A full Martian day is called *sol* and lasts 24.66 hours, so 40 minutes longer than length of the day on Earth. To make one revolution around the Sun from one point in its seasonal orbit to the equivalent point Mars needs about 687 sols, whereas for the Earth one year lasts 365.25 days. In case of Mars the tilt of the body's equator relative to the body's orbital plane is about 2 degrees. More details can be seen in Table 2.1.

2.2 Planet Mars

Mars is smaller in comparison with Earth. The radius of Mars is about half of the Earth one, and its mass is almost ten times smaller than our planet. What is interesting is that the entire surface of Mars is equivalent to the land surface of Earth. This is because Mars nowadays doesn't have oceans, see Figure 2.2.

Lack of water reservoir effects in less heat momentum of inertia which reveals faster temporal changes of temperature on Mars. The core of the

	Mars	Earth	Mars/Earth
Semi-major axis, 10^6 km	227.92	149.60	1.524
Perihelion, 10^6 km	206.62	147.09	1.405
Aphelion, 10^6 km	249.23	152.10	1.639
Sidereal orbit period, days	686.980	365.256	1.881
Tropical orbit period, days	686.973	365.242	1.881
Mean orbital velocity, km/s	24.13	29.78	0.810
Max. orbital velocity, km/s	26.50	30.29	0.875
Min. orbital velocity, km/s	21.97	29.29	0.750
Orbit inclination, deg	1.850	0.000	–
Orbit eccentricity	0.0935	0.0167	0.599
Sidereal rotation period, hrs	24.6229	23.9345	1.029
Length of day, hrs	24.6597	24.0000	1.027
Obliquity to orbit deg	25.19	23.45	1.074

Table 2.1: Orbital information about Mars and Earth, [16].

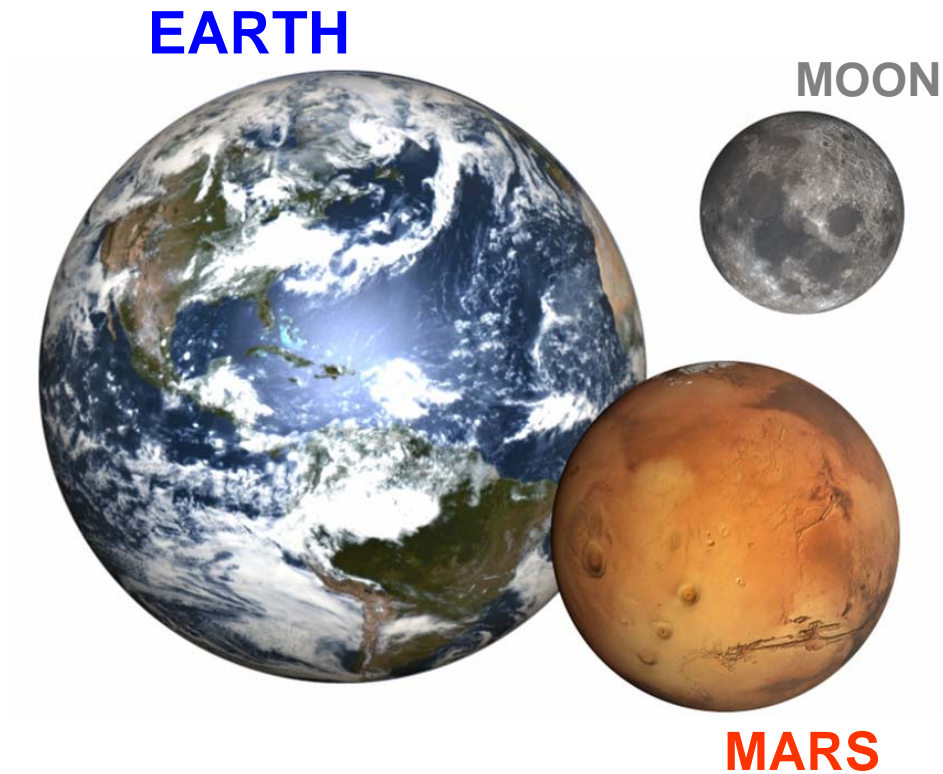


Figure 2.2: Earth, Mars and Moon in the same scale, [13].

	Mars	Earth	Mars/Earth
Mass, 10^{24} kg	0.64185	5.9736	0.107
Volume, 10^{10} km ³	16.318	108.321	0.151
Mean radius, km	3389.5	6371.0	0.532
Core radius, km	1700	3485	0.488
Mean density, kg/m ³	3933	5515	0.713
Surface gravity, m/s ²	3.71	9.80	0.379
Escape velocity, km/s	5.03	11.19	0.450
Solar irradiance, W/m ²	589.2	1367.6	0.431
Black-body temperature, K	210.1	254.3	0.826
Topographic range, km	30	20	1.5
Natural satellites	Phobos, Deimos	Moon	2

Table 2.2: Planetary information about Mars in comparison to Earth, [16].

Mars is a half size of the core of Earth but on that point similarities ends because Mars core is solid so it not produce a stable magnetic field which would protect planet from cosmic gamma rays. Mars has got two moons: *Deimos* and *Fobos*. Provided that Mars is much lighter planer than Earth we would expect also less gravitational field and indeed surface gravity on Mars is about 3 times weaker than on the sea level of Earth. Wider comparison has been presented in Table 2.2.

2.3 Atmosphere of Mars

Mars has its own atmosphere. What stands out at the first glance is that Mars atmosphere is much weaker in comparison with Earth. Mars surface pressure is about 150 times smaller than on Earth and its typical value is 6 mBar. As a consequence of the low pressure the surface density is also two orders of magnitude smaller in comparison to Earth. So the mass of 1 cubic meter of Martian air is about 20 g, whereas for Earth it is more than 1.2 kg. Smaller gravitational force for Mars makes pressure change with height larger than on Earth, so every 11.1 km of high the atmospheric pressure shrinks 2.72 times (factor e). Martian atmosphere details in comparison to Earths are show in Table 2.3.

Taking into account that Mars is a smaller planet than Earth and also its thin atmosphere it is not surprising that total mass of Martian atmosphere is about 200 times smaller than the one we are familiar with - literally there is very little atmosphere on Mars. Nevertheless, this small amount of Martian air rise scientific interest and provoke discussion about its characteristics and behavior. Mars, since is much farther away from the Sun than the Earth, receives lees solar radiation so is a colder planet. The average temperature near to the surface of Mars crust is about $-63^{\circ}C$. The rarefied atmosphere

2.3. ATMOSPHERE OF MARS

	Mars	Earth
Surface pressure, mbar	4...9	1014
Surface density, kg/m ³	0.020	1.217
Scale height, km	11.1	8.5
Total mass of atmosphere, kg	2.5 x 10 ¹⁶	5.1 x 10 ¹⁸
Average temperature, K (°C)	210 (-63)	288 (15)
Diurnal temperature range, K	184 ... 242	283 ... 293
Diurnal temperature range, °C	-125 ... +25	10 ... 20
Wind speeds, m/s	2 to 30	0 to 100
Mean molecular weight, g/mole	43.34	28.97

Table 2.3: Atmosphere's parameters of Mars and Earth, [16]

	Mars	Earth
Carbon Dioxide, CO ₂	95.32%	380 ppm
Nitrogen, N ₂	2.7%	78.08%
Argon, Ar	1.6%	0.934%
Oxygen, O ₂	0.13%	20.95%
Carbon Monoxide, CO	0.08%	0.10 ppm
Methane, CH ₄	0.0105 ppm	1.70 ppm
Water, H ₂ O	210 ppm	0.40%
Nitrogen Oxide, NO	100 ppm	-
Neon, Ne	2.5 ppm	18.18 ppm
Hydrogen-Deuterium-Oxygen, HDO	0.85 ppm	
Hydrogen, H ₂	-	0.55 ppm
Krypton, Kr	0.3 ppm	1.14 ppm
Xenon, Xe	0.08 ppm	0.09 ppm
Helium, He	-	5.24 ppm

Table 2.4: Atmospheric composition of Mars and Earth, [16, 17].

and the lack of oceans, which would accumulate heat energy, provokes high fluctuation of diurnal profile of temperatures which are driven by the sun energy. Martian atmosphere is composed mostly with CO₂ and other gases like N₂, Ar, O₂ and CO. Molecular oxygen is not present in the Martian atmosphere like it is on the Earth, and water vapor is just in the very little quantities in comparison to the Earth conditions, for more details see Table 2.4.

Mars is a dusty environment. The average size of the suspended dust particles is 1.5 μm .

Very low pressure on Mars influence the average distance covered by a gas particles between of successive impacts. This parameters is called the mean free path (λ). For an ideal gas modeled as rigid spheres can be related

to the atmospheric temperature (T) and pressure (P) via following equation:

$$\lambda = \frac{k_B T}{\sqrt{2} \pi d^2 P} \quad (2.1)$$

where k_B is Boltzman constant $k_B = 1.3806504(24)e^{-23}$, and d is the collision diameter of the molecules, mainly CO_2 , $d_{CO_2} = 4.426 \text{ \AA}$. Even though, Mars features much lower temperatures than Earth atmosphere and bigger collision diameter for carbon dioxide molecules than average value for terrestrial air $d_{AIR} = 3.711 \text{ \AA}$, a more than one hundred times lower pressure makes mean free path much larger, see Figure 2.3.

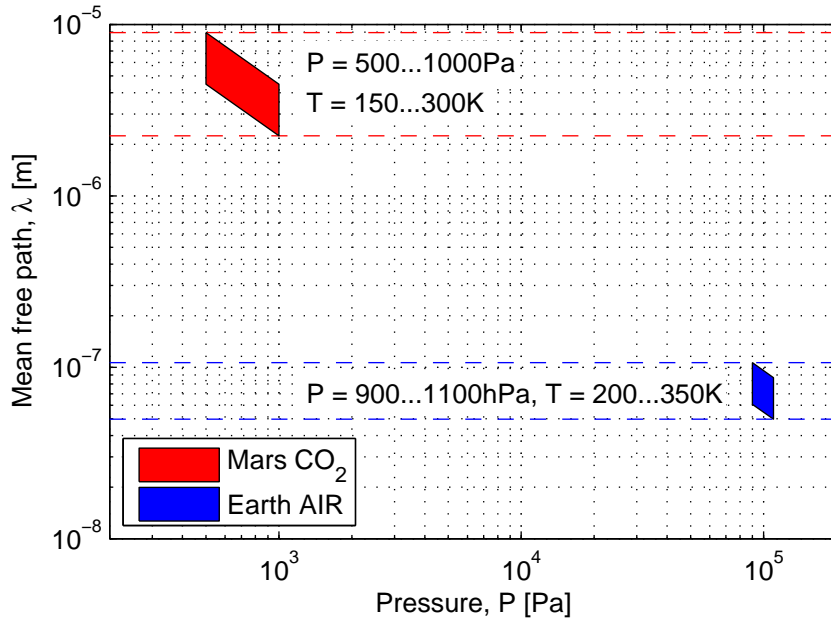


Figure 2.3: Comparison of mean free path for Mars and Earth atmosphere according to the typical pressure and temperature variation.

It stands out the the Mars mean free path is about two order of magnitude larger than on Earth. For Mars it is from 2 to 9 μm , whereas for Earth it is 50 to 100 nm. This fact will turn out to be crucial in defining the flow regimes in which wind measurement devices will be designed to work in.

From the 2.3 it can bee seen that have been considered possible pressure variation form 5 mBar to 10 mBar. This is so, because on Mars has been observer large diurnal and seasonal variation of the pressure. What's more, local ambient pressure would also depends on landing site elevation. This has been reported by Smith in [14] according to the Viking 1 and the Viking 2 planetary mission data and has been reproduced in this thesis in Figure 2.4.

The offset between the two curves in Figure 2.4 is caused by the elevation difference (1.2 km) between the two landing sites. Carbon dioxide cycles be-

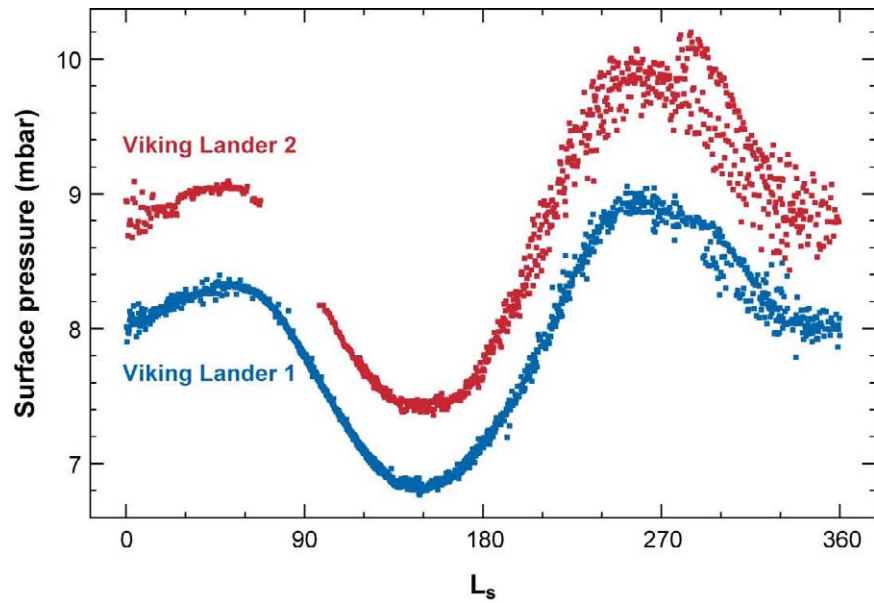


Figure 2.4: Surface atmospheric pressure over a Martian year, recorded by the Viking landers and showing seasonal fluctuation. The two landers recorded different absolute pressures because they were sited at different altitudes. Image courtesy of Annual Reviews [14].

tween the atmosphere and the polar caps, where it freezes out in winter, so that surface atmospheric pressure fluctuates by nearly 30% in a normal year.

Note that, Martian seasonal dates are usually given in terms of areocentric longitude (L_s), which describes the location of Mars in its orbit around the Sun. $L_s = 0^\circ$ is defined as Northern Hemisphere spring equinox (Southern Hemisphere fall equinox), with $L_s = 90^\circ$, 180° , and 270° , following as Northern Hemisphere summer solstice, fall equinox, and winter solstice, respectively.

Chapter 3

Thesis Background

In this chapter some aspects of the wind phenomena will be explained. The meaning of the word *wind* will be presented. The way wind affects different matters will be shown as well as the mechanism of its creation. Then it will be presented physical mechanism of heat transfer focusing on heat convection phenomena as it can be forced by the wind and is the base of thermal anemometry. Then series of the dimensionless numbers that helps to describe the flow regime and predict its behavior will be introduced.

3.1 Wind definition

Wind is the flow of gases on a large or local scale. On a planet like Earth or Mars, wind consists of the bulk movement of air. In meteorology, winds are often referred to according to their speed, and the direction it is blowing from. In *UXL Encyclopedia of Science*, [28] wind definition is stated as follow: "**Wind** refers to any flow of air above Earth's surface in a roughly horizontal direction. A wind is always named according to the direction from which it blows. For example, a wind blowing from west to east is a west wind. The ultimate cause of Earth's winds is solar energy. When sunlight strikes Earth's surface, it heats that surface differently. Newly turned soil, for example, absorbs more heat than does snow. Uneven heating of Earth's surface, in turn, causes differences in air pressure at various locations. Heated air rises, creating an area of low pressure beneath. Cooler air descends, creating an area of high pressure. Since the atmosphere constantly seeks to restore balance, air from areas of high pressure always flow into adjacent areas of low pressure. This flow of air is wind. The difference in air pressure between two adjacent air masses over a horizontal distance is called the pressure gradient force. The greater the difference in pressure, the greater the force and the stronger the wind."

In human civilization wind was always present. Was used as a power

source in transportation for ship voyages across the Earth's oceans as well as for hot balloon trips which, using the wind blow, reduced other fuel consumption. Man learned how to harness the wind to use its forces for mechanical work as it is in case of windmills and as a source of energy in case of wind power plants, see Figure 3.1. But wind also brings danger when it comes unexpected with destructive power. It can lead to hazardous situations for aviation vehicles, but also break down of the man-made construction, trees and other natural formations. From a planetary view, wind did and is constantly forming earth surface; it forms eolian soils, empowers erosion, arranges dunes in the desert zones. Wind also spreads wildlife by dispersing seeds or enabling reaching further distance for flying insects and birds population. But sometimes wind has a negative impact over wildlife. It affects animal stashed methodology when it brings cold temperature within and also changes hunting and defense strategies when it occurs in unpredictable patterns.

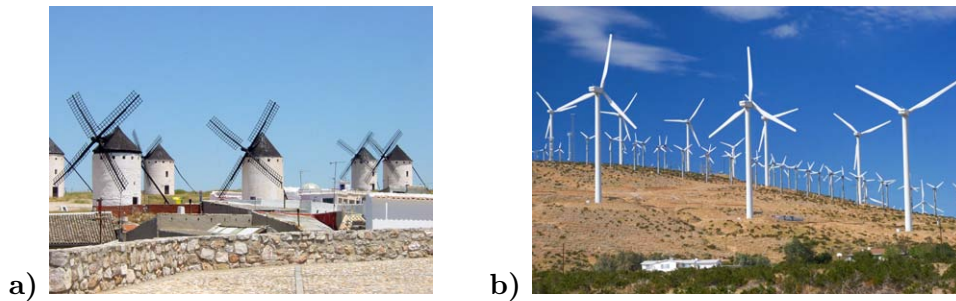


Figure 3.1: Example of how humans harness the energy of the wind a) windmill, b) wind power plant.

Wind is caused by differences in the pressure. Whenever a difference in pressure exists, the air accelerates from the higher pressure area to the lower pressure region. In case of rotating planet other cause for the wind occurrence will be related with Coriolis effect. Movements of air in the atmosphere are notable examples of this behavior: rather than flowing directly from areas of high pressure to low pressure, as they would on a non-rotating planet, winds and currents tend to flow to the right of this direction north of the equator, and to the left of this direction south of the equator whereas winds in the proximity to the equator line are not affected by this force. This effect is responsible for the creation rotational large cyclones and air wave phenomena.

There is no doubt that measuring the force of nature, which is the wind, is very important for a society. In order to characterize wind the typical measurement will consist on wind velocity and direction, which is reported by the direction from which it originates. A device which is used for wind measurement is often called an *anemometer*.

The *thermal anemometer* is a device which is normally operated with higher than ambient temperature what result in heat transfer to the ambient enhanced by the associated wind. This phenomena of forced cooling which is modulated be the wind parameters (speed and direction) was a motivation to employ physical mechanism of heat transfer in state of art wind transducer to operate on Mars.

3.2 Physical mechanism of heat transfer

Heat transfer is the mechanism that transfers heat energy to or from an object. There are three basics mechanism of heat transfer: conduction, convection and radiation. When two objects interchange heat, the heat transfer goes naturally from the higher temperature object to the lower temperature object. However, it is possible to transfer heat from the object of the lower temperature toward other object of higher temperature but in this process additional energy need to be provided for the system like it is in the case of *Peltier effect*. Focusing on natural heat transfer mechanism implies that in order to occur heat transfer there must be temperature difference. In solids heat transfer is by conduction but also radiation take place. In fluids, however, heat transfer mechanisms aren't the same. Whenever fluid is in motion we deal with convection, in case of no bulk fluid motion dominates heat transfer by the conduction. Actually the higher velocity of the fluid, the higher rate of heat transfer, and this is because it brings into contact hotter and cooler chunks of fluid increasing rate of the conduction. In gases the heat transport phenomena situation is even more biased to convection. Convection is the most complex mechanism of heat transfer. It depends not only on gas properties but also on geometry of solid surface and the type of the fluid.

The rate of the convection heat \dot{Q}_{conv} is observed to be proportional to the temperature difference according to Newton's law of cooling:

$$\dot{Q}_{conv} = hA_s(T_s - T_\infty) \quad (3.1)$$

where h is the convection heat transfer coefficient, A_s is the heat transfer surface, T_s is the temperature of the surface, T_∞ is the temperature of the fluid sufficiently far from the surface (in the infinite distance from the surface). The heat transfer coefficient encompasses all the complexity of the convection process and it is what makes it difficult to predict. Indeed, it can be simply determine from the equation (3.1) as a rate of heat transfer between a solid surface and a fluid per surface area and per temperature difference as follow:

$$h = \frac{\dot{Q}_{conv}}{A_s(T_s - T_\infty)} \quad (3.2)$$

In order to model convection heat transfer coefficient for arbitrary proposed shape and flow conditions additional variables are suggested for consideration. Common practice is to introduce dimensionless variables. The most commonly uses are: Knudsen number (Kn), Reynolds number (Re), Prandtl number (Pr), Nusselt number (Nu), and Mach number (Ma), Grashof number (Gr).

3.2.1 Knudsen number

The Knudsen number (Kn) is a dimensionless number defined as the ratio of the molecular mean free path (λ) length to a representative physical length scale sometimes known as a characteristic length (L_c).

$$Kn = \frac{\lambda}{L_c} \quad (3.3)$$

This length scale could be, for example, the radius or characteristic length of a body in a fluid or gas. Therefore, the Knudsen number determines the degree of gas rarefaction and is useful for determining whether statistical mechanics or continuum mechanics formulation of fluid dynamics should be used. According to the classification upon the magnitude of the Knudsen number systems are divided into three, sometimes four, regions, see Figure 3.2.

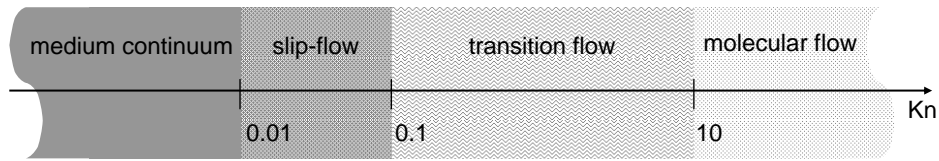


Figure 3.2: Four different flow regimes according to the Knudsen number value.

Region, where $Kn < 10^{-2}$, is known as *medium-continuum* and for this region Navier-Stokes equations which describes the motion of viscous fluid substances are valid. These complex equations are not required in this thesis and therefore won't be discuss here for simplicity.

In contrast, region where $Kn > 10$ is know as *free molecular flow* revealing ballistic effects where analysis is no longer possible.

In the middle of this two regime fluid can neither be considered an absolutely continuous medium nor a free molecular flow. Therefore, further sub-classification is introduced in another two regimes.

Thus, we have *slip-flow* for range of $10^{-2} > Kn > 10^{-1}$ where the Navier-Stokes equation still can be used to provide tangential slip velocity boundary conditions which are implemented along the solid walls.

Finally, situated in between free molecular flow and slip-flow regime $10^{-1} > Kn > 10$ we have a *transition flow* when continuum assumption starts to break down but still exist alternative methods of analysis using the Burnett equations or particle based on Direct Simulation Monte Carlo (DSMC). Nevertheless, in this last mention region, also shortly named *Montecarlo*, is very difficult to predict correct and recurrent solutions.

When we work in the continuum medium flow regime, the gas flowing over non-porous surface literally sticks to the surface in the close proximity so we assume a zero relative velocity to the surface. This phenomena is know as no-slip condition and it is responsible for development of velocity profile for flow. Because of the friction between each fluid layer, the layer that stick to the surface slows the adjacent fluid layer, which next slows another layer and this phenomena propagates. This non-slip condition is specially important when we want to provide reliable and recurrent calculation of convection heat transfer coefficient for the solid item immersed into fluid/gas environment.

3.2.2 Reynolds number

The Reynolds number (Re) is a dimensionless number that gives a measure of the ratio of inertial forces ($\rho U^2/L_c$) to viscous forces ($\mu U/L_c$) and consequently quantifies the relative importance of these two types of forces for given flow conditions. Therefore, Reynolds number can be calculated as follow:

$$Re = \frac{\rho U L_c}{\mu} \quad (3.4)$$

where ρ is the gas density, U is the velocity of the fluid, L_c is the characteristic size of length and μ is the dynamic viscosity of the fluid. Reynolds number differentiates between two flow regimes: laminar or turbulent. Laminar flow occurs at low Reynolds numbers, where viscous forces are dominant, and is characterized by smooth, constant fluid motion. Turbulent flow occurs at high Reynolds numbers and is dominated by inertial forces, which tend to produce random eddies, vortices and other flow instabilities. Graphical interpretation of both laminar and turbulent regimes are shown in Figure 3.3.

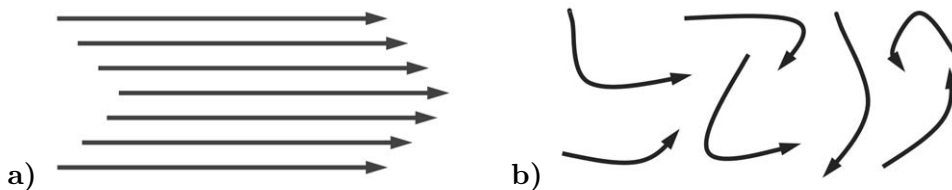


Figure 3.3: Character of different flow regimes: a) laminar, b) turbulent.

Thus, for given geometry and fluid condition, for small velocities flow has laminar character, whereas for high speed may happen that it will be turbulent. The Reynolds number at which the flow becomes turbulent is called the *critical Reynolds number* and its value is geometry dependent.

3.2.3 Nusselt number

The Nusselt number (Nu) is a dimensionless convection heat transfer coefficient which represents the enhancement of the heat transfer through the fluid layer as a result of convection in relation to conduction across the same fluid layer. Having the fluid chunk of thickness L_c and temperature difference ΔT at each side we have heat transfer drive by two different phenomena. If the fluid is motionless we will have conduction heat flux rate \dot{q}_{cond} given by equation:

$$\dot{q}_{cond} = k \frac{\Delta T}{L_c} \quad (3.5)$$

where k is the thermal conductivity of the fluid. But when fluid involves some motion we have somehow bigger convection heat flux rate \dot{q}_{conv} which can be describe as:

$$\dot{q}_{conv} = h\Delta T \quad (3.6)$$

Therefore, when fluid motion is present we observe the heat flux rate enhancement. The ratio between conduction heat flux against convection heat flux is being described as a Nusselt number Nu and can be found from both equation(3.5) and equation (3.6) as follow:

$$Nu = \frac{\dot{q}_{conv}}{\dot{q}_{cond}} = \frac{h\Delta T}{k\Delta T/L_c} = \frac{hL}{k} \quad (3.7)$$

The case, when $Nu = 1$, is when we deal with pure heat conduction across the fluid layer, no motion is registered.

3.2.4 Mach number

The Mach number (Ma) is defined as the speed of an object moving through air, or any fluid substance, divided by the speed of sound as it is in that substance

$$Ma = \frac{U}{U_s} \quad (3.8)$$

where U is the speed object relative to the medium, U_s is a speed of sound in the medium.

Therefore, we need to define the speed of sound U_s , which for the ideal gas is given by the equation:

$$U_s = \sqrt{\frac{\gamma RT}{M}} \quad (3.9)$$

where γ is heat capacity ratio, R is a ideal gas constant, T is a gas temperature, M is a molar mass.

Six different flow regimes can be distinguish depending on the Mach number value as a result of Equation (3.8):

- *subsonic*: $Ma < 1$
- *transonic*: $0.8 < Ma < 1.2$
- *sonic*: $Ma = 1$
- *supersonic*: $1 < Ma < 5$
- *hypersonic*: $5 < Ma < 10$
- *high-hypersonic*: $Ma > 10$

Mach number, however has another implication. It has been observed that knowing Ma value helps recognize whether gas flow can be modeled as compressible or incompressible. It is assumed that gas flow is incompressible when its density changes are less than 5% withing the analysis region. This happens when the flow relative velocity is less than 30% of speed of sound; what literally means the $Ma < 0.3$.

3.2.5 Grashof number

The Grashof number (Gr) is a dimensionless number in fluid dynamics and heat transfer which approximates the ratio of the buoyancy to viscous force acting on a fluid. It frequently arises in the study of situations involving natural convection. Grashof number is described be algebraic equation:

$$Gr = \frac{g \cdot \beta \cdot (T_s - T_\infty) \cdot L^3}{\nu^2} \quad (3.10)$$

where, g is acceleration due to Earth's gravity or other celestial body considered, β is the coefficient of thermal expansion (equal to approximately $1/T$, for ideal gases), T_s is the surface temperature T_{inf} is the bulk temperature and L is the characteristic size of the body exposed to the natural convection process. In case of o sphere, the characteristic size is its diameter.

3.2.6 Velocity boundary layer

If we have a parallel flow over a flat surface, at the edge of the surface flow approaches the object with the uniform upstream velocity profile U_∞ . Then, in case of medium continuum flow, where gas particles stick to the surface of the plate, we will have the very first layer of the gas with zero velocity. This layer will slow down the following layer so we will have piled numbers of layers of flow with different velocities till eventually on the top of it will exist layer with free flow velocity, see Figure 3.4.

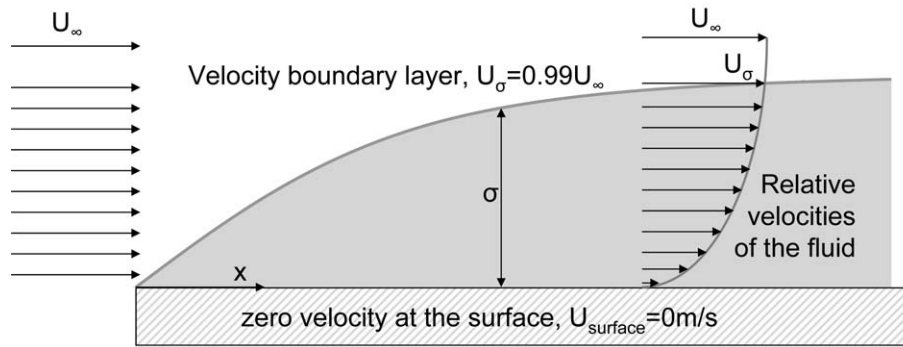


Figure 3.4: Velocity boundary layer for flow medium continuum regime.

Therefore, over the plate will exist a region where velocity will be smaller than free stream velocity U_∞ . This zone is called *boundary layer region* and his boundary layer thickness δ is defined as the distance where corresponding flow velocity is $U_\delta = 0.99 U_\infty$. The region between the surface of the plate and velocity boundary layer obeys the viscous shearing forces caused by fluid viscosity. Whereas, above this border δ frictional effects are neglected and velocity remains constant. This zone is called *inviscid flow region*.

3.2.7 Thermal boundary layer

Thermal boundary layer develops in very similar way as a velocity boundary layer. As the fluid with temperature T_∞ flow over the isothermal surface with uniform temperature T_s the temperature profile above the surface develops. The motionless fluid particles with contact with the surface will reach thermal equilibrium with plate and the same the temperature T_s . Then this particle will exchange heat with proximity particle above layer and so on. In a result of this process we will observe region above the hot surface where variation of the temperature between T_s and T_∞ is significant and this region will develop in the flow direction. The thickness of the thermal boundary layer is defined as the distance from the surface at which the temperature difference $T - T_s = 0.99 (T_\infty - T_s)$. It is worth to mention that thickness of the thermal boundary layer increases in the flow direction. Thermal boundary

layer has a special significance because temperature gradient at the location is directly related to the convection heat transfer. Therefore the shape of the temperature profile inside thermal boundary layer governs convection heat transfer between solid surface and the fluid flowing over it.

3.2.8 Prandtl number

The Prandtl number (Pr) is a parameter that relates the thicknesses of the velocity and thermal boundary layers. This dimensionless parameter defined as a ratio of the viscous diffusion rate to thermal diffusion rate is given by the following equation:

$$Pr = \frac{\nu}{\alpha} = \frac{\mu/\rho}{k/(\rho C_p)} = \frac{\mu C_p}{k} \quad (3.11)$$

where ν is the kinematic viscosity, α is the thermal diffusivity μ is the dynamic viscosity, ρ is the density of the fluid, k is the thermal conductivity and C_p is the specific heat at constant pressure.

Having developed both velocity boundary layer and thermal boundary layer we can deliberate which one has bigger impact on convection heat transfer process. But there is no doubt that this is a fluid velocity that has a strong influence on temperature profile. Thinking that way we conclude that development of the velocity boundary layer relative to the thermal boundary layer will have significant effect on the convection heat transfer.

Different materials reveals different Prandtl number value. Liquid metal has Prandtl number less than 0.01, when for heavy oils $Pr > 100000$. For gases Prandtl number is about 1 which means that both momentum and heat dissipate through the gas at about the same rate it also means that thickness of the velocity boundary layer will be similar to the thickness of the thermal boundary layer. It is worth to notice that Prandtl number no contains length scale in its definition and depends only on the fluid properties and the fluid state.

3.2.9 Mars atmosphere gas properties

To calculate dimensionless numbers in all cases it is necessary to know atmospheric gas properties. Since Mars is composed in more than 95% of carbon dioxide, the Martian atmosphere properties can be simplified to the CO_2 properties. Three of them depends only on temperature: thermal conductivity (k), dynamic viscosity (μ) and specific heat (C_p), whereas gas density (ρ) depends on temperature and pressure.

- **Thermal conductivity**, k [W/(m·K)] describes property of the gas medium to conduct heat and depends linearly of CO_2 absolute temperature T in Kelvin unit according to the [29] as follow:

$$k = [9.6 + 0.072 \cdot (T - 200)] \cdot 10^{-3} \quad (3.12)$$

- **Dynamic viscosity**, μ [$Pa \cdot s$] of a fluid expresses its resistance to shearing flows, where adjacent layers move parallel to each other with different speeds. This gas parameter depends on temperature as stated in Sutherland formula [30]:

$$\mu = \mu_0 \cdot \frac{T_0 + C}{T + C} \cdot \left(\frac{T}{T_0}\right)^{3/2} \quad (3.13)$$

where μ_0 , T_0 , and C are constants found experimentally for given specific gas. In case of carbon dioxide this constant have following values: $\mu_0 = 14.8 \cdot 10^{-6}$ Pa·s, $T_0 = 293.15$ K, $C = 240$ K.

- **Specific heat capacity**, C_p [J/(kg·K)] is the ratio of the heat added to (or removed from) an object to the resulting temperature change in relation to the unit mass. This properties depends directly to the carbon dioxide absolute temperature , which from lineal interpolation has been extrapolated from [31] and modeled as follow:

$$C_p = 530 + 1.037 \cdot T \quad (3.14)$$

- **Density**, ρ [kg/m³] (sometimes known as volumetric mass density) of a substance is its mass per unit volume. This properties for gases is strongly affected be temperature T and pressure P and for ideal gas can be described as:

$$\rho = \frac{M \cdot P}{R \cdot T} \quad (3.15)$$

where M is a molar mass and R is a ideal gas constant equal to 8.3144621 J/(mol·K). Molar mass of carbon dioxide molecule M_{CO_2} [g/mol] can be calculated as a sum of one molar weigh of atomic carbon (M_C) and two molar weight of atomic oxygen (M_O):

$$M_{CO_2} = M_C + 2 \cdot M_O = 12.0107 + 2 \cdot 15.9994 = 44.0095 \quad (3.16)$$

Thus, molar mass of carbon dioxide atmosphere is $M_{CO_2} \approx 44$ g/mol.

3.3 Thermal flow sensors

Based on the phenomena of the convection cooling of the hot object immersed in moving flow (liquid or gas) a whole variety of the flow sensors has been proposed. The rate of the heat being drained from the sensor/device to the ambient will depend not only on the flow parameters but sometimes when we got a group of hot elements also of its geometry and orientation in reference to the wind direction. It has been observed and is well known that part which are in upstream are refrigerated more efficient than those being in the thermal shadow of the rear side of the group. From these two facts, the thermal flow sensors can be divided into two groups:

- thermal anemometers
- calorimetric sensors

3.3.1 Thermal anemometers

Thermal anemometer is a single unit working in overheat to the ambient which is capable of measuring heat loss in the process of convection. Then this heat drain thanks to model of convection phenomena in reference to the achieved overheat is translated into wind speed parameter. The classic example of the thermal anemometer will be a hot wire wind sensor, where power P , overheat ΔT and wind speed U dependence is known today as a King's Law:

$$P = \left(A + B\sqrt{U} \right) \cdot \Delta T \quad (3.17)$$

where A and B are the constant that depends on many parameters among which are: gas parameters (k, Cp, μ, ρ) and wire geometrical properties (d, L) as well as heat conduction losses by the boundary support components. What was surprising and reported over century ago by the King in [32], was that particular thin hot cylinder/wire behavior can be modeled by simple Equation (3.17) which parameters A and B once found experimentally are valid for flow measurement purpose out of the lab of course for similar room temperature. King in his work has recommended also to work with higher overheat value making the same almost independent measurement of the ordinary variation of the room temperature.

Equation (3.17) is valid when wire axis is perpendicular to the flow direction, otherwise if we imagine the infinite wire only the perpendicular velocity component is being sensed from the wire meanwhile parallel one does not make any difference on the wire thermal behavior. Since then, the effective cooling velocity (U_{eff}) can be found from following relation:

$$U_{eff} = U \cdot \cos\beta \quad (3.18)$$

where β is the angle between the flow vector and the normal to the axis of the sensor.

Although, single wire can be employed to found effective flow velocity, using multiple wires in different spacial orientation it is possible to expand device capabilities for 2D and 3-D concept of absolute velocity and angle discrimination measurement accordingly to the number of wires used.

But thermal anemometer don't need to be only wires [33] it can have a shape of thin-films [34] or even sphere [35] or other geometries, [36]. In case of hot-film anemometers this is usually achieved by deposition of conducting metal who resistance depends on temperature (like platinum for example) on the resistive substrate of quartz or oxidized silicon, [37, 38]. Bigger size make the sensor more sturdy and less prone for decalibration but at the same time sensor frequency response becomes slower.

3.3.2 Calorimetric sensors

Calorimetric sensor uses the fact that heat drained from the hot element by the flow is transported and affect surroundings or directly the other components. Therefore, we will observe a heat transfer from the one component toward another which will affect heat distribution in the grade that will change either temperature or heat convection rate of that another component. The same temperature symmetry or heat dissipation conditions will depends on the position of the particular component in reference to to geometry of the structure and wind incoming angle, [39].

The way one element affect another or other way round depends not only on wind speed but also on wind direction, so very often the calorimetric sensor are not only 1-D realization [40] but mostly 2-D [41, 42] and even 3-D solution has been achieved [43].

Very often calorimetric sensors in which heat transfer affects symmetry of the convection coefficient of sensor units are being called for simplicity thermal anemometers.

3.4 Operating modes

One of the very important aspects of thermal flow sensor is which operating mode it employs. For thermal anemometers this division is simple and consist in two major modes:

- Constant Power Anemometry (CPA)
- Constant Temperature Anemometry (CTA)

Constant Power Anemometry (CPA) is a mode when Joule heat power delivers to the sensor does not change under changing wind parameters. As

the power delivered to the sensor is to balance convection heat in Equation (3.1), then the change in convection heat coefficient will result in adjustment of hot point working temperature. Constant Power Anemometry (CPA) according to the working circuit can have another abbreviation like: Constant Current Anemometry (CCA) and Constant Voltage Anemometry (CVA).

Constant Temperature Anemometry (CTA) mode has a different approach for driving wind sensor. Working in this mode wind sensor hot element is kept at the same temperature level and power demand is adjusted to the necessary value to once again satisfy the Equation (3.1). Therefore, whenever wind velocity rise what will result in rise of heat convection coefficient and in consequence power demand will rise to maintain overheat at the same level. Constant Temperature Anemometry (CTA) mode sometimes is not to set absolute value of temperature but rather is setting constant overheat in reference to the ambient temperature conditions. In that last case operating mode is same times called as Constant Temperature Difference Anemometry (CTDA).

Chapter 4

Thermal Anemometry in Mars Missions

Evolution of the Mars planet has always puzzled the scientific community. The understand of its magnetic field properties as well as dynamic atmosphere behavior together with spectrum of solar radiation and water content among others would shed light on if whenever this Red Planet could have been able to sustain life as we know on Earth. Therefore, there is no surprise than when technology for space mission presented its readiness the era of Mars exploration started for good. The first mission known as Marsnik 1 was launched in 1960 by Union of Soviet Socialist Republics (USSR) and was an intent Mars flyby but failed and even didn't reach the Earth orbit. Many others intents failed till United States of America (USA) mission Mariner 4, lunched in 1965 and flying by Mars in 1965 sent first pictures to Earth. This milestone was a great success and gave the leadership in Mars exploration to USA. Up to date there ahve been more than 40 missions targeting Mars more than half of them have been declared as failure, and the great majority of the missions that has succeeded were, as it has been in early days, from USA. What is even more striking is that the only successful mission that involved landers or rovers on Mars were from NASA. Those are, ordered by landing dates: Viking (1976), Mars Pathfinder (1997), Spirit & Opportunity (2004), Phoenix (2008) and Curiosity (2012). Each time a mission was planed specific landing site for vehicles has been carefully assigned, see Figure 4.1.

From the seven landers which succeed operating on Mars five of them were equipped with wind measurement instruments in order to characterize wind near Mars surface. This shows how big scientific inters is in characterizing flow structures on the neighbor planet. Only Spirit & Opportunity missed in their scientific program Martian atmosphere wind measurement goals. Both Vikings landers were equipped with thermal hot-film anemometers, Pathfinder were carrying on hot-wire anemometer and a dynamic pres-

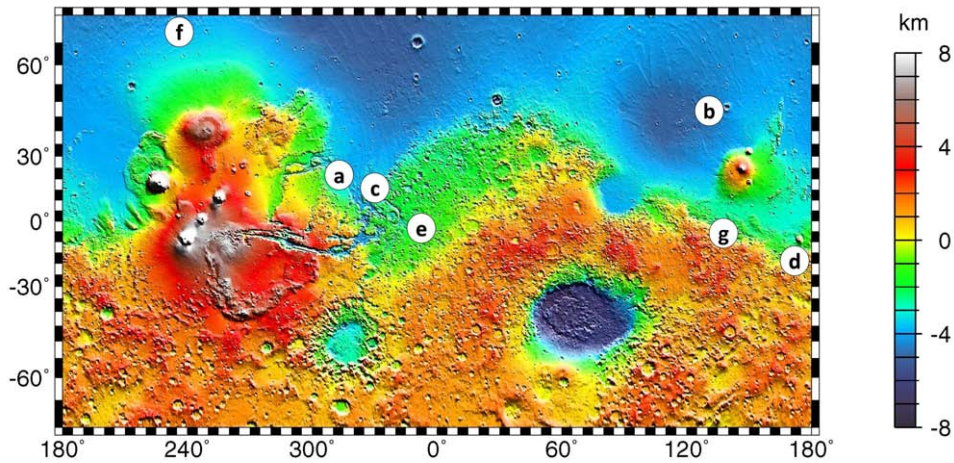


Figure 4.1: Mars landing sites for planetary missions: a) Viking 1, b) Viking 2, c) Mars Pathfinder, d) Spirit, e) Opportunity, f) Phoenix, g) MSL, superimposed on the topography map of the Red Planet. Courtesy NASA/JPL-Caltech.

sure set of wind socks, Phoenix lander was equipped with thin kevlar tube acting as a wind sock whose movement was read with an onboard camera, [44] and finally Curiosity included on board two booms around the camera mast pointed in different direction. Each meteorological boom have three complex wind sensors made out of four hot silicon dice arrays. This statistic shows that the thermal anemometry is a dominant technique in performing in-situ measurement of flows on the surface of Mars. This method of measuring wind magnitude and direction will be discussed in more details in further subsections in reference to the Mars missions: Viking, Pathfinder and Mars Science Laboratory.

4.1 Viking mission

Viking was a NASA Mission composed of two orbiters and respectively two landers. Both spacecraft was named after the mission name Viking 1 and Viking 2. Three main objectives was consider for the first planetary Mars mission. First to obtain high resolution for Red Planet surface. Then, characterize composition and behavior of atmosphere. Finally, to seek for any evidence of extraterrestrial life on Mars.

Viking 1 was launched on August 20, 1975 and arrived at Mars on June 19, 1976. The first month of orbit was devoted to imaging the surface to find appropriate landing sites for the Viking landers. On July 20, 1976 the Viking 1 Lander separated from the Orbiter and touched down at *Chryse Planitia* (22.48°N , 49.97°W planetographic, 1.5 km below the da-

tum (6.1 mbar) elevation). The Lander Viking 1 ended communication on November 13, 1982, after transmitting over 1400 images of the site, see one of the first photography in Figure 4.2, taking surface sample and analyzed them for composition and signs for life, studying atmospheric composition and performing meteorology experiments. Viking 1 Orbiter was powered down on August 17, 1980, after over 1400 orbits.

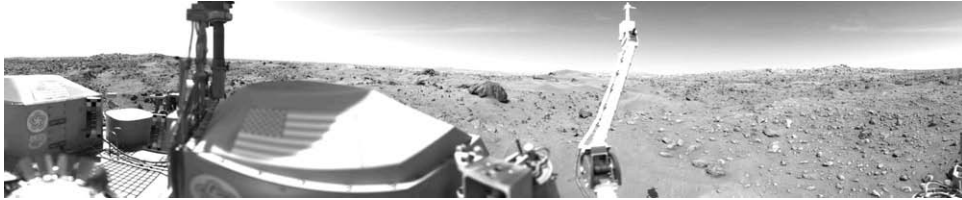


Figure 4.2: First panoramic image of *Chryse Planitia* taken by camera 1 on the Viking 1 Lander. The image was taken on 23 July 1976, three days after Viking 1 landed. The meteorology boom is at the center of the image and to the left is the support for the high-gain dish antenna, [15]. Courtesy NASA/JPL-Caltech.

Viking 2 was launched on September 9, 1975 and entered Mars orbit on August 7, 1976. The Viking 2 Lander touched down at Utopia Planitia (47.97°N, 225.74°W, 3 km below the datum elevation) on September 3, 1976. The Viking 2 Orbiter was powered down on July 25, 1978 after 706 orbits, whereas Viking 2 Lander ended communications on April 11, 1980, [45].

4.1.1 Viking wind sensor unit

Viking wind sensor solution consists three quadrant sensors to determine wind direction in planar perspective and a hot-film sensor to measure wind velocity. Besides this, there was an additional reference temperature sensor to measure ambient gas temperature. All those devices were placed on the top of the deployable meteorology boom arm. Therefore, overall wind characterization has been divided into specifically design instruments. From this group the only one which employs thermal anemometry is the velocity measurement. This was tackled with two orthogonally oriented, in the horizontal plane, rods covered with platinum thin film. Each of the rods had length 10.2 mm and diameter 0.51 mm and was covered with thin 0.635 μm platinum film on it, see Figure 4.3.

Total resistance of platinum film (R_{rod}) was described by equation:

$$R_{rod} = -1.05 \cdot 10^{-5}(T_{(K)} - 273)^2 + 0.02586(T_{(K)} - 273) + 10.7858 \quad (4.1)$$

where $T_{(K)}$ is temperature given in Kelvin.

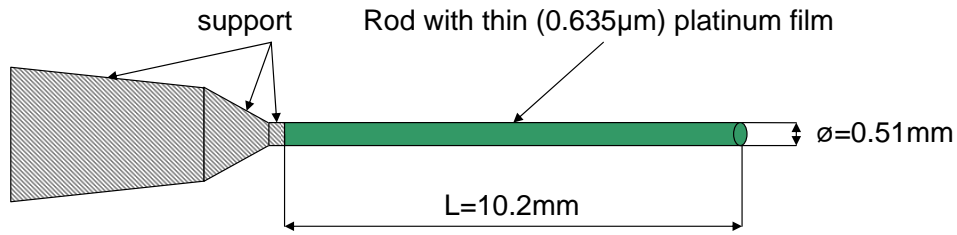


Figure 4.3: Viking wind speed sensor unit.

It was also stated that R_{rod} for 23°C is $11.375\ \Omega$ ($12.4\ \Omega$ with leads). For the Viking wind velocity sensor the CTA method was employed. Typical overheat of 100°C above ambient gas temperature was maintained. CTA principles were used to perform the measurement. Then the wind velocity normal to the sensor can be determined by measuring the power dissipating within the sensor element, [46].

The results from the Viking experiments gave the most complete view of Mars for that time. Volcanoes, lava plains, immense canyons, cratered areas, wind-formed features, and evidence of surface water are apparent in the Orbiter images. The planet appears to be divisible into two main regions, northern low plains and southern cratered highlands. Superimposed on these regions are the *Tharsis* and *Elysium Bulges*, which are high-standing volcanic areas, and *Valles Marineris*, a system of giant canyons near the equator. The surface material at both landing sites can best be characterized as iron-rich clay. Measured temperatures at the landing sites ranged from 155 to 250 K, with a variation over a given day of 35 to 50 K, [47]. Dust storms, surface winds, seasonal pressure changes, and transport of atmospheric gases between the polar caps were observed [48, 49]. The biology experiment produced no evidence of life at either landing site.

4.2 Mars Pathfinder mission

Mars Pathfinder mission in 1996 has very different approach from its precursor Viking. The cost of the Pathfinder was about 5% of the Viking cost this was due to a shift toward low cost space missions. The Pathfinder (19°N 33°W) landed on Mars on 4th July 1997 and transmitted data for only 92 Sols. What is worth to mention is that it included the first successful rover named *Sojourner* on Mars and this renewed the public interest on Mars. This mission was more technology demonstration than science. Advanced solar panels, high capacity rechargeable silver-zinc batteries, high-gain antenna for high-speed communication, main imaging system and Atmospheric Structure Instrument/Meteorology Packaged (ASI/MET) was on board of Pathfinder lander besides legendary free-ranging minirover, [50].

ASI/MET was designed to perform experiments for atmosphere characterization in entry descent and after landing phases of flight. The instrument I would like to focus on was a wind sensor on board of Pathfinder mission which was not planned in the beginning of the mission but has been added to increase capability of atmospheric event reconstruction. This was a good decision since Pathfinder mission has revealed the presence of frequent dust-devils on Mars surface, although wind measurement instrument turned out to be in the design limit for the thin Martian atmosphere.

4.2.1 Mars Pathfinder wind sensor unit

Pathfinder has been equipped with hot-wire wind sensor operating in CPA mode but actually in Constant Current Anemometry (CCA) mode. The instrument maximum overheat was thought out for 30 K (at zero wind speed) in reference to the ambient temperature. Pathfinder wind sensor was conceived as a multiple hot wire anemometers capable of amplitude and direction of the wind retrieval mainly for the flow below 20 m/s but also temporal gust up to 50 m/s, [22]. All hot wires are connected in series and operate at constant continuous current 51.5 mA. Global average temperature of the platinum/iridium wire would not depend on wind direction whereas local temperature variation would give a differential information of the wind incidence angle due to the wire group circular distribution around the cylindrical cone, see Figure 4.4.

The typical Pathfinder sensor frequency resolution was about 4Hz. Although a larger overheat would have been preferred (more than 30 K for still air) the power constraints made it impossible. This results in even small overheat (only few degrees) for real wind speed. As for accurate speed determination is required precise calibration of the relation between wind speed, air temperature, and sensor hot wire overheat under Mars surface conditions (not available), the only data corresponding to the wind direction measurement were published, [21]. Therefore, small temperature difference feature have made further wind speed data post processing very complicated.

The resistivity of Pathfinder wind sensor wire (ρ_{wire}) depends on temperature given in grade Celsius ($T_{(°C)}$) and is described by following equation:

$$\rho_{wire} = \rho_{Pt/Ir(0°C)} (1 + \alpha_{Pt/Ir} \cdot T_{(°C)}) \quad (4.2)$$

where $\rho_{Pt/Ir(0°C)}$ is resistivity at 0°C of platinum/iridium alloy and has value of $1.895e-7 \text{ } \Omega\text{m}$ and $\alpha_{Pt/Ir}$ is a temperature coefficient of resistivity which for this platinum/iridium wire has value of $0.003729 \text{ } /°\text{C}$.

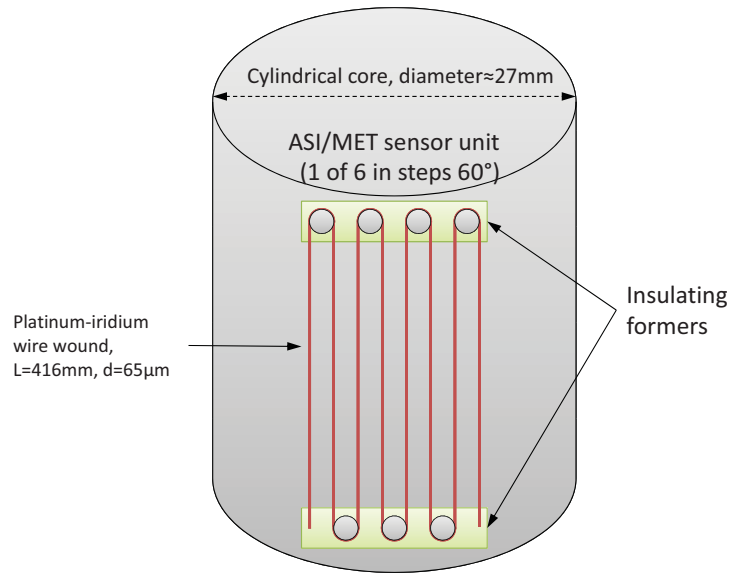


Figure 4.4: Mars Pathfinder wind sensor unit composed of platinum-iridium wire wound 7 times fold and attached to the insulating formers around circumference cone. Entire 2-D wind sensor was made out of 6 sensor units equally distributed with 60° radial step and 3 mm of separation from cylindrical cone shown here.

4.3 Mars Science Laboratory mission

Mars Science Laboratory (MSL) was scheduled to be launched in year 2009 but postponed for fall 2011. The main goal of the mission was looking for evidence of past life according to the white paper Mars exploration Strategy 2009-2020, issued by Mars Science Program synthesis group in April 2003, [51].

MSL rover *Curiosity* included on board Rover Environmental Monitoring Station (REMS). This station, included instruments which had the objective to register meteorological data from the surface of Mars. One of the instruments included was a wind measurement system. The REMS objectives related with the wind measurement on the surface of Mars are the measurement of wind magnitude and wind angle in 3-D. The 3-D wind sensor was based on the use of three 2-D Wind Transducer (WT) located around a boom that protrudes from the camera mast.

Three identical wind transducers placed around the mast of the boom form a complex Wind Sensor (WS) able to measure a 3-D flow characteristic, see Figure 4.5. The WT has been designed in order to figure out the wind velocity and direction in a rarefied Martian atmosphere. More details about this component could be found in Chapter 5.

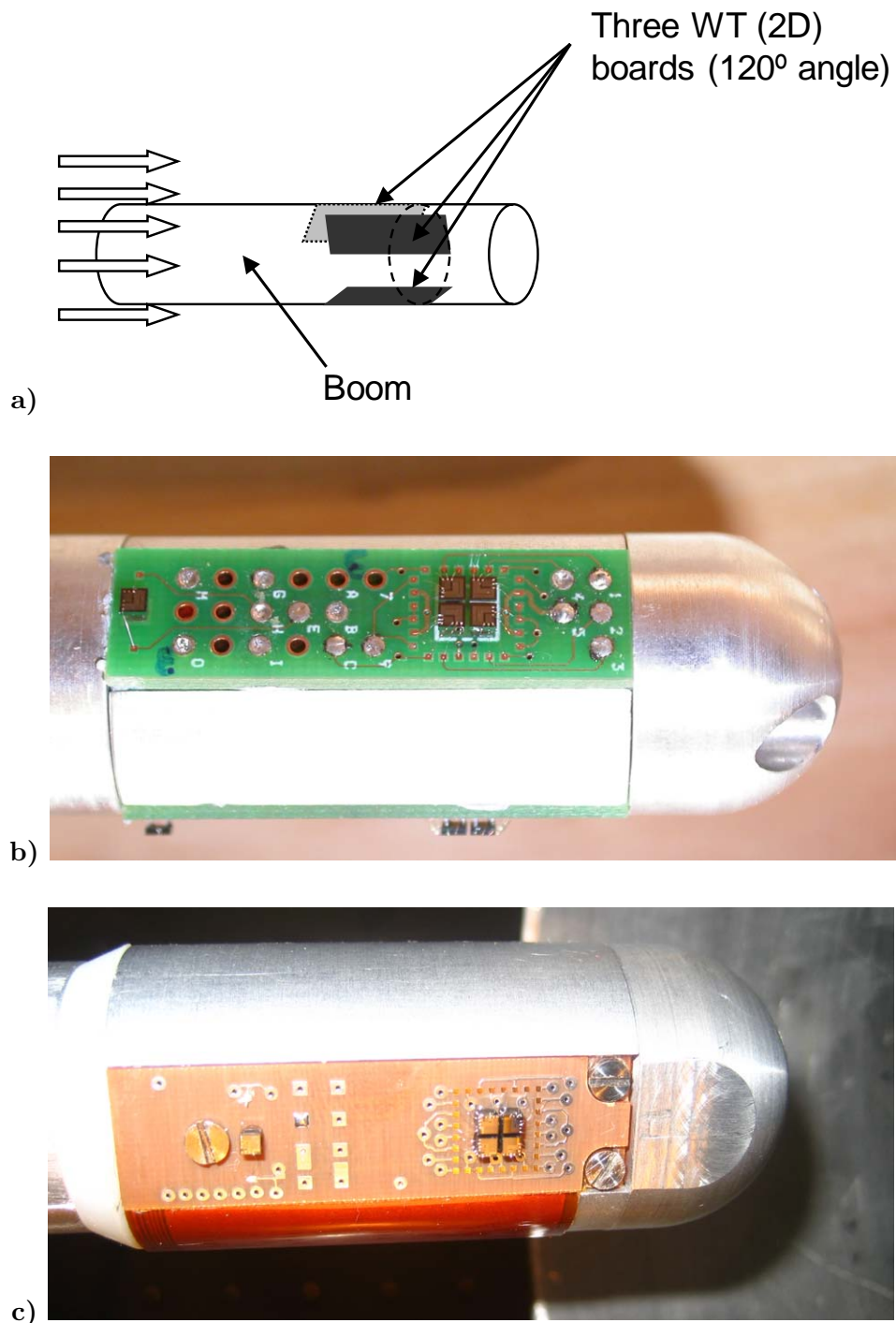


Figure 4.5: a) Concept of the three 2-D Wind Transducer (WT) boards located in 120° orientation around the boom to form 3-D wind sensor and enable reconstruction wind magnitude and direction, b) UPC prototype, c) CAB engineering model.

Chapter 5

REMS 2-D Wind Transducer

This chapter contains a brief presentation of the Rover Environmental Monitoring Station (REMS) project. The main concept of the new 2-D wind sensor being part of the REMS will also be described. Results of the numerical CFD simulation of the conceived structure will be shown. Step by step fabrication process silicon chip that is central to the sensor operation will be described. Afterwards the working circuit and measurement strategy will be explained. Then, thermal model of the sensor will be discussed together with some proof of concept measurements. Finally comparison of the REMS wind sensor with other thermal anemometers which has been on Mars in the past will be carried out, according to a first order thermal model for each sensor unit element.

5.1 REMS project

Rover Environmental Monitoring Station (REMS) is a set of meteorologic scientific devices dedicated to explore weather conditions on Mars. The work originated as a result of the selection of the REMS station proposed by an Spanish laboratory to the NASA to be one of the instruments on board of the rover Curiosity of the MSL [52]. JPL mission to Mars formerly was planned to be launched on autumn 2009, eventually postponed to autumn 2011, [53] has successfully arrived to Mars on August 2012, [54]. Under leadership of the CAB, a joint center of Consejo Superior de Investigaciones Cientificas (CSIC) - INTA. Project REMS is a Spanish Ministry of Education and Science contribution to the NASA mission, [55]. Although, under supervision of CAB the project would not be possible without collaboration of many science and technology institutions. Basically the alliance of three countries: Spain, USA and Finland enabled the realization of the project REMS, see logos of the collaborators in Figure 5.1.

The leadership of the project handled by the CAB whereas NASA is responsible for REMS instrument evaluation and integration with MSL rover.

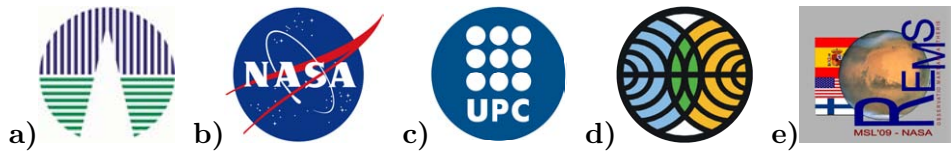


Figure 5.1: The logos of cooperative institutions: a) CAB, b) NASA, c) UPC, d) FMI, e) for REMS project.

The wind sensor design was commissioned to the Universitat Politècnica de Catalunya (UPC) and Finnish Meteorological Institute (FMI) was responsible for humidity sensor development.

At the UPC work for wind sensor development involved a team of 5 researchers: Lukasz Kowalski (author of this thesis work) , Manuel Domínguez-Pumar, Vicente Jiménez Serres, Jordi Ricart and Luis Castañer Muñoz. The team interacted frequently with researchers at the CAB namely Javier Gómez-Elvira, Sara Navarro, Josefina Torres and Julio Romeral, as well as with JPL Manuel de la Torre and with MariPaz Zorzano and Luis Vazquez from the Universidad Complutense de Madrid.

5.1.1 REMS objectives

According to the Luis Vazquez, former personal investigator of the REMS project and Javier Gómez-Elvira, current personal investigator and project leader, REMS was designed to enable realization of several science objectives. One of the objectives it to study Martian signature of general circulation and the mesoscale phenomena close to the ground surface like jets, fronts and wind tides. Second objective is to characterize and understand weather system in microscale; it basically refers observation and measurement of heat fluxes, wind blows boundary layer turbulence or dust devils. Another objective is to learn of local hydrological cycle, for example spatial and temporal variability and diffusive transport from regolith. Following objective is to estimate destructive potential of UV radiation focusing on dust optical properties, photolysis rates and oxidant production that will provide a basic link with the astrobiology studies on Mars. Finally the last objective is to assess subsurface habitability according to the ground-atmosphere interaction, [18, 56].

5.1.2 REMS instruments

In order to satisfy previously established scientific objectives, the specific weather station, known as REMS, is proposed, 5.2.

The recent shape of the station is a result of the compromise between payload mass and measurement ability of stat-of-art instruments. REMS

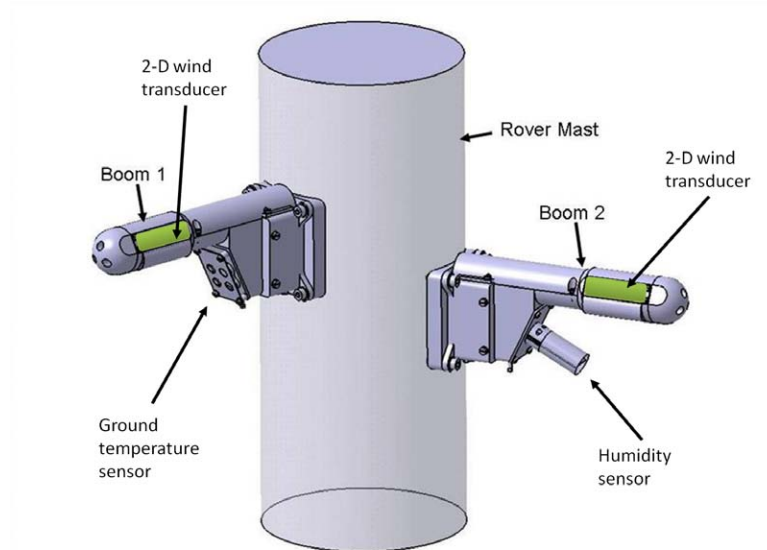


Figure 5.2: Curiosity rover mast with two booms pointed horizontally in two different direction with Wind Transducer (WT) position (three for each boom). Image credit: NASA/JPL-Caltech/INTA (Instituto Nacional de Tecnica Aeroespacial).

will measure and provide scientist with daily and seasonal reports on following parameters:

- ultra violet (UV) radiation from the sun at Mars surface
- ground temperature around the rover
- wind speed and direction
- atmospheric humidity
- atmospheric pressure
- air temperature

The measurement range, accuracy and resolution has been specified and presented in Table 5.1. Some of the measurements are pioneer and are going to be performed for the first time in history on the Red Planet surface. Thus, water vapor observation through atmospheric humidity study near the ground will potentially gain knowledge about surface-atmosphere exchange and atmospheric condensation processes. Whereas, notification of UV radiation on the Martian ground will yield insight into assessment of the present habitability or its past possible history, [57]. This mission also, for the first

Sensor type	Parameter	Range	Resolution	Accuracy
Ground	temperature	150-375 K	2 K	10 K
Air	air temperature	150-300 K	0.1 K	5 K
Humidity	relative humidity	200-323 K	1%	10%
UV radiation	photodiode UVA	335-395 nm		5%
...	photodiode UVB	280-325 nm		5%
...	photodiode UVC	220-275 nm		5%
...	photodiode UVD	210-380 nm		5%
...	photodiode UVE	245-290 nm		5%
...	photodiode UVF	310-335 nm		5%
Pressure	absolute pressure	1-1150 Pa	20 Pa	0.5 Pa
Wind flow	horizontal speed	0-70 m/s	0.5 m/s	1 m/s
...	vertical speed	0-10 m/s	0.5 m/s	1 m/s
...	direction	360°	1°	30°

Table 5.1: Scientific requests for the REMS instruments, [18]

time, will be able to perform three dimensional characterization of the wind flows which form separately climate behaviour.

Four sensors are located around two booms attached to the Remote Sensing Mast (RSM) whereas the ultraviolet sensor is assembled at the rover top deck and the pressure sensor is placed inside the rover body with tube connection with external atmosphere. Also inside the rover body integral part of harness electronics called Instrument Control Unit (ICU) is positioned. Two booms are placed about 1.5 m about ground level with 50 mm high difference between units. Both of them are also separated in azimuth by 120°. This allocation has been thought out in order to minimize the possibility that the RSM perturbs the measurements at both booms. Due to JPL constrains the length of the booms is comparable with RSM diameter so a high perturbation due to the mast is expected in the worst case. Boom 1, which is oriented to the side and slightly to the rear of ahead direction of the rover host a set of wind sensors and the ground temperature sensor. Boom 2 is pointing accordingly to the rover face and apart from the another set of wind sensor hosts also the relative humidity sensor. Each boom will be also equipped with an air temperature sensor separated from the boom structure by a small rod.

Ground Temperature Sensor (GTS)

REMS Ground Temperature Sensor (GTS) is the device which enable the remote measurement of the ground temperature. It is based on the temperature measurement from infrared radiation. This sensor is located entirely on boom 1, see Figure 5.2 and is composed of three thermopiles with different

wavelength bands; 8-14 um, 15 um, 16-20 um in order to avoid carbon dioxide (CO₂) absorption band [52]. An additional thermistor on board provides sensor housing temperature to calibrate the thermopile readouts. [58].

Air Temperature Sensor (ATS)

REMS Air Temperature Sensor (ATS) has been designed as a FR4 rod with two standard PT1000 thermistors bonded to it. First one is glued to the rod at his middle position and another at the end of the rod, out of the boom thermal boundary layer. In this configuration knowing two temperatures allows with the previous characterization to work out the air temperature with desired resolution and accuracy, [59].

Humidity Sensor (HS)

REMS Humidity Sensor (HS) is located in the boom 2 which is pointing in the driving direction of the rover. This device has been developed by FMI in reference to the Vaisala transducer, [52]. In order to not harm the sensor by the Martian dust particles it is cloaked inside protective cylinder and interface with atmosphere trough the dust filters, see Figure 5.2. The HS provides REMS weather station with relative humidity readout, [18].

Ultraviolet Sensor (UVS)

REMS Ultraviolet Sensor (UVS) in difference to the previously described devices is located on the rover deck pointing to the Martian sky in the zenith direction a 60 degree field of view. Device is composed of six photodiodes adjusted to the specific bands indicated on Table (5.1). For each photodiodes a strong round magnet has been included in order to decrease dust deposition. Furthermore, visual control of the thickness of the dust layer will be performed in order to identify the level of dust accumulation, [52].

Pressure Sensor (PS)

PS is located inside REMS-ICU box. It is composed by two transducers located on the multi-layer Printed Circuit Board (PCB) and protected by FR4 Faraday cage. Each of transducer has two *Vaisala Barocap* heads (single-crystal micromachined device) and two *Thermocap* (temperature sensors). Change in the atmospheric pressure moves the capacitor plates of the instrument. The capacitance characterized for the Mars conditions is ranging from 10 to 15pF and is calibrated for different temperature scenario. The accuracy of the PS is 1 Pa.

Wind Sensor (WS)

Every boom is composed of three equal Wind Transducer (WT) . Each WT is 2-D wind sensor. WT boards are based on the wind hot film anemometry concept and are placed on boom surface with an angular separation of 120° . Using a set of three independent WTs 2-D measurements inverse algorithm finds out the real 3-D wind parameters, [52]. This inverse algorithm post-evaluation is possible due to the special aerodynamical simulations and careful characterization and calibration tests performed inside the wind tunnel.

When Micro and Nanotechnology (MNT) Group from UPC join to the REMS team we get to know about specific wind sensor requirements which have been indicated by NASA, [9]. As wind variations reflect the local components of the circulation, there is a strong belief that wind measurement will provide information about surface-layer turbulence and mean vertical gradients, as well as the presence of vortices and convective plumes. Therefore, to meet the scientific community needs on Mars landing site, the wind sensor requirements has been set as follow:

- The REMS shall be able to measure horizontal wind in the range of 0 to 70 m/s with a resolution of 0.5 m/s and an accuracy of 1 m/s.
- The REMS shall be able to measure the direction of horizontal wind with a resolution and accuracy better than 30 degrees.
- The REMS shall be able to measure vertical wind in the range of 0 to 20 m/s with a resolution of 0.5 m/s and an accuracy of 1 m/s.
- The REMS shall be able to measure over the range of air temperatures 150 to 300 K.
- The REMS shall be able to operate in the Martian atmosphere (which is nearly 96% of CO_2) pressure in the range of 500 to 1000 Pa.
- The REMS shall be capable of collecting and storing sensor data at a sampling rate of 1 Hz, 5 minutes each hour.

Besides this critical constraints there were others which have to be always taken under consideration when developing device for space application, which are: small weight and size (so the entire volume) and low power consumption.

Therefore, each one of the Wind Transducer (WT) included in REMS had to be sensitive to a range of wind speeds from 1 to 60 m/s with magnitude precision of 0.1 m/s and angle resolution of 10 degree and operate with a time response of 1 second. REMS wind sensor instrument needs to estimate 3-D wind direction and flow velocity and is composed of two booms in horizontal position to the ground but pointing in two different direction

with an angular difference of 120° . This duplication has been proposed due to the possible flow perturbation against most of the rover where booms are attached, see Figure 5.2. Therefore, only the redundancy solution assure that at any wind direction at least one from the booms receives original unchanged flow, [59].

5.2 Concept of the REMS 2-D wind transducer

The concept of the REMS Wind Transducer (WT) is based on two elements located in separated points of the transducer board. One is named hot point and the second one cold point. They are working at a known temperature difference between each other. Both hot and cold points use identical silicon dice (Sensor Unit) that include three platinum resistors: one (R_{sens}) to measure the die temperature, another (R_{heat}) to heat it as needed and a third one (R_{delta}) to set a temperature difference. The cold point consists on one silicon die, whose temperature can be measured using a patterned platinum resistor. As this sensor should be in equilibrium with the air surrounding it, only its measurement resistor is connected. The hot point consists of four identical silicon dice: A, B, C and D identical to the previous cold point die. The group of four dice are located close to each other to produce thermal shadow effect. The separation of the hot and cold points minimize direct interactions but is small enough so that the wind temperature will be the same on both sensors, see Figure 5.3.

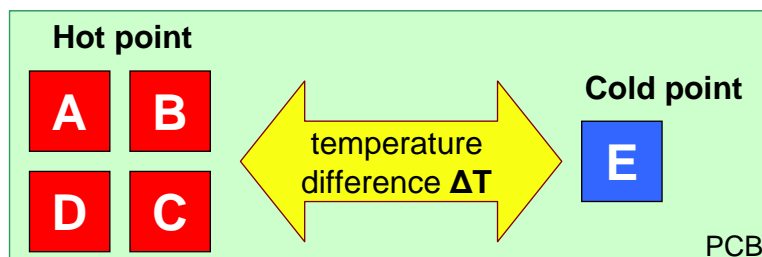


Figure 5.3: Concept of the wind sensor unit with its cold point and hot point elements.

As described previously, silicon dices on the hot point includes one resistance that measures its temperature and another resistance that can be used to heat the dice. The cold point is a single silicon square die considered as a reference die E. His role is to introduce to system real ambient temperature of the atmosphere were the measurements are taken.

The cold point terminal is being named *cold* in sense that there is no power deliberately given to it. In contrary, the hot terminals are being named *hot* since there is constant temperature difference - an overheat (ΔT) - between these four hot points and reference point established by adequate

power pulses. Whole process is realized as a close loop method and is controlled by sigma-delta converter, see Figure 5.4 .

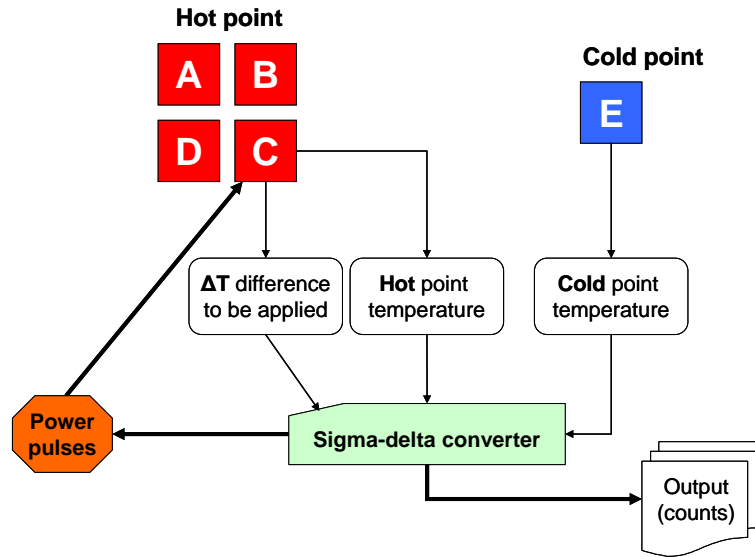


Figure 5.4: Sigma-delta closed loop diagram of the REMS wind transducer. Only the blocks associated with one of the hot points (namely hot point C) are shown.

Each of the hot points is heated to a high temperature value which is subtracted to the lowest temperature output of the cold point. This temperature difference between hot and cold points is compared to a preset value of ΔT determined, as will be explained, by the use of an special ΔR term. For situation when the temperature difference is smaller than ΔT the sigma-delta converter gives power pulses in order to heat up the die up to demanded temperature level. At the same time the information about the comparison results is being stored in a counter, so that it counts up each time cycle that a high power pulse is sent to the dice. The counter is reset after some number of clock cycles defined as a frame. The counter value at the end of the frame is related to the average power delivered to the hot die. Therefore, every frame we are obtaining the average power dissipated in each of the hot dice to maintain the hot point temperature. The final result provided by the wind transducer electronics is the data represents average power consumption of each hot point dice at the end of each frame time. From the data of the six WT for the two booms, an estimation can be calculated for wind velocity and 3-D wind direction using an inverse algorithm.

5.2.1 REMS wind sensor unit

The common element, which repeated five times compose an entire wind transducer can be described as a sensor unit. This element is presented on Figure 5.5.

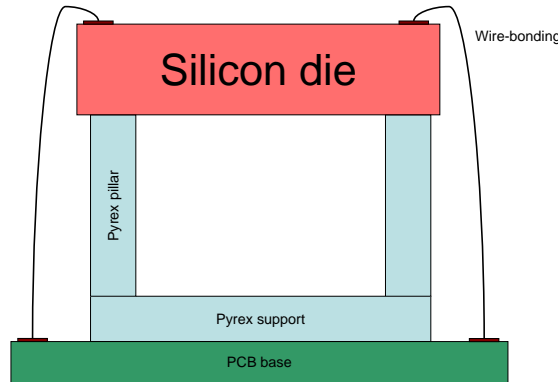


Figure 5.5: MSL - REMS wind sensor unit concept

Wind sensor unit is built with three basic elements:

1. Silicon chip with three platinum resistances patterned over it,
2. Pyrex support in the form of inverted table,
3. Gold wire-bonding connection.

The role of the silicon die is to distribute on its whole volume the heat generated according to the Joule law in the heater R_{heat} resistor on top of the silicon structure. Second, but not less important function of the silicon die is the thermal coupling by convection on its external surface with surrounding atmosphere. A Pyrex inverted table structure is used to provide mechanical support for the suspended silicon die and thermally provide good thermal isolation of the hot die from the PCB base. Later in the project the support material was changed due to reliability problems but it provided the same functionality. Finally wire-bonding provides electrical connection of the instrumental resistances on the top of the silicon die with external electronic circuits.

Silicon chip

Silicon chip fabrication is detailed in Section (5.5). Onto an oxidized silicon wafer surface there are three different resistances; R_{sens} , R_{heat} and R_{delta} as is distinguished on Figure 5.6. From the same figure can also be seen six pads which are basic termination of each resistance to connect electrically through wire-bonding to the external circuits. In photography we can see two more

pads that are used to connect the silicon bulk. As they are redundant, only one of them was used so, in total, each hot dice used 7 bonding wires.

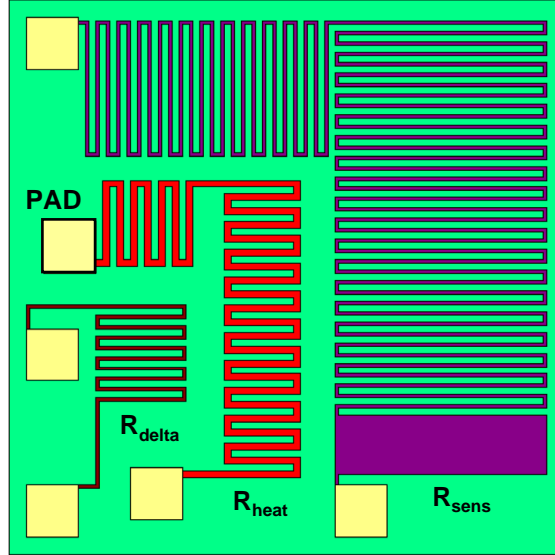


Figure 5.6: Front view of silicon die with three resistances: R_{sens} , R_{heat} , R_{delta} and six PADS.

Each of the resistances has a particular role to play in the system. R_{sens} known as a sensing resistance works as a temperature sensor and deliver to the system the value of its temperature which represents the temperature of entire die. Then, R_{heat} which is an abbreviation for heating resistance is working as a heater in the way that conducting through it a heating current I_{heat} provokes, according to the *Joule effect*, generation of heat. Finally, R_{delta} , which is a key resistance that presets temperature conditions for the overheat value.

All three resistances are patterned as platinum paths (R_{path}) which are deposited on the silicon die previously oxidized and obey the same temperature dependence of its resistance:

$$R_{path} = R_{path(0^{\circ}C)} (1 + \alpha_{Pt/Ti} \cdot T(^{\circ}C)) \quad (5.1)$$

where $R_{path(0^{\circ}C)}$ is resistance path measured at $0^{\circ}C$ and $\alpha_{Pt/Ti}$ is a temperature coefficient resistance which has been experimentally found to have value of $0.003 / ^{\circ}$, which is typical for thin film platinum resistors, [60]. All three resistances on the top of the silicon chip have the same lineal dependence on the temperature.

Silicon die itself has a two different but both important function for the sensor operation. On one hand, die boundary surface is in contact with surrounded gas and under wind forced convection drains heat to the ambient

whenever is in overheat conditions in reference to the ambient atmosphere. On the other hand high thermal conductance of silicon bulk material provides good condition for uniform temperature distribution along the entire die, detailed in [4, 8]. Finally the thin silicon dioxide surface isolates electrically each set of resistances of each other and the silicon bulk at the same time provide a thermal connection to enable a good distribution of the heat, which is generated in R_{heat} and spreads along all silicon volume so also through the other resistances R_{sens} and R_{delta} .

5.2.2 Constant temperature overheat anemometer

REMS wind sensor is an anemometer working in Constant Temperature Difference Anemometry (CTDA) mode. The principal diagram of working sensor present constant temperature difference between separated die being named the cold point and array of four dice known as hot point, as shown in Figure 5.3. The typical value of temperature difference between cold and hot point is between 20...40°C and depends on T_{ref} and nominal value of resistances R_{sens} and R_{Δ} , which is a combination of R_{delta} resistances from four silicon chips, see Section 5.7. Since the reference die is not heated its temperature is approximately equal to the temperature of the ambient or it is close to this value ($T_{amb.} \simeq T_{cold}$). Therefore hot point elements in normal operation work will work at a set temperature, which is above the ambient atmosphere temperature according to the constant overheat value (ΔT).

5.3 Numerical experimentation

The concept of the four hot dice array is based upon the idea that all four hot components together are working at thermal anemometer in CTA mode to provide wind magnitude information. Whereas, the differential behaviour between hot dice could be interpreted as a calorimetric sensor that provides necessary information for wind angle reconstruction, [1]. To test the proposed geometry a series of CFD simulations based on FEM were developed using the platform ANSYS.

5.3.1 Simulations parameters

In order to perform numerical simulations, adequate flow properties were necessary to be known. From this assumption rise a question if Martian atmosphere conditions should be considered incompressible. In order to examine this problem Mach number with reference to its ambient temperature in carbon dioxide atmosphere has been depicted on Figure 5.7.

It stands out that all winds on Mars, at least if they are slower than 60 m/s are within the incompressible flow range. This limit becomes even

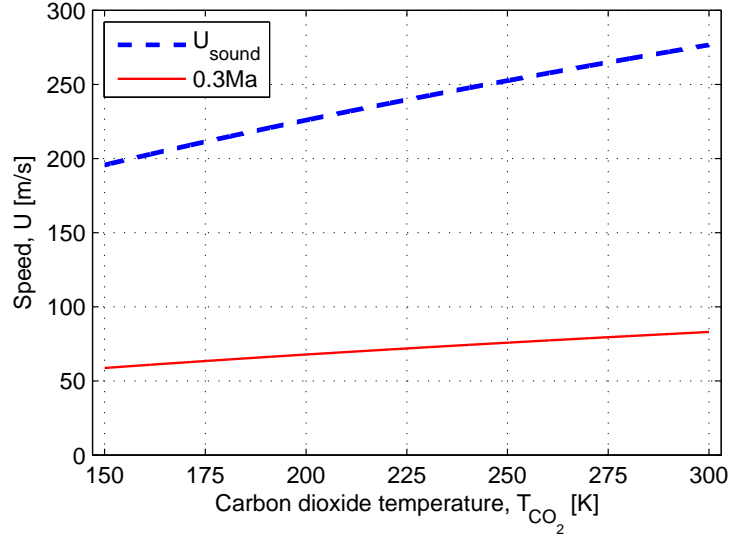


Figure 5.7: Sound of speed and incompressible flow speed limit ($0.3 Ma$) for Martian (CO_2) atmosphere.

higher as the ambient temperature rise and the same make us sure that we deal with incompressible air flow.

All flow properties have been calculated for pure carbon dioxide in the range of the typical temperature and pressure at Mars surface. To find these parameters ambient temperature of 220 K has been selected together with CO_2 pressure of 670 Pa. Some temperature-dependent gas properties for full range of temperatures are presented in Figure 5.8.

Therefore, parameters k , μ , Cp can be read from Figure 5.8 for typical temperature $T = 220$ K.

Meanwhile, the CO_2 density has been calculated taking under account atmospheric pressure reference set for $P = 670$ Pa by solving the following equation:

$$\rho = \frac{M \cdot P}{R \cdot T} \quad (5.2)$$

where, M is the molar mass in this case the molar mass of carbon dioxide molecule ($M_{CO_2} = 44.0095$ g/mol), P ambient pressure, R ideal gas constant ($R = 8.3144621$ J/(mol·K)) and T ambient temperature.

All FEM simulation at this stage of the project were run on the engineering simulation software ANSYS with these fixed gas parameters:

- thermal conductivity, $k = 0.010841$ W/mK,
- dynamic viscosity, $\mu = 11.053$ uPa·s,

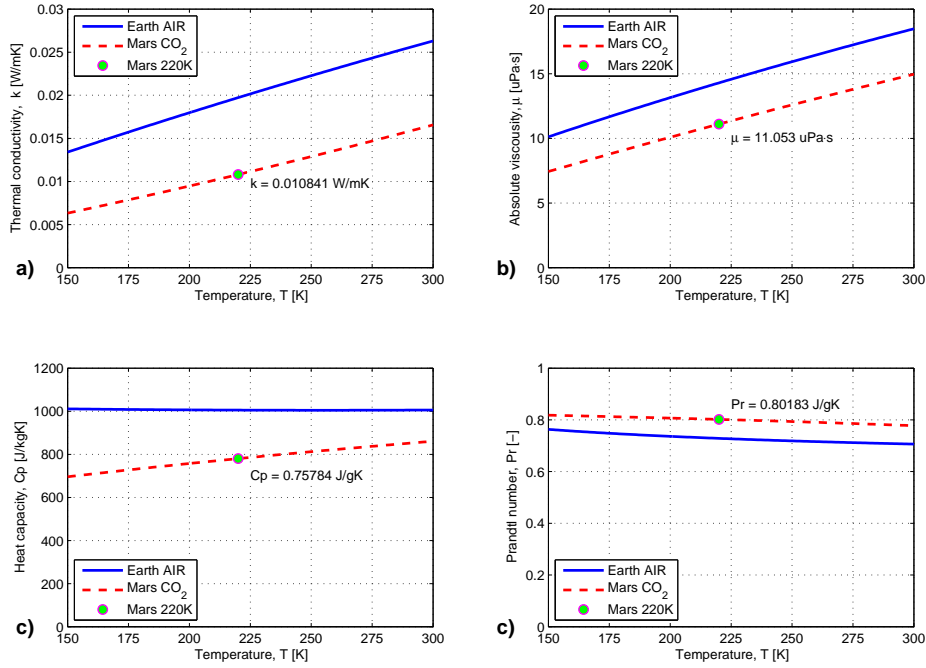


Figure 5.8: Typical Martian atmosphere (CO_2) parameters variation as a function of temperature: a) thermal conductivity, b) dynamic viscosity and, c) specific heat, d) Prandtl number with reference to the same Earth AIR atmosphere parameters.

- specific heat, $C_p = 0.75784 \text{ J/gK}$,
- density, $\rho = 0.016121 \text{ Kg/m}^3$.

5.3.2 Different geometries

Based on the previous experience of the MNT Group reported in [61–64] it was decided to we employ CTA as this is the most promising method to obtain a good time response [65]. In order to control device hot temperature classic first order sigma delta modulation has been chosen, [39]. Here in the UPC we had also experience in working with silicon wafers so it was rather automatic choice to use silicon technology in which the sensor is fabricated. The challenge was high and we were trying to avoid errors like the one that put wind sensor of Pathfinder mission into the range where measurement is very unstable [22]. On the other hand we did realize the Viking wind sensor does not give us wind direction information and his power consumption was to high to be accepted for the MSL mission. We need to come out with an innovative solution which meets all mission requirements. So we start to analyze several different geometries under Martian typical conditions ($T_{\text{CO}_2} = -53^\circ\text{C}$, $P = 670 \text{ Pa}$, $U = 5 \text{ m/s}$), see Figure 5.9.

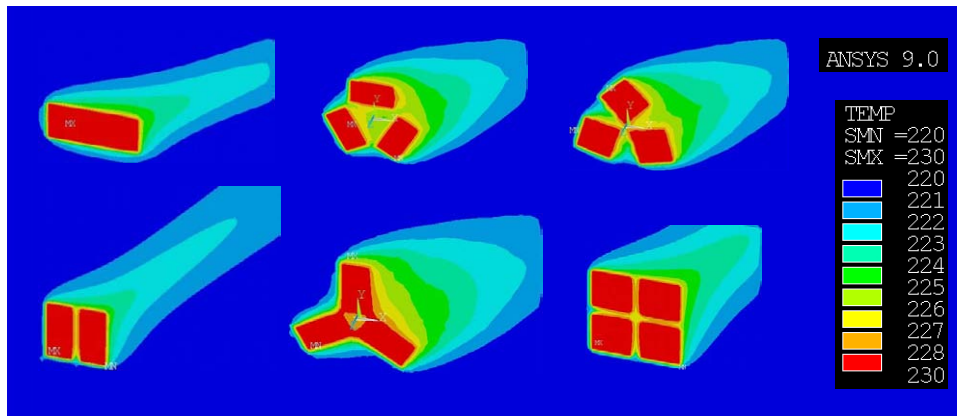


Figure 5.9: Several sets of geometry candidates for wind sensor to Mars surface under FEM simulation.

As the most promising geometry we select the four silicon dice array whose perimeter forms another square. There were several reason why we choose this structure. First was that the silicon chip technology with deposited platinum resistances was already available for our team but post-process limits us to cut into rectangular sections. Secondly the group of four dice together creates perimeter of another square but about twice the size of each of its components what makes simpler perception of the new established geometry. Finally having regular structure with four symmetry lines reduce the number of simulation to the angle range $\langle 0^\circ \dots 90^\circ \rangle$. Whats more, four dice structure gives opportunity to establish differential parameters: *North-South* and *East-West* which for the angle reconstruction makes inverse algorithm independent form the heat loses variation. Dice are separated from each other provided elimination of cross thermal flow from one silicon die to another, see Figure 5.10.

The size of the sensor has been proposed in such a way that flow interaction with the sensor components would be for any temperature and pressure possible to happened on Mars inside medium continuum range, described in Section (3.2.1), see Figure 5.11.

5.4 Fluidical-thermal simulation

Fluidical-thermal simulation has been carried out in the ANSYS platform. This CFD-FEM simulation reflect static behaviour of proposed structure. At first, one single die has been taken under consideration. Then, as the following step, array of four equally shaped and align dice has been taken under scrutiny.

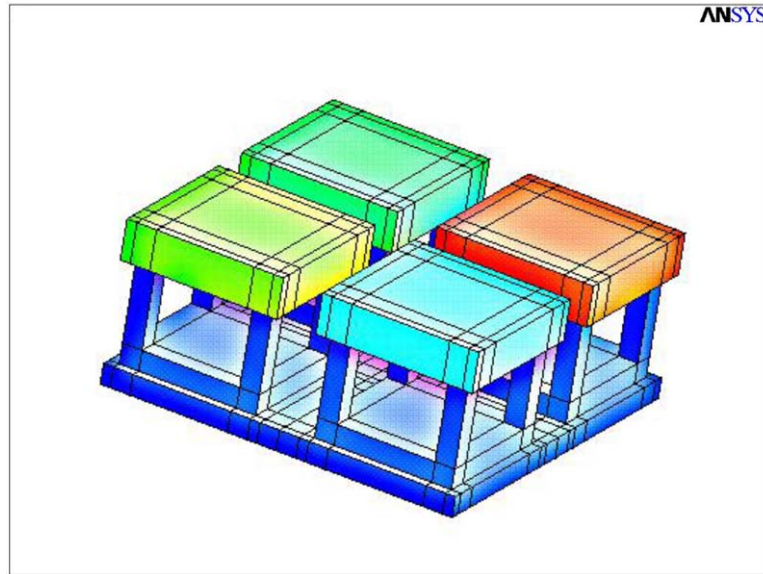


Figure 5.10: Concept of the REMS wind sensor geometry of four silicon dice array fixed on the Pyrex inverted table in ANSYS finite element method simulation software.

5.4.1 Single unit simulation

In this simulation a single die of the size of 1.6 mm x 1.6 mm x 0.4 mm has been simulated in suspension. This die has been surrounded aside by the air of 6.4 mm and from the above and below by 1.6 mm air margin. In order to proceed with CFD simulation the corresponding parameters of the gas, which is involved into simulation has been precised the same way as in Section (5.3.1):

- *absolute viscosity,*
- *thermal conductivity,*
- *specific heat,*
- *density*

This time, the carbon dioxide parameters: absolute viscosity, thermal conductivity, specific heat and density has been calculated for Mars CO₂ pressure 600 Pa and flow temperature $T_f = 200.5$ K. The flow temperature has been calculated as a medium temperature between T_{air} to be 200 and T_{hot} of 201 K, with 1 K of overheat.

The first experiment has been carried out to find out if the single square die is sensible for different angle of incidence. To do so, series of simulation

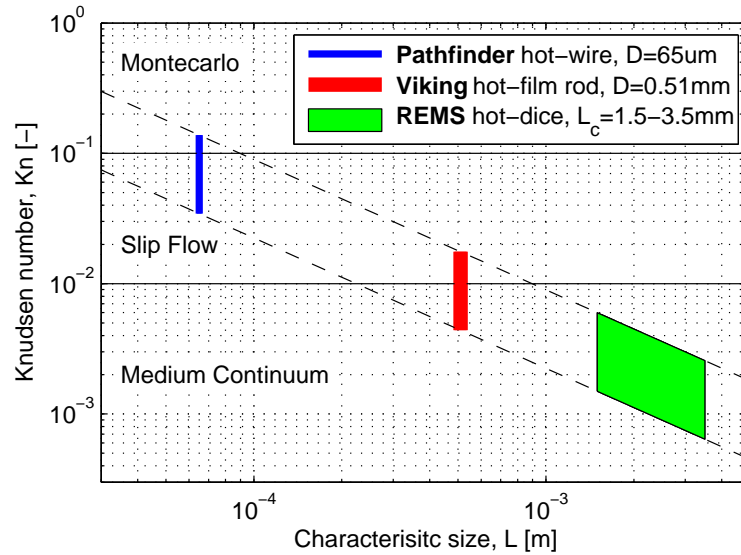


Figure 5.11: Knudsen number calculation for different geometry thermal anemometers on board of Mars planetary mission for entire atmospheric range; temperature from 150 to 300 K and pressure from 500 to 1000 Pa.

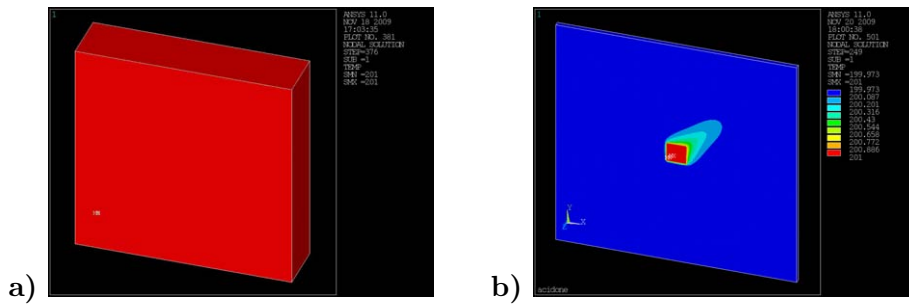


Figure 5.12: REMS wind sensor unit a) boundary conditions: temperature $T_{hot} = 201$ K for ANSYS static FEM simulation under the CO_2 wind of 10 m/s from southwest direction and ambient temperature $T_{amb.} = 200$ K, b) temperature cross section graph for non-compressible flow solution.

in the horizontal XY space with variation of the wind incidence angle, ϕ for boundary conditions has been planned. Taking under account that the square does have four symmetry line, see Figure 5.13, number of incidence angle could have been reduced. Therefore, in order to cover full 360° angle of wind incidence direction, there is a need to execute simulation of at least 45° wide window of different rotation angles. This minimum window is calculated from equation 5.3:

$$\phi_{window} = \frac{360^\circ}{2^4} = \frac{360^\circ}{16} = 45^\circ \quad (5.3)$$

where 360° is a full circle, 2^4 represents for symmetry lines for square geometry.

Nevertheless to be sure of simulation results we have proposed incidence angle window of 90° choosing the simulation range of ϕ as $\langle 270^\circ \dots 360^\circ \rangle$. The results of this simulation can be observed on the Figure 5.13.

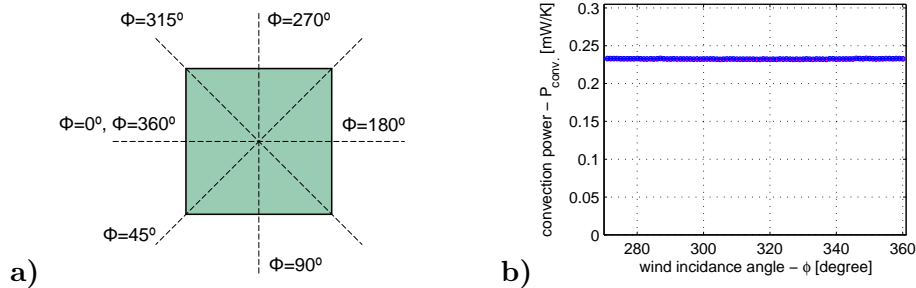


Figure 5.13: a) The symmetry of the wind incidence angle in reference to the square die geometry b) simulation of the hot die convection as a function of the wind direction ϕ for the range of $\langle 270^\circ \dots 360^\circ \rangle$. Convection power has been measured for 600 Pa CO_2 flow where die temperature was set for 201 K, whereas gas temperature was set for 200 K.

Second simulation to carry out was the simulation where for the same fixed incidence angle different velocities were simulated. For this experiment wind direction angle ϕ has been set for 315° . Then in every step of simulation wind velocity has been increasing from 0 m/s with step of 0.5 m/s when reached final velocity of 60 m/s. Achieved in this manner point has been gather into curve presented on the Figure 5.14

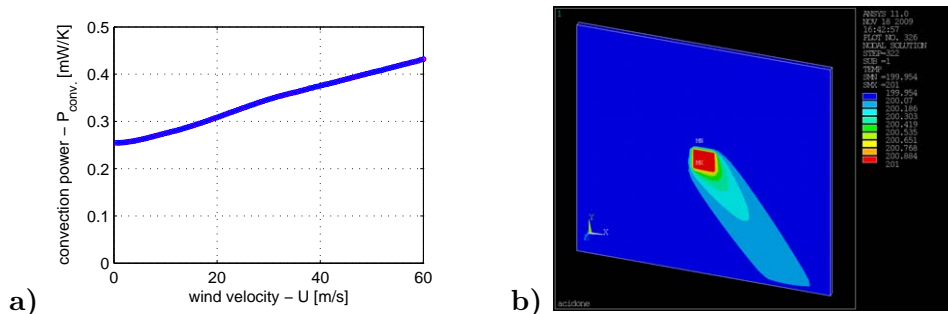


Figure 5.14: a) Power convection in function of the wind flow velocity U , b) example for wind incidence angle $\phi = 315^\circ$, CO_2 pressure 600 Pa where die temperature was set for 201 K and gas temperature was set for 200 K.

It is clearly seen from Figure 5.13 that particular sensor unit heat convection doesn't depend on wind incidence position but only of its magnitude as has it been depicted in Figure 5.14. This makes an standing alone hot sensor unit insensible to the wind direction and sensible to the wind speed. Things are getting different when array of hot silicon dice is taken under test.

5.4.2 Four hot dice array

These fluidic-thermal static state simulations shade light for sensor angular responsiveness for planar angle reconstruction as well as wind velocity and angle algorithm retrieval. One of the test was to find out about sensor response for different angle incidence and as a function of different velocities from 10 m/s to 60 m/s with 10 m/s step, see Figure 5.15

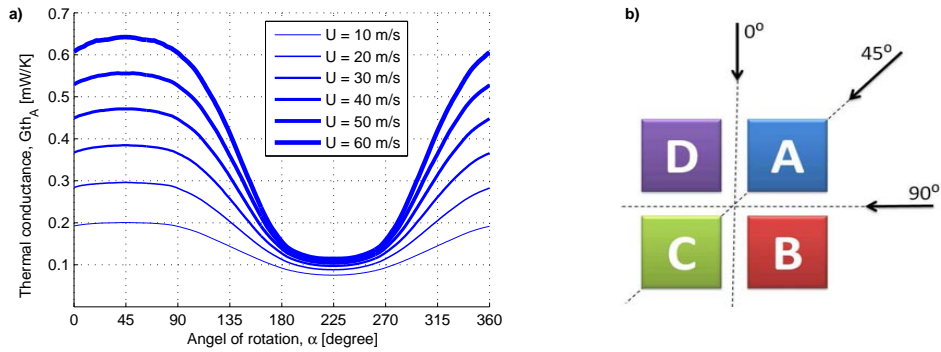


Figure 5.15: FEM simulation results of: a) thermal conductance of the die *A* as a function of incidence angle and wind speed, b) four silicon dice array orientation according to the wind incidence angle directions.

It can be seen from the Figure 5.15 that die *A* has its thermal conductance minimum at wind angle 225° whereas maximum is at 45° for all speeds.

Curves corresponding for other dice *B*, *C*, *D* are the same in shape and properly shifted, as it is shown for the low speed of 10 m/s in Figure 5.16.

Thermal conductance curves seen at Figure 5.15 don't cross each other and G_{th} becomes bigger as the velocity grows. What is interesting for this structure is that the average thermal conductance for all four dice is independent on wind angle and can be used for wind magnitude reconstruction, similarly as in case on one die shown in Figure 5.13. Insensitivity of the four hot dice array structure for the incidence angle is shown in Figure 5.17

From the Figure 5.17 stands out that for low speed up to 30 m/s four dice array average thermal conductance shows a uniform behaviour independent

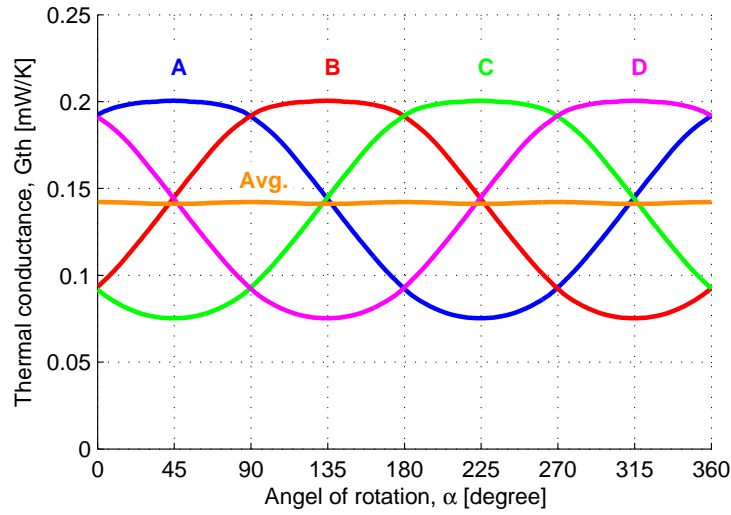


Figure 5.16: Thermal conductance for the four hot dice array as a function of rotation angle for the same wind speed of 10 m/s.

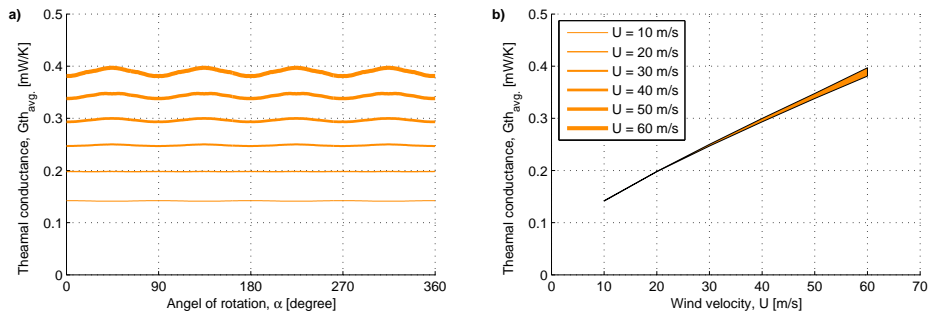


Figure 5.17: Average thermal conductivity for the four dice array, a) as a function of wind incidence angle for different wind speeds, b) as a function of wind speed, having its variation for full range of the rotation angles.

on the wind incidence angle and as the velocity goes up to 60 m/s only the small variation in averaged thermal conductance is observed.

This simulations show that wind direction could be resolved out of the measurement of the thermal conductances of four coplanar silicon chips.

Basis on the thermal conductances: A , B , C , D new terms like: *North*, *South*, *East*, and *West* can be calculated, as a combinations of A , B , C and D of particular hot dice as follow:

$$\begin{aligned}
 North &= A + D \\
 South &= B + C \\
 East &= A + B \\
 West &= C + D
 \end{aligned} \tag{5.4}$$

Then from this new terms another differential terms which are: *North-South (NS)* and *East-West (EW)* are obtained to show even higher sensitivity of the structure for incidence angle variation, see Figure 5.18.

$$\begin{aligned}
 NS &= North - South = (A + D) - (B + C) \\
 EW &= East - West = (A + B) - (C + D)
 \end{aligned} \tag{5.5}$$

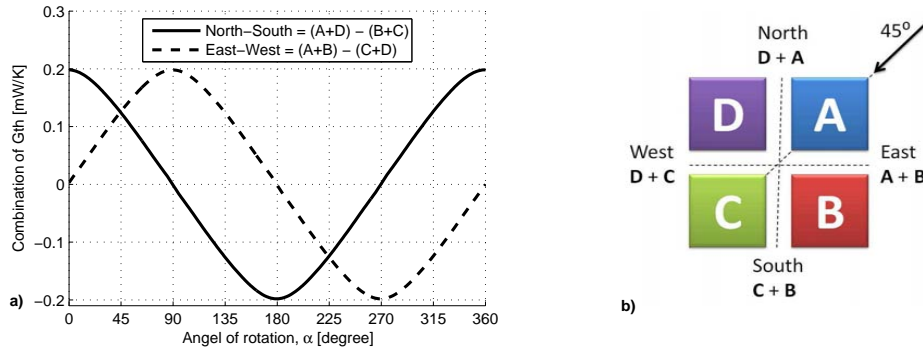


Figure 5.18: Combination of thermal conductances a) for terms: *North-South* and *East-West* b) and what is their position in function of the wind incidence angle.

The work with differential therms is especially important since any radiation component or thermal conduction loses when the same for all dice are automatically cancel out.

5.4.3 Angular sensitivity

In order to find out theoretically the sensor sensitivity to the change of rotation angle α a numerical calculation of the angle derivatives for the thermal conductivities of the four hot dice has been obtained from following equation:

$$S_{ABCD,\alpha} = \frac{\sqrt{\left(\frac{\partial Gth_A}{\partial \alpha}\right)^2 + \left(\frac{\partial Gth_B}{\partial \alpha}\right)^2 + \left(\frac{\partial Gth_C}{\partial \alpha}\right)^2 + \left(\frac{\partial Gth_D}{\partial \alpha}\right)^2}}{Gth_A + Gth_B + Gth_C + Gth_D} \cdot 100\% \tag{5.6}$$

The same the sensitivity factor $S_{ABCD,\alpha}$ show what is the percentage change in thermal conductivities of separated dice: A , B , C and D for wind direction change (α) in reference to the thermal conductance of the whole hot array composed out of four dice. Result of the, shown in Figure 5.19,

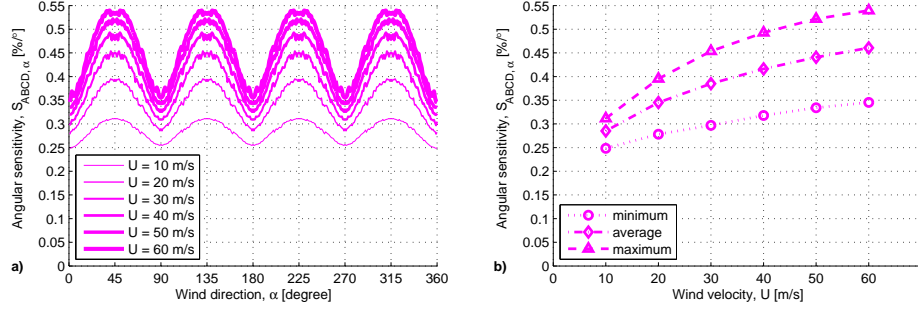


Figure 5.19: Angular sensitivity for the hot dice array: A , B , C , D a) as a function of the wind direction (α), b) as a function of the wind velocity (U)

From the Figure 5.19a) can be seen that the angular sensitivity for given wind velocity changes with repetition period of 90° . Four dice structure has minimum angular sensitivity for wind angle of 0° (wind blowing from directions: North, South, East or West) and maximum angular sensitivity for wind angle of 45° (wind blows from one of the diagonal directions). Variation of the angular sensitivity in reference to the mean angular sensitivity is within the 22% for low wind speed up to 42% for the higher wind velocities.

The smallest mean angular sensitivity is for low wind speed of 10 m/s and it is about 0.28 %/° and rise as the velocity is faster and for maximum wind speed of 60 m/s the mean angular sensitivity is about 0.46 %/°, see Figure 5.19b).

Lets consider the situation when differential terms NS and EW are analysed. In this case an angular sensitivity $S_{NSEW,\alpha}$ is defined by following equation:

$$S_{NSEW,\alpha} = \frac{\sqrt{\left(\frac{\partial Gth_{NS}}{\partial \alpha}\right)^2 + \left(\frac{\partial Gth_{EW}}{\partial \alpha}\right)^2}}{2 \cdot (Gth_A + Gth_B + Gth_C + Gth_D)} \cdot 100\% \quad (5.7)$$

The factor 2 in the denominator in Equation (5.7) appears since to produce both terms NS and EW thermal conductance of every from four dice: A , B , C and D is used twice. This sensitivity of new terms has been present in Figure 5.20.

Use of differential terms (NS , EW) gives almost the same angular sensitivity as it was in case of four separated dice, see Figure 5.20. So it could be said that for four dice structure we had that $S_{NSEW,\alpha} \simeq S_{ABCD,\alpha}$. This is a very good situation because the use of differential terms eliminates com-

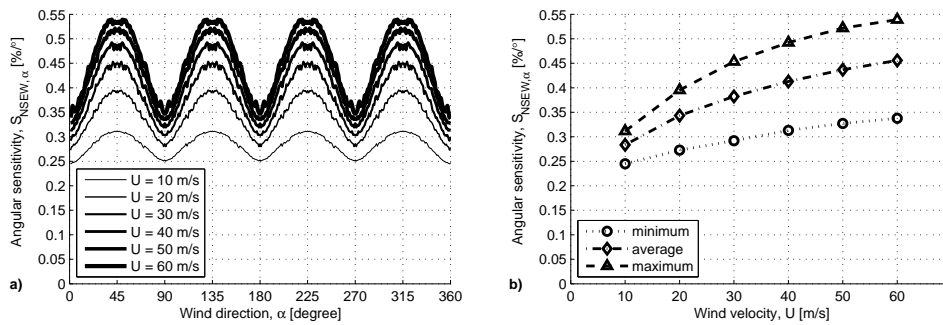


Figure 5.20: Angular sensitivity for the the differential terms *North-South* and *East-West* a) in the function of the wind direction (α), b) in function of the wind velocity (U)

mon thermal losses and common radiation components at the same time preserves reasonable angular sensitivity.

5.5 Fabrication and assembly

In the following section we will explain the design and fabrication process of the silicon chip witch has taken place entirely at clean room facility of Universitat Politècnica de Catalunya (UPC). Furthermore characterization of the most important chip parameters will be provided. Then, geometry and size of the support structure will be presented. Then custom PCB base will be shown. Finally, through assembly process of all basic component the whole sensor will be conceived as this, seen in Figure 5.21.

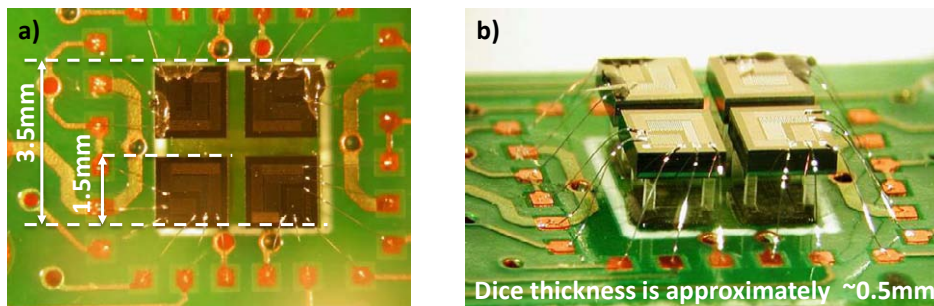


Figure 5.21: View of UPC-REMS wind sensor prototype, a) from the top where square array dimension is depicted, b) from the perspective where dice thickness can be see.

5.5.1 Chip mask layout

As it has been decided to fabricate dice in silicon technology the appropriate layout has been design. The reference target of particular square dice size was $1600 \mu\text{m} \pm 100 \mu\text{m}$. At that time we didn't now exact size of the saw which will be employed for cutting silicon wafer but its size should be from $50 \mu\text{m}$ to $150 \mu\text{m}$. Therefore, the decision we make was to make a design of a silicon square dice with a pitch of $1700 \mu\text{m}$. According to the concept of the wind transducer each of the silicon dice should have three resistive path which are: R_{heat} - responsible for delivering Joule heat to the chip, R_{sens} - temperature sensing resistance according to the Platinum lineal dependence on its temperature and R_{delta} , which is responsible for setting up overheat value, more explanation in a Section (5.7). Target values for each of the resistances was set to be: $R_{heat} \sim 700 \Omega$, $R_{sens} \sim 7 \text{ k}\Omega$ and $R_{delta} \sim 700 \Omega$.

Since both R_{sens} and R_{delta} has a purpose of temperature measurement were driving with low current of about 100μ . A we thought of using path width of $10 \mu\text{m}$. Whereas, R_{heat} which has a heating purpose and is to be conducting significant current of several mA was thought to have double width, in this case $20 \mu\text{m}$. At the end of each resistance we add square PADS $150 \mu\text{m}$ in size to provide a bonding surface. Further more, in order to prevent the build-up of electrostatic charge in silicon bulk we thought to connect the bulk to additional pads for future purpose of grounding, The grounding of the die has been designed as a a ring around the heater resistance to minimize crosstalk. This features together with UPC- MNT logotype and names of the team which has been working for the REMS project occupies chip field of $1500 \mu\text{m} \times 1500 \mu\text{m}$. Two different kind of topology has been proposed, sometimes denominated as chip *type L* and chip *type N* due to visual shape of the R_{sens} resistive path, see Figure 5.22.

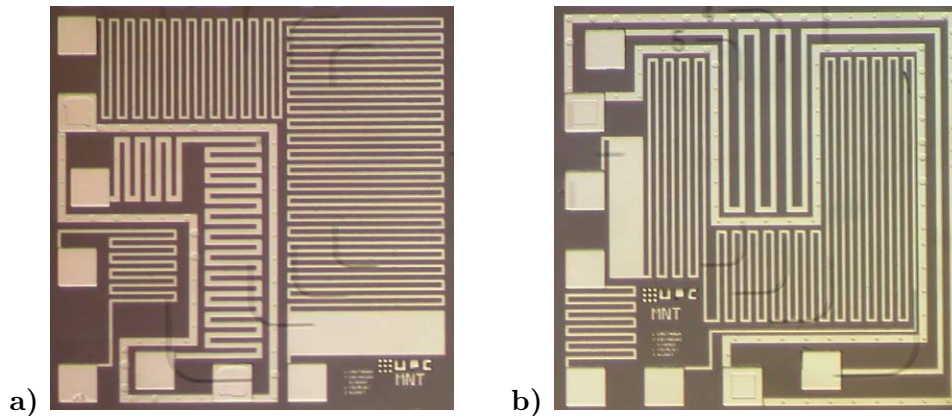


Figure 5.22: Microscope photography of the silicon die of wind transducer after fabrication: a) *type L*, b) *type N*

What can be seen from the Figure 5.22 is that for dice type L has a heater resistor being placed in the central part of the die whereas other die type N has its heater resistor on the border of the chip area. For the rest of the project we choose to use dice type L as the resistance value obtained were closer to the target. Three masks are needed for fabrication of the silicon chips. They are named: Mask A - Contact Windows, Mask B - Titanium/Platinum Paths, Mask C - Pads, see Figure 5.23

What is also seen from the masks at Figure 5.23 is that there are additional symbols outside of the chip field area. Their purpose is to enable proper alignment of the consecutive masks. This alignment has been done at the level of photolithography masks and can be appreciated from the superposition of the all three masks, see Figure 5.24.

5.5.2 Silicon chip fabrication

Fabrication process of the silicon chip which has taken place entirely at clean room facility of Universitat Politècnica de Catalunya (UPC). There are several fabrication constraints that must to be taken under consideration in the process of fabrication of REMS wind sensor chip:

- materials and their integration must mechanically withstand very low temperatures because they will be working under Martian atmosphere conditions,
- bulk material should provide very good thermal conductivity coefficient in order to provide for the entire chip uniform distribution of temperature within its boundary,
- material used for sensing part must have temperature coefficient very lineal with temperature so it will have ability to properly recognize temperature value,
- sensing and heating resistances must be electrically isolated from each other as well as from the bulk volume,
- both heating and sensing components need to have good adherence with the bulk material,
- bulk need to have an electrical connection to prevent static charge build-up,
- fabrication process should be feasible and repeatable.

As a bulk material for sensor volume pure silicon wafer has been chosen. We used silicon type N grown by Chocralski method genuinely sliced into 4 inch wafer of 400 μm thickness and resistivity ranging from 1 to 10 $\Omega\cdot\text{cm}$. In order to separate resistance from semiconductor base silicon dioxide has

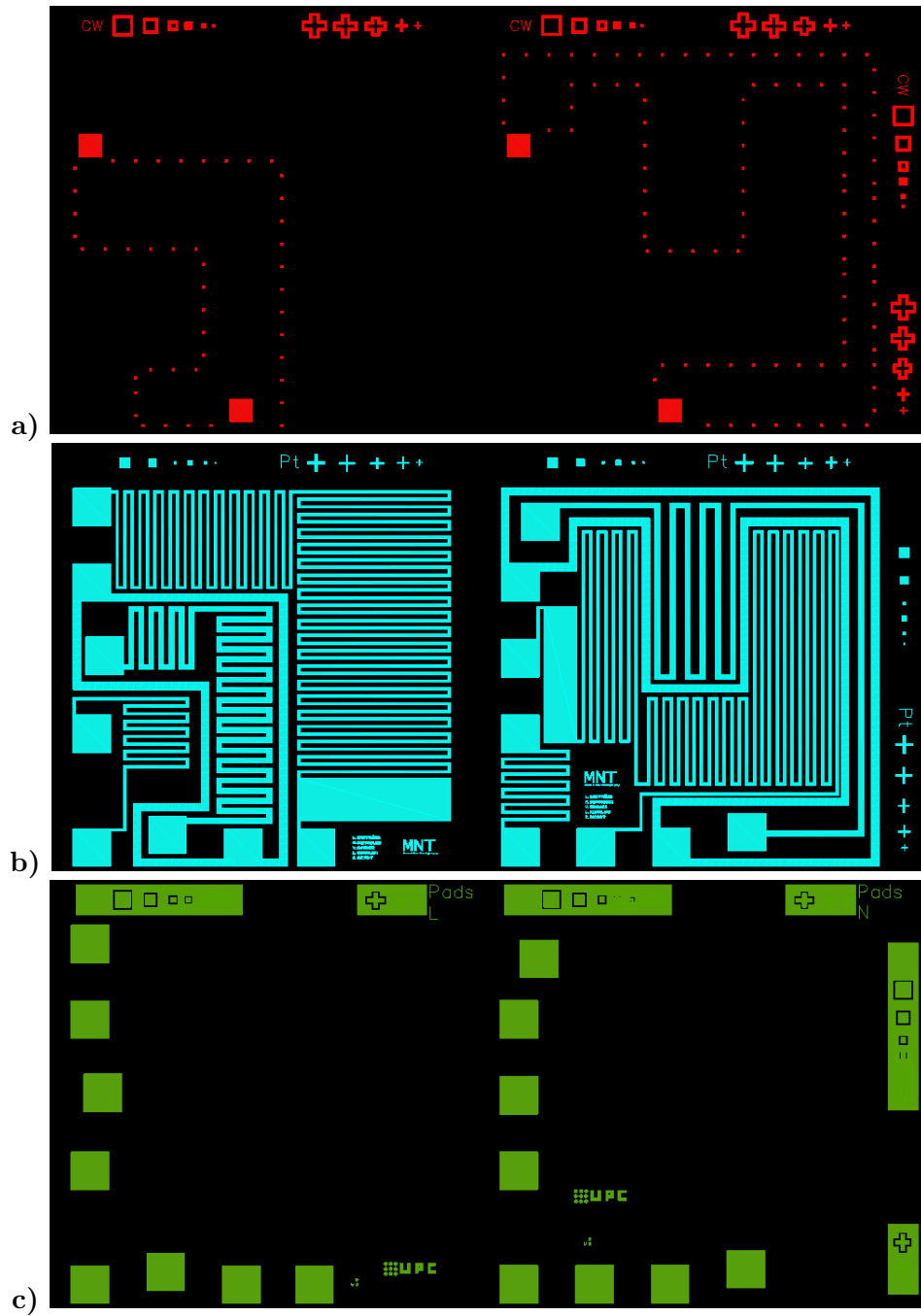


Figure 5.23: Set of photolithography masks for UPC-REMS wind sensor chip:
a) Mask A - Contact Windows, b) Mask B - Titanium/Platinum Paths c)
Mask C - Pads

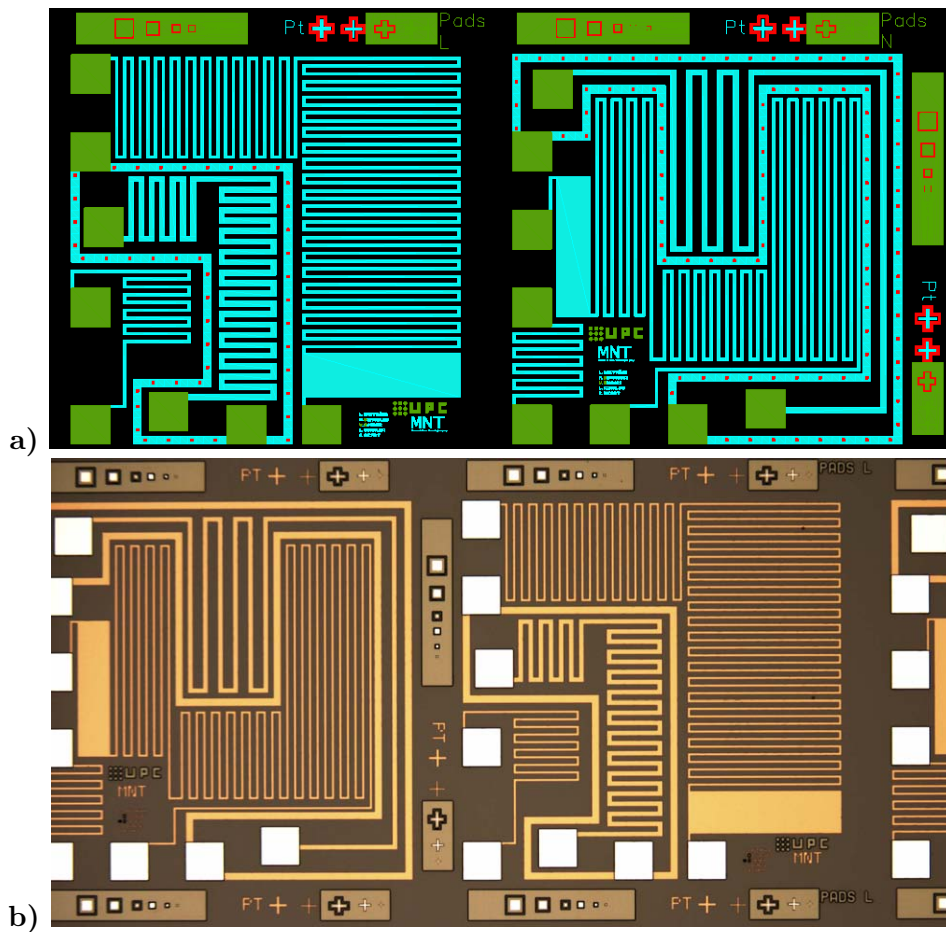


Figure 5.24: Superposition of the three layouts: A, B and C with its perfect alignment a) mask design b) photograph of the real wafer.

been carefully grown on the surface of silicon. Sensing and heating resistance has been made of platinum because of its linear dependence of the temperature in wide from -200°C to $+480^{\circ}\text{C}$, [66,67]. In order to improve adherence of Platinum material to the oxidized silicon surface previously Titanium layer was sputtered. Although we will see further on that it has changed slightly thermal coefficient but significantly strengthen material adherence and hence that enable chip fabrication, [68].

5.5.3 Fabrication process

Fabrication process could be identified by four main blocks:

block 1: Wafer oxidation process,

block 2: Contact windows to the substrate,

block 3: Titanium/Platinum sputtering,

block 4: Additional material sputtering for PAD's strength.

This four blocks, however, have many intermediate steps that will be described hereafter in more detailed steps:

1 step: Starting with silicon wafer

As a bulk material for sensor volume pure silicon wafer has been chosen. We used silicon type N grown by Czochralski method genuinely sliced into 4 inch wafer of 400 μm thickness and resistivity ranging from 1 to 10 $\Omega\cdot\text{cm}$.



Figure 5.25: Silicon Wafer N-Cz 1-10 $\Omega\cdot\text{cm}$, thickness 400 μm .

2 step: RCA cleaning

At first wafer is sinked into RCA solution 5:5:1. Secondly wafer is sinked into 2.5% solution of HF. Next wafer is sinked once again into new RCA solution 5:5:1. Finally wafer is sinked into 5% solution of new prepared HF. This standard procedure guarantee minimum number of external organic dirt.

3 step: Oxidation process

Wafers are placed in furnace at 1040°C for 90 minutes with 12 liter flow of O_2 and 30 mm flow of DCE. This process guarantee growth of silicon dioxide layer of about 120 nm, see Figure 5.26.



Figure 5.26: Silicon oxide, thickness 120 nm.

4 step: First resin

In this process we deposit an uniformly distributed thin layer of photoresist positive resin along the oxidized silicon wafer. Firstly we clean wafer in 25°C with Aceton solution for 5 minutes. Then wafer is cleaned in 25°C in Propanol solution for another 5 minutes. Then

in order to get rid of humidity wafer is placed in stove at temperature of 105°C for 15 minutes. Next one is the process of photoresist distribution. To achieve this wafer is placed on the spinner attached by the suction pump and the spoon of resin SPR-220 1.2 is carefully deposited in the center of the wafer. Later on programmed previously sentence of rotational speed is applied, see Figure 5.27.

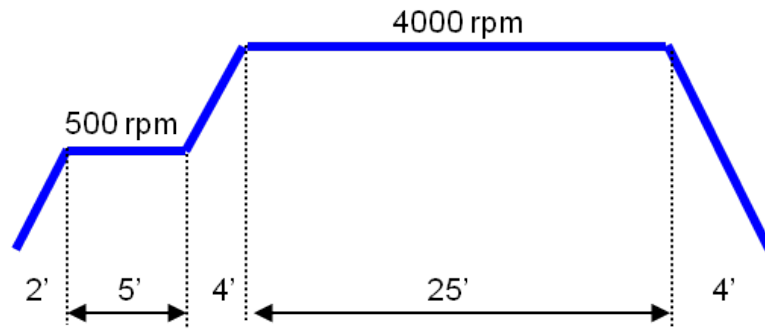


Figure 5.27: Thin resin spinning RPM profile.

Once spinning is accomplished wafer is placed into an stove this time for 15 minutes in temperature 105°C in order to dry up 1 μm thick layer of resin, see Figure 5.28.



Figure 5.28: Resin SPR-220 1.2, thickness 1 μm .

5 step: First photolithography

Directly after step 4 wafer is being exposed during 10 seconds for UV radiation going through aligned *mask A*, see Figure 5.23a). Once exposure to the radiation is finished the resin is removed from the areas where the metal layer should connect to the silicon surface. This corresponds in our case to the transparent areas of the mask. In this process wafer is sinked into developer MF-24-A two times for 60 s each in separate solution. Once the photolithography is finished the shape of the feature is revealed on the sacrificial resin level, see Figure 5.29.



Figure 5.29: First photolithography

6 step: Opening contact window

This attack on SiO_2 has been performed with Ammonium Fluoride during 150 s and results in opening a channel through the oxide, see Figure 5.30.



Figure 5.30: Contact window opening.

7 step: Resin take off

This step is realized by an acetone bath for 5 min, see Figure 5.31.



Figure 5.31: Second resin lift-off.

8 step: Silicon bulk doping with impurities type N

In this step the wafer is exposed to the high temperature profile shown in Figure 5.32.

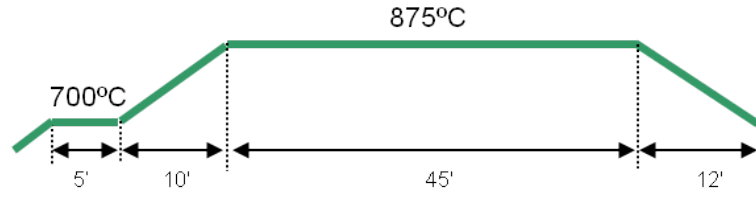


Figure 5.32: Temperature profile of doping.

By this process we got better contact with bulk according to the higher concentration of impurities type N, see Figure 5.33.

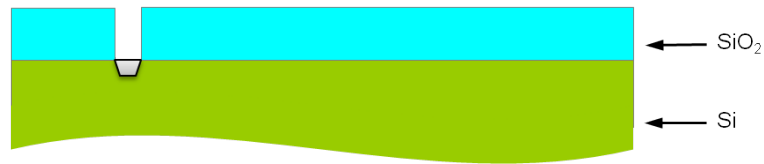


Figure 5.33: Bulk doping with impurities type N.

9 step: Second resin

The same as the step 3. In result we got wafer as shown in Figure 5.34.



Figure 5.34: Silicon wafer after second resin step.

10 step: Second photolithography

The same as the step 5 but with adequate mask B. In result we got wafer as shown in Figure 5.35.



Figure 5.35: Second photolithography.

11 step: Pattern engrave in silicon dioxide

This step is similar to the opening contact window from step 5, but this time wafer is exposed to the less aggressive solution of HF(2,5%) for only 15 s. In result we got following wafer structure with engrave in silicon dioxide pattern as it has been at photolithography mask, see Figure 5.36.

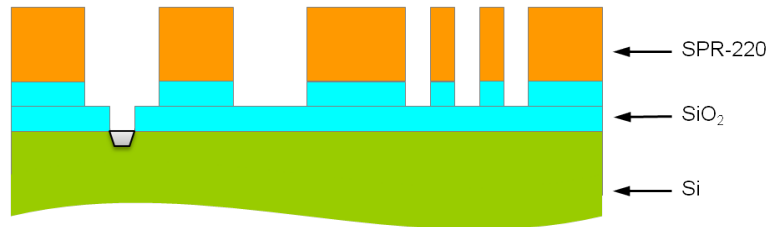


Figure 5.36: Pattern engrave in silicon dioxide.

12 step: Titanium deposition

Once wafer is allocated at sputtering machine so the titanium target. During 3 minutes deposition process with RF power of 100 W and deposition pressure of $5 \cdot 10^{-3}$ mBar whereas base pressure is $1,3 \cdot 10^{-6}$ mBar under the constant rotation of the target. As a result a thin titanium layer of about 10 nm is growth as depicted on Figure 5.37. The reason why we use a titanium layer is to provide better adhesion of consecutive platinum deposition in next step.

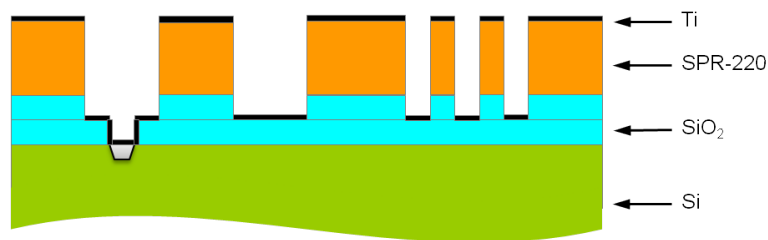


Figure 5.37: Titanium sputtering, thickness 10 nm.

13 step: Platinum deposition

Directly after Titanium deposition second target is activated and this time Platinum deposition is taking place. Platinum sputtering process lasts for 20 minutes at 60W RF power. This process is performed under the same pressure conditions as Titanium deposition and also with rotating wafers. Platinum deposition results in approximate growth of 70 nm layer of Platinum on the top of the Titanium layer, see Figure 5.38.

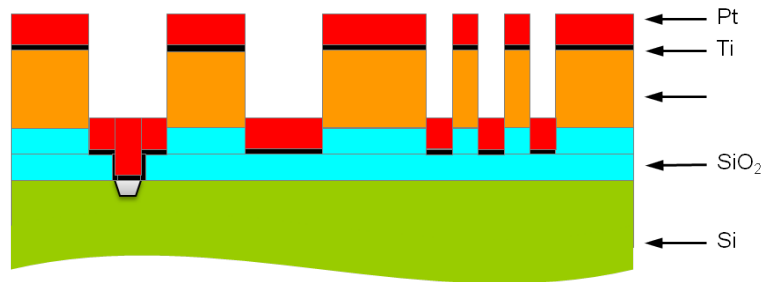


Figure 5.38: Platinum sputtering, thickness 70 nm.

14 step: Second resin lift-off

This is exactly the same procedure as one at step 7. Then we got wafer as at Figure 5.39.

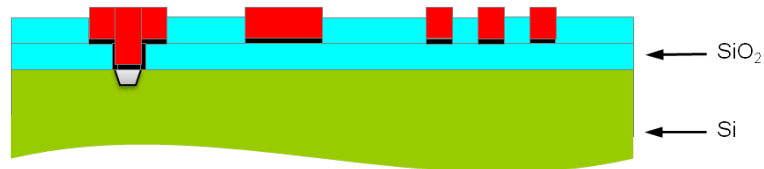


Figure 5.39: Second resin lift-off.

15 step: Third Resin

This process has as a goal uniformly distribute thick layer of photoresist positive resin along the oxidized silicon wafer. Firstly we clean wafer in 25°C with Aceton solution for 5 minutes. Then wafer is cleaned in 25°C in Propanol solution for another 5 minutes. Then in order to get rid of humidity wafer is placed in stove at temperature of 105°C for 15 minutes. Next one is the process of photoresist distribution. To achieve this wafer is placed on the spinner attached by the suction pump and the spoon of resin SPR-220 7.0 is carefully deposited in the center of the wafer. Later on programmed previously sentence of rotational speed is applied, see Figure 5.40.

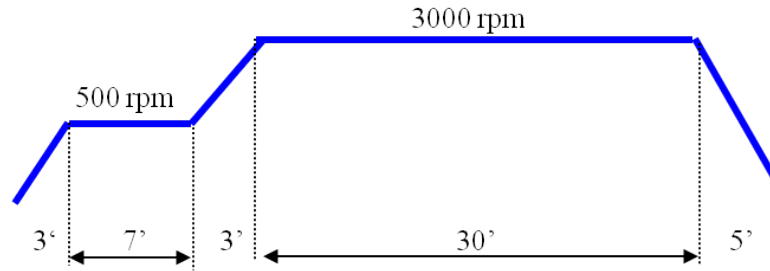


Figure 5.40: Thick resin spinning RPM profile.

Once spinning is accomplished wafer is placed into a stove this time for 15 minutes in temperature 105°C in order to dry up 7 um thick layer of resin, see Figure 5.41.

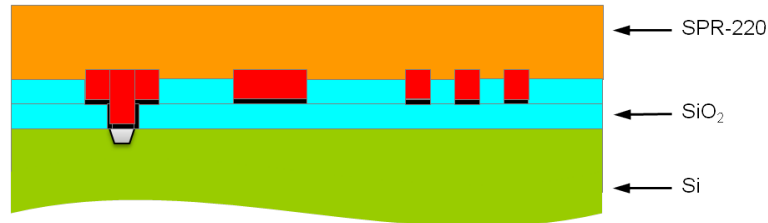


Figure 5.41: Resin SPR-220 7.0, thickness 7 um.

16 step: Third Photolithography

The same as the step 5 and 10 but with adequate mask C. In result we got wafer as shown in Figure 5.42.

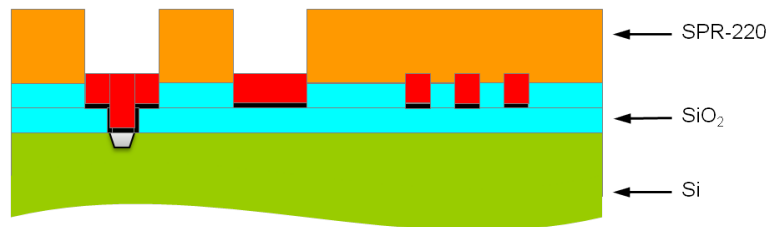


Figure 5.42: Third photolithography.

17 step: Additional Platinum sputtering for pads

This time platinum sputtering process lasts for 53 minutes which 50W RF power. This process is performed under the same pressure conditions as at steps 12 and 13. Platinum deposition results in approximate growth of another 100 nm layer of Platinum on the top of the previous platinum layer, see Figure 5.43.



Figure 5.43: Platinum sputtering for PADs, thickness 100 nm.

18 step: Third resin lift-off

This is similar procedure as one at step 7 and 14 but because the resin used in step 15 was thick this time step is Acetone bath last for 6 min. Result of the step can be seen in Figure 5.44.

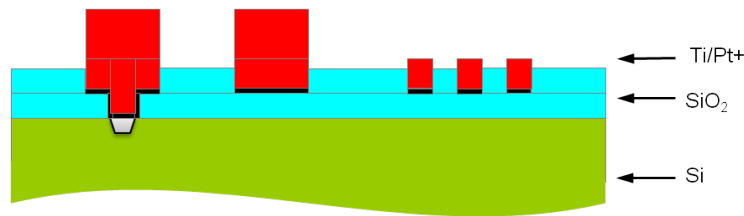


Figure 5.44: Third resin lift-off.

19 step: Forming gas annealing

In this last step wafer is exposed to the temperature of 400°C during 30 minutes under forming gas to anneal previously sputtered Titanium and Platinum in steps 12,13 and 17 silicon dioxide background.

Figure 5.45 how silicon wafer looks like just after finishing all fabrication steps from 1 to 19.

5.5.4 Resistance measurements

Some resistance measurement has been carried out right after silicon chip fabrication on the wafer. First measurements has been done on two types of dice L and N , whose geometry has been in lithography mask section. For each die all set of resistances: R_{sens} , R_{heat} and ΔR has been measured under laboratory temperature ($\sim 25^\circ\text{C}$) conditions. Result of few arbitrary dice from the silicon wafer are presented in Table 5.2.

Measurement Table 5.2 shows that resistances of dice *type L* are closer to the target our target which has been defined as: $R_{sens} = 7 \text{ k}\Omega$, $R_{heat} = 700 \Omega$ and $\Delta R = 700 \Omega$, at 0°C temperature. For resistance *type N* has been found



Figure 5.45: New fabricated wind sensor chips on a silicon wafer. Image Courtesy: Dr. Jordi Ricart.

N.	Dice type L			Dice type N		
	R_{sens} [Ω]	R_{heat} [Ω]	ΔR [Ω]	R_{sens} [Ω]	R_{heat} [Ω]	ΔR [Ω]
1	7140	713	699	5369	730	588
2	7020	705	686	5452	715	572
3	7030	706	689	5571	728	595
4	7070	707	690	5450	712	575
5	7043	709	692	5491	726	587

Table 5.2: Measurement table of resistances R_{sens} , R_{heat} and ΔR resistances for several dice *type L* and *type N* at ambient temperature $\sim 25^\circ\text{C}$.

that R_{sens} , ΔR value are lower than target and this was due to the shorter resistive path as shown in geometry Figure 5.46.

As only for several chips examined have been noticed that there could be not homogenous distribution in resistance value so was decided to look closer for the issue of resistance distribution for particular die location along silicon wafer.

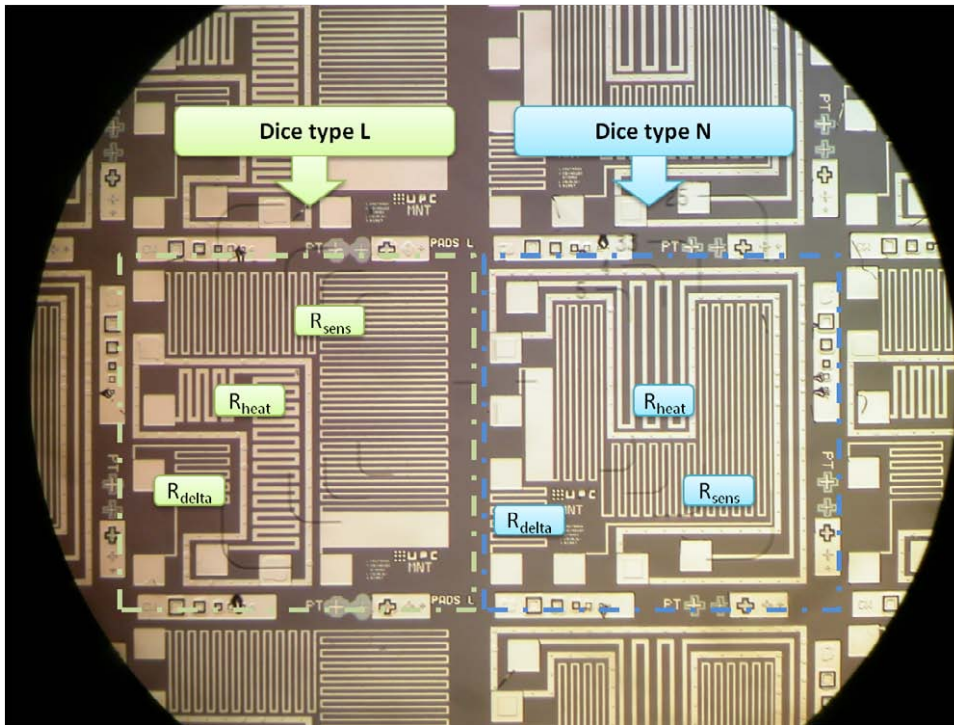


Figure 5.46: Geometry and position of the resistances R_{sens} , R_{heat} and ΔR according to the type of the dice.

5.5.5 Resistance distribution

For the fabrication process we have noticed some dispersion in platinum thickness sputtered onto to silicon substrate according to the position of the wafer in reference to the Platinum target location. By measuring R_{heat} resistance of various chips we have been able to plot topography along the wafer structure, see Figure 5.47.

Topology of R_{heat} distribution along the silicon wafer is especially important due to the constraint of providing the group of five dice with similar value of resistance measured at the same temperature. As a consequence around 1000 chips grouped in sets of 6 dice (4 dice array and one reference die plus another redundant die just in case) has been delivered by UPC-MNT to our partner for further assembly to form part of the REMS instrument onboard of MSL Curiosity rover to Mars.

5.5.6 Alpha coefficient

Since, all the resistances has been mainly fabricated mainly from the Platinum material sputtered on the thin Titanium layer they should have linear temperature coefficient of resistance within the range of those two materials,

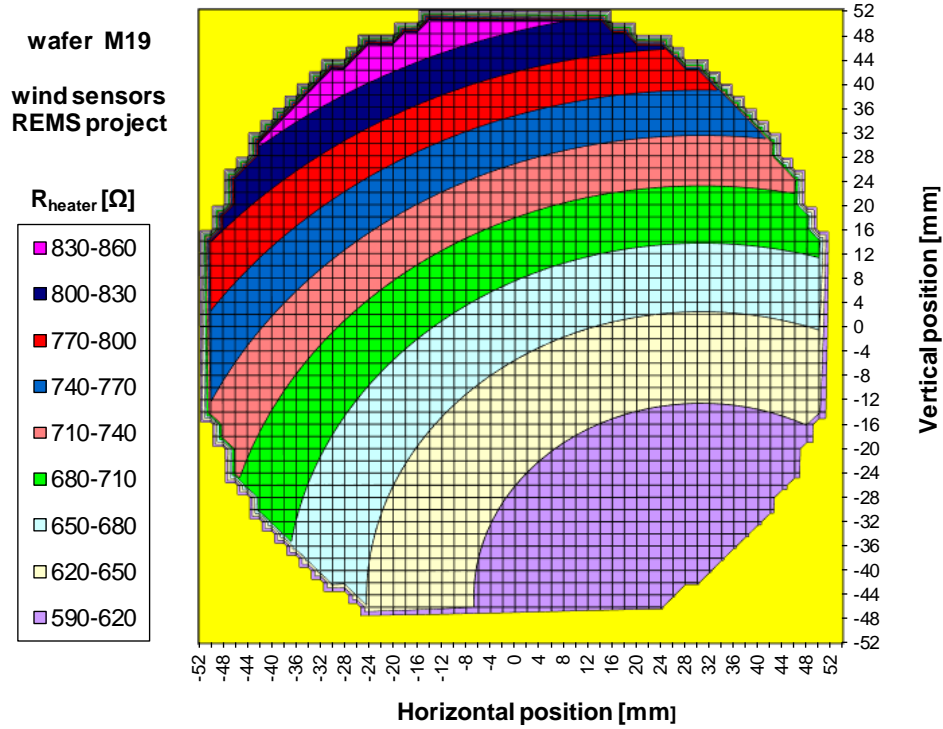


Figure 5.47: Example of R_{heat} distribution along the silicon wafer. Resistance has been measured in laboratory temperature conditions $\sim 25^\circ\text{C}$. Circular pattern results from rotatory base equipment during platinum raw material sputtering process.

although smaller value of α coefficient are expected due to alloy formation on this two metals interface, [69]. In order to find experimentally value of the α several measurements of the one from R_{sens} has been effectuated at different temperatures. From this experiment has been observed that all resistance point in function of the temperature align smoothly on the straight line, see Figure 5.48.

Measurement resistance R_{sens} from the Figure 5.48 can be developed into following equation:

$$R_{sens} = 5170.6 \cdot (1 + 0.003 \cdot T_{hot}) \quad (5.8)$$

This means that resistivity temperature coefficient for this resistance is $\alpha = 0.003 \Omega/^\circ\text{C}$. It means that coefficient is smaller value that for pure platinum $\alpha_{Pt} = 0.00392 \Omega/^\circ\text{C}$, but this is expected for a thin film platinum layer. Nevertheless, there is no doubt that resistance dependence on temperature has strong linear character ($R^2=0,9999$). The same test has been perform for other R_{sens} and R_{delta} resistances giving same result of α

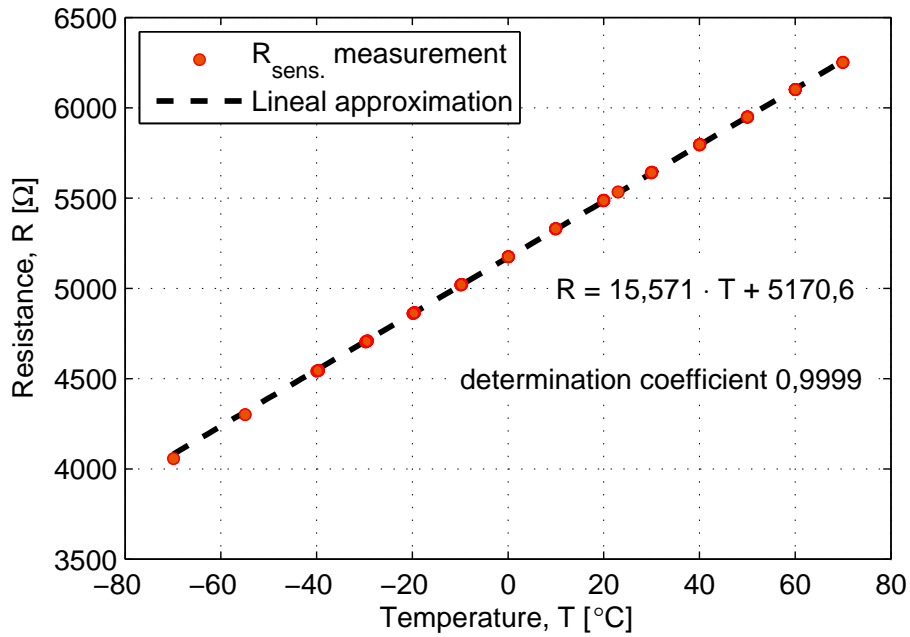


Figure 5.48: Measurement of temperature-dependent titanium/platinum thin film resistance as a function of temperature, with its perfect match by lineal approximation function.

coefficient.

Once dice have been fabricated and their resistance has been characterized they were cutted into squares using a diamond saw with width of $50 \text{ } \mu\text{m} \pm 10 \text{ } \mu\text{m}$. Eventually square dice has a absolute length of $1675 \text{ } \mu\text{m} \pm 10 \text{ } \mu\text{m}$. Some of them put together inside gel pack box are show in Figure 5.49.

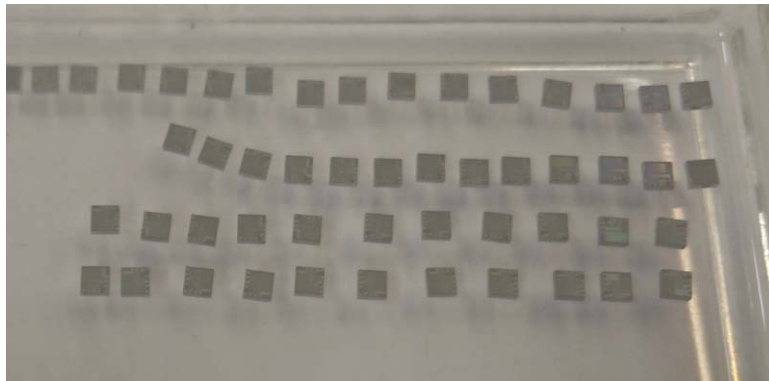


Figure 5.49: Square dice after cutting procedure with nominal size of $1675 \text{ } \mu\text{m} \pm 10 \text{ } \mu\text{m}$.

This was the last element of silicon chip fabrication so the next step will be to take this silicon dice and perform 2-D wind sensor assembly.

5.6 2-D wind sensor assembly

Every 2-D wind sensor transducer is made out of array of dice known as hot points and one, standing alone, reference die that is adequately separated from the hot dice group, see Figure 5.50

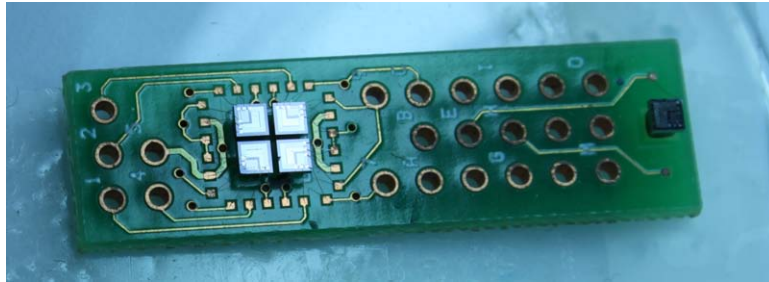


Figure 5.50: Photography of the 2-D wind sensor.

So the hot point dice are working at overheat value in reference to the ambient temperature whereas the reference die is typically at ambient temperature. There is another difference between these dice. Every hot point die is connected to the base with 6 wires to satisfy connection of three separated resistances R_{heat} , R_{sens} and R_{delta} later on a 7th wire was added to prevent electrostatic discharge build-up. While the same die used for as a reference die just need to have two wire-bonding since only R_{sens} is being used for purpose of ambient temperature sensing, see Figure 5.51.

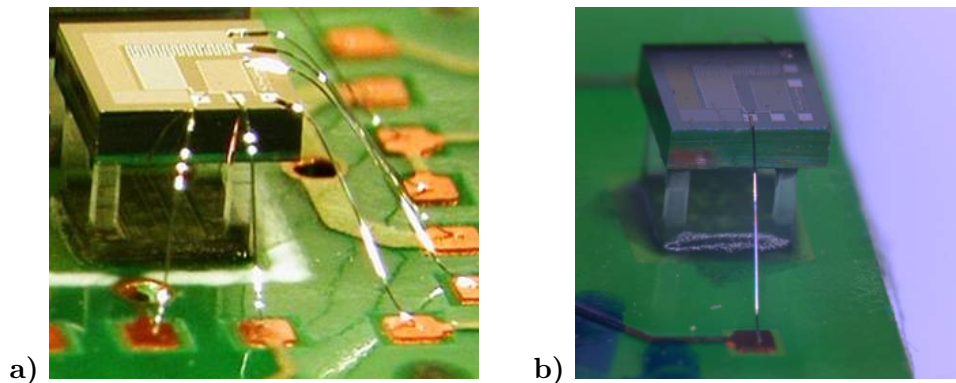


Figure 5.51: Difference in numbers of dice wire-bonding according to the a) hot point b) cold point.

Besides those difference it can be said that 2-D wind sensor unit is made out of four main components:

- PCB custom design base for sensor allocation,
- supporting structure made out of pyrex material,
- silicon die (which fabrication process has been explain in previous section),
- electrical wire-bonding of chip terminals with PCB,

The simplified diagram of 2-D wind sensor single unit is shown in Figure 5.5.

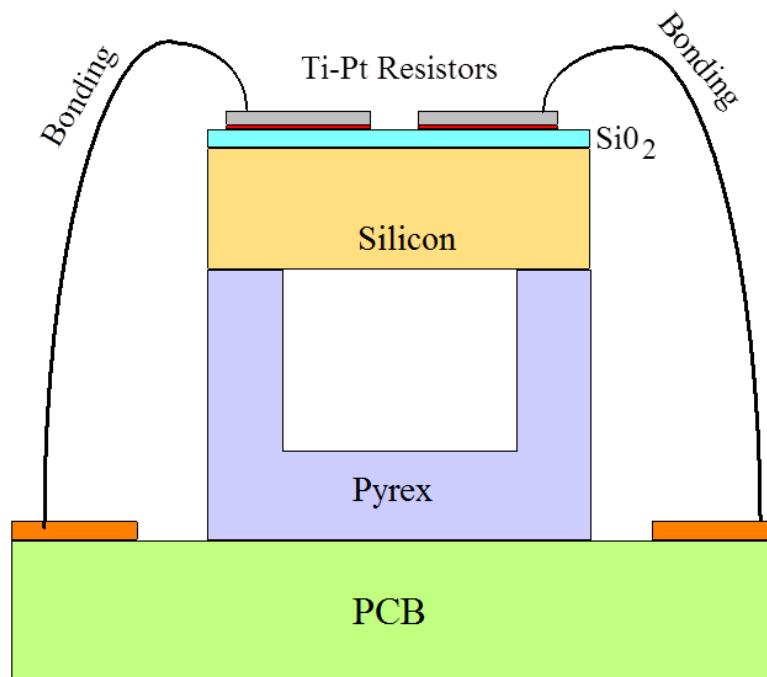


Figure 5.52: Basic diagram of the assembled sensor with PCB, pyrex support, oxidized silicon chip with Titanium/Platinum resistances on it and gold wire bonding.

5.6.1 Printed Circuit Board (PCB) base

This is a custom PCB developed to test the 2-D operation of the WT, see Figure 5.53. The final boards for the project were developed at Computadoras, Redes e Ingeniería, S.A.U. (CRISA) from UPC requirements.

5.6.2 Pyrex support

Pyrex is made from thermal resistant borosilicate glass. The composition of Pyrex 7740 is given as: 80.6% SiO₂, 12.6% B₂O₃, 4.2% Na₂O, 2.2% Al₂O₃,

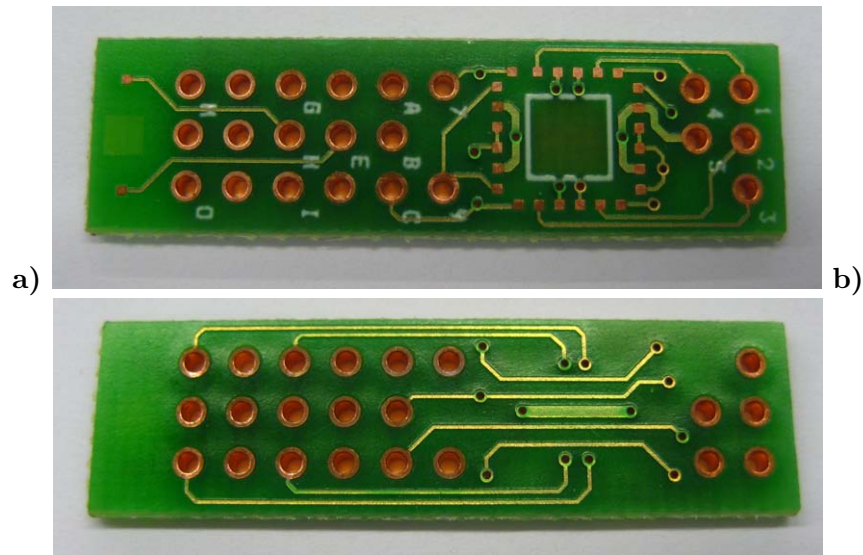


Figure 5.53: Custom designed PCB base a) front view with visible pin-out, b) rear view.

0.04% Fe_2O_3 , 0.1% CaO , 0.1% Cl and 0.05% MgO . Pyrex is interesting for this project because of its high thermal resistivity of $k_{\text{pyrex}} = 1.1 \text{ W/mK}$. Besides being low heat conductor it has also another very good characteristic, which is very low thermal expansion coefficient that is compatible with silicon. Putting both together and adding that pyrex can withstand high temperature, can be anodic bonded to silicon and is well known its process of fabrication this material was used for support design for sensor unit, see Figure 5.54.

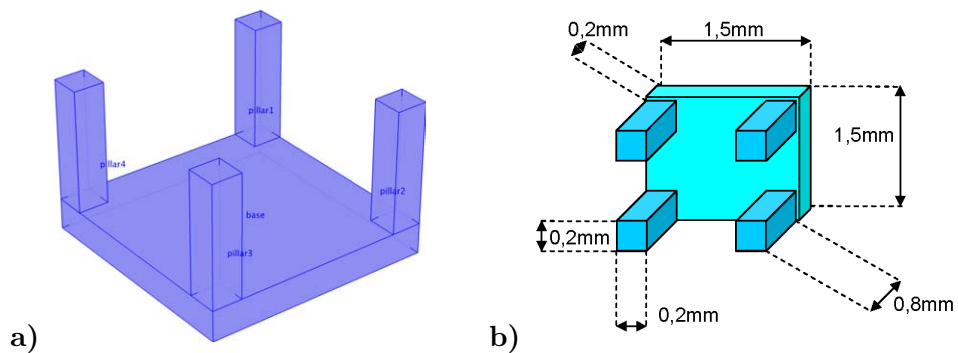


Figure 5.54: Pyrex support *inverted table* shape a) lateral view, b) dimensions.

The silicon dice assembly with PCB and pyrex support, as well as wire bonding process, was realized by CNM.

5.6.3 Wire bonding process

Wire bonding was done using gold wires with diameter of $25 \mu\text{m}$. Wire bonding has been realized in ultrasound soldering process according to the connection scheme between silicon chips and terminal of custom PCB shown in Figure 5.55 .

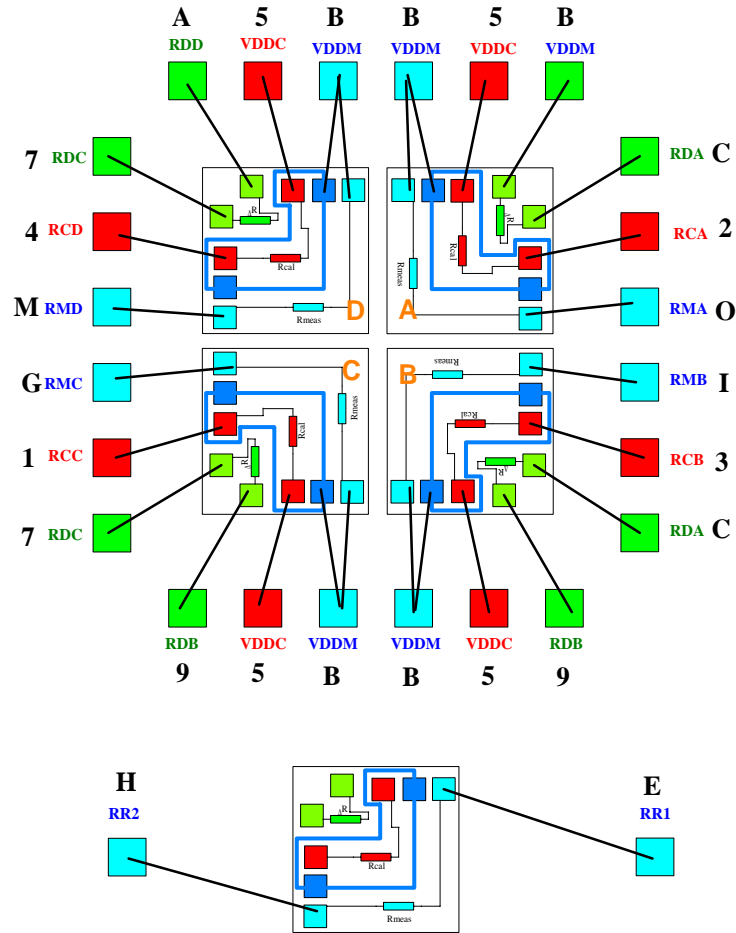


Figure 5.55: Schematic of the 4x7 wire bonding for the hot element array plus 2 wires for the reference die at the bottom of the figure.

Letters and numbers from the Figure 5.55 corresponds to the PCB terminals from the Figure 5.53a) .

5.7 Measurement circuit

In this section the main concept of the sensor is described, namely the electro-thermal sigma delta feedback modulator. As an extension of the

basic sigma delta modulator blocks its electronic implementation will be presented. Finally there will be developed an equation for thermal conductance measurement independently of the ambient temperature.

5.7.1 Electro-thermal sigma-delta modulator

The heart of the whole wind sensor is a sigma-delta feedback loop. The complete wind sensor is composed by four circuits identical, each of them measuring the thermal conductance between one of the hot points and the wind. The operation of one of such sigma-delta circuits is better understood looking the block diagram in Figure 5.56, where two temperature sensors are used to measure the value of the temperature at the hot point (T_{hot}) and at the cold point (T_{amb}).

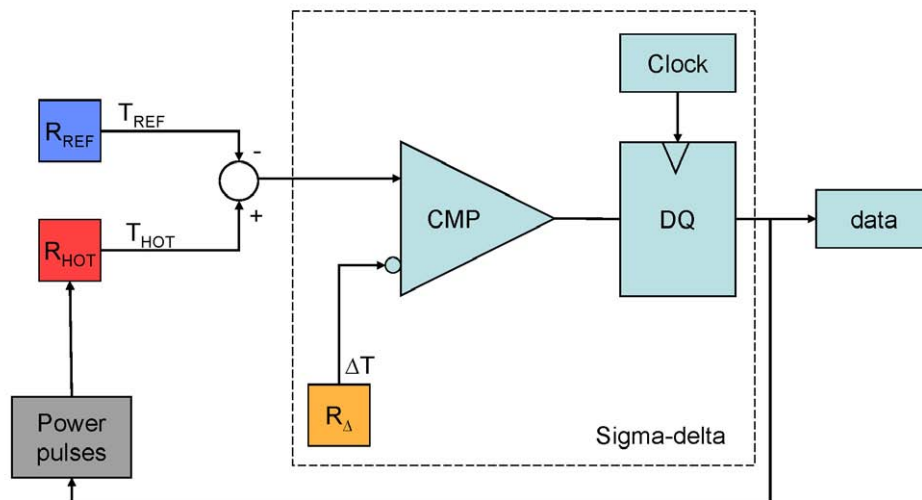


Figure 5.56: Block diagram of the electro-thermal sigma-delta converter for the REMS wind sensor die.

Both temperature sensors are immersed in the wind flow, the hot point is heated to a temperature higher than the wind temperature whereas the cold point sensor is not heated and hence it senses the wind temperature. In the REMS design, described here, platinum resistors have been used because of their linearity and the wide temperature range. The difference of the two temperatures are then compared to a pre-set value ΔT_0 and the result is sent to the data input of a clocked bistable circuit, that sets at the output node the value of the input at the each clock cycle rising edge. The resulting bit stream is used as output of the circuit and simultaneously sent back to control a power circuit sending power pulses to a heater. The closed loop operation ensures that enough power is delivered to the hot point, in order to keep the difference of temperatures between the reference

and the hot point equal to the pre-set value of ΔT_0 . When the wind speed is increased, there is more heat convection and the power required to keep ΔT_0 is larger hence, a measure of the wind speed is given by the number of heat pulses delivered in a given window of time. The power pulses take two discrete values, P_{max} and P_{min} , if we define λ as the ratio of the number of clock cycles in which a power P_{max} is applied to the heater, divided by the total number of cycles in a given window of time:

$$\lambda = \frac{\text{number of cycles with } P_{max}}{\text{total number of cycles}} \quad (5.9)$$

the average value of the power delivered to the hot point is given by:

$$\bar{P} = P_{min} + (P_{max} - P_{min}) \cdot \lambda \quad (5.10)$$

Defining the temperature difference between the hot point and the reference point as:

$$\Delta T = T_{hot} - T_{amb}. \quad (5.11)$$

and If the clock frequency is high enough, the temperature of the hot point will have a small ripple, and hence it can be assumed that:

$$\Delta T_0 = \Delta T \quad (5.12)$$

The thermal conductance G_{th} between the hot point and the ambient is given by

$$G_{th} = \frac{\bar{P}}{\Delta T} = \frac{P_{min} + (P_{max} - P_{min}) \cdot \lambda}{\Delta T_0} \quad (5.13)$$

Although, average power delivered to the hot element can be easily calculated as a sum of P_{max} and P_{min} pulses per frame, in order to find out about the thermal conductance exact value overhear need to be known. And since overhear is a difference between hot temperature and the ambient one this last need to be monitored as it can vary due to well known ambient temperature variation happening in Martian atmosphere. In order to overcome the necessity of permanent monitoring of T_{amb} parameter the specific electronic circuit to drive wind sensor die has been proposed.

5.7.2 Electronic circuit

On each die of the REMS wind transducer are placed three different in shape and length electrical resistances: R_{sens} , R_{heat} and R_{delta} , see Section (5.5.1). Whereas for working circuit, shown in Figure 5.57, we have four resistances denominated as: R_{HX} , R_{ref} , ΔR and R_{ref} but only two of them correspond to the same silicon chip working in hot. To the hot chip belong the measurement resistance R_x known as the R_{sens} and also heating purpose resistance

R_{HX} which corresponds to R_{heat} . The third resistance that is also hot is a resistance that sets overheat value ΔR and could directly be a R_{delta} but also could be a combination of different R_{delta} , which belongs to the group of four hot chips: A, B, C, D. Finally, the reference resistance R_{ref} which is working in ambient temperature conditions is a R_{sens} of the fifth reference chip that not belongs to the hot array group.

Now it is directly shown on the Figure 5.57 that R_H and ΔR and R are working at hot temperature whereas R_{ref} is at ambient (sometimes denominated as cold) temperature. We want to know the thermal conductance G_{th} that relates to the mean power and overheat as shown on the following equation:

$$G_{th} = \frac{\bar{P}}{\Delta T} \quad (5.14)$$

This equation is true whenever we consider ideal case when thermal losses be conduction ($P_{cond.}=0$) and radiation ($P_{rad}=0$) are equal to zero, so:

$$\bar{P} = P_{conv.} + P_{cond.} + P_{rad.} \quad (5.15)$$

otherwise conduction power losses and radiation power losses must be considered and characterized. Let's now analyse ideal case where power transfer by the convection process, in the equilibrium, equates the power delivered to the particular hot die by Joule heating pulses given by equation:

$$\bar{P} = [I_{min}^2 + (I_{max}^2 - I_{min}^2) \lambda] \cdot R_H \quad (5.16)$$

where, I_{min} is a current of low energy pulse, I_{max} is a current of high energy pulse, λ is a number of high energy pulses for entire frame and R_H is a heater resistance at hot temperature. This last can be written as:

$$R_H = R_{H0} \cdot (1 + \alpha \cdot T_{hot}) \quad (5.17)$$

where R_{H0} is a heater resistance at the 0°C temperature and α is a temperature coefficient of resistance for all resistances.

The role of the heating pulses is to achieve circuit equilibrium which is reached when voltages on amplifier entrance V_x and V_{ref} are equal, this happen when

$$I_x \cdot R_x = I_{ref} \cdot (\Delta R + R_{ref}) \quad (5.18)$$

Typically $I_x=I_{ref}$ and $R_{x0}=R_{ref0}$ what simplifies equation to

$$R_{ref(hot)} = \Delta R_{(hot)} + R_{ref(cold)} \quad (5.19)$$

which can be expanded as:

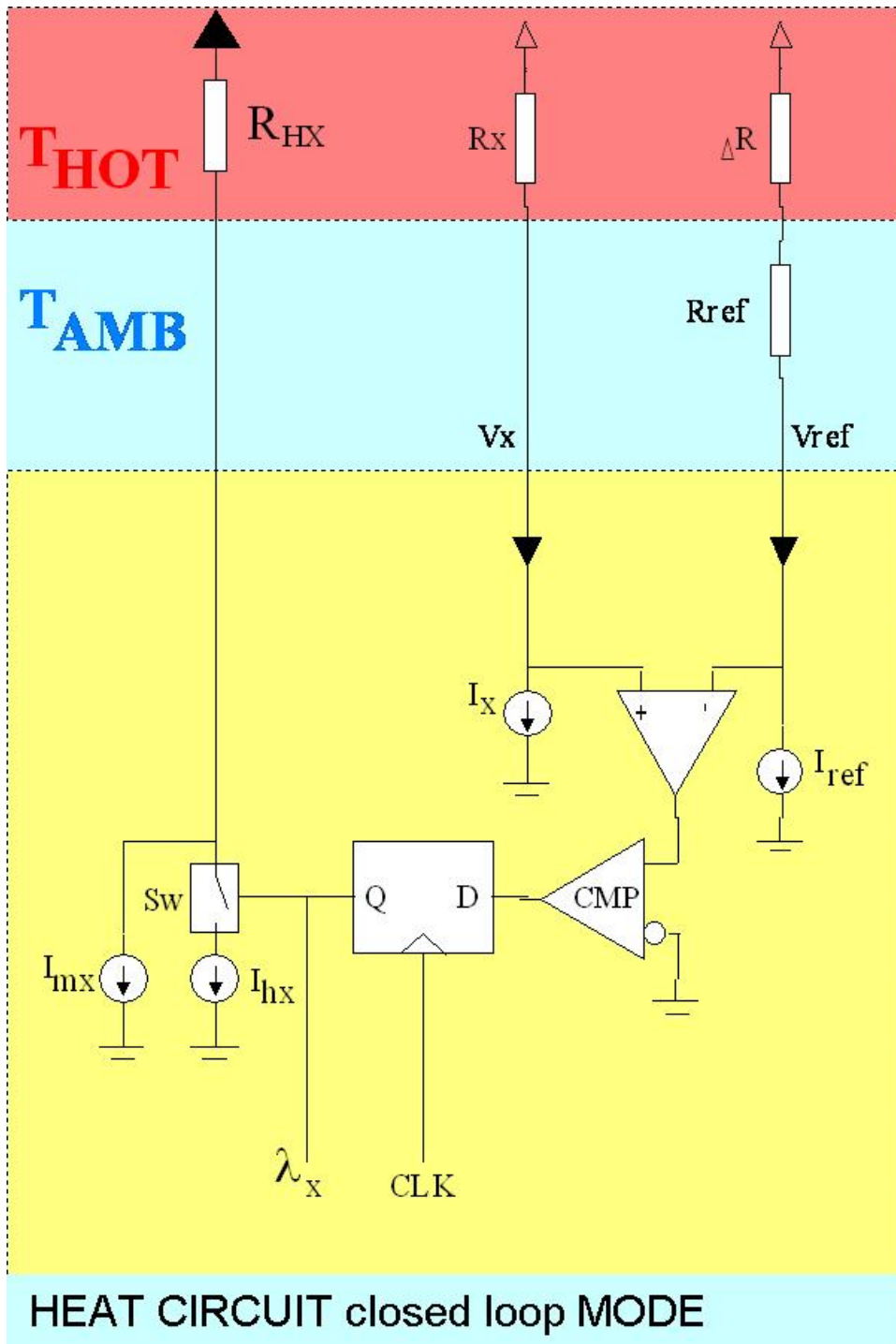


Figure 5.57: Close loop mode circuit to maintain constant temperature over-heat of the hot element in reference to the ambient temperature, where reference die is located.

$$R_{ref0}(1 + \alpha \cdot (T_{amb.} + \Delta T)) = \Delta R_0(1 + \alpha \cdot T_{hot}) + R_{ref0}(1 + \alpha \cdot T_{amb.}) \quad (5.20)$$

and, simplifies to:

$$R_{ref0} \cdot \alpha \cdot \Delta T = \Delta R_0(1 + \alpha \cdot T_{hot}) \quad (5.21)$$

what gives equilibrium condition as:

$$1 + \alpha \cdot T_{hot} = \frac{R_{ref0} \cdot \alpha \cdot \Delta T}{\Delta R_0} \quad (5.22)$$

From that point we can combine thermal conductance equation with equilibrium conditions so we have:

$$G_{th} = \frac{[I_{min}^2 + (I_{max}^2 - I_{min}^2) \lambda] \cdot R_{H0} \cdot \frac{R_{ref0} \cdot \alpha \cdot \Delta T}{\Delta R_0}}{\Delta T} \quad (5.23)$$

what finally makes thermal conductance independent from the ambient temperature variation:

$$G_{th} = \frac{\alpha R_{ref0} \{I_{min}^2 + (I_{max}^2 - I_{min}^2) \lambda\} R_{H0}}{\Delta R_0} \quad (5.24)$$

This electronic circuit has been implemented using standard PCB technology, see Figure 5.58. This test circuit was later integrated in an Application Specific Integrated Circuit (ASIC) in the final REMS flight system.

5.7.3 Overheat value

As explained, sensor chips as for thermal anemometer work with an overheat value that depends on the ambient temperature. As has it been mentioned sensor works in CTDA mode which means that proper shift according to the ambient temperature is provided for the hot point element. This overheat value can be find by developing equilibrium conditions from the electronic circuit from the Equation (5.22) into form:

$$\Delta R_0 + \Delta R_0 \cdot \alpha \cdot (T_{amb.} + \Delta T) = R_{ref0} \cdot \alpha \cdot \Delta T \quad (5.25)$$

And this be the next step becomes:

$$\Delta R_0 (1 + \alpha \cdot T_{amb.}) = \Delta T \cdot \alpha (R_{ref0} - \Delta R_0) \quad (5.26)$$

to give a final equation for overheat value of:

$$\Delta T = \frac{\Delta R_0 (1 + \alpha \cdot T_{amb.})}{(R_{ref0} - \Delta R_0) \cdot \alpha} \quad (5.27)$$

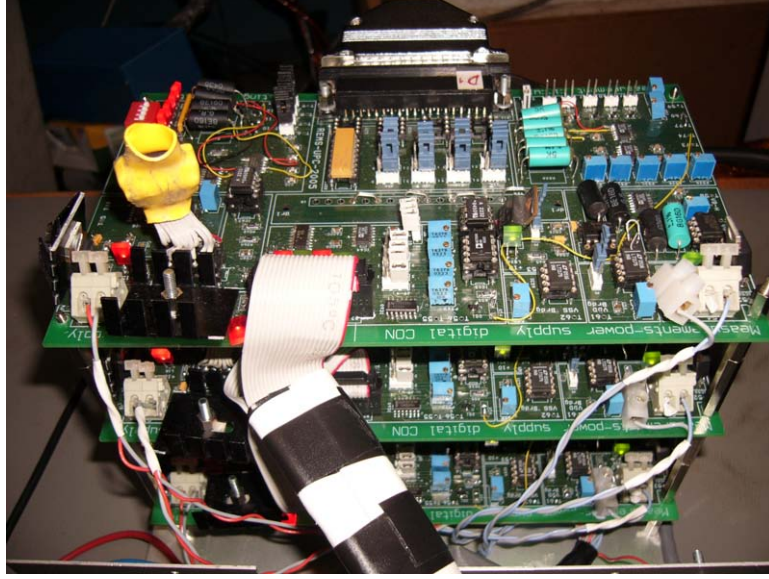


Figure 5.58: Electronic circuit board implemented electro-thermal sigma-delta control.

It is clear from the Equation (5.27), that overheat value is constant whenever $T_{amb.}$ is constant. As the temperature conditions changes the overheat parameters are readjusted properly. To have better insight of how overheat value is changing we can rewrite Equation (5.27) so:

$$\Delta T = \frac{\Delta R_0}{(R_{ref0} - \Delta R_0)} \cdot \left(\frac{1}{\alpha} + T_{amb.} \right) \quad (5.28)$$

As all hot dice A, B, C and D are at the same T_{hot} temperature, any R_{delta} for all four dice can be selected. Moreover, different R_{delta} equivalent values can be selected by properly connecting the 4 R_{delta} resistors of the 4 hot dices in different parallel and serial configurations. In the end, ΔR_0 is a serial and parallel combination of four hot dice resistances: ΔR_A , ΔR_B , ΔR_C , ΔR_D . For example if for the ΔR_0 we choose only that $\Delta R_0 = \Delta R_A$ we will have following situation: $R_{ref0} = 7000 \Omega$, $\Delta R_0 = 700 \Omega$, $\alpha = 0.003 \text{ } ^\circ\text{C}$. Taking this into Equation (5.27) we got that overheat is set as it is shown in Figure 5.59.

It can be seen from Figure 5.59, that we have a linear overheat variation from 23 K for coldest ambient condition up to 40 K for maximum ambient temperature, for $T_{amb.} = 0^\circ\text{C} = 273 \text{ K}$ gives an overheat value 37 K. This was because $\Delta R_0 = \Delta R_A$, but there are as many as 12 different combination of four $\Delta R_{A,B,C,D}$ resistances that could give different overheat at $T_{amb.} = 0^\circ\text{C}$ point, see Table 5.3.

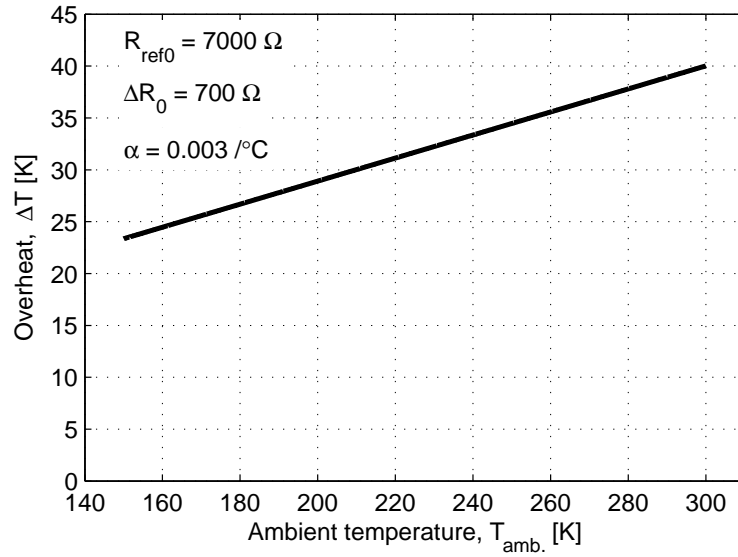


Figure 5.59: Overheat as a function of ambient temperature for particular resistance set.

$\frac{\Delta R_0}{\Delta R_A}$ [-]	$\frac{\Delta R_0}{R_{ref0} - \Delta R_0}$	$\Delta T_{(0^\circ C)}$ [K]
0.2500	0.0256	8.5470
0.3333	0.0345	11.4943
0.5000	0.0526	17.5439
0.6667	0.0714	23.8095
1.0000	0.1111	37.0370
1.3333	0.1538	51.2821
1.5000	0.1765	58.8235
1.6667	0.2000	66.6667
2.0000	0.2500	83.3333
2.5000	0.3333	111.1111
3.0000	0.4286	142.8571
4.0000	0.6667	222.2222

Table 5.3: Table of overheat value for ambient temperature at $0^\circ C$, where chip resistance parameters are as follow: $R_{ref0} = 7000 \Omega$, $\Delta R_{A,B,C,D} = 700 \Omega$ and $\alpha = 0.003 /^\circ C$.

5.8 Convection heat model

In order to better understand the sensor behaviour two models has been considered. First one is the separate silicon die in suspension for evaluation

of convection heat as a function of ambient parameters and has been solved algebraically. The second model is based on the numerical solution for finite elements where sensor hot unit has been mashed together with pyrex support structure in order to add thermal heat losses to the convection. In the FEM model heat is dissipated in a heater resistor path as it happens in the real case. The main reason behind this model was to confirm the hypothesis about homogenous temperature distribution along the entire die structure.

5.8.1 Algebraic equation model

In Figure 5.60 a schematic diagram of the measurement technique is shown. A hot volume is kept at temperature (T_{HOT}), which is higher than the surrounding air temperature (T_{AIR}). If we call P_{conv} the convection power lost by the volume in presence of wind, the ratio of P_{conv} to the over-heat ($\Delta T = T_{HOT} - T_{AIR}$) is defined as the thermal conductance (Gth),

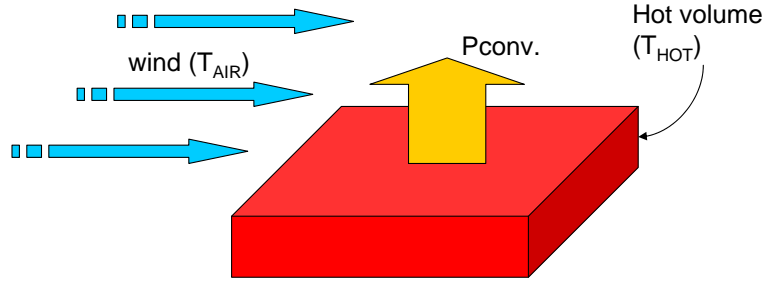


Figure 5.60: Schematic diagram of hot volume convection model.

$$Gth = \frac{P_{conv}}{\Delta T} \quad (5.29)$$

It is well know that the convection power (P_{conv}) is related to the convection coefficient (h) by

$$P_{conv} = h \cdot Area \cdot \Delta T \quad (5.30)$$

where, $Area$ is the surface of hot element exposed to the convection flow, hence

$$Gth = h \cdot Area \quad (5.31)$$

Since the area of the hot volume, interactuating with the flux, can be accurately determined, the convection coefficient is the key parameter governing the thermal conductance. The convection coefficient is described by:

$$h = \frac{Nu \cdot k}{L} \quad (5.32)$$

where, k is the air conductivity, which depends on the temperature, L is a characteristic length of the hot volume and Nu is the dimensionless Nusselt number which for a flat surface under tangential flow, see Reference [70], can be approximated by:

$$Nu = 0,664 \cdot Re^{\frac{1}{2}} \cdot Pr^{\frac{1}{3}} \quad (5.33)$$

where, Re is the Reynolds number and Pr is the Prandtl number; both are dimensionless numbers, [70]. The Prandtl number is defined by the ratio of the momentum diffusivity and the thermal diffusivity:

$$Pr = \frac{\mu \cdot Cp}{k} \quad (5.34)$$

where, μ is the gas viscosity, Cp is the gas specific heat at constant pressure and k is, as mentioned above the gas conductivity. All three parameters are temperature-dependent. The Reynolds number is given by:

$$Re = \frac{\rho \cdot v_f \cdot L}{\mu} \quad (5.35)$$

where, ρ is the gas density and v_f stands for the wind speed. From the ideal gas law, the gas density can be related to the gas pressure and temperature as follows:

$$\rho = \frac{\tilde{M} \cdot P}{R \cdot T_f} \quad (5.36)$$

where, $T_f = \frac{T_{hot} + T_{air}}{2}$ is the 'film' temperature, \tilde{M} is the molar mass and R is the ideal gas constant. Therefore the Reynolds number can be written as:

$$Re = \frac{\tilde{M} \cdot P \cdot v_f \cdot L}{R \cdot T_f \cdot \mu} \quad (5.37)$$

Finally bringing all together to equation (5.31) gives us the following expression:

$$Gth = \left(\frac{0,664 \cdot Area \cdot \sqrt{\tilde{M}}}{\sqrt{R \cdot L}} \right) \cdot \left(\frac{Cp_{(T_f)}^{\frac{1}{3}} \cdot k_{(T_f)}^{\frac{2}{3}}}{\rho_{(T_f)}^{\frac{1}{6}} \cdot T_f^{\frac{1}{2}}} \right) \cdot \sqrt{P \cdot v_f} \quad (5.38)$$

This equation can be split in three terms:

$$Gth = D_{const} \cdot F_{(T_f)} \cdot \sqrt{P \cdot v_f} \quad (5.39)$$

where, D_{const} is a constant depending on the dimensions, and $F_{(T_f)}$ is a function of the gas parameters, which depends only on the gas temperature. D_{const} and $F_{(T_f)}$ are easily identified from the above equation (5.38). Therefore the value of the wind velocity is given by:

$$v_f = \frac{Gth^2}{D_{const}^2 \cdot F_{(T_f)}^2 \cdot P} \quad (5.40)$$

From equation (5.38) it becomes clear that, in order to accurately measure the wind velocity, we require an independent measurement of Gth , which means a measure of the convection power and of the overheat (ΔT) temperature. If we consider an ideal system without conduction or radiation losses, all the power delivered to the hot volume goes into convection in equilibrium, hence a simple measurement of the electric power delivered to the volume and of the temperature would be enough. Moreover the term $F_{(T_f)}$ can be accurately known from the properties of the atmosphere composition and it is also clear that the measurement has also to be corrected using the instantaneous value of the pressure (P).

As it is shown in simplified equation (5.40), the thermal conductance depends on the ambient parameters like temperature and pressure as well as on the wind velocity. Figure 5.61 shows a plot where lines of constant values of the thermal conductance are depicted as function of the air temperature and the air pressure by air velocity product. The temperature range has been chosen to include martian temperatures as well as typical laboratory test conditions. Mass flow has been set to a maximum velocity of 50 m/s with a standard martian pressure of 600 Pa.

It can be noticed that typical thermal conductance values in the range of wind velocities up to 50 m/s, with typical martian pressure around 600 Pa are below 0.35 mW/K, see Figure 5.61. It also means that for maximum wind speed of 50 m/s with carbon dioxide pressure value of 600 Pa and 30°C of overheat, the average heat convection power for one hot element is about 10 mW.

First part of the equation (5.38) depends of the sensor geometry and second one on the carbon dioxide atmosphere parameters which are linked to the temperature. But what stands out directly and is interesting for us is that \bar{G}_{th} depends directly on the pressure and velocity product ($P \cdot U$) in the square root relation. It means that thermal conductance is constant even for different P and U providing that $P \cdot U$ is constant of course for the same temperature conditions. Having equation (5.38) as a base theoretical thermal conductance for gas temperature ranging from 150 to 350 K has and $P \cdot U$ product ranging from 0 to 30.000 Pa·m/s has been found and plot in Figure 5.61. From this graph can be seen that thermal conductivity not only rise when the $P \cdot U$ product rises but also when ambient temperature is getting warmer. It can be said that for colder ambient we observe

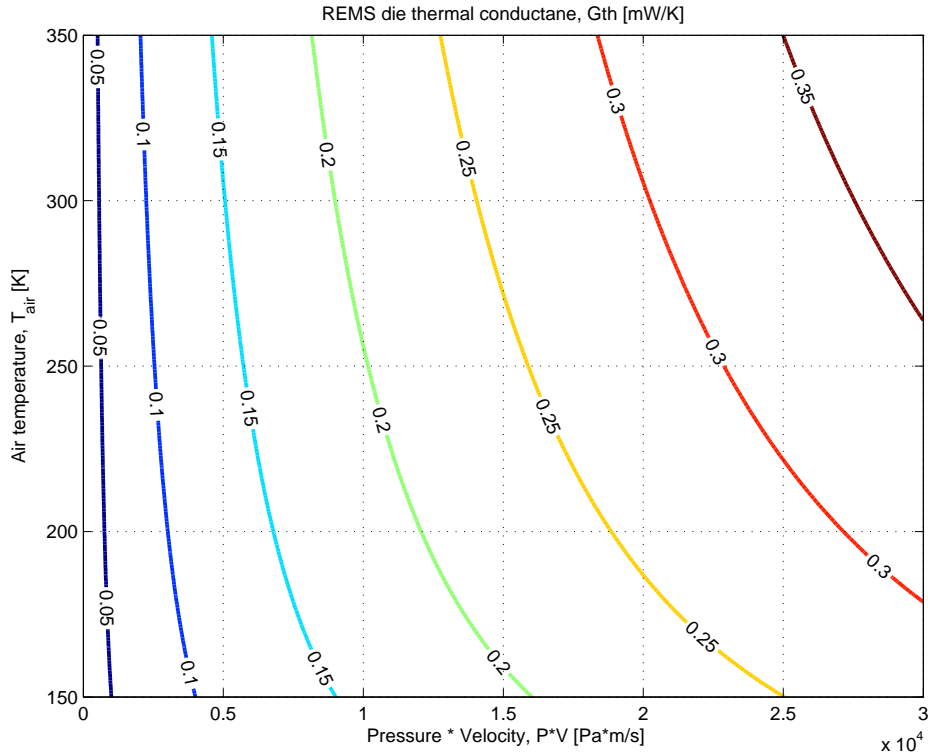


Figure 5.61: Isothermal conductance curves in the 2-D graph as a function of air temperature and mass flow product.

less thermal coupling of the atmosphere with hot element as carbon dioxide gas parameters vary within temperature resulting in less efficient convection processes. Looking closer on the Figure 5.61 we can observe more than seven-fold increase, from 0.05 to 0.35 mW/K, of the thermal conductance from minimum for low velocities up to maximum for high temperature and maximum $P \cdot U$ which for typical Mars pressure of 600 Pa results in flow velocity of $U = 50\text{m/s}$. Analytical solution for die unit reconfirmed thermal conductance sensitiveness to the flow velocity variation what has been provided by CFD simulations and shown in Figure 5.15. What's more this analytical solution seems to be in a good agreement to the numerical solution. It is shown that average thermal conductance of the single die depends on wind speed and pressure but not the incidence angle, see Figure 5.62.

Plotted from CFD simulation, that thermal conductance of each from the group of four dice in array strongly depends on incidence angle of cooling gas flow. Average value of thermal conductance for array structure remains constant, whereas variation of about 50% from this average value can be observed as the wind direction vary from 0 to 90 degree as depicted in Figure 5.62. We observe heat drain reallocation in between hot dice components

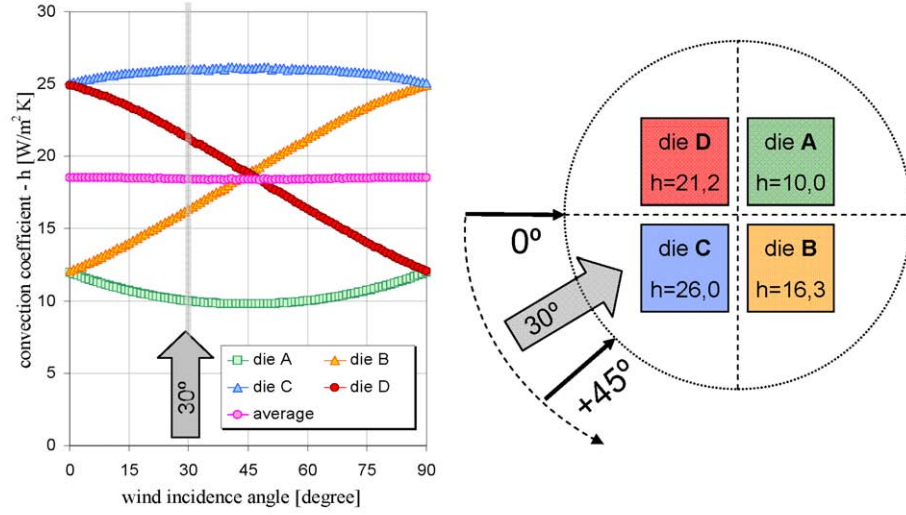


Figure 5.62: Numerical simulation of four hot dice structure for $P_{amb.} = 600 \text{ Pa}$, $T_{amb.} = 220 \text{ K}$ and $U = 10 \text{ m/s}$.

as die position changes from the front of the head flow (where convection is maximum) to the side and rear position being in the thermal shadow of other dice (where convection has its minimum). Thus, variation of all dice convection coefficients in reaction to the wind incidence angle. Now, for the example considered in Figure 5.62. Lets calculate average heat convection coefficient from FEM simulation, so we will have:

$$\bar{h} = \frac{h_A + h_B + h_C + h_D}{4} = \frac{21.2 + 10 + 26 + 16.3}{4} = 18.375 \text{ W/m}^2 \text{ K} \quad (5.41)$$

Then assuming unit die dimensions to be $1.5 \times 1.5 \times 0.5 \text{ mm}$ we have that A_{conv} is:

$$A_{conv} = 2 \cdot (1.5 \text{ mm})^2 + 4 \cdot (1.5 \text{ mm} \cdot 0.5 \text{ mm}) = 4.5 \text{ mm}^2 + 3 \text{ mm}^2 = 7.5 \text{ mm}^2 \quad (5.42)$$

We can find the average thermal conductance from this using Equation (5.29), as follow:

$$\bar{G}_{th} = \bar{h} \cdot A_{conv} = 18.375 \text{ W/m}^2 \text{ K} \cdot 7.5 \text{ mm}^2 = 0.137 \text{ mW/K} \quad (5.43)$$

As FEM simulation has been executed for atmospheric temperature 200 K and pressure 600 Pa for wind velocity 10 m/s , therefore the pressure and velocity product will be $P \cdot U = 6 \text{ kPa} \cdot \text{m/s}$. What stands out that

this average thermal conductivity which has been calculated for the FEM results fits very well with the analytical solution when checked from the Figure 5.61 for $T_{air} = 200$ K and for $P \cdot U = 0.6 \cdot 10^4$ Pa·m/s correspondingly to the numerical simulation conditions.

5.8.2 Finite Element Method (FEM) model

In this section we combine in multi-physics finite element methods simulation two natures of the sensor behaviour: it's electronic circuit made out of platinum deposited path on top of is silicon die and thermal physics which is present for all solid components of the sensor structure. The purpose of this is to model in full 3-D space with support geometry and taking under consideration wire bonding parameters in order to find out about temperature profile. This work was to extend study on temperature distribution along the silicon sensor die. Work has been implemented in numerical platform Computers and Solutions (COMSOL). For this analysis following geometry has been considered:

- Silicon die of particular size 1.6 x 1.6 x 0.4 mm,
- Platinum paths with 80 nm thickness of original geometry copied from the chip layout ended wit gold pads of 150 x 150 μm and the same as platinum thickness,
- Support made out of for pyrex pillars of the size 0.2 x 0.2 x 0.8 mm growing up from pyrex base 1.4 x 1.4 x 0.2 mm respectively,
- Seven gold wire-bonding with length of 4 mm and diameter 25 μm .

Photo of the entire assembled structure can be seen in Figure 5.51 . Equation that describes physical behavior of the sensor could be divided into three domains: electrical, elctro-thermal and thermal. So in electrical domain we will have path resistance equation ΔR which depends on physical dimensions and electrical resistivity of platinum material. In electro-thermal domain we will find formula for platinum resistivity ρ_{Pt} as a function of temperature and equation for generated power P_{gen} in Joule heat effect by current flow through resistive way. Finally thermal domain will acomodate equation for convection power P_{conv} and conduction power P_{cond} respectively. Those, equation can be found in the paper [8] and has been gathered together in table 5.4

For a purpose of the simulation sensor has been forced to work as CCA. Therefore, as a candidate to flow through heating resistor and generating Joule power a current of value 5 mA has been chosen. To satisfy this an appropriate current density ± 222 kA/m² calculated for the pad area was set as a boundary conditions for both R_{heat} terminals. Pyrex base boundary

Domain	Equations
Electrical	$\Delta R = \Delta L_{Pt} \cdot \rho_{Pt} / (W_{Pt} \cdot H_{Pt})$
Electro-Thermal	$\Delta P_{gen} = I^2 \cdot \Delta R$, $\rho_{Pt(T)} = \rho_{Pt0} \cdot (1 + \alpha_{Pt})$
Thermal	$P_{cond} = -k \cdot A_{cross} \cdot \Delta T / \Delta x$, $P_{conv} = h \cdot A_{conv} \cdot \Delta T$

Table 5.4: Domains and equations

conditions has been set for fixed temperature of 280 K. Entire heat convection coefficient (h) has been set for the value of 5 W/(m²K), what for given geometry is equal to thermal conductance (G_{th}) of 0.0384 mW/K which according to the divagation in Figure 5.61 would correspond to the heat convection drain for faint wind speed less than 1 m/s. Finally, thermal losses which occurs through thin in size but very heat conductive wire-bonding has been added to the model. It has been added be proportional change in heat convection coefficient corresponding to the resistive pads - places where electrical wires are bonded with silicon chip. Additional heat convection coefficient calculus for PADs result in value of $h_{add} = 1700$ W/(m²K) which reveals 350 fold increase in reference to the typical heat convection coefficient applied for whole structure.

After all the boundary conditions were set the static simulation was run to obtain temperature profile of whole structure, see Figure 5.63a).

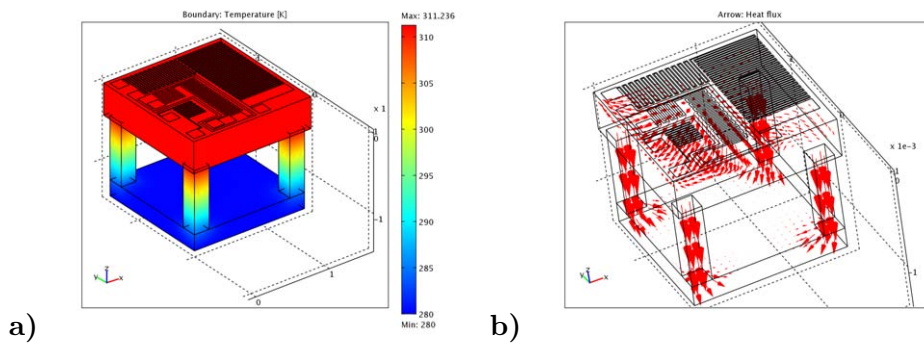


Figure 5.63: Static FEM simulation of the REMS wind sensor unit under constant heat convection cooling, a) Temperature solution, b) Heat flow channels.

From the results has been found that overheat achieved for the silicon chip in reference to the ambient temperature of 280 K was about 31 K as

the temperature of the die was between 311.10 and 311.23 K. What is also seen from the Figure 5.63b) that the main heat draining channel are through pyrex pillars and wire bonding PADs terminals.

Simulation also has shown that temperature variation withing hot die is only 0.13 K what in reference to the overheat value gives less than 0.5% of variation. Therefore, it can be said the this FEM simulation reconfirm the assumption that along the sensor unit temperature is uniform, see Figure 5.64.

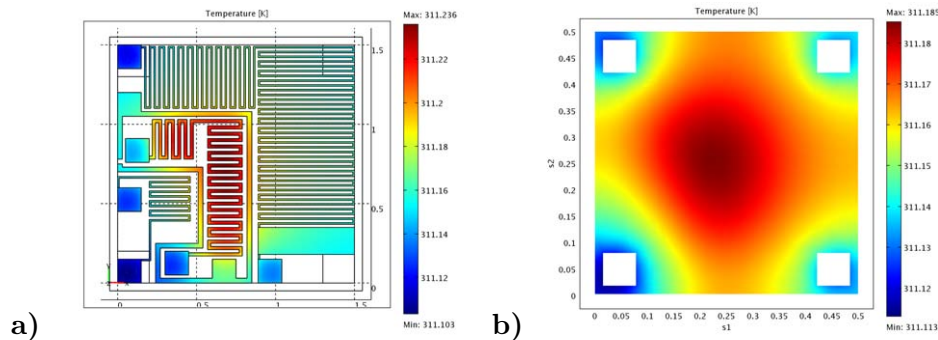


Figure 5.64: Close look for the FEM simulation of the REMS chip under constant heat convection cooling, a) up the surface , b) down the surface.

Furthermore, as the main thermal loses are associated with supportive pyrex pillars structure and electrical wire-bonding the sections where those are connected with silicon die are the places were lower temperature is registered, as seen in Figure 5.64b) for pyrex pillars and in Figure 5.64a) for wire-bonding. Also in Figure 5.64b) we can see that central part of the chip surface where heating resistor is printed on is where greater temperature is registered, what has been expected as this resistor is an unique heating generating element for the entire die structure. Nevertheless, of the particular geometry of the heating source and heat draining terminals overall temperature homogenous distribution is provided thanks to the high thermal conductivity of the silicon material use in a fabrication of the dice.

5.9 Measurement campaign

This section will give a global overview of different wind tunnel facilities where some basic measurements on the wind sensor prototype on the wind sensor has been done. Some measurements that proof the sensor ability to fulfill project requirements will be shown. Some tests are developed in carbon dioxide low pressure atmosphere featuring a cold temperature to be similar of Mars real conditions.

It will be shown that sensor four dice structure as a whole is sensible for the wind magnitude and not for that horizontal angle. Differential die

measurements however will provide sensitivity for horizontal angle discrimination. Measurements also confirm that thermal conductance depends on $P \cdot U$ product. Finally test of immediate change in wind conditions will shed light on how fast could be the reaction of the sensor to estimate its response time.

5.9.1 Wind tunnel facilities

Wind tunnel facilities used to test the REMS sensor can be divided into four categories.

Wind tunnel categories:

1. **Rotating arm**, CRISA ambient room facility with 3m arm,
2. **Re-circulating**, Aarhus University AWSTI facility [71],
3. **Open circuit**, Oxford University wind nozzle [72],
4. **Linear** with steal air, CAB facility at CSIC-INTA, [73].

Each of the wind tunnels have a different mechanism of wind flow control. Simplified way how they work is presented in Figure 5.65.

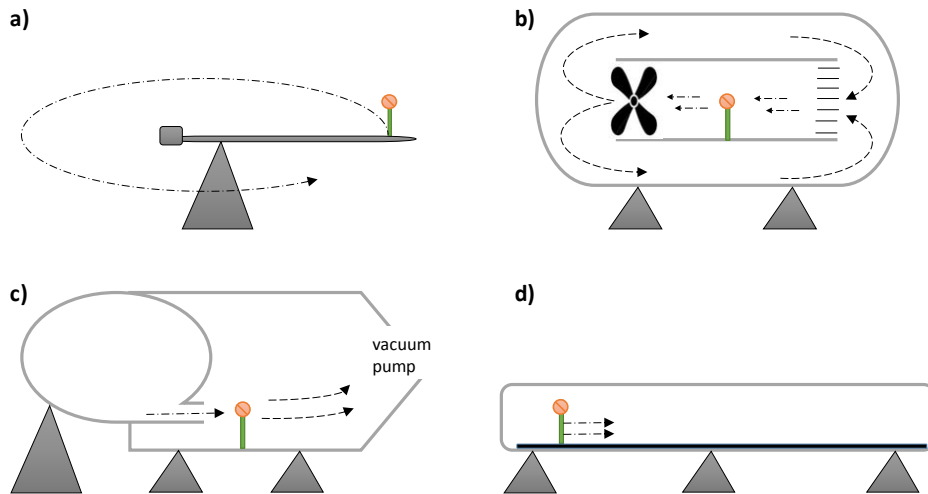


Figure 5.65: Wind tunnel facilities: a) rotating arm, b) re-circulating, c) open circuit, d) linear. Wind sensor under test has been symbolised by the red hot ball on the green support, where arrows represent either movement of the flow or wind sensor unit.

Each of the facilities has their pros and cons that need to be carefully considered before the decision about what kind of installation employ.

Rotating arm wind tunnel need a big room to operate and its gas parameter are those of the room (air at ambient temperature and pressure). The air is considered to be still and the sensor moves with lineal speed, which is a product of rotation in full turns per unit time by circumference ($2\pi R_{arm}$). In the facility the arm was not capable to support a heavy load, so the interface circuits needed to be at the center of rotation. This solution was prone to generate a lot of electrical noise.

Re-circulating wind tunnel can work with any gas that can be pumped-in and its pressure can be adequately adjust. If the chamber seal is good this composition can stay there for a long time. Also velocity can smoothly be tuned by the rotating fan speed. Cooling down the ambient gas to reach Martian like temperatures is difficult but some range of temperature below the zero could be achieved that involves cooling down entire chamber or at least interior crust of the chamber that is thermally isolated from the main chassis. A big disadvantage of all the re-circulating wind tunnel is that it is difficult to introduce sudden changes in either wind temperature or velocity.

Open circuit wind tunnel is a kind of facility where gas we want to work with is gathered in the preparation chamber at given pressure and then be the process of expansion it reduces its pressure but gains the velocity and at the same time cools down in adiabatic pressure. This process is driven by the heavy duty vacuum pumps at the other end of the circuit. Sensor unit is placed just on the way out of the outflow nozzle. This tunnel enable us to tune two out of three flow parameters which are Temperature (T), Pressure (P), Velocity (U) whereas the third one is directly driven from the ideal gas equation. In case of working with gas different from air we need to have huge reserves of it and when working with poisoning gases like CO_2 all the safety measure at exhaust are obligatory.

Lineal wind tunnel as the recirculating tunnel it can be filled with any gas under the pressure we like and cooling down is rather difficult. The difference is in how its working. The air need to be static and the device is moving with lineal velocity on the rail along the tunnel longer dimension. As the rail speed can be well known the precision in wind speed is good the inconvenience comes from the limited size of the tunnel, so when the devices reaches the end of the rail measurement need to be finished That typically takes several seconds and then it is necessary to wait enough time in order to settle all the gas particles, which have been moved by the sensor, to the static velocity 0 m/s. Nevertheless, the big advantage of this solution is that the velocity of the wind sensor device could be updated on instant so that enables dynamic test and response time measurements.

5.9.2 Re-circulating wind tunnel in Aarhus

The main goals of the Aarhus measurements were to confirm sensor prototype sensitivity for wind magnitude and direction and also made some rough estimation about time response of the proposed geometry. In order to perform measurements wind sensor have been allocated inside wind chamber as is depicted in Figure 5.66.

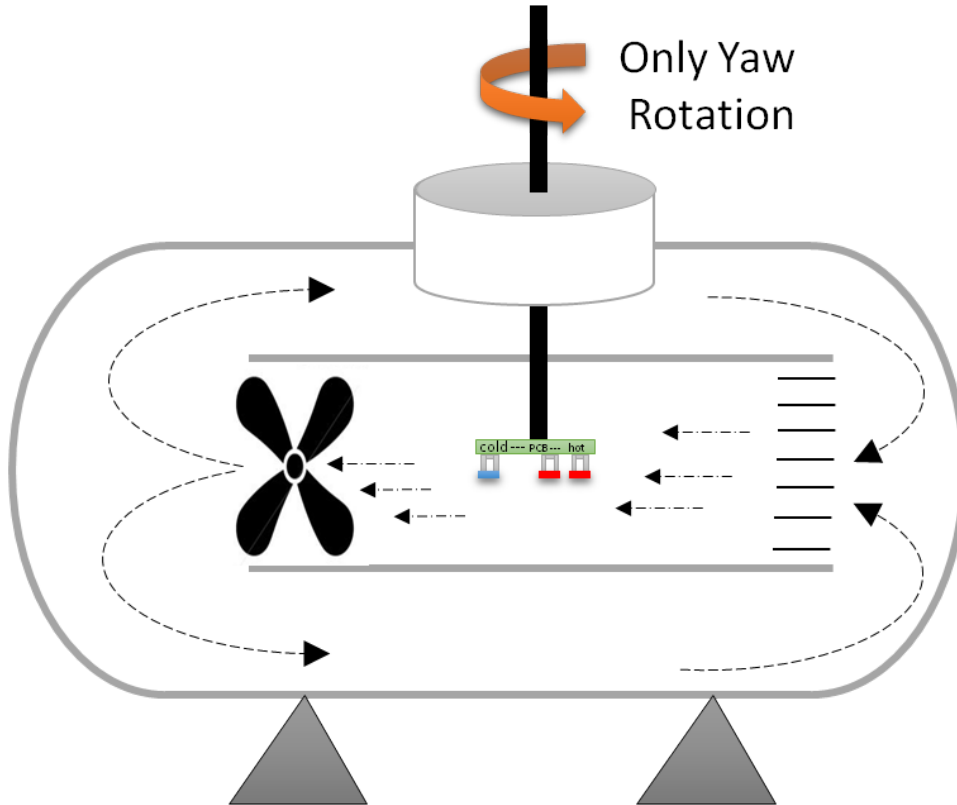


Figure 5.66: REMS wind 2-D transducer set up inside Aarhus AWSTI wind tunnel facility.

As it can be seen from the Figure 5.66, the sensor board has been placed upside down with four hot point being placed ahead of the wind blow. As the rotation axis enables only Yaw angle (ϕ) configuration it was in the same angle orientation as for the simulation in the Figure 5.15.

5.9.3 Sensitivity to the wind speed

The idea of this experiment was to show that sensor for hot dice structure as a whole is sensitive to the wind speed, what has been predicted by FEM simulation in Figure 5.17. To do that wind tunnel chamber was filled with carbon dioxide (CO_2) at low pressure 6 mBar and at laboratory temperature

of 25°C. Thermal overheat of the hot elements was set for 23°C. Test has been carried out ranging wind velocity from 0.3 m/s up to 20 m/s, calibrated with Laser Doppler Anemometry (LDA) technique, [74]. Measurements has been performed for different Yaw rotation angles. For each velocity and incidence angle position 100 samples, each sampled with frequency of 1 Hz, has been registered. An example of the of registered samples of the averaged power delivered to the four group of sensor for different wind speed is shown in Figure 5.67a). For each time when 100 samples has been registered during 100 s of sensor work the acquisition has been stopped and the wind flow velocity has been readjusted.

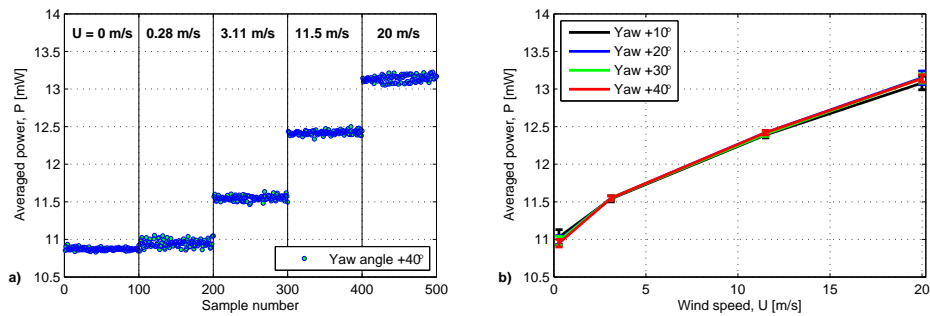


Figure 5.67: Averaged power dissipated per silicon die to the ambient temperature CO₂ at 6 mBar a) raw data as sampled with frequency of 1 Hz b) as a function of the wind velocity and incidence angle (ϕ).

In Figure 5.67b) the averaged power delivered to the four hot dice has been plotted as a function of the wind speed but for different incidence angle ranging from 10° to 40° with 10° step. This experiment confirms results from the simulation that array of hot silicon chips as whole is sensitive to the changes in wind velocity what reflects in rise of the power for higher wind velocity flow, see Figure 5.67. The resolution of our wind sensor is better than 0.3 m/s in the range 0.3 m/s to 20 m/s as tested and sensor is capable of detecting as faint wind blows as the 0.3 m/s, what was the smallest wind speed tested (as calibrated using a laser meter) .

This test also has shown significant offset for the zero wind velocity in power demand of the sensor and this is because of the wind thermal losses through the support structure and wire bonding. Only about 10% of the power delivered to the hot element is being modulated by forced convection to the ambient whereas remaining 90% are drained to the PCB and conducted to the cold enclosing.

5.9.4 Sensitivity to the wind direction

We have shown from Figure 5.67b) that averaged dice power doesn't depends on wind direction. The situation is different if we look on the power

dissipation of particular dice and make calculation for differential terms as (North-South) and (East-West) as mentioned in Figure 5.18. Therefore for different wind velocities (U) and wind direction angle (ϕ) we got following power read out listed in Table 5.5.

Yaw	U_{flow}	P_A	P_B	P_C	P_D	N-S	E-W
ϕ [°]	[m/s]	[mW]	[mW]	[mW]	[mW]	[mW]	[mW]
+40	0.28	11.3242	10.7707	11.2785	11.4669	0.7418	-0.6505
+40	3.11	12.3492	11.3682	11.4173	12.1810	1.7446	0.1191
+40	11.5	13.6820	12.1245	11.8886	13.1904	2.8593	0.7275
+40	19.99	14.5374	12.6587	12.3075	14.3419	3.9132	0.5468
+30	0.28	11.3542	10.8065	11.3117	11.4974	0.7334	-0.6484
+30	3.11	12.3175	11.2606	11.4484	12.2936	1.9021	-0.1639
+30	11.5	13.6409	11.8819	11.8962	13.4038	3.2667	0.2229
+30	19.99	14.5313	12.3926	12.3570	14.5849	4.3666	-0.0180
+20	0.28	11.3354	10.8537	11.3513	11.4803	0.6107	-0.6427
+20	3.11	12.2824	11.1972	11.4843	12.3485	1.9493	-0.3532
+20	11.50	13.5920	11.7651	11.9908	13.5439	3.3799	-0.1776
+20	19.99	14.4936	12.1830	12.5391	14.6965	4.4680	-0.5591
+10	0.28	11.3458	11.0171	11.2986	11.5392	0.5693	-0.4749
+10	3.11	12.2009	11.1346	11.5609	12.3626	1.8680	-0.5880
+10	11.5	13.4232	11.6544	12.0808	13.5936	3.2815	-0.5967
+10	19.99	14.3658	12.0162	12.5748	14.6397	4.4146	-0.8325

Table 5.5: Averaged power of each from four hot dice array: P_A , P_B , P_C , P_D with its differential therms: *North-South* ($N-S$) and *East-West* ($E-W$) for different wind flow velocity (U_{flow}) and yaw (ϕ) incidence angle.

Lets look closer on the data from Table 5.5. Instead of taking for analysis the average power of four dice structure we will study the differential therms which are the linear combination of the power from each pair of the four dice ($N-S$ and $E-W$). By introducing the differential terms, conduction looses should cancel out or at least be reduced significantly. As a result we see that the silicon dice array has sensitivity for the wind incidence angle (ϕ), see Figure 5.68.

From the Figure 5.68 could be seen four things. First, as the wind blows from the *North* direction (angles ranging from $+10^\circ$ to $+40^\circ$) the stronger the wind is the bigger is component *North-South* which is calculated from following term: $N-S=(P_A+P_D)-(P_B+P_C)$, Second, as the wind inclination angle grows for constant wind velocity (U_{flow}) so the head of the flow moves toward *East* the differential component *East-West* grows whereas at the same time component *North-South* is slightly decreasing. The third conclusion is that for the very low velocity, in this case 0.2 m/s, there is some problems with angle recognition and the same with wind direction sensi-

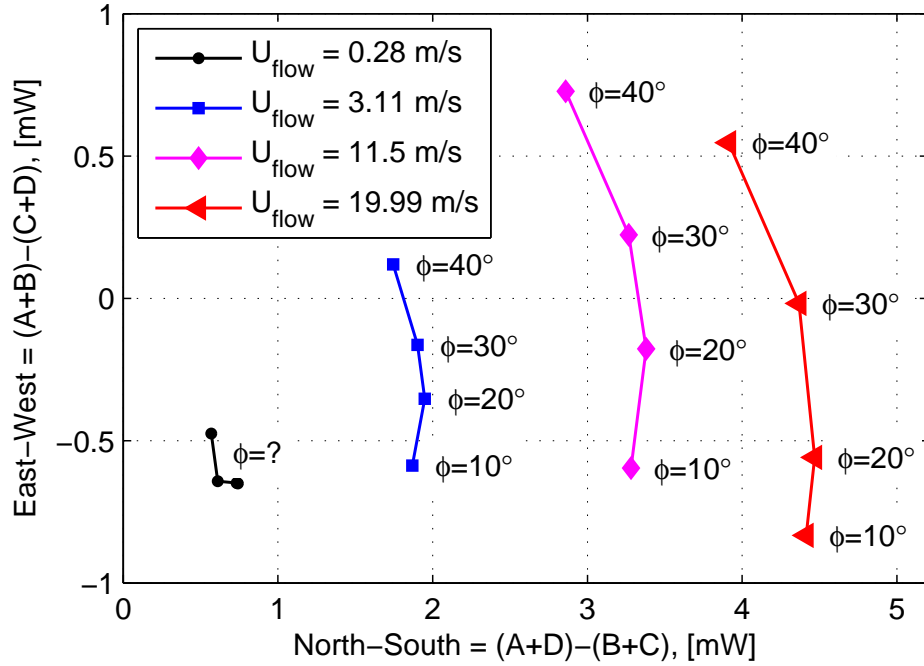


Figure 5.68: Visual interpretation of the data from Table 5.5.

tivity. Finally for the higher velocities: 3.11 m/s, 11.5 m/s, and 20 m/s it is very clear that sensor shows very good sensitivity for wind direction and ability to distinguish between two direction is far better than 10° in angle of incidence. More information about this results were published in reference [2], see Appendix B.

5.9.5 Sensitivity to the atmospheric pressure

Typical pressure in Mars surface is 600 Pa although in the Hellas Planitia it can reach 1200Pa. It is clear that the pressure can affect the output of the measurement as it has been shown in algebraic model Equation (5.38) and is typical for hot film anemometry. In order to confirm the hypothesis, that sensor is sensitive to the pressure by velocity product, we have planed and performed an experiment where power required for an overheat of 38 K was set for all four silicon dice array of the wind transducer inside Aarhus wind chamber under several low pressure conditions of carbon dioxide atmosphere at laboratory temperature. Analysed the pressure effect on the results of our model described above and the values of the power required for given overheat of the mean power for all four dice are presented in Figure 5.69.

If we plot the power required to achieve a given overheat temperature, as a function of the Velocity (U) up to 20 m/s for different pressure we got three separate curves see Figure 5.69a). Situation becomes different if we

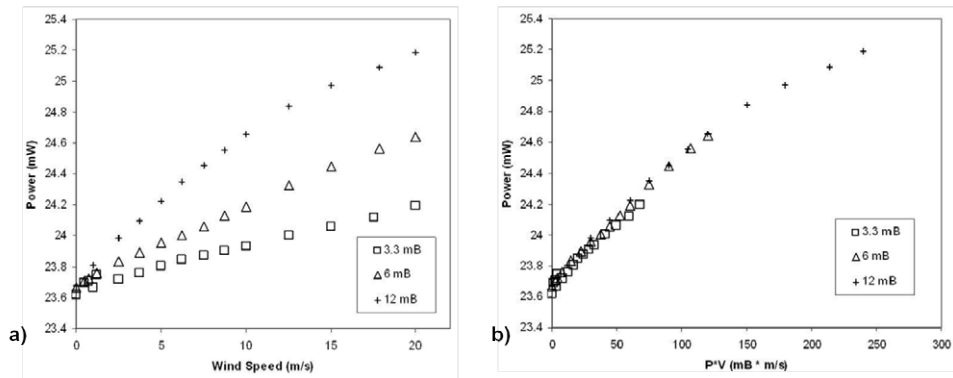


Figure 5.69: Averaged power delivered to the four dice structure as a function of a) velocity, b) velocity by pressure product.

plot the same when we plot average power delivered to the four dice as a function of velocity by pressure product ($V \cdot P$), then all three curves align smoothly as it would be one curve, see Figure 5.69b). This result has been verified for each die from the group of dice separately, see Figure 5.70.

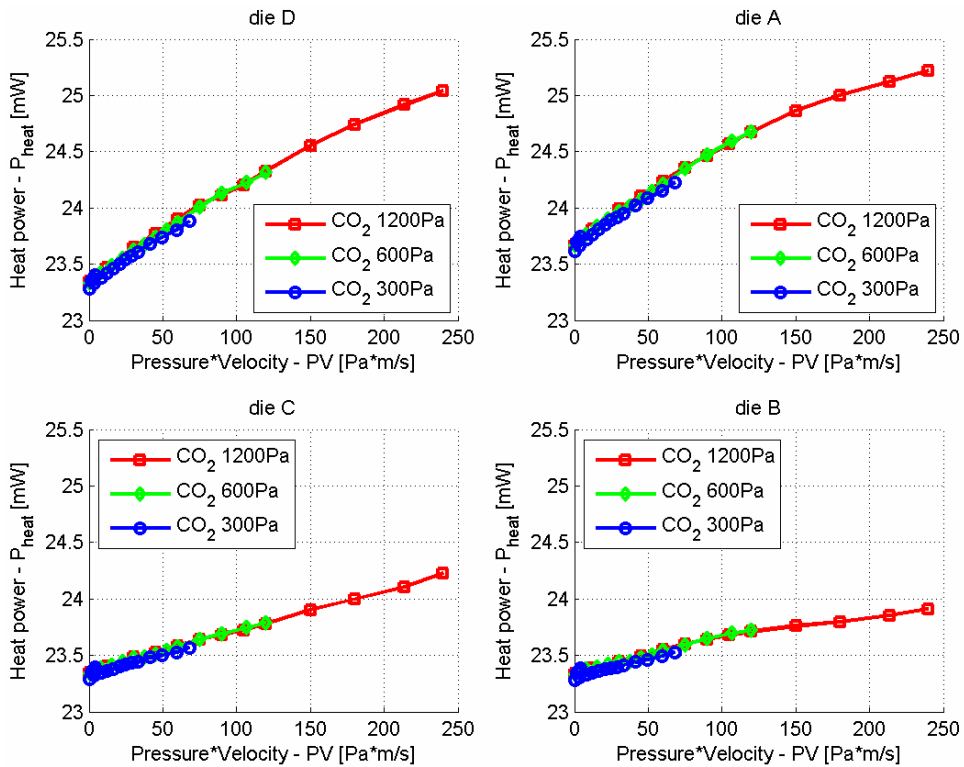


Figure 5.70: Power delivered to the four dice A, B, C, D as a function of velocity by pressure product.

it stands out from the graph that all the points indifferently on the atmospheric pressure align on the same curve nicely. Dice who were in front of the head flow (A & D) drained more heat than the pair which were located in the rear of the group (B & C). This particular geometry does not change this basic behavior so it is confirmed that the sensor is actually measuring the mass flow which is a $P \cdot U$ product. Therefore, in order to get to know wind velocity magnitude independent pressure measurement of the atmospheric pressure need to be provided. This requirement is fulfilled in the case of REMS instrumental meteorology set-up, see Section (5.1.2).

5.9.6 Time response experiment

The REMS sensor is lightweight and hence, would be expected that the time response can be fast enough to cover rapid changes in the wind speed and direction on Mars. Nevertheless, we wanted to evaluate the time response in simulated Martian atmospheric conditions. This test has been arranged in the Aarhus University wind tunnel. Since changes of wind speed inside the low-pressure tunnel are slow (about 10-15 s), changes in the angle orientation of the sensor can be made very fast (manual turn). The result of a steep change of 40 degrees in yaw rotation angle (from -20 degree to +20 degree) was performed. The results are shown in Figure 5.71, where the registered change in the thermal conductance is observed.

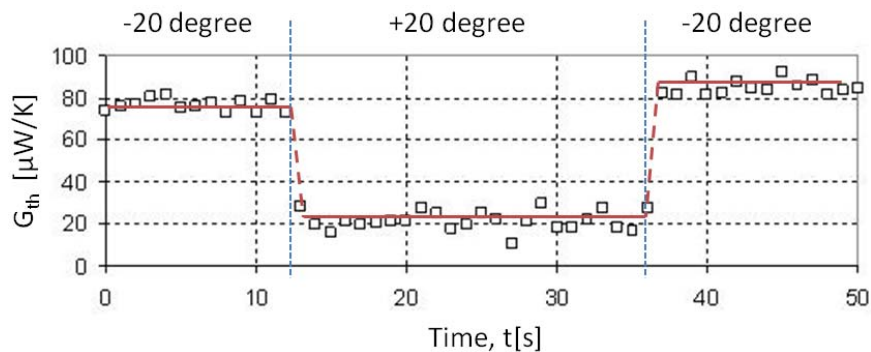


Figure 5.71: Thermal conductance in result of the steep change in direction of the wind yaw angle (from -20 degree to +20 degree and then back to the -20 degree). Measurement conditions: carbon dioxide pressure 6 mBar, ambient temperature -50°C , hot point overheat 23°C , wind speed 10 m/s.

An experiment was set for following atmospheric conditions; $U = 10$ m/s, $P = 6$ mBar, $T_{amb} = -50^{\circ}\text{C}$, $\Delta T = 23^{\circ}\text{C}$ with 1 s sampling rate of the electronics. As can be seen in Figure 5.71 the transient is followed by the sensor response and the time response of the sensor is in 1 second range.

5.9.7 Open circuit wind tunnel in Oxford

In another measurement campaign, this time in the Oxford open circuit wind tunnel, we have repeated an experiment where REMS wind sensor was exposed for three slightly different pressure conditions 5, 6, and 7 mBar of carbon dioxide cooled down to -30°C . The prototype of the boom fixed to a dummy mast has experienced different wind velocities from the boom pointing direction. The whole set up is presented in Figure 5.72.

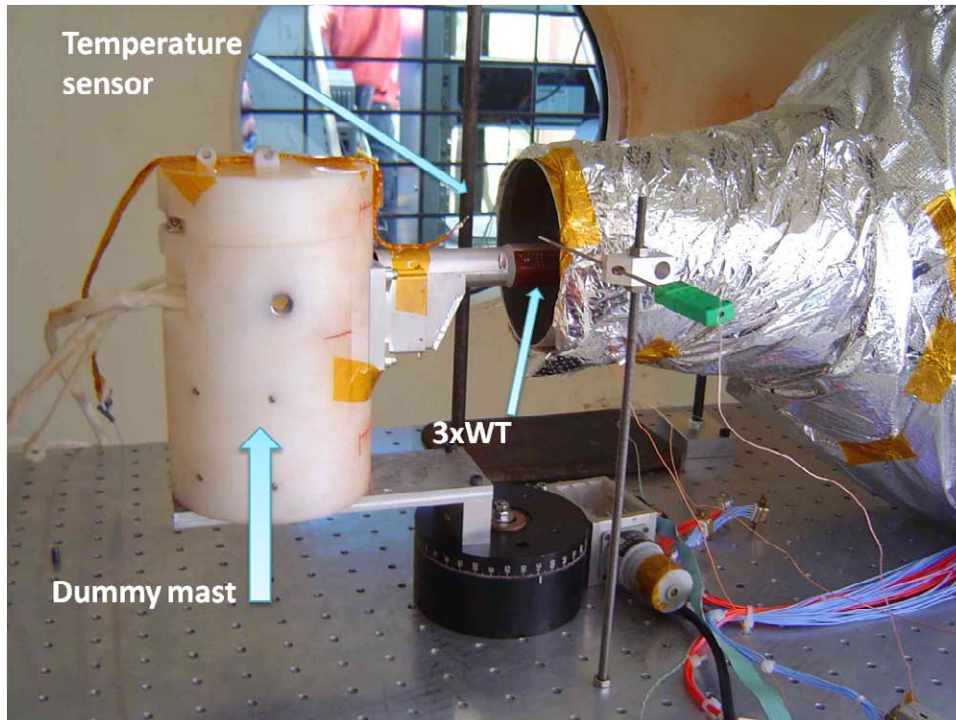


Figure 5.72: Prototype of the REMS wind sensor boom set-up for experiments inside Oxford open circuit wind tunnel chamber

It can be seen that sensor head has been placed in a very central part of the wind nozzle, where the wind has got laminar behavior, and that wind direction angles were $Yaw = 0^{\circ}$ and $Pitch = 0^{\circ}$. Therefore, for all three WT boards local 2-D wind flow was from the *North* direction. Three WT boards are located around boom with angular step of 120° where board 3 was placed upside down and board 1 shows in front of the viewer and can be seen on Figure 5.73, whereas board 2 and board 3 are in the rear of the picture according to the boom cross section shown in the top-right corner of the same Figure 5.73.

Three tests at ambient temperature and three different pressures 5, 6, and 7 mBar were performed in Oxford. An increase of pressure means an increase of density and more particles are in contact with the sensor and higher

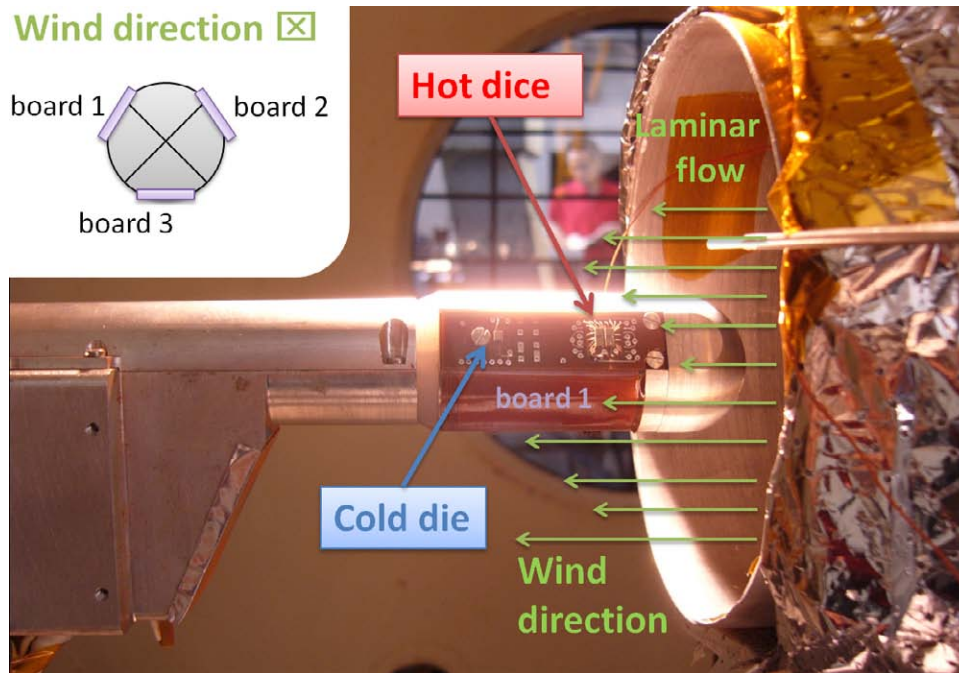


Figure 5.73: Orientation of the REMS boom and its three WT boards for the $Yaw = 0^\circ$ and $Pitch = 0^\circ$

conductance have been registered. The pressure rise also results in rise of differential terms in $North - South = (A + D) - (B + C)$, see Figure 5.74a). As in the other examples this pressure effect could be modelled easily if we represents thermal conductance as a function of $P \cdot U$ product rather than function of wind velocity, see Figure 5.74b).

From Figure 5.74 only differential term for board 3 starts from 0 mW/K whereas in board 1 an offset of 9 mW/K and in case of board 2 offset of -26 mW/K is observed, that could be associated to the not ideal symmetry in the thermal conductivity conditions through the support components.

5.10 REMS wind sensor in comparison to Viking and Pathfinder

Comparison between those three sensors can be perform at two levels. One is when we take under consideration entire sensor system. Other when we look into details and make comparison at the basic transduction level. In order to properly judge differences between each wind sensor unit simplified first order model has been developed.

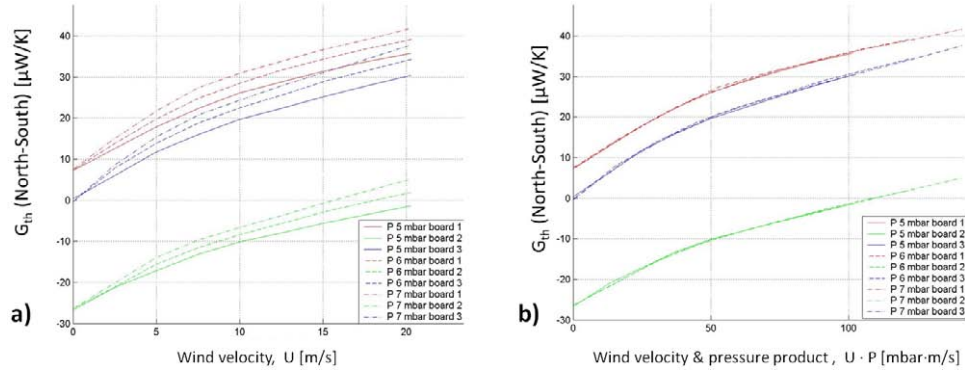


Figure 5.74: Longitude thermal conductance (G_{th}) differential term: $North - South = (A + D) - (B + C)$ for three WT board of REMS boom prototype as a function of a) wind velocity b) wind velocity and pressure product. Experiment was run for three ambient pressure 5, 6 and 7 mBar and same temperature and overheat conditions

5.10.1 First order model

Appropriate thermal modeling of the Viking, Pathfinder and REMS sensor units would enable an unbiased comparison of these three sensors, although representing different anemometry approach. In this section will be describe a simplified 1-D model of the heat flow of each sensor unit element. The unit element considered for the Viking sensor is a single rod coated with a thin film of Platinum, as shown in Figure 5.75(a). The unit element for the Pathfinder sensor that we have considered here, is a thin Platinum-Iridium wire, as shown in Figure 5.75(b) and the unit element of the REMS sensor is one single silicon chip with a heating resistor as shown in Figure 5.75(c).

We consider that the element has a length L and eventually there are at the two ends a certain length L_s for the supports of the hot element to the body of the instrument. Details of the geometry and properties of these three sensors are described in Reference [19] for Viking, in Reference [22] for Pathfinder and in Reference [2] for MSL-REMS. We have summarized the values of the main geometrical parameters in Table 5.6 for the three cases, where applicable.

The heat flow balance for a Δx slice of the unit element can be written as follows:

$$P_{in} + P_{gen} = P_{out} + P_{conv} \quad (5.44)$$

Where P_{in} is the power entering the differential volume, P_{out} is the heat flow going out of the differential volume, P_{conv} is the heat flow going out of the volume boundaries by convection and P_{gen} is the heat flow generated in the volume by Joule effect. Radiation components have been neglected for

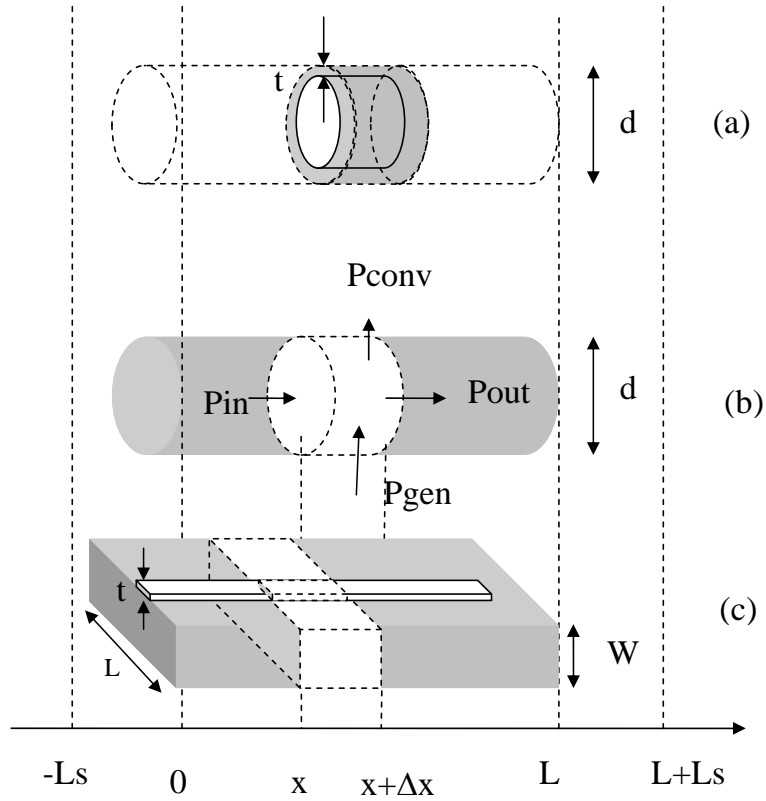


Figure 5.75: 1-D model of wind sensors from different Mars planetary missions: a) Viking, b) Pathfinder, c) MSL-REMS.

simplicity.

According to Fourier law, it can be written:

$$P_{in} = -kA_{cond} \left. \frac{dT}{dx} \right|_x \quad (5.45)$$

and:

$$P_{out} = -kA_{cond} \left. \frac{dT}{dx} \right|_{x+\Delta x} \quad (5.46)$$

Where k is the thermal conductivity of the corresponding material and A_{cond} section for the heat conduction flow.

By expanding term P_{out} in Taylor series we have:

$$P_{out} = -kA_{cond} \left. \frac{dT}{dx} \right|_x - kA_{cond} \Delta x \left. \frac{d^2T}{dx^2} \right|_x \quad (5.47)$$

The convection power out of the volume is given by:

	Viking	Pathfinder	MSL-REMS
Concept	hot film	hot wire	hot die
Rod/wire diameter	$d = 0.51 \text{ mm}$	$d = 65 \text{ }\mu\text{m}$	NA
Element length	$L = 1.02 \text{ cm}$	$L = 41.6 \text{ cm}$	$L = 1.5 \text{ mm}$
Film thickness	$t = 0.635 \text{ }\mu\text{m}$	NA	$t = 100 \text{ nm}$
Resistor width	NA	NA	W'
Die thickness	NA	NA	$W = 0.5 \text{ mm}$
Die width	NA	NA	$L = 1.5 \text{ mm}$
A_{cond}	πdt	$\pi d^4/4$	LW
A_{conv}	$\pi d\Delta x$	$\pi d\Delta x$	$2(L + W)\Delta x$
A_{cross}	πdt	$\pi d^4/4$	tW'
Thermal conductivity	$k_{Pt}=75\text{W/mK}$	$k_{Pt}=75\text{W/mK}$	$k_{Si}=150\text{W/mK}$
Characteristic length	$L_c=d=0.51\text{mm}$	$L_c=d=65 \text{ }\mu\text{m}$	$L_c=L=1.6 \text{ mm}$

Table 5.6: Main parameters of thermal unit elements (NA - Not Applicable).

$$P_{conv} = hA_{conv}\Delta T \quad (5.48)$$

Where h is the convection coefficient, ΔT is the overheat temperature over the ambient temperature and A_{conv} is the convection area. Finally the heat rate generated by Joule effect is given by:

$$P_{gen} = I^2 dR \quad (5.49)$$

where I is the electrical current flowing through the resistive material, and dR is the resistance of the differential of volume considered in Figure 5.75. Equation (5.44) becomes the well know hot wire equation:

$$\left. \frac{d^2 T}{dx^2} \right|_x = \frac{hA_{conv}\Delta T}{kA_{cond}\Delta x} - \frac{I^2 dR}{kA_{cond}\Delta x} \quad (5.50)$$

In Equation (5.50), the right values for the convection and conduction areas have to be considered for each of the sensors according to Table I. We do not consider at this point any conduction losses trough the material of the rod in the Viking sensor.

The differential resistor dR is given by:

$$dR = \frac{\rho}{A_{cross}} \Delta x \quad (5.51)$$

where ρ is the electrical resistivity of the material: Platinum film for Viking , Platinum-Iridium for Pathfinder, whereas for the REMS sensor it is the resistivity of the Platinum resistor (which is the heating element) and not of the silicon substrate. A_{cross} is the cross section area of the resistor which is equal to A_{cond} in Viking and Pathfinder but not in REMS, see Table 5.6. In all three cases the resistivity (ρ) is a function of the temperature (T).

5.10. REMS WIND SENSOR IN COMPARISON TO VIKING AND
PATHFINDER

Equation (5.50) now becomes:

$$\left. \frac{d^2 T}{dx^2} \right|_x = \frac{hA_{conv}\Delta T}{kA_{cond}\Delta x} - \frac{I^2\rho(T)}{kA_{cond}A_{cross}} \quad (5.52)$$

and is valid for the unit element of the three sensors designs analysed here. In Table 5.6 the corresponding expressions and values for the main parameters are gathered together to be employed for thermal solution of the one dimensional convection model presented here.

Equation (5.52) can be easily solved numerically taking into account how the circuit embodying the sensing element works in the cases considered. The Viking circuit worked at CTA, thereby the circuit was meant to apply a power until a given overheat temperature is reached and thereupon the power supplied dynamically adapts to the convection and conduction losses in order to keep constant this overheat while the wind speed does not change. On the contrary, the Pathfinder sensor worked at CCA thereby indicating that a constant current was applied and the equilibrium overheat temperature adapts also dynamically to the convection and conduction terms. As the heating power is constant, different hot wire temperature correspond to different wind speeds.

Therefore, the solution of Equation (5.52) for the Pathfinder sensor involves the use of $I = 51.1\text{mA}$ for all wind speeds. In the case of the REMS sensor, the circuit works at CTDA between the silicon chip and the ambient, and hence the power delivered adapts to the wind speed to keep ΔT constant. The solution of Equation (5.52) provides the temperature profile $T(x)$ at any point of the length of the element for given values of the convection coefficient h . From that, the average temperature is calculated. Equation (5.52) has to be solved iteratively for the case of Viking and REMS sensors, as the target parameter is the average temperature, so several values for current I are used until the desired overheat value is reached.

In addition, the integration of equation (5.52) requires the application of appropriate boundary conditions. As schematically depicted in Figure 5.75. to the right and left of the main device (and indicated by L_s), there are supports to hold the hot unit elements to the body of the sensor in all three cases. In Viking design the small rod has a free end at $x = L$, Pathfinder has supports at both ends and REMS has four free sides of the die and four pyrex legs to hold the chip. In absence of details of the construction of Viking and Pathfinder supports, we have considered as boundary condition, that the temperature at the supports in these two cases is the ambient temperature, and assumed negligible the convection at the free end of the Viking rod. For REMS we have considered as boundary conditions, the conduction losses by the pyrex supports (considering the thermal conductance of the pyrex material and the geometry of the pyrex pillars) and a convection term taking place at the two lateral sides of the chip. An example, Figure 5.76 shows an example of the temperature profiles for $h = 80 \text{ W}/(\text{m}^2\text{K})$ and $T_{amb} = 300 \text{ K}$.

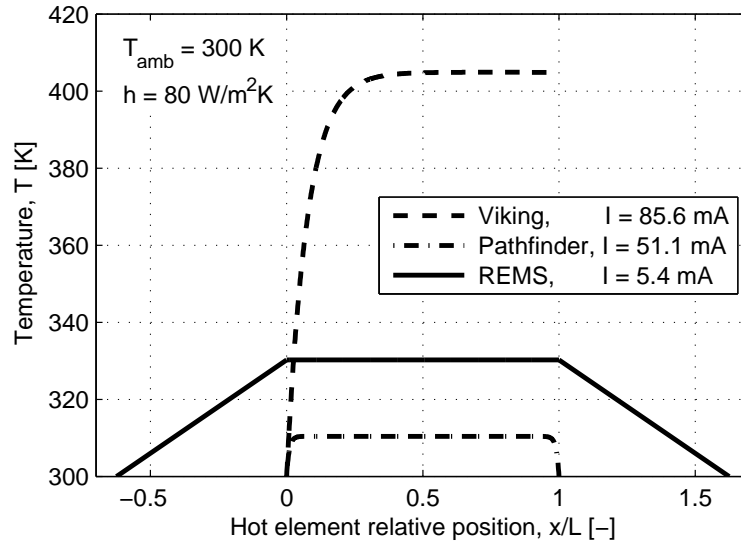


Figure 5.76: Temperature profile for 1-D thermal model solution for anemometers at Mars conditions ($h = 80 \text{ W}/(\text{m}^2\text{K})$ and $T_{amb} = 300 \text{ K}$). The typical overheat values for Viking 100 K, for Pathfinder 10 K and for REMS 30 K can also be deduced from this plot.

As can be seen in Figure 5.76, the temperature gradients observed along the length in Viking, for the beginning and end of the terminals in case of Pathfinder element contrast with the negligible temperature gradient within the bulk of the silicon chip observed in REMS element, due to the high thermal conductivity of silicon. Figure 5.76 also shows the temperature drops along the pyrex supports until the ambient temperature is reached at the end of the supports ($x = -L_s$ and $x = L+L_s$). Taking closer look only for the hot die itself ($0 < x/L < 1$) in case of the REMS element we will see that the temperature profile along silicon chip is not exactly flat and mostly is associated to the pyrex pillars and wire bonding heat drains, see Figure 5.77.

For silicon die in suspension there would be only 0.01 K temperature gradient withing the whole die, pyrex pillars add another 0.02 K wheres wire-bonding add 0.025 K to the temperature gradient Figure 5.77. Nevertheless, maximum temperature difference along the silicon chip die is less than 0.06 K, which in reference to the overheat of 30 K is less than 0.2% and for the further consideration could be assumed that entire hot dice is at one homogenous temperature, namely T_{hot} .

Let us now relate the solution of Equation (5.52) to the relevant magnitude for a wind sensor which is the local wind velocity, U . As wind speed is related to the Reynolds number and the convection coefficient h , is proportional to the Nusselt number, a correlation relating the Nusselt number to

5.10. REMS WIND SENSOR IN COMPARISON TO VIKING AND
PATHFINDER

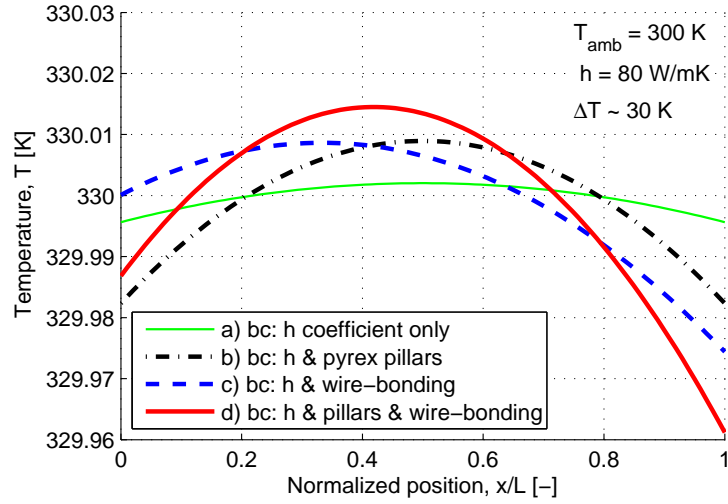


Figure 5.77: Temperature profile for the 1-D thermal model of hot silicon REMS die according to the die boundary conditions (*bc*) considered.

the Reynolds number provides the required link between h and U . However the properties of the atmosphere are also involved in the Reynolds number and in the Nusselt number correlations, and these properties are pressure and temperature-dependent. So the solution of Equation (5.52) will require loop iterations to finally converge.

In order to make simpler the numerical solution, our approach has consisted in :

- (i) solving Equation (5.52) for given values of the convection coefficient (h) and getting the temperature profile ($T(x)$),
- (ii) computing the average temperature (T_{avg}),
- (iii) calculate the film temperature (T_f) as the arithmetic mean value between the average temperature and the ambient temperature,
- (iv) computing the values of the properties of the atmosphere which depends on temperature: density, the absolute viscosity, the specific heat at constant pressure, thermal conductivity,
- (v) calculating the Nusselt number, $Nu = hL_c/k_{gas}$,
- (vi) finding dimensionless Prandtl number (Pr) from gas properties,
- (vii) calculating the Reynolds number (Re),
- (viii) finally calculating the wind velocity (U).

The Nusselt number is related to the Prandtl and Reynolds numbers (for Reynolds numbers smaller than 4000) by the Churchill and Bernstein [75], correlation for flow over a cylinder. This correlation is suitable for the Viking and Pathfinder cases as the unit element is a cylinder:

$$Nu = 0.3 + \frac{0.62Re^{1/2}Pr^{1/3}}{\left[1 + \left(\frac{0.4}{Pr}\right)^{2/3}\right]^{1/4}} \quad (5.53)$$

In the case of the REMS sensor the geometry is assumed to be that of a flat surface in tangential flow. In that case the Nusselt number correlation for $Re < 5e^5$ is given in Reference [76] by simple equation:

$$Nu = 0.664Re^{1/2}Pr^{1/3} \quad (5.54)$$

The Churchill and Bernstein correlation in Equation (5.53) works fine for values of the Nusselt number greater than 0.3. In the cases considered in this work and due to the low pressure of the Mars atmosphere, a correction of the Nusselt number has been used, [77]:

$$\frac{1}{Nu_c} = \frac{1}{Nu} + 2Kn \quad (5.55)$$

where Nu_c is the corrected number and Nu is given by Equation (5.53) and Kn is the Knudsen number, which is defined as the ratio of the mean free path of the gas molecules divided by the characteristic length, see Section (3.2.1).

In the case of the Pathfinder model, and due to the low pressure and also to the small value of the characteristic length, instead of the correction shown in Equation (5.55) we have used the following correction which takes into account the low values of the Mach number, [19, 78]:

$$\frac{1}{Nu_c} = \frac{1}{Nu} + 10.3\frac{M}{Re} \quad (5.56)$$

The procedure described above and enumerated from (a) to (h) enables, for given ambient conditions $P_{amb.}$ and $T_{amb.}$, to correlate following parameters : wind velocity (U), Reynolds number (Re), Nusselt number (Nu), average temperature (T_{avg}), heat convection coefficient (h) and global heat convection power ($P_{conv.}$) among others. The same, three thermal anemometers Viking, Pathfinder and REMS, although different in construction and functioning, can be contrasted according to the deliberately choose correlation factors. Same examples of these three sensor comparison take place in [3].

Here we compare for an hypothetical pressure ($P = 670$ Pa) and temperature ($T = 220$ K) how would all three sensors behave in power and overheat aspects, see Figure 5.78.

5.10. REMS WIND SENSOR IN COMPARISON TO VIKING AND PATHFINDER

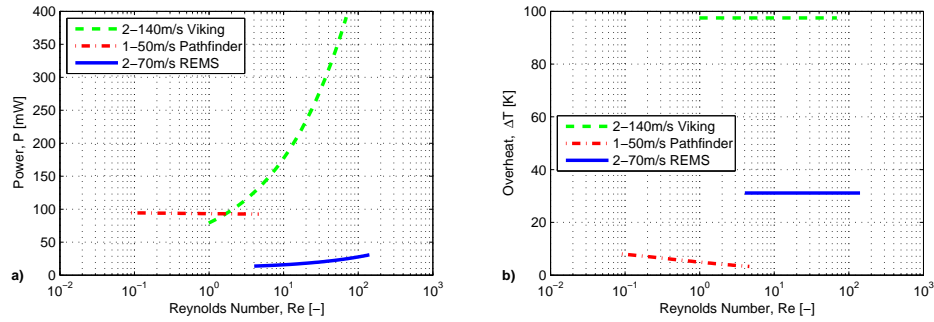


Figure 5.78: Comparison of the three wind sensor: Viking, Pathfinder and REMS in a) total power and b) overheat for whole wind velocity range specified for each sensor and at given atmospheric conditions ($P = 670$ Pa, $T = 220$ K).

It can be seen from Figure 5.78a) that only Pathfinder wind sensor unit has the same constant power of about 100 mW, for REMS wind sensor unit as Reynolds number grows power roughly rise from 15 mW up to 31 mW, whereas for Viking wind sensor unit we observe much higher growth from 80 mW up to almost 400 mW, indeed Viking wind sensor was more power hungry from the group of wind sensors here considered. If we compare the overheat from the Figure 5.78b) we can see that Viking for the whole range was working with overheat of about 100 K for REMS wind sensor unit it was less but constant overheat of 30 K, whereas for Pathfinder wind sensor unit overheat starts with value of 10 K and as the Reynolds number grows the overheat was decreasing to reach about 3 K at full speed. Putting these two graphs from Figure 5.78a) and Figure 5.78b) we can have power to overheat ratio, as a function of Reynolds number for full velocity range, see Figure 5.79.

It can be seen from the Figure 5.79 that REMS sensor is much more power efficient which means that for the same power the REMS sensor would work with higher overheat than Viking or Pathfinder. In the next section there will be more details about power efficiency aspects.

5.10.2 Power efficiency

By solving first order model of all three sensors unit we got a Figure 5.80 which puts in contrast the novel REMS wind sensor die with particular unit of Viking sensor and Pathfinder one. In this figure can be seen that three sensors: Viking, Pathfinder and REMS are working in three different regimes. REMS wind sensor for entire air temperature and pressure range is situated in continuum medium regime, Viking wind sensor was in majority in continuum medium regime whereas for high wind speed and pressure it was in

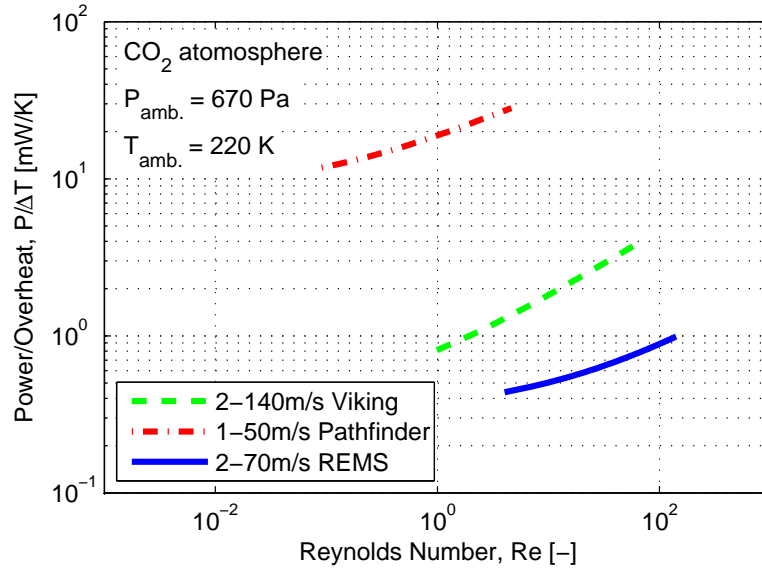


Figure 5.79: Comparison of the three wind sensor: Viking, Pathfinder and REMS in total power to overheat ratio as a function of the Reynolds number for whole wind velocity range specified for each sensor and at given atmospheric conditions.

slip-flow regime. Finally Pathfinder wind sensor works in the range where slip-flow meets with transition flow regime what makes it highly probabilistic issue.

From the figure of merit 5.80 could be read another important factor which is power to overheat ($P/\Delta T$). This factor says about efficiency of the sensor to set hot point temperature in reference to the power demand to satisfy energy balance equation for given ambient conditions: T_{amb} , P , U and ΔT . It stands out that REMS sensor unit achieved better performance and its power to overheat ratio in the worst conditions is less than 1 mW/K and this has been achieved mostly due to the effort put in adequate thermal isolation of supporting pyrex structure, more details found in next Section (5.2).

The merit figure presented in 5.80 represents wind sensor unit and can be extended to the complex wind sensor for wind measurement in 3-D space.

Therefore, each sensor unit power to overheat ratio has been adequately multiplied according to the technical specification accordingly for Pathfinder unit x6 times, Viking unit x2 times and REMS unit x4 times. The variation of Knudsen number has been calculated from equation 3.3 having in mind the mean free path for the flow temperature (T_f), and wind sensor unit characteristic size which for Viking is a rod diameter, for Pathfinder hot wire diameter and for REMS silicon die width, see Table 5.6. Flow temperature has been found as a mean of the ambient temperature and

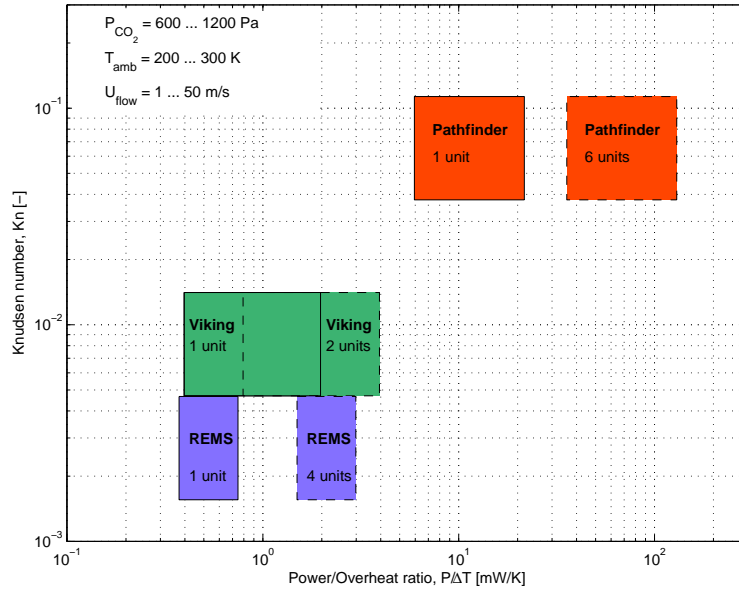


Figure 5.80: Space design of the three thermal anemometers used in Mars planetary mission in comparison of the Kn regime and $P\Delta T$ ratio for any possible variation of Martian conditions: pressure, temperature and flow velocity. Single unit and global wind sensor are shown for clarification.

the average hot element temperature ($T_f = T_{amb}/2 + \bar{T}_{hot}/2$). In order to find coordinates of rectangular form which represent each of the sensor all combination of the utmost parameters were evaluated (eight combination). From that, maximum and minimum values have been extracted to form the representative rectangle in the merit Figure 5.80. The procedure of finding power to overheat ratio first order model presented in Section (5.10.1) has been depicted in Figure 5.81.

5.11 REMS 2-D wind transducer summary

To sum up the whole chapter, the main contributions of the REMS 2-D wind transducer are:

- Broadening of hot-wire concept even further than hot-film establishing new nomenclature called hot-volume unit, see Figure 5.10,
- Use of sigma-delta concept for the small silicon die as thermal-electrical transducer with digital read out, see Section (5.7.1),
- The new CTDA working mode witch adapts to the changing ambient temperature conditions and provide thermal conductance mea-

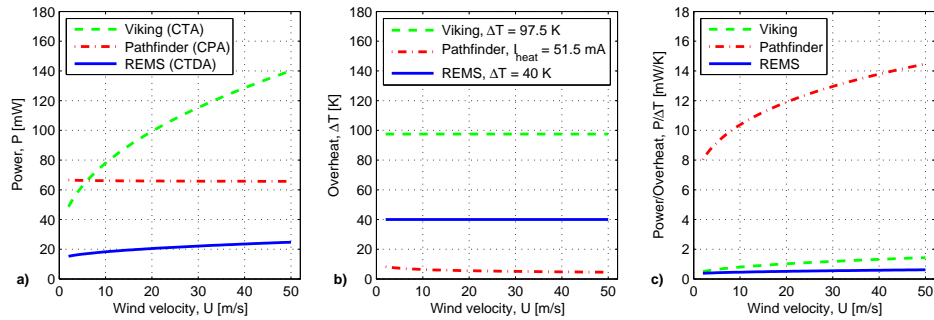


Figure 5.81: Viking, Pathfinder and REMS wind sensor units in comparison for velocity range from 2 to 50 m/s for Martian atmosphere conditions adjust to: pressure 600 Pa and temperature 300 K. Different working behaviour for these three thermal anemometers have been reflected in a) power demand, b) temperature overheat, c) power to overheat ratio.

surement independently to the temperature of the medium, see Section (5.7.2),

- The new concept based on geometry of four dice array made of four equal die unit where differential measurements enable to cancel out common thermal losses which profit this method especially in the rarefied gas convection conditions, see Section (5.4.2),
- The first order numerical model developed enables to analyze and compare different working mode anemometers, see Section (5.10.1),

The investigation work I have been part of in general has made an scientific footprint in terms of patent, few conferences with one plenary session as well as articles made in the MNT group and with collaboration with other institutions. Some of the achievements are listed below:

Reference [1], Appendix A

M. Domínguez, L. Kowalski, V. J. A. Moreno, L. Castañer, and J. Ricart, “Método para la medida de la velocidad del aire y de su dirección en dos dimensiones para aplicaciones aeroespaciales y de baja presión,” 2007. PATENTE DE INVENCION. Número de solicitud: 200700259. Número de publicación: 2342953. Fecha de presentación: 25.01.2007. Fecha de la concesión: 20.05.2011

Reference [2], Appendix B

M. Domínguez, V. Jiménez, J. Ricart, L. Kowalski, J. Torres, S. Navarro, J. Romeral, and L. Castañer, “A hot film anemometer for the Martian atmosphere,” *Planetary and Space Science*, vol. 56, pp. 1169 – 1179, June 2008

Reference [3], Appendix C

V. Jiménez, M. Domínguez-Pumar, J. Ricart, L. Kowalski, S. Navarro, J. Torres, J. Romeral, J. Merrison, and L. Castañer, “Applications of hot film anemometry to space missions,” in *Euroensors XXII*, (Dresden, Germany), September 2008. ISBN 978-3-00-025217-4

Reference [4], Appendix D

L. Kowalski, J. Ricart, V. Jimenez, M. Domínguez-Pumar, and L. Castañer, “Sensitivity analysis of the chip for REMS wind sensor,” in *7th Spanish Conference on Electron Devices (CDE 2009)*, (Palma de Mallorca, Spain), pp. 289–292, February 2009

Reference [5], Appendix E

L. Kowalski, “Contribution to advanced hot wire wind sensing,” in *1st Barcelona Forum on Ph.D. Research in Electronic Engineering*, pp. 7–8, Universitat Politècnica de Catalunya (UPC), Centre de Publicacions del Campus Nord SCCL (CPET), October 2009. ISBN978-84-7653-398-7

Reference [6], Appendix G

L. Kowalski, J. Ricart, V. Jiménez, M. Domínguez, and L. Castañer, “Thermal modelling of the chip for the REMS wind sensor,” *International Journal of Numerical Modelling: Electronic Networks, Devices and Fields*, vol. 23, pp. 340–353, July - October 2009. Special Issue on the 7th Spanish Conference on Electron Devices (CDE2009)

Reference [8], Appendix H

L. Kowalski, L. Castañer, M. Domínguez, and V. Jiménez, “Multi-physics simulation of REMS hot-film anemometer under typical Martian atmosphere conditions,” in *COMSOL Conferenece 2010*, (Paris, France), October 2010

Reference [9]

J. Gómez-Elvira, C. Armiens, L. Castañer, M. Domínguez-Pumar, M. Genzer, F. Gómez, R. Haberle, A.-M. Harri, V. Jiménez, H. Kahanpaa, L. Kowalski, A. Lepinette, J. Martín, J. Martínez-Frías, I. McEwan, L. Mora, J. Moreno, S. Navarro, M. de Pablo, V. Peinado, A. Peña, J. Polkko, M. Ramos, N. Renno, J. Ricart, M. Richardson, J. Rodríguez-Manfredi, J. Romeral, E. Sebastián, J. Serrano, M. dela Torre Juárez, J. Torres, F. Torrero, R. Urquí, L. Vázquez, T. Velasco, J. Verdasca, M.-P. Zorzano, and J. Martín-Torres, “REMS: The environmental sensor suite for the Mars Science Laboratory rover,” *Space Science Reviews*, vol. 170, pp. 583–640, July 2012

There have been also other positive implication from participation of UPC-MNT group in MSL-REMS mission. We have been honored with

Group Achievement Award from NASA, see Appendix K. Our invention, the 2-D wind transducer for Mars mission has been exhibited in an exposition for 200 years of patents, see Appendix J. The perception from the Spanish community was good with lot of appreciation including local university authorities, see Appendix J. Significant number of interview our group were glad to perform and many press releases had place, see Appendix F. All these in consequence increase interest in youths to study engineering subject and to realize few master thesis with collaboration with MNT related to the Martian wind sensors development, [79–81].

	Viking	Pathfinder	MSL-REMS
Concept	hot-film	hot-wire	hot-volume
Dimension	2-D	2-D	3-D
Anemometry	CTA	CCA	CTDA
Overheat	100°C	4-25°C	25-40°C
Heater form	thin film 635nm	folded wire	serpentine path
Heater material	platinum (100%)	platinum(0.9) /iridium(0.1)	platinum(70nm) /titanium(10nm)
Sensor shape	orthogonal rods	wire wound	4 dice arrays
Characteristic length of unit	diameter 0.51mm (10.2 mm long)	diameter 0.65μm (416 mm long)	1.67×1.67 mm (0.5 mm thick)
Units/sensor	2	6	12
Location	Top mast 1.6 m	Top mast 1.1 m	Mid mast
Measurement range	2-25 m/s 25-150 m/s	0-50 m/s	0-20 m/s 0-70 m/s
Speed accuracy	±4 m/s or 20%	10% for wind speed<10m/s	1 m/s
Speed resolution	0.5 m/s	1m/s (low speed) 4m/s (high speed)	0.5 m/s
Direction accuracy	±10° (5-25 m/s)	-	30°
Direction resolution	±10° (5-25 m/s)	10°	10°
Sampling frequency	less than 0.8 Hz	0.25 Hz & 1 Hz	1 Hz
Time response	2 s	1 s	1 s
*Power	140 mW / unit	66 mW / unit	24 mW / unit
Total power	280 mW	396 mW	288 mW

Table 5.7: Comparison of the wind sensor system for Viking [19, 20], Pathfinder [21, 22] and MSL-REMS [9]. *Power consumption data has been calculated according to the first order model proposed in Section (5.10.1) for CO₂ atmosphere: 300K, 600Pa, 50m/s.

5.11. REMS 2-D WIND TRANSDUCER SUMMARY

Finally, conceived and developed at UPC 2-D wind transducer adequately repeated is part of the REMS wind sensor instrument that is up to date operating aboard of the MSL Curiosity Rover. By performing in-situ wind measurements, REMS device has contributed to better knowledge of Martian meteorology. Among others wind events, the whirlwind in the *Gale Crater* has been recognized, see Appendix K. The specification of the REMS wind sensor has been put in contrast with Viking and Pathfinder sensors for comparison in Table 5.7, as the REMS wind sensor has joined the elite group of the thermal anemometers that has an opportunity to face a challenge of Mars wind measurement. The wind sensor become the first three-dimensional wind sensor on the *Red Planet*, since the Viking and Pathfinder systems were only for 2-D wind measurement within a horizontal plane. Though, the total power consumption of the REMS sensor is lower than for the Pathfinder one and in agreement with the Viking wind sensor.

Chapter 6

3-D Hot Sphere Anemometer

In this chapter, It will be said few words about MEIGA project within which new 3-D spherical sensor has been developed. Then the author of the thesis will give a motivation that was upon new spherical geometry proposed for the sensor design. The way numerical simulation has been executed to find numerical convection model of the sensor will be presented. Rapid prototyping procedure will be described. Finally, the first measurement on the newly conceived structure will take place in this thesis to finish with the discussion on the new spherical sensor behavior.

6.1 MEIGA project

Mars Environmental Instrumentation for Ground and Atmosphere (MEIGA) is a project financed by Spanish Ministry of Science and Innovation (code: AYA2008-06420-C04-01/ESP) under scientific director leadership of professor Luis Vazquez from Madrid Complutense University. MEIGA is a part of bigger Mars planetary mission Meteorological Network (MetNet). MetNet is a international joint effort of many scientific institution under the leadership of FMI, where the others institutions were: Russian Space Research Institute (IKI), Lavochkin Association (LA) and from Spain INTA. The MetNet mission to Mars is based on a new type of semi-hard landing vehicle called MetNet Lander (MNL), [82]. As a continuation of MetNet Precursor Mission several tens of MNLs will be deployed on the surface of Mars equipped with specialized payloads. MEIGA was about to bring new vision for Mars exploration by providing instrumentation made in Spain for the next generation lander international mission for Martian atmospheric science. Among instruments developed in the course of MEIGA project are: magnetometer MOURA [83], Solar Irradiance Sensor (SIS) [84], Dust Sensor (DS) [85] and Spherical Wind Sensor (SWS) [11].

6.1.1 MEIGA wind sensor

It is a general goal in all wind sensors for Mars to achieve accuracy in the range of 0.1m/s to 0.5m/s, for wind velocity range from 0 to 15m/s and 10-30 degrees accuracy in wind direction, and doing that in a compact design consuming low power. For MEIGA project, the responsibility of MNT group was to present engineering concept of 3-D wind sensor to satisfy mission call for versatile robust and power efficient constraints in in-situ flow measurements on the surface of Mars.

Thermal flow sensors have been investigated extensively for a long time. Many of the 2-D thermal flow sensors concept have been realized [42, 86–88]. However to our knowledge the 3-D anemometers are built using multiple 2-D anemometers [89]. In three dimensions the wind direction can be measured by placing several 2-D wind sensors in different planes and using an inverse algorithm to retrieve the wind direction from the values of the thermal conductances, as it is the case in the REMS wind sensor [9]. This algorithm can be awkward depending on the specific geometry of the sensor and may not be equally sensitive to all angles. In this case, the spherical geometry simplifies the problem and is intrinsically 3-D.

We have in mind all advantages and inconveniences as well as huge experience from participation in REMS project. The design of the wind sensor for the Curiosity rover was to a large extent conditioned by the design of the mast of the rover itself as REMS is a cylinder-like structure protruding out of the camera mast. It is the complexity of the design and of the operation is usually computationally demanding to cover all incidence angle and wind speeds. This time, the purpose was to develop a design framework to reduce computational time and to apply the procedure to a novel geometry for wind sensors in low Reynolds number environment, based on a spherical shape to gain in compactness and to provide symmetry. It is intended to serve, not only for future missions to Mars but also to other low-pressure applications in aeronautics or meteorologic balloons, to improve wind measurements in higher troposphere and stratosphere, [90].

Flow over a sphere provides an ideal flow geometry and the local heat dissipation coefficient on the sphere skin is a function of the wind direction and of the velocity [91]. Therefore, we came with an idea of a spherical thermal anemometer with deliberately divided into sectors external shell, subject to the wind flow. A spherical shape has been adopted because the flow around it is axis-symmetrical and stable for low Reynolds numbers [92]. The multi-physic simulations of convection, thermal losses problem divagation, proof of concept as well as prototype fabrication and preliminary measurements were the main issue to address during the development of this novel device.

MEIGA project constraints according to the wind sensor specification are:

- wind velocity measurement range 1..10 m/s,

- wind velocity resolution 0.2 m/s,
- wind velocity precision 20%,
- horizontal incidence angle measurement in full range,
- vertical incidence angle measurements $\pm 30^\circ$,
- reasonable measurement frequency in order of 1 Hz.

Additional suggestions to consider for Mars wind sensor:

- good sensitivity of the wind signal,
- elimination of the thermal leakage,
- predictable scenario for any wind conditions within range of measurements,
- possible angle discrimination for all angles, no blind zones.

Although there was no simple solution at first but during the development step by step improvements has led as to the reasonable and good solutions, described in next section.

6.2 Hot sphere anemometer concept

In order to satisfy MEIGA project constrains and suggestions and having as a base previous legacy of REMS wind sensor device we came up with novel solution concept of spherical thermal anemometer working as a hot point with overheat to the ambient conditions as it has been presented in Figure 6.1.

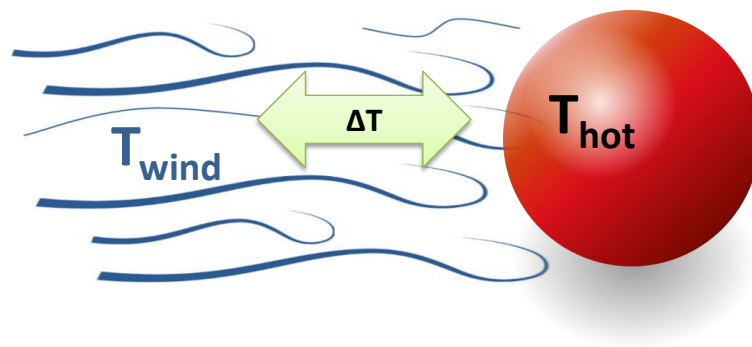


Figure 6.1: Spherical thermal anemometer concept of the hot point working with overheat to the wind ambient temperature.

As a wind flow pass the hot sphere the phenomena of heat drain from the hot point to the atmosphere occurs known as forced wind convection, [70]. This issue has been extensively studied and many empirical models for entire sphere convection heat has been proposed among others I would like to mention those of Whitaker, [93] and Feng&Michaelides, [91]. What is common and well know form, these work is that heat convection approximately rises with wind speed proportionally to the root square of the wind velocity, see Figure 6.2.

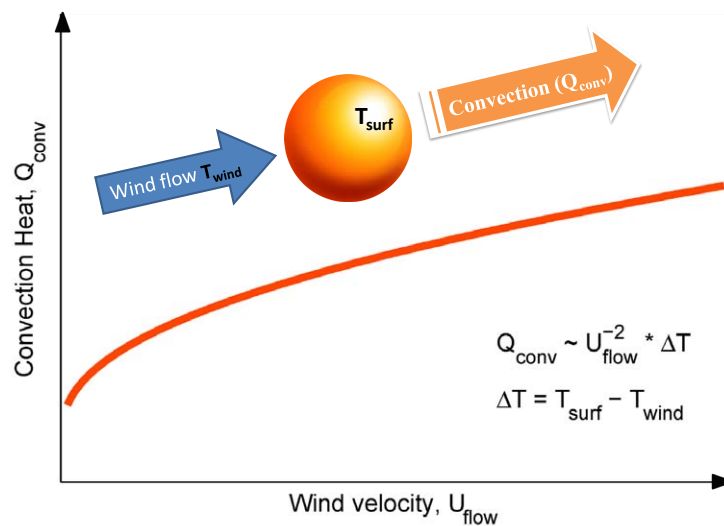


Figure 6.2: Heat convection proportional to the root square of the wind speed and to the overheat value.

For the operation mode we choose CTA for two reasons. First is that would make sensor time constant smaller and the same faster sensor, [39]. A second reason for choosing constant temperature mode was the fact that making an assumption of the uniform temperature across the spherical sensor surface makes empirical model valid as well as FEM thermal-fluidic simulation a way easier to perform and analyse. In the process of forced wind convection phenomena as the wind pass be the sphere surface heat from the external shell crust will be drained to the ambient with a different efficiency which depends on the wind parameters. Therefore, having monitored basic atmosphere parameters like pressure and temperature as well as total convection heat we will be able to retrieve wind velocity component, whereas from the difference of the heat convection in-between of the sphere sectors numerical models will enable recovery of the 3-D incidence angle in reference to the spherical wind sensor geometry.

6.2.1 Hot sphere transducer

As the hot sphere is working with overheat conditions to the ambient temperature, therefore to maintain this hot conditions there must be heat delivered to the sensor surface ($\dot{Q}_{surf.}$). This total heat which is delivered to the sensor shell could be split into three basic components:

$$\dot{Q}_{surf.} = \dot{Q}_{conv.} + \dot{Q}_{cond.} + \dot{Q}_{rad} \quad (6.1)$$

where $\dot{Q}_{conv.}$ is a heat that is drained to the ambient by the convection processes, $\dot{Q}_{cond.}$ represents conduction heat losses, \dot{Q}_{rad} represents radiation loss. Schematic diagram of the heat equation for the spherical sensor has been shown in Figure 6.3.

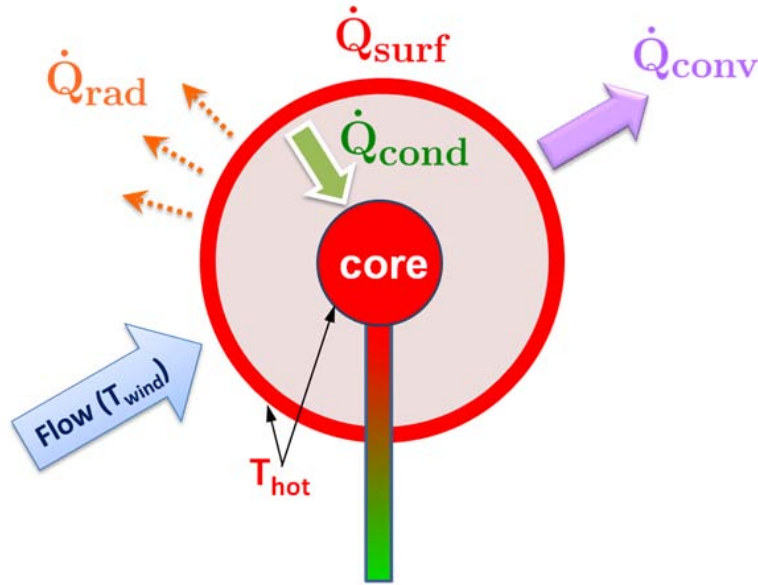


Figure 6.3: Heat delivered to the sensor surface split into three component of convection, conduction and radiation.

By proposing the central heat core at the same T_{hot} temperature and providing high thermal resistance between them thermal losses by the conduction can be canceled out since:

$$\dot{Q}_{cond.} = (T_{surf.} - T_{core}) / R_{th(loss)}$$

$$\dot{Q}_{cond.} \Big|_{(T_{surf.} = T_{core})} = 0 \quad (6.2)$$

In order to reduce radiation heat transfer external surface shell is polished to the mirror-like surface with very low emissivity factor (ϵ) down to

0.02-0.03. By that, radiation heat transfer could be suppress significantly and will be considered 0 for further divagation:

$$\dot{Q}_{rad} = \epsilon \cdot \sigma \cdot (T_{surf}^4 - T_{wind}^4)$$

$$\dot{Q}_{rad} \Big|_{\epsilon \rightarrow 0} \cong 0$$
(6.3)

The advantage of the sensor is to provide that all power delivered to the sensor shell would be drained in the convection processes. The same sensor will work as a transducer that converts wind velocity into power demand that satisfies heat convection equilibrium for particular overheat conditions:

$$\dot{Q}_{surf.} = \dot{Q}_{conv.} = G_{th} \cdot (T_{surf} - T_{wind})$$

$$G_{th} \sim \sqrt{(U_{flow} \cdot P)}$$
(6.4)

What is also seen from the Equation (6.4) is that the heat delivered to the surface ($\dot{Q}_{surf.}$) will be drained by the convection process to the ambient ($\dot{Q}_{conv.}$) and the rate of this phenomenon commonly known as thermal conductance (G_{th}) would depend on wind velocity (U_{flow}) but also on atmospheric pressure (P). Total heat rate is also proportional to the overheat value defined as ($T_{surf} - T_{wind}$).

6.2.2 Hot sphere diameter

The size of the sphere is related to the Reynolds number and this can plot for different values of the sphere diameter as a function of the flow velocity as shown in Figure 6.4.

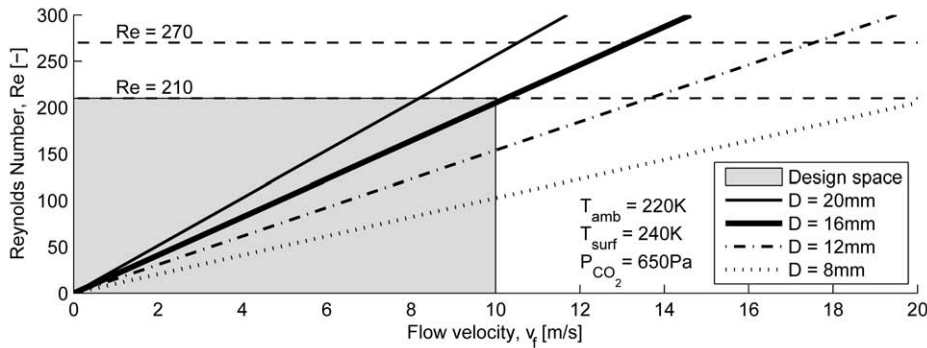


Figure 6.4: Reynolds Number as a function of flow velocity for given sphere diameter (D).

As can be seen, for the flow velocity up to 10 m/s in order to have $Re < 210$ the sphere diameter can be up to 16 mm. The size imposes a

fundamental restriction for the sensor design. $Re < 210$ is characteristic for axis-symmetric and stable flow [92, 94]. The value of the gravity in Mars allows us to estimate whether the natural convection is important in the range of values of the flow velocity. Natural convection occurs due to the buoyancy of the gas and can be neglected when $Re^2 \gg Gr$, see Section (3.2.5). Therefore, having in mind this particular condition and by use of Reynolds number Equation (3.4) and Grashof number Equation (3.10) it follows that the forced convection is dominant provided:

$$v_f \geq \sqrt{10 \cdot g \cdot D \frac{\Delta T}{T_f}} \quad (6.5)$$

For this particular Mars conditions, the result is that for a flow velocity greater than 0.22 m/s the natural convection component can be neglected. Whenever conceived sphere has a smaller diameter than 16 mm the minimum velocity restriction, from the natural convection processes becomes smaller, the same time, maximum velocity limit becomes bigger since it depends directly on the $Re < 210$ conditions. Therefore, there is a strong recommendation for smaller sensor size. Thus for the consecutive project steps we were shrinking the nominal size of the sphere diameter as follow: 16 mm, 15 mm, 11.2 mm, 10 mm to finish at the nominal size of 9 mm.

For the sphere with diameter 9 mm working with overheat of ~ 20 K we would have minimum velocity limit equal and smaller than 0.2 m/s calculated for Mars gravity 3.71 m/s^2 . For the same atmospheric conditions but recreated on the Earth where gravity is 9.80 m/s^2 the minimum velocity limit is 0.33 m/s. The maximum velocity limit is due to the Reynolds number constraint ($Re < 210$) to provide stable and axisymmetric flow and it has a value of 10 m/s for ambient temperature of -150 K and rise with temperature to more than 30 m/s for $T_{amb} = 300$ K, see Figure 6.5. Maximum velocity limit doesn't depend on the gravity and is equal in case of both Earth and Mars planets.

The exact measurement range of maximal and minimal wind velocity as a function of ambient temperature has been presented in Figure 6.5.

6.3 Hot sphere convection model

If we take under consideration a sphere as one hot element there has been many empirical equations to model heat drained by the convection of the flow past a hot sphere. Commonly reported in the literature are sphere convection model proposed by Whitaker [93] or Feng&Michaelides [91]. This model provides Nusselt number for the sphere as an empirical approximation combining Reynolds number and Prandtl number adequately as proposed by its authors. The same we obtain an algebraic solution for the sphere as a whole where power convection or thermal conductance could be easily found.

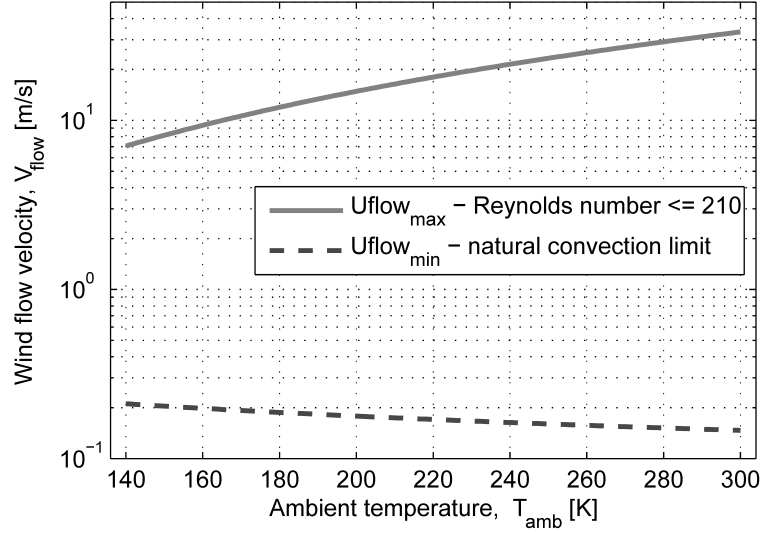


Figure 6.5: Measurement maximal and minimal wind velocity limit on Mars as a function of ambient temperature for hot sphere anemometer ($D = 9$ mm) working with constant overhear $\Delta T = 20$ K.

The situation becomes more complex if we want to find the thermal conductance of the deliberately cut section from the spherical shell. To provide model of that there must be very well known heat convection profile along the hot (ΔT) sphere ($D_{sph.}$) external surface which will strongly depend not only of the ambient parameters: temperatures ($T_{amb.}$), pressure (P_{atm}), wind velocity (U_{flow}) but also on wind incidence 3-D angle (Θ, Φ). This complex issue, which extends to a huge number of combination, has been addressed in this section and will be based on fluidic-thermal simulation to be in agreement with well know an algebraic solution for a sphere.

6.3.1 Algebraic solution for sphere

The power lost by convection, is related to the temperature difference between the sphere skin and the ambient as follows,

$$P_{conv} = G_{th} \cdot \Delta T \quad (6.6)$$

where G_{th} is the thermal conductance that can be related to the mean heat convection coefficient h and the sphere area $A = \pi D^2$ as,

$$G_{th} = h \cdot A \quad (6.7)$$

The heat convection coefficient h is related to the dimensionless Nusselt number Nu , the sphere diameter D and the gas thermal conductivity, k , calculated at the flow temperature as follows

6.3. HOT SPHERE CONVECTION MODEL

$$h = \frac{Nu \cdot k}{D} \quad (6.8)$$

From equation (6.7) and (6.8) it follows:

$$G_{th} = \pi \cdot Nu \cdot k \cdot D \quad (6.9)$$

An empirical equation (6.10) presented in [91] relates the Reynolds (Re), Nusselt (Nu) and Prandtl (Pr) numbers,

$$Nu = 0.922 \cdot Pe^{1/3} + 0.1 \cdot Re^{1/3} \cdot Pe^{1/3} \quad (6.10)$$

where Pe is a Peclet number the product of the Reynolds number and Prandtl number:

$$Pe = Re \cdot Pr \quad (6.11)$$

At that stage, we could estimate mean convection power for the sphere as a whole. By solving the empirical approximation we could also have a tool for verification of the fluidic-thermal simulation, we will run. An example of the hot sphere thermal conductivity for particular Mars-Like conditions is shown in Figure 6.6.

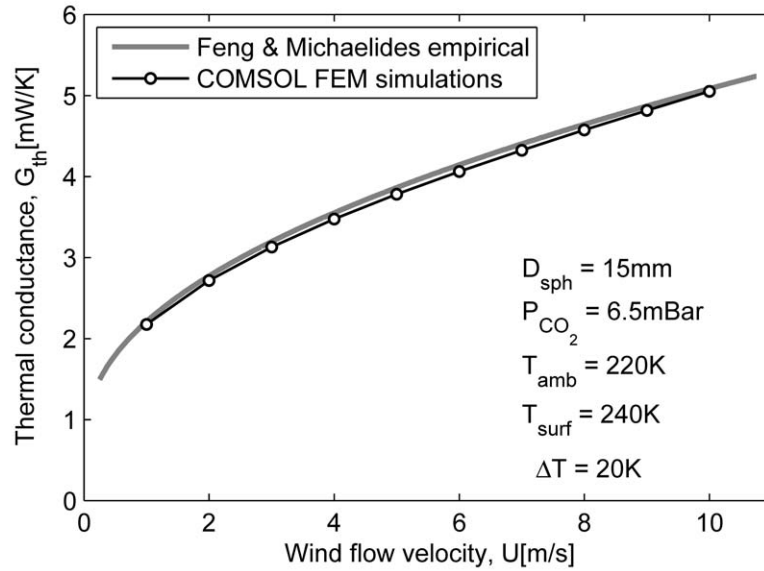


Figure 6.6: Thermal conductance of the overheated sphere as function of flow velocity for Mars-like atmospheric condition.

6.3.2 Fluidic-thermal simulations

For FEM simulation, we consider sphere immersed in a cylindrical volume of gas as described in Table 6.1.

Atmosphere temperature, T_{amb}	220 K
Sphere surface temperature, T_{surf}	240 K
Overheat, ΔT	20 K
Flow Temperature, T_f	230 K
Pressure, P	650 Pa
Flow speed, U_f	1,2,3,4,5,6,7,8,9,10 m/s
Sphere diameter, D	15 mm
Gas composition	CO_2 (100%)
Air size ahead of Sphere	10 · sphere diameter
Air size aside of Sphere	10 · sphere diameter
Air size at rear of Sphere	15 · sphere diameter
Air size of infinite lawyer	5 · sphere diameter

Table 6.1: FEM simulation conditions and geometry parameters.

Whereas boundary conditions that have been applied are gathered in Table 6.2. The **IN** boundary surface has an assigned normal to the surface inlet flow (U_f) speed and ambient temperature (T_{amb}). For the **OUT** surface, a zero pressure and thermal outflow with no temperature gradient have been assigned. Finally, slip conditions have been assigned for the **SIDE** of the cylindrical simulation volume with thermal isolation whereas at the **SPHERE** surface non-slip conditions and hot surface temperature (T_{surf}) have been considered.

Surface	CFD	Thermal
IN	U_f	T_{amb}
SIDE	slip	isolation
OUT	$P = 0$ Pa	outflow
SPHERE	non slip	T_{surf}

Table 6.2: FEM simulation boundary conditions

The geometry mesh has been set with a maximum element size of 0.4 mm for the entire sphere thereby the sphere skin results divided in 5964 triangles. For the rest of the volume, a tetrahedral shape extra fine size element has been used as can be seen in Figure 6.7.

Therefore, the complete mesh consists of 272808 elements with a total number of degrees of freedom 230700. Figure 6.8 shows an example of the simulation results where a wind speed of 1 m/s from the top surface has been considered as well as overheat $\Delta T = 20$ K. The simulation considers that

6.3. HOT SPHERE CONVECTION MODEL

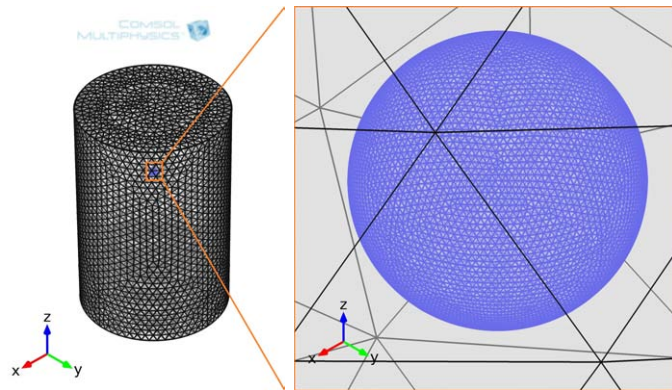


Figure 6.7: Mesh geometry of the sphere skin and the cylindrical volume.

overheat is kept constant. In order for this to be possible, different values of heating power have to be delivered (heat flux) to the point of the surface of the sphere depending on the local convection due to the flow incidence angle, its velocity and ambient gas temperature and pressure.

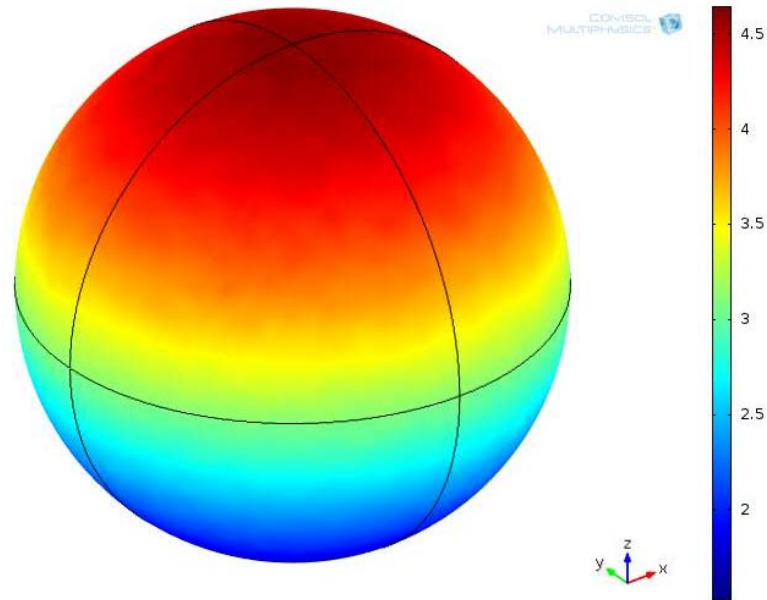


Figure 6.8: Local heat flux, H [W/m^2K] over the 20 K overheated sphere surface with regard to the CO_2 wind flow velocity of 7 m/s incoming from $-\vec{Z}$ direction.

The heat flux, H in units of [W/m^2K] is the surface power density per degree of overheat, it is shown in Figure 6.8 where it can be seen that the larger value is located at the top point of the sphere surface as expected

from the incoming direction of the flow.

6.3.3 Local heat flux modelling

As we are interested in a local heat flux for any point \mathbf{P} of the sphere we can define it by using spherical coordinates which are in case of constant radius two angles ϕ and θ , as shown in Figure 6.9.

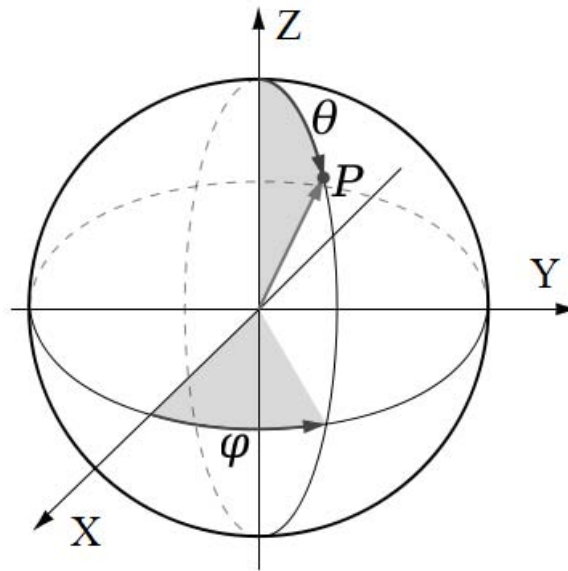


Figure 6.9: Spherical coordinates system.

The interesting thing of course is that the spherical symmetry allows to draw a simple plot of the local heat flux value as a function of the θ angle valid for all values of ϕ , that is to say along any meridian of the sphere passing by point \mathbf{P} , as shown in Figure 6.8. This allows a simplification as we only need to know the variation of the local heat flux along the θ angle as shown in Figure 6.10a). Similarly, Figure 6.10b) shows the same information of the local heat flux as a function of the Z -coordinate of the corresponding point of the surface of the sphere. In order to simplify the mathematical calculations, the simulation results of the local heat flow shown in Figures 6.10a) and 6.10b) can be fitted using a 6th grade polynomial curve, which is superimposed.

Similarly, by doing the same simulation for several wind velocities and fitting 6th grade polynomial approximations, enough information to know the local heat flux on the entire surface sphere for all ranges of velocities is found. So, when the direction is against the Z -axis the local heat flux H only depends on the z and is given by:

6.3. HOT SPHERE CONVECTION MODEL

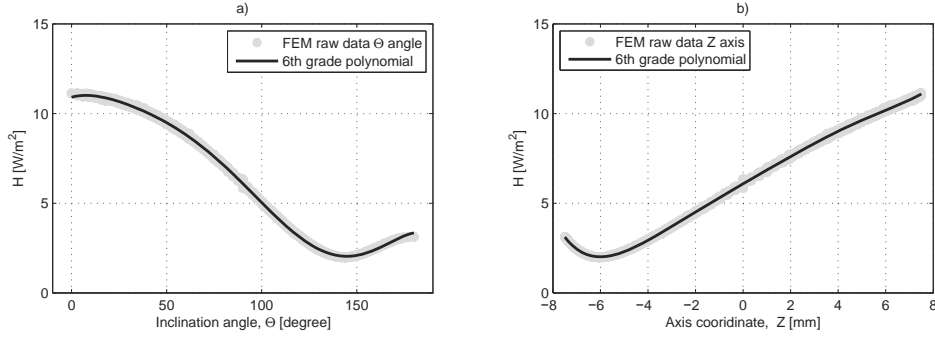


Figure 6.10: a) Local heat flux, H approximation for sphere position as a function of ϕ angle; b) function of Z coordinate for $D = 15$ mm $PCO_2 = 650$ Pa, $T_{amb} = 220$ K, $T_{surf} = 240$ K, $U_f = 7$ m/s

$$H(X, Y, Z) = H(Z) = C_0 + \sum_{i=1}^6 C_i \cdot Z^i \quad (6.12)$$

To extend these results to any wind direction, the (x, y, z) space where $-\vec{z}$ is the wind blow direction has to be rotated to our (X, Y, Z) space. This is not complicated since both spaces are related among each other by the Euler rotation matrix (E) as follow:

$$\begin{bmatrix} X \\ Y \\ Z \end{bmatrix} = E \cdot \begin{bmatrix} x \\ y \\ z \end{bmatrix} \quad (6.13)$$

where:

$$E = \begin{bmatrix} \cos\alpha \cdot \cos\beta - \sin\alpha \cdot \sin\gamma \cdot \cos\beta & & \\ -\cos\alpha \cdot \sin\gamma - \sin\alpha \cdot \cos\gamma \cdot \cos\beta & \dots & \\ \sin\alpha \cdot \sin\beta & & \\ \dots & \sin\alpha \cdot \cos\gamma + \cos\alpha \cdot \sin\gamma \cdot \cos\beta & \sin\gamma \cdot \sin\beta \\ & -\sin\alpha \cdot \sin\gamma + \cos\alpha \cdot \cos\gamma \cdot \cos\beta & \cos\gamma \cdot \sin\beta \\ & -\cos\alpha \cdot \sin\beta & \cos\beta \end{bmatrix} \quad (6.14)$$

where rotation angles yaw (α) and pitch (β) are depicted in Figure (6.11). Due to the axial symmetry the results are independent on the value of the angle γ which is the rotation around the Z -axis. From that the Z position can be related with the x , y and z coordinates using the Euler transformation (6.13) by its matrix (6.14) which gives:

$$Z = x \cdot \sin\alpha \cdot \sin\beta - y \cdot \cos\alpha \cdot \sin\beta + z \cdot \cos\beta \quad (6.15)$$

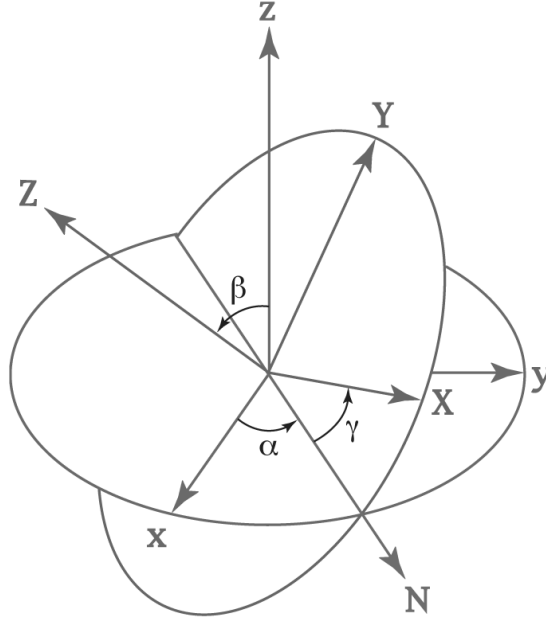


Figure 6.11: Euler Rotation Angles

From Equations (6.12) and (6.15) we can relate the local heat flux polynomial fit $H(Z)$ in the rotated axis to the non-rotated coordinates (x, y, z) and riation values of yaw (α) and pitch (β) angles, as follow:

$$\begin{aligned}
 H(Z) &= H(x, y, z, \alpha, \beta) = \dots \\
 \dots &= C_0 + \sum_{i=1}^6 C_i \cdot (x \cdot \sin\alpha \cdot \sin\beta - y \cdot \cos\alpha \cdot \sin\beta + z \cdot \cos\beta)^i
 \end{aligned} \tag{6.16}$$

Finally the x , y and z cartesian coordiantes for each point \mathbf{P} of interest, see Figure 6.9, can be related to its spherical coordinate R , θ , ϕ by following equations:

$$\begin{aligned}
 x &= R \cdot \sin\theta \cdot \cos\phi \\
 y &= R \cdot \sin\theta \cdot \sin\phi \\
 z &= R \cdot \cos\theta
 \end{aligned} \tag{6.17}$$

For our design, based on a limited number of spherical sectors, each of the them is defined by angular limits $\theta_1 > \theta_n > \theta_2$ and $\phi_1 > \phi_n > \phi_2$, for each sector n . We can then calculate the total thermal conductance of the sector as:

$$G_{th} = R^2 \int_{\theta_1}^{\theta_2} \int_{\phi_1}^{\phi_2} H(x, y, z, \alpha, \beta) \cdot \sin\theta \cdot d\phi \cdot d\theta \tag{6.18}$$

What it is gained here is that for only one entire sphere CFD simulation we got local heat flux curves that could be used for thermal conductance calculation for any shape of the sector under all possible wind incidence angle what really speed up the modelization process.

6.3.4 Convection model verification

Figure 6.12 shows the thermal conductance of two sector shapes as a function of the two angles of incidence of the airflow α and β . Each sector is a fraction of the entire sphere surface. The results are split into two columns in Figure 6.12. Figure 6.12a) shows the results for a sphere split into two vertically oriented hemispheres, Figure 6.12b) for eight sectors. The middle row shows plots of the thermal convection conductance for all incidence angles α in the horizontal axis and β in the vertical axis. The plots in the middle row show lines of equal values of thermal conductance of the spherical sector concerned, for example in a) the values are the hemispherically averaged value of the thermal conductance for all angles of incidence. For example when the flow is blowing along the y-axis in the negative direction $-\vec{y}$, it blows from the right towards the hemisphere. This direction is $\alpha = 180^\circ$ and $\beta = 90^\circ$. As can be seen in this direction the amount of power that should be delivered to the hemisphere in order to keep 1 K overheat in every point of the hemisphere surface according to equation (6.18) is larger than 3 mW/K which is maximum in that case. The opposite direction will be the minimum (smaller than 1.4 mW/K) as the flow will blow from the opposite direction and most of it will be deflected by the second hemisphere not shown to the left of the Figure 6.12a) in the third row. Similarly Figure 6.12b) for eighth of sphere sectors. Of course, the smaller the spherical sector, smaller is the value of the integrated thermal conductance of equation 6.18.

The method described in this work largely simplifies the estimation of the thermal conductances of arbitrary spherical sectors when they are exposed to a flow of arbitrary direction. The polynomial approximation and the use of the rotation matrix allow full results with finite element simulation on just one direction of the wind blowing instead of numerous computational fluid dynamics simulations for every incidence angle and thereby reducing the computational budget significantly. Simultaneously, the results shown provide the method to design wind sensors of spherical shape as the angle sensitivity can be tailored by splitting the sphere into different numbers of sectors.

6.4 Wind magnitude and temperature issue

As has it been said in the previous section for a hot sphere convection heat rate and the same power which is transferred to the ambient in convection processes strongly depend on the wind magnitude. In literature

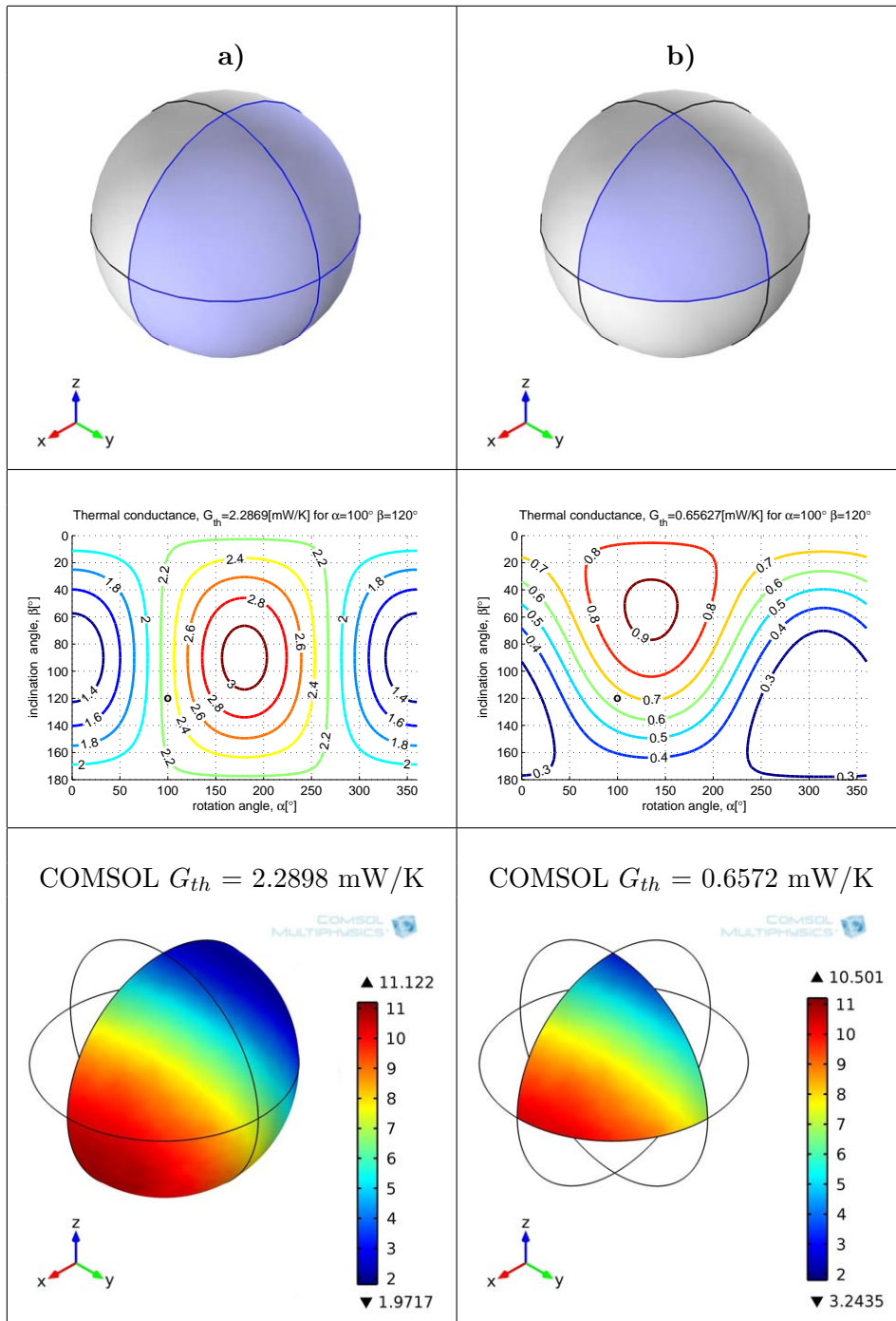


Figure 6.12: Thermal conductance G_{th} [mW/K] for different sector shapes and possible 3-D wind direction angle for wind flow $U_{flow} = 7$ m/s of $P_{CO_2} = 650$ K and $T_{amb} = 220$ K, $T_{surf} = 240$ K; a) two hemispheres, b) the eighth of the sphere.

is known many empirical correlations but we based on that proposed by Feng&Michaelides in [91] as fits with our simulation model, see Figure 6.6. Base on this correlation we can predict what would be the power demand to keep a constant overheat ($\Delta T = 20$ K) as the wind velocity changes from 0.2 m/s up to 20 m/s. These calculations besides velocity and pressure product also take into consideration carbon dioxide properties which strongly depends on temperature, see Section (3.2.9). Based on that, we obtained that total sphere convection power could change from 10 mW up to 75 mW providing constant overheat with a wide range of ambient temperature and wind velocities scenario, see Figure 6.13.

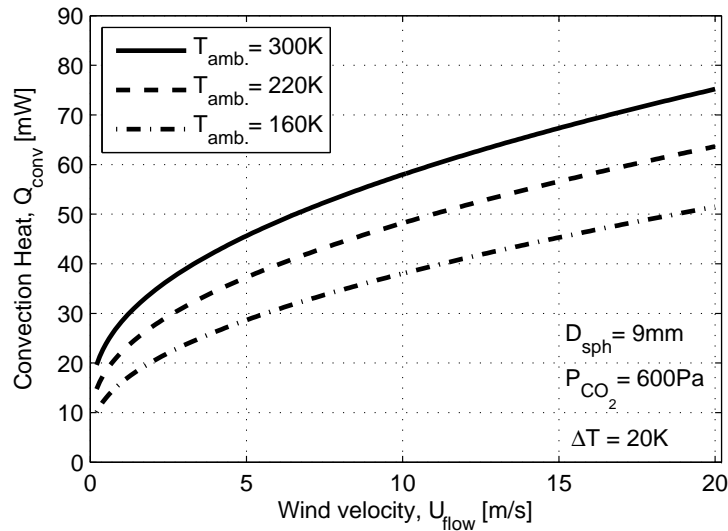


Figure 6.13: Total convection heat for sphere as a function of wind magnitude for three ambient temperatures

The Figure 6.13 shows the spherical sensor is sensitivity to the change in wind magnitude in a full range of velocities and temperature, showing higher sensitivity for lower wind speeds. It also stands out that the higher the ambient temperature is the higher the rate of heat convection to the ambient. As the T_{hot} temperature is controlled and the same well-known in order to properly figure out the overheat value independent ambient temperature measurement is crucial. The same, to properly estimate the wind velocity from the global sphere power demand readout ambient temperature and pressure need to be provided.

6.5 Wind direction issue

Spherical geometry has many advantages that come from the inherent isotropy. Considering a solid sphere with diameter 9 mm and 20 K of overheat is sub-

ject to a wind flow, the thermal conductance will be independent on the wind direction but will only depend on wind velocity for given atmospheric conditions ($T = 220$ K, $P = 600$ Pa), see Figure 6.14.

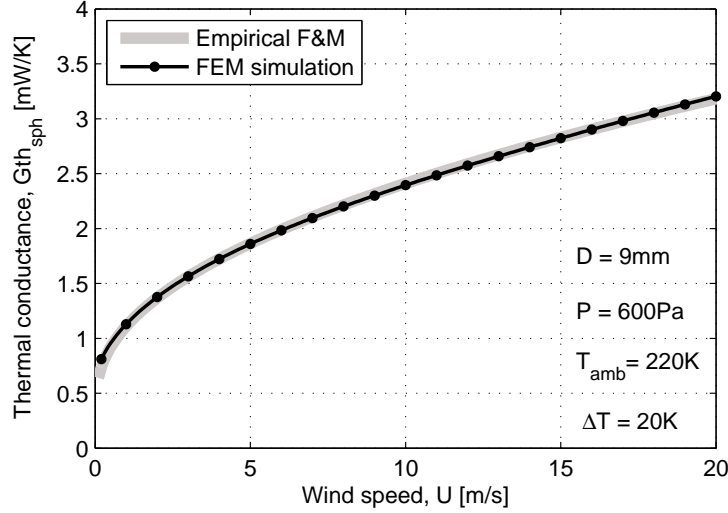


Figure 6.14: Thermal conductance for the whole sphere as a function of the wind speed. Empirical model based on Feng&Michaelides (F&M) compared to FEM simulation results

Therefore, the wind magnitude will be given by the sphere thermal conductance (or heat transfer coefficient) of all sectors together. Furthermore, the sphere can be split into several spherical sectors that can be independently controlled. The sectors that are more exposed to the wind will lose heat more than the others and hence a measurement of the difference between sectors will provide the wind direction, Figure 6.12. Variation in local heat flux coefficient is obtained for from CFD numerical simulation in the case of a particular wind speed of 5 m/s has been presented in Figure 6.15 .

Let us now describe how the wind direction can also be measured using as baseline the spherical geometry just described. This is achieved by breaking the sphere surface into spherical sectors physically separated as depicted in Figure 6.16 where an example of four independent sectors is shown.

In this thesis, four sectors were used to solve for the two angles of the wind direction (Θ, Φ), extending the results where two hemispherical sectors were used that allow only to solve for one angle as reported in [11]. We have considered not using more than four sectors for practical fabrication issues and because the angle sensitivity achieved with four sectors - as will be shown below - is currently above the typical requirements in Mars missions. The four sectors geometry shown in Figure 6.16 are spherical triangles having the centers located at points with coordinates for sector #1 at ($\Theta=54.74^\circ$ and $\Phi=90^\circ$), for sector #2 at ($\Theta=125.56^\circ$ and $\Phi=180^\circ$), for

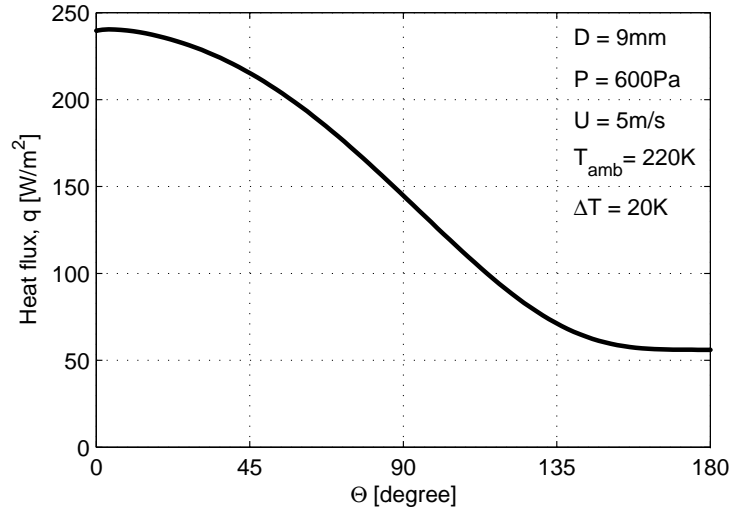


Figure 6.15: Local heat flux at any point of a sphere as a function of angle Θ for wind incidence angle to be from $-\vec{Z}$ direction

sector #3 at ($\Theta=54.74^\circ$ and $\Phi=270^\circ$) and for sector #4 at ($\Theta=125.56^\circ$ and $\Phi=360^\circ$). This particular geometry was obtained by expansion of an exploded tetrahedron over a spherical shell.

The local heat flux, according to the Figure 6.15, integrated along the surface of each sector gives the convection heat rate \dot{Q}_i

$$\dot{Q}_i = \oint_{A_i} q \cdot dA \quad (6.19)$$

where q is a local heat flux along the surface A of the sector i . The total heat rate for whole sphere \dot{Q}_{sph} is given by

$$\dot{Q}_{sph} = \dot{Q}_1 + \dot{Q}_2 + \dot{Q}_3 + \dot{Q}_4 \quad (6.20)$$

The percentage heat share p_i which corresponds to a given sector i is

$$p_i = \dot{Q}_i / \dot{Q}_{sph} \cdot 100\% \quad (6.21)$$

The values of p_i are shown in Figure 6.17 where the convection heat rate of sector #1 is plotted in a percentage of the global heat rate of the whole sphere as a function of the direction angles of the wind vector (Θ, Φ).

As can be seen, the maximum percentage of the heat rate value is 37.84% of the total sphere and it is achieved when the wind comes from the direction ($\Theta=54.74^\circ$ and $\Phi=90^\circ$) - directly into the center of the sector #1 - and has a minimum of 12.15% when the wind comes from the direction ($\Theta=125.26^\circ$ and $\Phi=270^\circ$) - the opposite direction to the sector's central point where the other three sectors: #2, #3, #4 join together. The plot, shown in

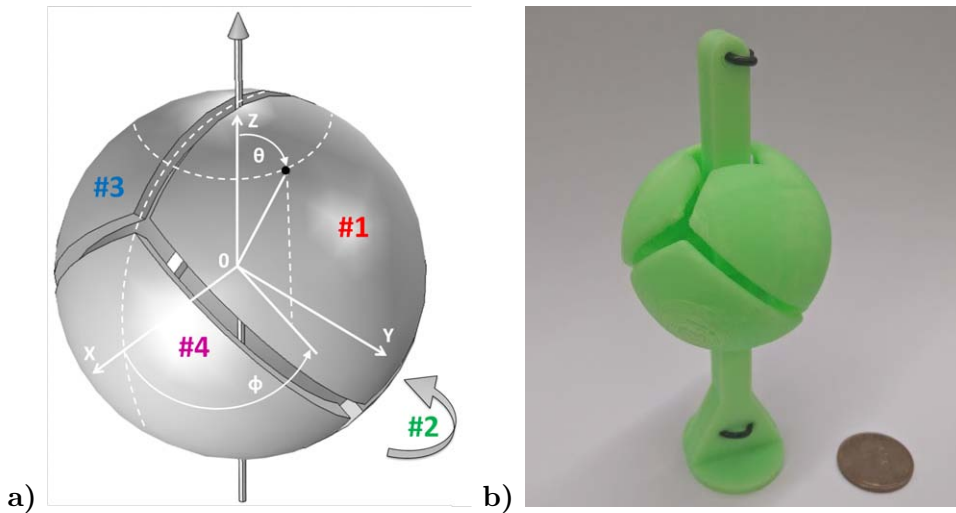


Figure 6.16: a) Physical model of spherical shell division based on tetrahedron geometry into separated from each other four triangular sectors, b) real model has been made out in 3D printing technology from ABS material with upscale 5:1 (1 cent coin added for size reference). Sectors: #1, #3, #4 can be seen from the picture, whereas sector #2 is in the rear of the plot. Sectors orientation, according to the Cartesian coordinate system, is shown as well as theoretical wind incidence point (represented by black dot) described with polar angles Θ and Φ .

Figure 6.17 for sector #1 is numerically the same for the other three sectors provided a proper shift in the axes for the angles Φ and Θ since all sectors have exactly the same geometry. Whenever 3-D incidence angle changes there is a percentage reallocation of the convection heat rate between of four tetrahedral sectors, whereas the global power remains constant. This will be the principal mechanism that will allow us to estimate wind angle.

6.5.1 Simple yaw rotation

Now let's consider a case when we deal with the wind within the horizontal plane, where $\Theta=90^\circ$, and full rotation along Φ angle is considered. In that case data for sector #1 can be easily extracted from Figure 6.17. This has been done also for the other three sectors and the results are shown in Figure 6.18.

The curves resemble shifted sinusoidal functions. It can be seen that percentage convection heat rate for each sector changes from 15% up to 30% as the wind impinging rotates around wind geometry.

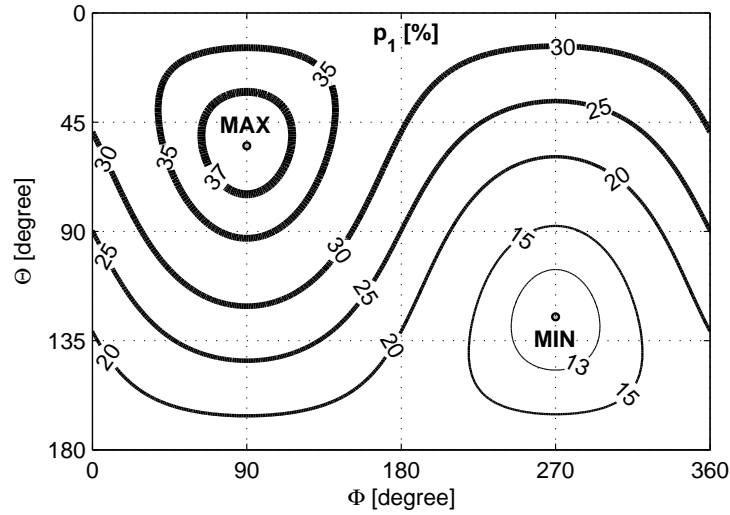


Figure 6.17: Percentage of the total sphere convection heat rate transferred to the ambient by the triangular sector #1 as function of the wind direction angles (Θ , Φ). Values produced from the simulation data presented in Figure 6.15 according to the sector #1 orientation shown in Fig. 6.16.

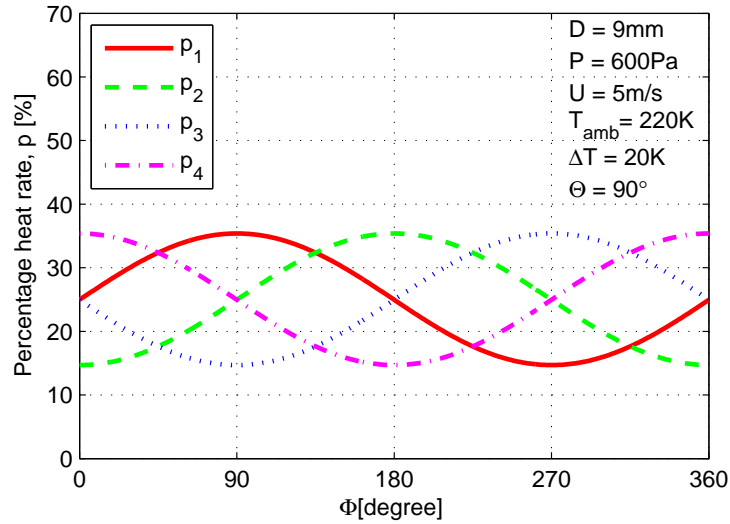


Figure 6.18: Percentage of the total sphere convection heat rate which goes to the each of the four sectors as a function of wind angle Φ , for $\Theta=90^\circ$.

6.5.2 Angular sensitivity

In order to find out theoretically the sensor sensitivity to the change of incidence angle a numerical calculation of the angle derivatives of the convection heat rate for the four sectors that allows to calculate angle sensitivities, S_Θ

and S_Φ has been performed:

$$\begin{cases} S_\Theta = \frac{\left\| \frac{\partial \vec{Q}}{\partial \Theta} \right\|_2}{Q_{sph}} \cdot 100\% \\ S_\Phi = \frac{\left\| \frac{\partial \vec{Q}}{\partial \Phi} \right\|_2}{Q_{sph}} \cdot 100\% \end{cases} \quad (6.22)$$

where $\left\| \frac{\partial \vec{Q}}{\partial \Theta} \right\|_2$ and $\left\| \frac{\partial \vec{Q}}{\partial \Phi} \right\|_2$ are the norms of the heat vectors derivative given by:

$$\begin{cases} \left\| \frac{\partial \vec{Q}}{\partial \Theta} \right\|_2 = \sqrt{\sum_{i=1}^4 \left(\frac{\Delta \dot{Q}_i}{\Delta \Theta} \right)^2} \\ \left\| \frac{\partial \vec{Q}}{\partial \Phi} \right\|_2 = \sqrt{\sum_{i=1}^4 \left(\frac{\Delta \dot{Q}_i}{\Delta \Phi} \right)^2} \end{cases} \quad (6.23)$$

The angular sensitivities are shown in Figure 6.19.

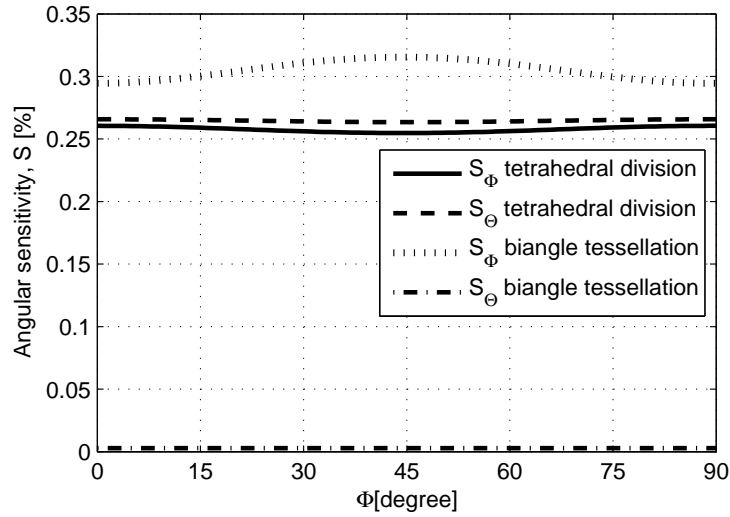


Figure 6.19: Angular sensitivity plots for two type of spherical geometries division into four equal sectors. Traditional biangle tessellation has been contrasted with a tetrahedral division. S_Θ and S_Φ for both geometries and wind speed of 5m/s can be observed for Φ rotation range 0° to 90° and for $\Theta=90^\circ$.

The curves have been plotted for $\Theta=90^\circ$ and for values of Φ ranging from 0° to 90° which covers the entire rotation due to the symmetry. The results show that both sensitivities S_Θ and S_Φ are very similar and very homogeneous for all rotation angles. In this example, a 1° change in the wind direction angle results in the redistribution of 0.25% of total heat rate

delivered to the whole sphere among the sectors, whereas the total heat rate remains constant. This is compared in the same figure with similar calculations for a sphere classical biangular division into four equal sectors. As can be seen in this case the sensitivity is larger for angle Φ and not homogeneous but at the same time sensitivity for Θ is very small. Those results motivated our decision to work with four sectors divided into triangular sectors as shown in Figure 6.16.

Sensibility analysis for the tetrahedral structure has been extended not only for the Φ angle rotation where $\Theta=90^\circ$ but for whole possible 3-D angle range with is $\Theta=\langle 0^\circ \dots 180^\circ \rangle$ and $\Phi=\langle 0^\circ \dots 360^\circ \rangle$. As a result of this analysis we generated the plots of angular sensitivity all 3-D angles, see Figure 6.20.

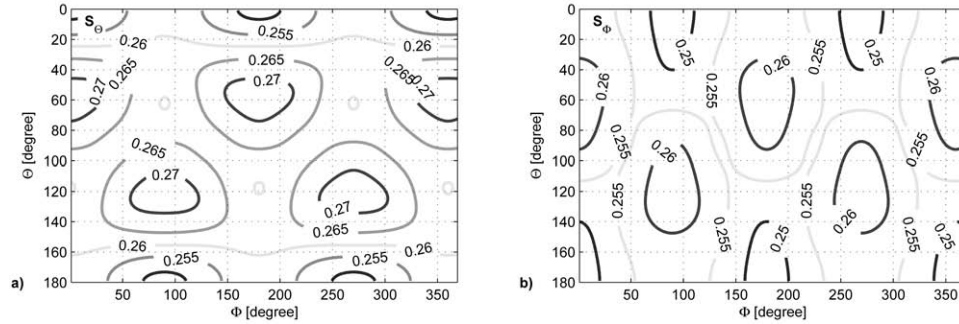


Figure 6.20: Angular sensitivity plots for tetrahedral sphere division a) S_Θ b) S_Φ . Analysis was done for particular ambient conditions: $T_{amb} = 220$ K, $U_{flow} = 5$ m/s, $\Delta T = 20$ K

Sensitivity analysis for the full 3-D angle range in Figure 6.20 has shown that tetrahedral sensor structure has a very homogeneous sensibility for any possible incidence angle and only minimal variation in the value of sensibility from 0.2488% to 0.2713% has been registered. This encourages us to introduce the minimum sensitivity parameter (S_{min}) defined as the smallest of S_Θ and S_Φ values. For this particular ambient parameters case, it would be that $S_{min} = 0.2488\%$ and its means that in the worst case the sensibility of the tetrahedral structure for any possible change in angle direction is at least 0.2488%.

The same procedure has been extended for different wind speeds and for few ambient temperatures. see Figure 6.21.

The sensitivity of 0.2% and higher for the velocity in the range 3-20m/s are found, whereas it decreases for lower wind speed values.

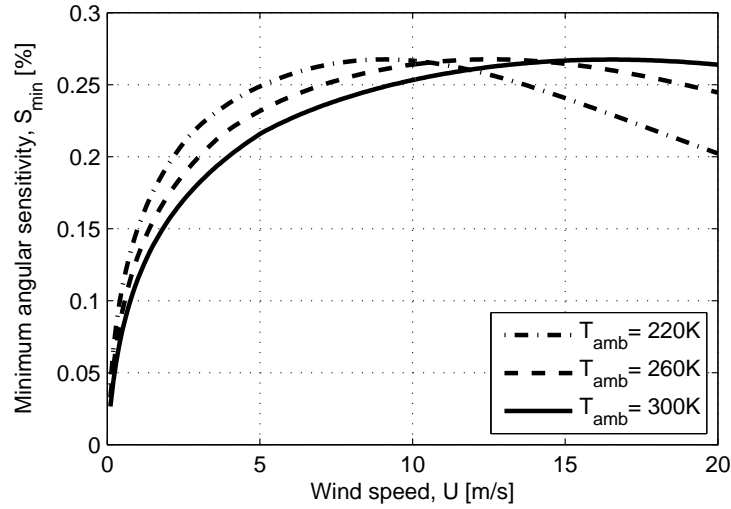


Figure 6.21: Minimum angular sensitivity analysis of tetrahedral sphere structure working in CO₂ 600Pa atmosphere as a function of wind speed and for different ambient temperatures scenario at constant overheat 20°C.

6.5.3 Angle inverse algorithm

As has been proved in the previous section, the hot sphere divided into tetrahedral sectors shows important sensitivity for 3-D wind angle. The algorithm to find out the wind direction from the measurement of the power of the four sectors is graphically illustrated in Figure 6.22, where an Example is illustrated for wind direction: $\Theta_{Ex}=97^\circ$, $\Phi_{Ex}=111^\circ$. We known from the CFD simulation that for this 3-D angle the corresponding heat rate, and calculated percentage shares, will be as presented in Table 6.5

sector	Heat [mW]	percentage [%]
#1	12.38	33.71
#2	10.88	29.62
#3	5.33	14.51
#4	8.14	22.16
Sph	36.72	100.0

Table 6.3: Percentage heat rate share

For the particular sector, this percentage solution is valid not only for the 3-D wind angle *Example* but for many others different wind incidence angles which graphically has been plotted as the lines in bold for each from the tetrahedral sphere sectors, see Figure 6.22.

In the next step, the superposition of the plots of percentage of the heat rate of the four sectors is performed. As can be seen, there is only a point

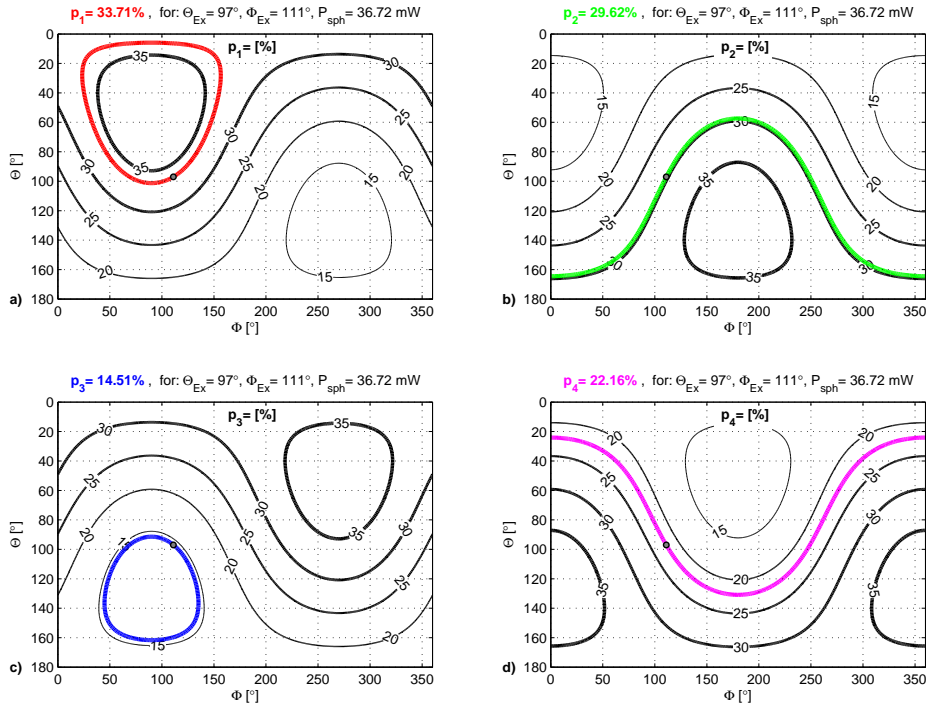


Figure 6.22: Percentage heat rate solution for 3-D incidence angle example (Θ_{Ex} , Φ_{Ex}) together with other wind angle possibility that satisfies this particular share of each from the tetrahedral sectors.

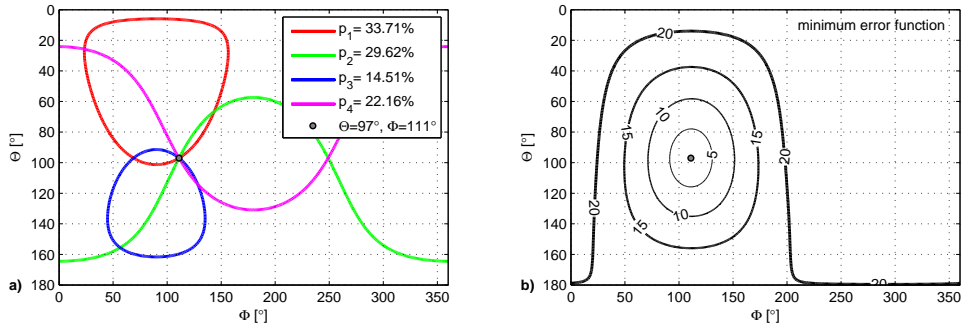


Figure 6.23: Wind incidence angle discrimination from CFD simulation model of the power delivered to four triangular sectors, a) the Iso-percentage curves were superposed in order appoint cross section zone, b) the final wind incidence angle point ($\hat{\Theta}$, $\hat{\Phi}$), was determined by minimizing an error function.

where all four plots intersect, see Figure 6.23 and this is our incidence angle that has been chosen for the example.

It could happen that for the real measurement that there is not a sin-

gle intersection point for all curves as theoretically predicted in the example shown in Figure 6.23a), but several intersection points for each pair of curves close to each other. And this could be due to measurement errors or imperfection of geometry conceived in the fabrication process. In order to get the angle of incidence of the wind more precisely, we calculated the value of the mean square error between the measured values and all possible obtained from CFD simulations as follows,

$$\begin{aligned} (\hat{\Theta}, \hat{\Phi}) = \underset{\substack{\Theta \in [0, \Pi] \\ \Phi \in [0, 2\Pi]}}{\text{Arg Min}} \left\| \vec{p}_m - \vec{p}_s(\Theta, \Phi) \right\|_2 \end{aligned} \quad (6.24)$$

where \vec{p}_m is the vector of the percentage value of the heat rate for the measurement at unknown 3-D wind angle,

$$\vec{p}_m = \begin{pmatrix} p_1 \\ p_2 \\ p_2 \\ p_4 \end{pmatrix} \quad (6.25)$$

and \vec{p}_s is the vector of the percentage value of the heat rate from the CFD simulation calculated for all possible incidence angles (Θ, Φ) ,

$$\vec{p}_s = \begin{pmatrix} p_1(\Theta, \Phi) \\ p_2(\Theta, \Phi) \\ p_2(\Theta, \Phi) \\ p_4(\Theta, \Phi) \end{pmatrix} \quad (6.26)$$

Therefore, resolving Equation (6.24) we obtain the coordinates $(\hat{\Theta}, \hat{\Phi})$, which give the minimum of the function declared in this equation - that is our wind incidence angle. This minimum error function has been also shown in 6.23b). With no surprise, the minimum error is found to be for angle: $\Theta=97^\circ$ and $\Phi=111^\circ$, the same as the intersection point for all particular sector solutions.

6.6 Tetrahedral 3-D sensor prototype

The fabrication of the wind sensor prototype includes the fabrication of the shell, the printed circuit board design, the integration and assembly of the pieces along with the platinum resistors for a heater purpose. This is schematically drawn in Fig. 6.24.

The spherical sectors are shown in Fig. 6.24a) where software models of the outer and inner faces of the shell are depicted as well as a 3-D picture of the assembly of the four sectors Fig. 6.24d). All four sectors are interchangeable with each other and are modified spherical triangles to allow the

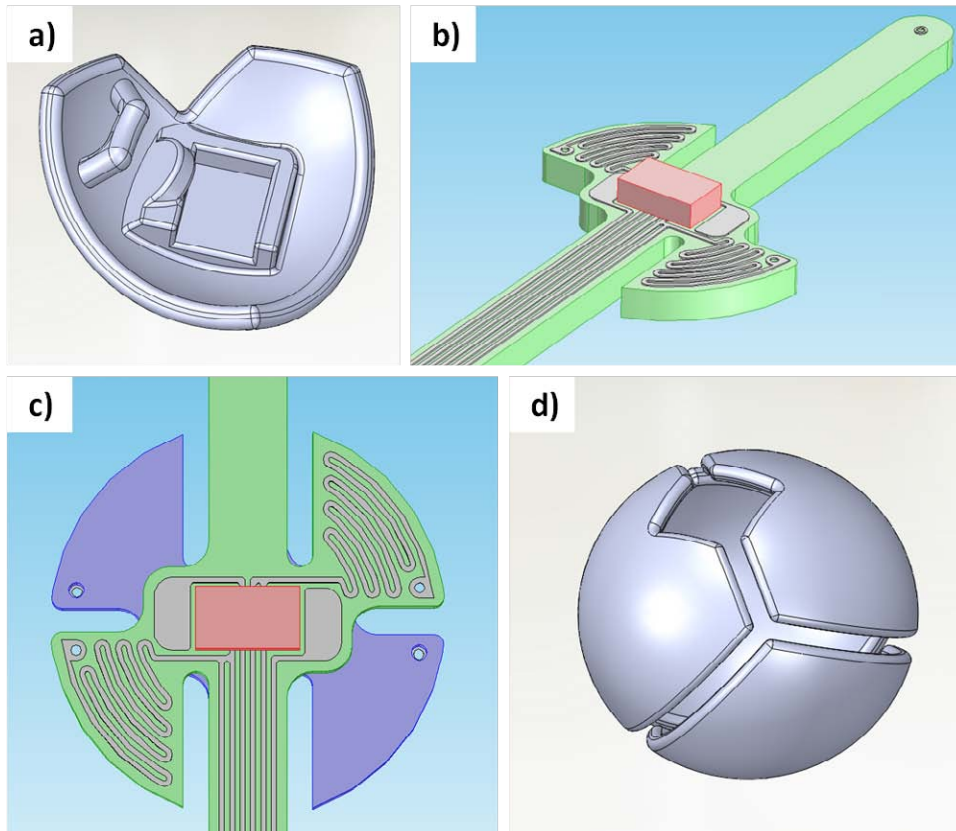


Figure 6.24: Models of the spherical wind sensor components, a) triangular sector with its interior heat resistor mold, b) PCB with electrical layout and central core resistor, c) union of the two PCB's where mechanical support and electrical wiring are provided for each sector, d) four triangular sectors assembly.

PCB to pass inside. As can be seen, the inner face of the shell includes protrusions to accommodate the platinum resistor and to hold the PCB. The part of the PCB that passes inside the shell is shown in Fig. 6.24b), where the copper layout is clearly seen and also the bonding PAD's. The connection between the PAD's and the main frame of the PCB is serpentine shaped to increase the thermal resistance of this path. Moreover, there are also shown the connecting PAD's of a core resistor that is placed on the PCB itself and that has the function to keep the temperature of the PCB at the same temperature as the spherical shell. The printed circuit board was designed in a complementary way that once rotated 180 degree becomes compatible with a second PCB and creates the structure to give mechanical support and electrical wiring for the four sectors, as shown in Fig. 6.24c).

This specific design solution was selected on purpose to, on the one hand,

separate thermally each sector from the others to avoid heat cross effects and, on the other hand, to suppress the heat conduction losses defined by

$$\dot{Q}_{cond} = \frac{T_i - T_{PCB}}{R_{th}} \quad (6.27)$$

where T_i is the hot point temperature of #i sector, T_{PCB} is the temperature of the central core region of the PCB and R_{th} is a thermal resistance of the path from the sector to the PCB support.

The heat conduction thermal losses \dot{Q}_{cond} are cancelled when T_i and T_{PCB} have the same value (T_{hot}). More details are given elsewhere [11].

For the shell fabrication, a stereo-lithography 3-D printing process of silver 92.5% and copper 7.5% in weight was chosen. This material provides a very high thermal conductivity and allows to achieve a homogeneous temperature distribution. The thickness of the shell is 0.5 mm and the separation between sectors is also 0.5 mm. Once the sectors were manufactured they were polished by using a tumbler with plastic pellets progressively going from rough to smooth until mirror finish was achieved. After that, a 100 nm thin gold layer was sputtered on the outside. The process steps can be seen in Fig. 6.25 from manufactured, a) to polished, b) and finished, c). The gold coating and the polish process are meant to reduce radiation heat losses by lowering the surface emissivity factor as much as possible [95].

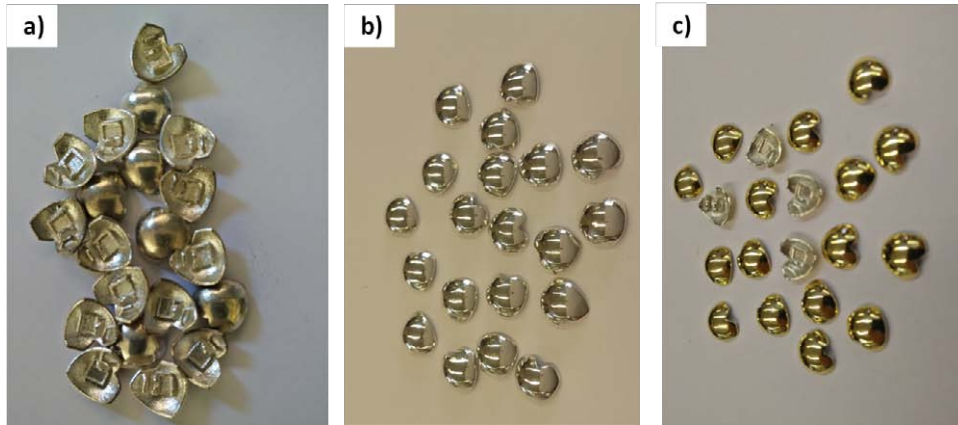


Figure 6.25: Pictures of wind sensor triangular sectors, a) made out of Silver Sterling material (alloy Au 92.5%, Cu 7.5%) in a stereolithography 3-D printing commercial process, b) after tumbler polishing operations with progressive grit, c) after gold thin film (100 nm) deposition on the outer surface.

The heater resistors are surface mount 100 Ω platinum resistors having temperature coefficient $\alpha_T = 0.00385$ 1/ $^{\circ}$ C, using different encapsulation; SMD0603 for the spherical sectors and SMD0805 for the PCB.

A picture of the prototype assembled is shown in Fig. 6.26 where the outer face of the spherical sensors and the PCB passing through the inside volume can be seen. The six platinum resistors, one per each sector, and two for the PCB are hidden inside.

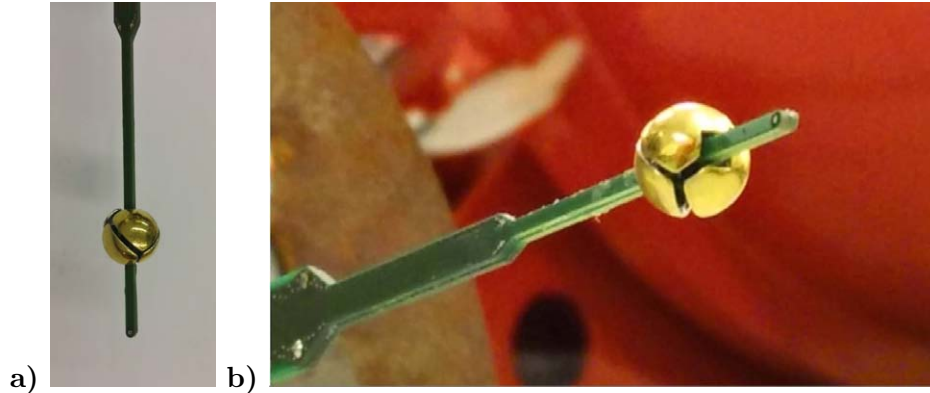


Figure 6.26: Picture of the spherical 'tetrahedral' wind sensor prototype, a) in the upside-down position for the wind tunnel chamber, b) in a perspective view after measurements in a Mars-like conditions.

6.7 Preliminary measurements

As the prototype sensor was fabricated, the substantial set of measurements were performed in the University of Aarhus Mars wind tunnel facility AWTSI, where low pressure and low temperature can be independently set [71].

6.7.1 Measurements set-up

The tunnel has an internal cylinder where the boom is located, see Figure 6.27a).

The spherical wind sensor head was placed upside down inside the chamber, at its central point, and could be rotated in a horizontal plane for 90 degrees, see Figure 6.27b).

The measurement conditions are described in Table 6.4.

6.7.2 Measurements sequence

The typical set of measurements performed was for wind speed changing every 200 s. For each wind speed the rotation angle Φ was varied from 45° to 135° with intermediate values: 75° , 90° , 105° and then back to 45° before flow velocity was changed. An example set of measurement for CO_2 at $P = 10\text{mbar}$ and $T_{amb} = -18^\circ\text{C}$ and overheat $\Delta T = 40^\circ\text{C}$ is shown in

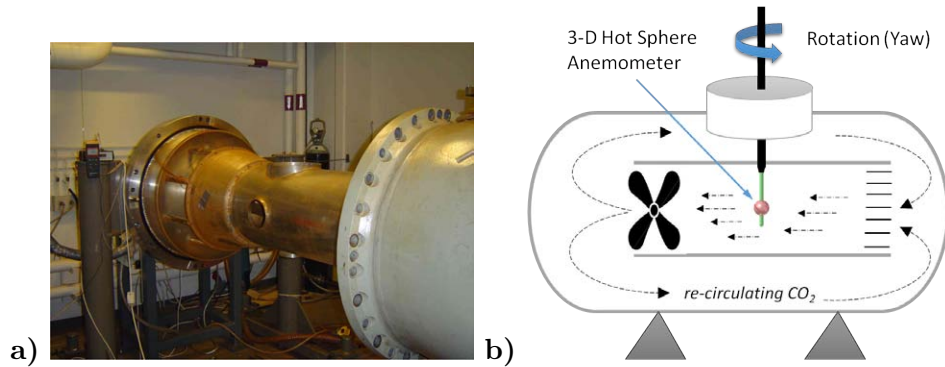


Figure 6.27: a) Aarhus Mars wind tunnel facility AWTSI when opened b) 3-D hot sphere wind sensor setup with yaw rotation angle degree of freedom

Atmosphere	CO ₂
P [mBar]	10
T _{amb} [°C]	0, -8, -18
ΔT [°C]	25, 40
U [m/s]	1, 2, 4, 7, 10, 13
Θ [degree]	90
Φ [degree]	45, 75, 90, 105, 135

Table 6.4: Measurement conditions.

Figure 6.28, where values of the average power for each sector calculated during the corresponding slot of velocity and flow direction are plotted.

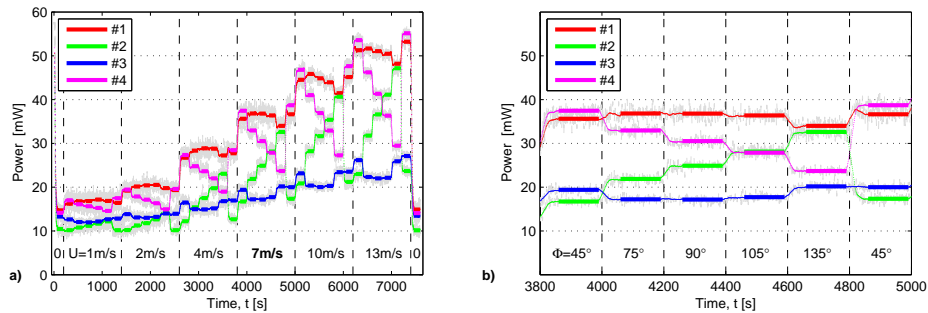


Figure 6.28: Power delivered to the sectors, a) for different wind velocities and for wind direction angle Φ sequence $[45^\circ, 75^\circ, 90^\circ, 105^\circ, 135^\circ]$, b) zoom on the section where the wind velocity was 7m/s and only wind direction sequence is on display. CO₂ atmosphere at $P = 10$ mBar and $T_{amb} = -18^\circ\text{C}$ conditions, for $\Theta = 90^\circ$ and overheat $\Delta T = 40^\circ\text{C}$.

Figure. 6.28a) shows for each velocity the raw data of the power delivered to each sector as a function of the Φ angle from 45° to 135° . As can be seen,

the sensor has sufficient sensitivity to the incidence angle of the wind as the four different sectors require a different amount of power to keep the same overheat temperature above the ambient.

Precisely, this difference is what is used to calculate the value of the incidence angle of the wind thereby providing direction sensitivity. This is clearly seen for the plot Figure 6.28b) or the same wind velocity $U = 7$ m/s and consecutive wind angles: 45° , 75° , 90° , 105° , 135° and back to 45° , whereas as predicted by the isotropy of the sphere the sum of the sector's power is independent of the wind incidence angle thereby providing with the wind speed value.

Figure 6.29 shows the measured data (filtered from the raw data) of the power delivered to every spherical sector as a function of the angle of incidence and of the magnitude of wind speed.

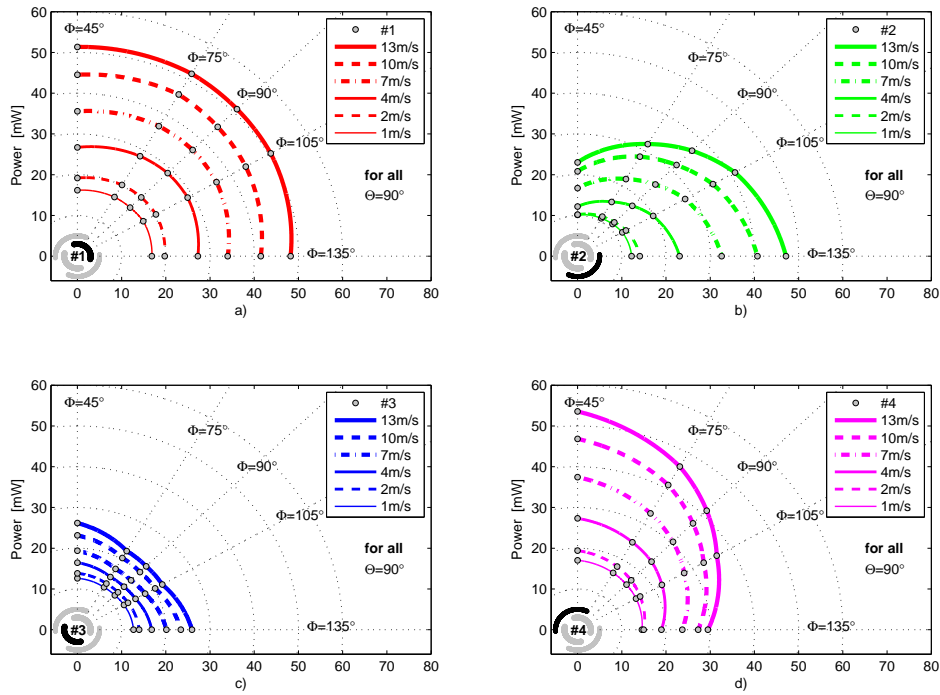


Figure 6.29: Polar plot of the average power delivered to the four sectors: a) sector #1, b) sector #2, c) sector #3, d) sector #4 as function of the wind speed and wind direction Φ , for $\Theta = 90^\circ$.

6.7.3 Yaw rotation experiment

As the experimental set up did not allow to change the angle Θ , which was fixed to 90° , the angle that we changed was Φ from 45° to 135° . We were satisfied with this range since the tetrahedral division of the sphere shows

symmetry in the power readout every 90° as can be seen in Figure 6.18.

Results obtained for the sector #2 are shown in Figure 6.29b). This sector has an orientation relative to the tunnel axis as shown in the inset. This is a polar plot where the radius is the value of the power. Each line corresponds to different wind speeds and the data points correspond to the various angles explored. For example, sector #2, under wind speed of 13m/s from direction $\Theta = 90^\circ$ and $\Phi = 45^\circ$, required a power of 23 mW to keep an overheat temperature of 40°C above the ambient. As can be seen, due to the position of this particular sector in the sphere shell, the power required increases as the angle increases. Similar information is shown for the other three sectors in figures Figure 6.29a), c) and d). This plot provides an interesting overview of the sensor behavior especially if we look at the pair of sectors with opposite location around the PCB. From the pair of sectors #1 and #3 we see that when the wind blows into sector #1 it requires maximum power, whereas the opposite sector #3 demands minimum power. On the other pair of the sectors #2 and #4 we can observe that when the wind incidence angle is changing toward the center of the sector #2 its power increases whilst the same angular change results in changing wind incidence angle away from the sector #4 its power decreases. What also stands out from Figure 6.29 is that power plots for different velocities but for the same angles do not cross each other.

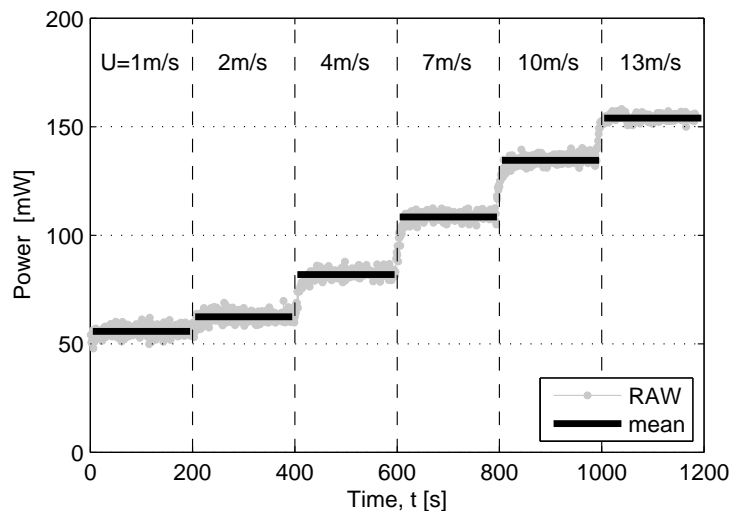


Figure 6.30: Raw measurements of total power delivered to the sphere for different wind speed blowing from direction $\Phi = 45^\circ$ and $\Theta = 90^\circ$ together with mean power value calculated for each wind direction slot.

6.7.4 Wind velocity steps

In Figure 6.30 the value of the sum of the power delivered to the four sectors is plotted as a function of time for constant wind direction angle $\Phi = 45^\circ$ and $\Theta = 90^\circ$. The wind speed corresponding to every time slot is also shown. As can be seen, velocities of wind ranging from 1m/s up to 13m/s were produced at the ambient pressure of 10 mBar and at local CO_2 temperature of -18°C . A custom acquisition board that maintains the target temperature in each sector has been developed and used for the measurement. Thermal control circuit implements a CTA mode using a constant voltage feedback loop, in similar way the ASIC designed in the course of the project, [12].

The raw data, shown in Figure 6.30 demonstrate sensitivity to the wind speed and sufficient stability of the measurement taking into account that the ambient temperature and pressure were set at the beginning of each experiment, and some temperature and pressure drifts were recorded during measurements. As the wind velocity grows, an increase in the global sphere power demand was registered.

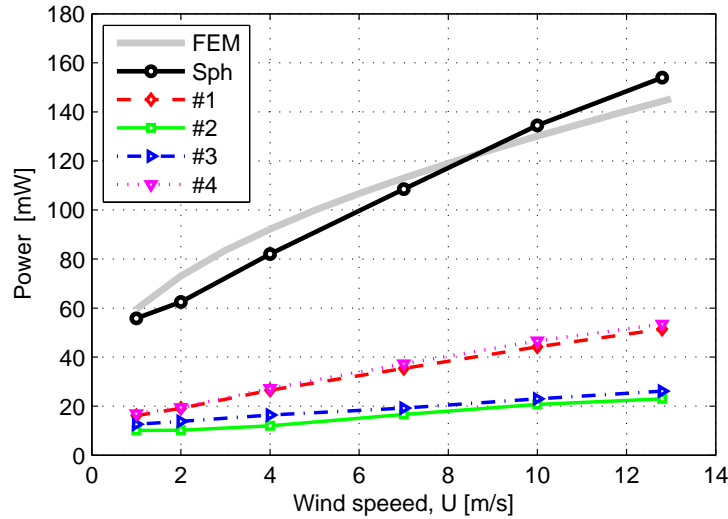


Figure 6.31: Mean power delivered to each sector and total sphere demand as a function of the wind speed for wind direction $\Theta = 90^\circ$ and $\Phi = 45^\circ$. Data selected from the Figure 6.28, whereas CFD curve was added from multi-physics numerical simulation for the same ambient parameters

Figure 6.31 is an example of power demand for a particular sphere orientation relative to the wind direction $\Theta = 90^\circ$ and $\Phi = 45^\circ$. The averaged power delivered to each sector of the sphere is plotted against the wind velocity value as well as power for the whole sphere. In the same figure numerical simulation results obtained by CFD were added. This multi-physics simulation was performed using COMSOL for the same ambient conditions

as inside the wind tunnel chamber during the experiment. What stands out from this figure is that the power convection curve from the simulation is in good agreement with experimental data obtained in measurements. Another interesting thing observed in Figure 6.31 is that for all wind speeds the power drained by sectors #1 and #4 is similar and much higher than power delivered to the pair of sectors #2 and #3 (also quite the same) and this is what has been predicted for a wind direction within horizontal plane for angle $\Phi = 45^\circ$ in Figure 6.18.

6.7.5 3-D wind angle discrimination

The algorithm to find out the wind direction from the measurement of the power of the four sectors has been illustrated in Section 6.5.3. The same algorithm has been applied for data interval from 3800 s to 4000 s from the measurement set shown in Figure 6.28b). Thus, the percentage share of the power which corresponds to each sector has been calculated and shown in Table 6.5.

sector	Power [mW]	percentage [%]
#1	35.40	32.63
#2	16.56	15.30
#3	19.23	17.75
#4	32.27	34.31
Sph	108.46	100.0

Table 6.5: Percentage power share from measurements.

As we took the data values for the four sectors corresponding to an experimental incidence angle set for: $\Theta = 90^\circ$ and $\Phi = 45^\circ$ and wind velocity $U = 7$ m/s, we performed numerical simulations for the same wind atmospheric conditions in order to reproduce the percentage plots, similarly to what we have done in Figure 6.22 for every incidence angle. To verify that we can use an algorithm to retrieve the incidence angle from the measurements we have taken the values of percentage power share: p_1 , p_2 , p_3 , and p_4 from Table 6.5, then have plotted iso-power plots for every combination of the incidence angles. In consequence, we have obtained the four plots shown in bold line in Figure 6.32.

As it can be seen, there is not a single intersection point for all curves as theoretically predicted in the example shown in Figure 6.23a) but several intersection points for each pair of curves close to each other. This is due to the experimental conditions that may have drifted from the initial settings in the experimental chamber and also to measurement errors. In order to get the angle of incidence of the wind more precisely, we calculated the value of the mean square error between the measured values and all possible obtained from CFD simulations. Resolving Equation (6.24) we obtain the coordinates

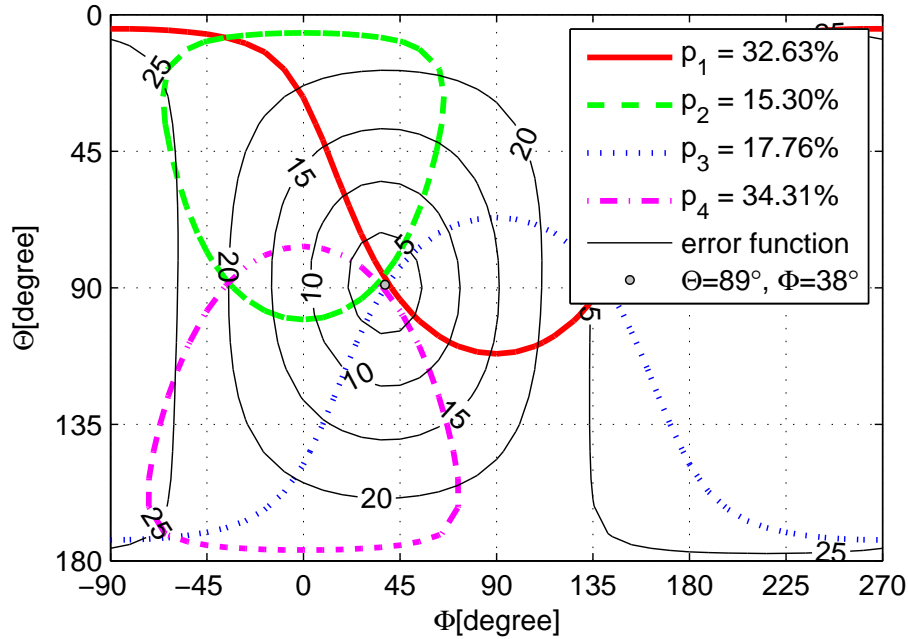


Figure 6.32: Wind incidence angle discrimination from the real measurement of the power delivered to four triangular sectors. Iso-percentage curves were superposed in order appoint cross section zone. Final wind incidence angle point (Θ, Φ) was determined by minimizing an error function.

$(\hat{\Theta}, \hat{\Phi})$, which give the minimum of the function declared in this equation - that is our wind incidence angle. This error function is superimposed in the same Figure 6.32 and the minimum error is found to be for angle: $\Theta = 89^\circ$ and $\Phi = 38^\circ$, within an error of 7 degrees of the experimental wind direction.

6.8 3-D hot sphere anemometer summary

Although MEIGA hot spherical sensor was not approved for Mars MetNet Precursor Mission (MPPM) which is scheduled for launch in 2015/2016, [96], the substantial amount of work from conception through development, modelling, prototyping and preliminary measurements and evaluation have been done by MNT group in UPC according to the projects AYA-2010-20847 and AYA-2011-29967-C05-04.

To sum up the main contributions of the MEIGA 3-D spherical wind sensor we could mention:

- Extending four hot dice concept of measuring wind speed and direction in 2-D space from REMS wind transducer toward full 3-D spherical wind sensor based on tetrahedral division, see Section(6.5),

- Elimination of unwanted thermal losses (either conduction or radiation) be proper design and fabrication process, see Section (6.2.1),
- Providing the new efficient tool that enables to model convection heat of any arbitrary shape of the spherical sector for all possible 3-D wind direction, see Section (6.3),
- Minimalization of necessary number of CFD simulations to extend for whole scenario of possible ambient conditions (T_{amb} , P_{amb} , U , and $direction(\Theta, \Phi)$) to exactly predict power demand for each sector, see Section (6.3.4),
- Design and assembly of fully operational spherical wind anemometer made out of four tetrahedral sectors to enable proof of concept tests, see Section (6.6),
- Preliminary measurement that has confirmed hypothesis for sensitivity of the wind speed and wind direction and also ability to estimate those wind parameters based on the CFD simulation model proposed,

Besides the contributions listed below author of the thesis has been responsible for building provisional UPC-MNT wind tunnel facility, and evaluation of the simplified concept of the hot sphere anemometer made out of two hemispherical sectors. This part of the investigation work has been reflected in following conference proceedings:

Reference [10], Appendix I

L. Kowalski and M. Garcia, "Hypobaric chamber for wind sensor testing in Martian conditions," in *8th Spanish Conference on Electron Devices (CDE 2011)*, (Santiago de Compostela, Spain), pp. 1–4, February 2011

Reference [11], Appendix L

L. Kowalski, V. Jiménez, M. Domínguez-Pumar, S. Gorreta, S. Silvestre, and L. Castañer, "Low pressure spherical thermal anemometer for space missions," in *IEEE SENSORS 2013*, (Baltimore, United States), pp. 1–4, November 2013

Reference [12]

S. Gorreta, E. Barajas, L. Kowalski, T. Atienza, M. Domínguez-Pumar, and V. Jiménez, "A self-calibrating closed loop circuit for configurable constant voltage thermal anemometers," *Electronics Letters*, September 2015

Chapter 7

Conclusions

In this chapter, author of the thesis will discuss main aspects of the two novel wind sensors he has been working on. Later author will present suggestion for further research to carry out.

7.1 Discussion

7.1.1 2-D Wind Transducer

When the preparation to the MSL mission began so the REMS project and the challenge to develop 2-D wind transducer was high due to demanding instrument requirements to operate in a very thin atmosphere of Mars.

When the REMS MSLrover project began, it was clear from the start that measuring the wind in the thin atmosphere of Mars was a challenging subject. We were in charge of the primary transducer, the 2-D wind sensor, so we knew that it will be difficult to get a working prototype. From the first day the MNT group, based on his experience with flow meters design, bet on thermal anemometer concept working in CTA mode, where the close-loop sigma-delta modulator provides digital power readout. In this approach we need an electro-thermal converter that on one hand would provide fast, reliable and stable coupling with atmosphere, and, on the other hand, may provide homogenous temperature distribution to run accurately CFD simulations for further thermal modelling. The idea of using silicon wafer cut into square shape chips has satisfied these requisites.

For predictable convection heat transfer rate, the sensor had to be sized so that it works in medium continuum region. This was compatible with a chip size greater than 1 mm. We knew that it was a critical subject as the Pathfinder hot-wire sensor wasn't able to perform reliable measurement due to deep slip-flow conditions. We also knew that the only system that was able to provide reliable wind data from Mars was the Viking hot-film sensor that featured a characteristic size of the hot element of 0.51 mm.

CFD simulation of one square shape die ($1.6 \times 1.6 \times 0.4$ mm) shown that convection heat in 2-D flow does not depend on wind direction but only on $P \cdot U$ mass flow product. This concept has been expanded to the array of four coplanar silicon dice with minimum separation between them of approximately 0.5 mm. This separation was selected to provide thermal isolation between the dice, due to the very low thermal conductivity of the Martian atmosphere. At the same time, from the flow dynamics point of view, the separation is small enough so that the group of dice would perform as a one scaled up the hot component ($\sim 4 \times 4 \times 0.4$ mm). Indeed, the average thermal conductance of group of four dice has shown sensitivity to the wind magnitude preserving independent character on the wind direction, only for higher velocity range (30...60 m/s) there has been some fluctuation in thermal conductances. When going down to the individual thermal conductances of separated dice (A, B, C, D) has been observed a significant dependence on the wind direction angle resembling sinusoidal function. For each velocity, the difference between a maximum and a minimum of thermal conductance value is in the range of average value ($G_{th_{max}} - G_{th_{min}} \approx G_{th_{avg}}$). This mechanism of thermal conductance reallocation between hot dice, while an average conductance remains constant, has provided sensitivity for the wind angle identification. Minimum angular sensitivity was for low speed (~ 0.25 %/degree for 10 m/s) and rise for higher velocities. For the same wind velocity, angular sensitivity variation is within 22% to 42%, where maximum sensitivity is for winds coming from diagonal directions and minimum sensitivity is when the wind blows perpendicularly to the dice orientation. Based on the four hot dice concept the differential terms *NS* (*North-South*) and *EW* (*East-West*) has been introduced. By using those terms there is no important variation in angular sensitivity, and, at the same time, we eliminate common conduction losses and external radiation component. The same, newly conceived four hot silicon dice structure becomes the state of art 2-D wind transducer where we get the wind speed from the average power delivered to the four dice, and we also get the wind direction from the power differences between dice.

There were two main reasons why for the hot die element silicon material has been adapted. Silicon bulk material, thanks to its high thermal conductivity provides a uniform temperature distribution within die volume. That was confirmed solving 1st order thermal model and through FEM analysis that has shown a maximum thermal gradient of 0.2% in reference to the applied overheat. Working with silicon technology also has permitted deposition of three platinum resistances isolated by the good quality silicon thermal oxide. First of this resistances called R_{sens} will provide temperature feedback due to its linear dependence on the temperature; indeed in characterization has been found that $\alpha = 0.003$ 1/degree, which is characteristic for platinum film thinner than 100 nm. Second resistance R_{heat} forms a resistive circuit, which converts short electrical current pulses into heat

generated according to the Joule effect and dissipated into the silicon chip. Finally R_{delta} is an additional resistance located at hot die element for the purpose of setting up an appropriate overheat. For the fabrication process, which has been entirely handled by UPC clean room facility, the resistance targets was set for $R_{sens} = 7k \Omega$, $R_{heat} = 700 \Omega$ and $R_{delta} = 700 \Omega$. This has been achieved by sputtering approximately 20 nm of titanium adhesion layer and then consecutively 80 nm of platinum resistive material among many steps carefully described in this thesis. The other important aspect of the fabrication is that silicon bulk has been connected through contact window to external potential to prevent electrical charge to be build up in this component.

Besides the array of the four dice working as hot points that dissipate heat to the ambient by convection, there is another fifth die called a *Reference* which estimates ambient temperature so that the system can operate at a preset overheat temperature. Each hot dice included a R_{delta} resistance. A connection network gives a ΔR value from a combination of R_{delta} resistances. The circuit was designed in the way that the hot dice overheat was automatically set from R_{sens} and ΔR values. Appropriate serial/parallel connection of the four R_{delta} resistances gives 12 combinations of different overheat profiles to be set-up. In the end, all four hot dice in a group follows the same overheat profile respect to the ambient temperature. We choose the overheat temperature profile of the hot dice so that the duty cycle read-out of the system is proportional to the thermal conductance of the dice although the delivered power depends on ambient temperature. To achieve this, each hot die component instead of working with CTA mode is working in CTDA mode where the ambient temperature is constantly monitored by *Reference* die and used to select an ambient temperature dependent overheat. As a result, overheat temperature changes so that it adapts to the changes in the heater resistance so that the obtained sensor responds only on each hot dice thermal conductance.

To understand better heat convection phenomena at the single die level an algebraic model of the single die was analyzed for a wide range of temperatures, pressure and velocities taking into consideration variations of all Martian "air" parameters (k , C_p , μ , ρ). This analysis has been contrasted with CFD numerical simulation with good agreement.

Preliminary measurements have shown that the group of four dice has good sensitivity to the wind speed in the range of 0.3-20 m/s and angular sensitivity to the wind direction for the velocities higher than 0.3 m/s. Yaw rotation experiment has shown that sensor has the ability to recognize wind angle with higher resolution than 10° . Experiments carried out in Aarhus re-circulating wind tunnel as well as in Oxford open wind tunnel has confirmed that thermal conductances of the group of four dice as well as for the single die unit depends on the $P \cdot U$ product, so that the velocity component (U) can be obtained providing independent ambient pressure measurement.

Measurement campaign has also shed light on the aspects of thermal isolation of the hot dice component from the PCB base. It stands out that the heat drain through pyrex support structure is the same rate as it is through the wire-bonding connection. Moreover, measurements show that only about 10% of the power delivered to the hot element is transferred to the ambient in the convection processes, whereas other significant 90% of the power is classified as thermal losses. In order to reduce thermal losses and improve the mechanical properties of the setup, the dice support material was changed from pyrex to glass-fiber.

Finally, elaboration of the first order heat convection model gives us a tool for comprehensive comparison of Viking (CTA), Pathfinder (CPA) and REMS (CTDA) thermal anemometers units, besides the fact that their working modes were different. This study has shown that only REMS hot die element have uniform temperature along entire hot volume, where for Viking rod temperature gradient is observed for half of the hot-film structure and in the case of Pathfinder wire bound each end of the hot-wire experienced temperature drop. Compared for the same wind conditions, REMS wind sensor shown better efficiency in Power/Overheat ratio and is slightly more power efficient than Viking wind sensor unit and much more efficient than Pathfinder wind sensor unit. This result is also true for 3-D wind transducers when extended this analysis by multiplying power of each unit per a number of units that compose full 3-D wind sensor.

7.1.2 3-D Hot Sphere Anemometer

Another call for the anemometer to Mars was within the course of the MEIGA project that has been a part of bigger MetNet mission undertaking. The specific requirements, assigned to MNT group, according to the wind sensor development have been different from that from the REMS project. The measurement range was limited to the wind velocities from 1 m/s up to 10 m/s, and the sensor had to be more resistant to a shock of about 300 g to withstand the landing procedure. But the most important thing was that the sensor developed in the MNT had to be a full 3-D transducer for wind velocity and wind direction. Based on the previously experience gained in REMS we thought that once again it will be a thermal anemometer working in CTA mode. Nevertheless, this time the geometry that we came should give a better-conditioned response. We came with the idea of a sphere as the body with higher isotropy possible. Also this time we bet on the sphere divided into sectors and as it stands out from the analysis that a sphere division into four sectors is just right to get enough information for full 3-D angle decomposition.

The concept of the new 3-D hot sphere anemometer has been enriched in several interesting aspects in reference to the array of four hot silicon dice. Crucial was an introduction of the central core working with the same

temperature set point as the external shells that are in contact with surrounding gas. By this treatment, we have displaced all thermal losses as the core is kept at the same temperature as the sphere surface. Therefore, there was not need to use very high thermal resistivity materials to isolate hot spherical sectors from the cold base as this spherical sectors were physically connected to the core working at the same temperature. The role of the FR4 board is to give mechanical support for the spherical sectors and also to provide electrical wiring. It needs to provide some thermal isolation, but the requirements are relaxed by having a centrally heated core. It means that for spherical wind sensor are not required to use the thin wire-bonding connection, and we can use a more traditional PCB technology. By that, the sensor has become more robust to physical damage like the contact with small pebbles when descending or landing. As we wanted to simplify to the minimum the required wirings, we thought that it would be possible to use just one resistance for a measure and heating purpose. Eventually commercial PT100 resistances were adapted for this purpose with thermal coefficient characteristic for platinum $\alpha_{Pt} = 0.00385$ 1/degree.

The diameter of the sphere was optimized as a result of many factors. At first we knew that it had to be, as it was in the previous case at least 1 mm or more just to be sure that we are operation in medium continuum range. From the fabrication point of view, we knew that prototype part must be feasible, so this shifted the size of the sensor rather into a bigger size of several millimeters. There have been many publications about the flow behaviour when passing over a hot sphere and there is a fact that to have stable and axisymmetric flow around the sphere the Reynolds number must not exceed the value of 210. This in relation to the Mars atmospheric conditions situates our sphere to be not bigger than 10 mm in diameter for very low temperatures ($T_{amb} < 200$ K). That gave our final size limitation.

There exist many empirical approximations that give average heat convection rate for a sphere, as Whitaker or Feng&Michaelides. This is, however, true for the sphere as a whole and could give us information about the overall sphere behaviour but not of the arbitrarily shaped sectors. To be able to separate the convection power at each sector, there have been run many CFD simulation of a hot sphere for variations in CO₂ temperature, flow velocity U , and overheat ΔT . From these simulations the local heat flux data, the simulated shell surface, has been obtained. In the next step, the simulated data has been approximated by polynomials as a function of the position on the wind direction axis. From this polynomial functions, we can know the local heat flux at any point on the sphere concerning the impinging point of the wind direction without the need of all numerical raw simulation data. This was just a step to know the thermal conductance of arbitrary assign sector by integration of the local heat flux over corresponding sector's area. All this postprocessing of the CFD simulations gives us a tool that greatly speeds up the modelling of the convection of a hot sphere

divided into sectors.

As for now we have achieved the minimum size of spherical wind sensor to be 9 mm in diameter, which is about twice the characteristic size as it was in the case of the group of four silicon chips in REMS wind transducer. Spherical sectors were fabricated on Sterling Silver material using a commercial 3-D printing service. The Silver alloy was selected to provide maximum temperature uniformity within the sector boundary. As 3-D printing gives rough surfaces before sectors assembly started, they have been polished with progressive grit to obtain mirror finished external surface and then the thin layer of gold (100 nm approx.) has been deposited on top of it. The polishing and gold plating procedure was selected to minimize radiation effects. At the same time, gold passivation protects the silver surface from oxidation.

The four piece tetrahedral geometry was selected as a result of an angular sensitivity analysis. It stands out that for tetrahedral sphere division the angular sensitivity along entire sphere is almost homogenous, this mean that there are no blind zones where angle can not be determined or has bad sensitivity. For the range of velocities from 3 m/s to 20 m/s and within the ambient temperature of 220 K to 300 K the angular sensitivity for the full 3-D angle is bigger than 0.2 %. The maximum angular sensitivity of 0.25 % is reached for the velocities range from 10 m/s to 15 m/s (the same value was for REMS at 10 m/s for 2-D angle discrimination). Hot sphere ($D = 9$ mm) immersed in CO_2 atmosphere ($P = 600$ Pa) could change its global thermal conductance ($G_{th_{sph}}$) from 0.5 mW/K for low wind 0.2 m/s at ambient temperature 220 K up to 3.9 mW/K for a maximum wind speed of 20 m/s with ambient temperature 300 K. For the particular tetrahedral sector, its thermal conductance ($G_{th_{sector}}$) may vary from 10% to 40% of the global sphere thermal conductance depending on wind incidence angle according to the sector position. Each spherical sector dissipates maximum power when the wind blows directly in its center, and the minimum convection heat is observed when the wind is coming from the opposite to its central point.

For tetrahedral sphere geometry, an algorithm for wind angle determination was proposed. It is based on the numerical simulation results. It relies on iso-percentage curves in the angular space that have the same fraction of power being delivered. Drawing the iso-percentage curves for the four sectors gives a solution intersection point. The intersection point where four curves cross each other gives wind impinging point and if the curves don't cross at the same point, the argument for the minimum error function conclude the 3-D wind angle. For both, wind magnitude and wind direction, estimation the ambient temperature need to be provided. Nevertheless, as the sphere works at constant temperature is much more resistant for ambient temperature error as it operates on the relative (percentage values) of heat power delivered to the sectors in equilibrium conditions in the case of the wind angle estimation.

Measurements performed in Mars-like conditions confirmed high sen-

sitivity of the spherical sensor to the wind speed and direction. In one experiment by changing velocity from 1 m/s up to 13 m/s it has been registered a global sphere thermal conductance shift from 1.375 mW/K up to 3.875 mW/K. Also, substantial changes for each sector thermal conductances to the ambient were registered when wind direction angle was changed for all range of velocities (1, 2, 4, 7, 10, 13 m/s). Finally, an algorithm for wind angle discrimination has succeeded with 3-D angle estimation within an error of 7 degrees of the experimental wind direction, despite the imperfection in sensor prototype fabrication and temperature/pressure drifts in the measurement chamber. As a result of all experiments, it has been proved that spherical thermal anemometer build up from four identical tetrahedral sectors could be considered for a mission to Mars as a reliable 3-D wind sensor alternative.

7.2 Suggestion for further research

The author of the thesis together with other researchers from the MNT group from UPC are currently involved in the development of the improved version of the REMS wind transducer to be part of the MEDA instrument on board of the rover for Mars 2020 mission. The rover for Mars 2020 mission would be based on the Mars Science Laboratory (MSL) rover configuration. Meteorology instruments will be provided by CAB-INTA. The principal investigator of MEDA Jose Rodriguez-Manfredi has said that: "a set of sensors will provide measurements of temperature, wind speed and direction, pressure, relative humidity and dust size and shape".

According to the MEDA wind sensor improvement there are few worth to mention that are under consideration for 2-D wind transducer board:

- Resistance on chip reduction to only two R_{heat} and R_{sens} that would reduce conduction losses to the substrate as the number of wire-bonding will also be reduced from 7 to 4 for die (additional wire-bonding ground connection that prevents the electrical charge to be build up will be joined with one of the R_{sens} terminals),
- Further improvement of thermal isolation between hot dice elements and PCB base by thinner wire bondings with diameter of 18 μm and higher supporting pillars,
- Better wind signal coupling by using a higher overheat. This achieved due to changes in ASIC performance as well as by putting hot dice deeper in the wind according to the new support elevation,
- We want to provide hot dice group with lower resistance dispersion among them and enumerated chips for better traceability during the entire assembly process.

Respect to the 3-D wind spherical sensor there is also a plan for further improvements and studies to carry out. We are extending sensor thermal simulation for the dynamic behaviour to understand better what are the sensor limitations in the time response. The study is based on surface control theory and diffusive representation that shed light on the sensor reaction in the frequency domain. We believe that this research would indicate us where is still a place for sensor improvement. Besides this study we are planning to:

- Perform full sensor characterization involving measurement in temperature and pressure control environment for entire *yaw* and *pitch* spectrum of the wind angle and entire range of velocities,
- Estimate the distortion effect of the PCB protruding-arm which provides support for the spherical hot element tetrahedral shape sectors that are in contact with surround air,
- Improve assembling procedure and the same to lower asymmetry imperfection that could affect convection heat profiles,
- Extend wind speed range by performing mixed natural and forced convection CFD simulations for the low-velocity limit as well as laminar-turbulent simulation to broaden high wind velocity limitation,
- Incorporate a silicon chip - instead of a commercial PT100 resistor - as a heating and sensing component to improve wind sensor performance in the frequency domain due to the high thermal conductivity of silicon compared with the typical materials used in commercial PT100 components.

Bibliography

- [1] M. Domínguez, L. Kowalski, V. J. A. Moreno, L. Castañer, and J. Ricart, “Método para la medida de la velocidad del aire y de su dirección en dos dimensiones para aplicaciones aeroespaciales y de baja presión,” 2007. PATENTE DE INVENCION. Número de solicitud: 200700259. Número de publicación: 2342953. Fecha de presentación: 25.01.2007. Fecha de la concesión: 20.05.2011.
- [2] M. Domínguez, V. Jiménez, J. Ricart, L. Kowalski, J. Torres, S. Navarro, J. Romeral, and L. Castañer, “A hot film anemometer for the Martian atmosphere,” *Planetary and Space Science*, vol. 56, pp. 1169 – 1179, June 2008.
- [3] V. Jiménez, M. Domínguez-Pumar, J. Ricart, L. Kowalski, S. Navarro, J. Torres, J. Romeral, J. Merrison, and L. Castañer, “Applications of hot film anemometry to space missions,” in *Euroensors XXII*, (Dresden, Germany), September 2008. ISBN 978-3-00-025217-4.
- [4] L. Kowalski, J. Ricart, V. Jimenez, M. Domínguez-Pumar, and L. Castañer, “Sensitivity analysis of the chip for REMS wind sensor,” in *7th Spanish Conference on Electron Devices (CDE 2009)*, (Palma de Mallorca, Spain), pp. 289–292, February 2009.
- [5] L. Kowalski, “Contribution to advanced hot wire wind sensing,” in *1st Barcelona Forum on Ph.D. Research in Electronic Engineering*, pp. 7–8, Universitat Politècnica de Catalunya (UPC), Centre de Publicacions del Campus Nord SCCL (CPET), October 2009. ISBN978-84-7653-398-7.
- [6] L. Kowalski, J. Ricart, V. Jiménez, M. Domínguez, and L. Castañer, “Thermal modelling of the chip for the REMS wind sensor,” *International Journal of Numerical Modelling: Electronic Networks, Devices and Fields*, vol. 23, pp. 340–353, July - October 2009. Special Issue on the 7th Spanish Conference on Electron Devices (CDE2009).
- [7] L. Castañer, M. Domínguez, V. Jiménez, J. Ricart, and L. Kowalski, “Chip UPC para la medida del viento en Marte,” tech. rep., presented for 7th Premio Duran Farell de Investigación Tecnológica, Barcelona, Spain, June 2010.

BIBLIOGRAPHY

- [8] L. Kowalski, L. Castañer, M. Domínguez, and V. Jiménez, “Multi-physics simulation of REMS hot-film anemometer under typical Martian atmosphere conditions,” in *COMSOL Conferenece 2010*, (Paris, France), October 2010.
- [9] J. Gómez-Elvira, C. Armiens, L. Castañer, M. Domínguez-Pumar, M. Genzer, F. Gómez, R. Haberle, A.-M. Harri, V. Jiménez, H. Kahanpaa, L. Kowalski, A. Lepinette, J. Martín, J. Martínez-Frías, I. McEwan, L. Mora, J. Moreno, S. Navarro, M. de Pablo, V. Peinado, A. Peña, J. Polkko, M. Ramos, N. Renno, J. Ricart, M. Richardson, J. Rodríguez-Manfredi, J. Romeral, E. Sebastián, J. Serrano, M. dela Torre Juárez, J. Torres, F. Torrero, R. Urquí, L. Vázquez, T. Velasco, J. Verdasca, M.-P. Zorzano, and J. Martín-Torres, “REMS: The environmental sensor suite for the Mars Science Laboratory rover,” *Space Science Reviews*, vol. 170, pp. 583–640, July 2012.
- [10] L. Kowalski and M. Garcia, “Hypobaric chamber for wind sensor testing in Martian conditions,” in *8th Spanish Conference on Electron Devices (CDE 2011)*, (Santiago de Compostela, Spain), pp. 1–4, February 2011.
- [11] L. Kowalski, V. Jiménez, M. Domínguez-Pumar, S. Gorreta, S. Silvestre, and L. Castañer, “Low pressure spherical thermal anemometer for space missions,” in *IEEE SENSORS 2013*, (Baltimore, United States), pp. 1–4, November 2013.
- [12] S. Gorreta, E. Barajas, L. Kowalski, T. Atienza, M. Domínguez-Pumar, and V. Jiménez, “A self-calibrating closed loop circuit for configurable constant voltage thermal anemometers,” *Electronics Letters*, September 2015.
- [13] Wikipedia, “Earth Mars Moon celestia.” [Online], January 2010. http://commons.wikimedia.org/wiki/File:Earth_mars_moon_celestia.jpg.
- [14] M. D. Smith, “Spacecraft observations of the martian atmosphere,” *Annual Review of Earth and Planetary Sciences*, vol. 36, no. 1, pp. 191–219, 2008.
- [15] NASA, “First camera 1 panorama of Chryse Planitia on Mars.” [Online], February 2010. <http://nssdc.gsfc.nasa.gov/planetary/viking.html>.
- [16] NASA, “Mars Fact Sheet.” [Online], January 2010. <http://nssdc.gsfc.nasa.gov/planetary/factsheet/marsfact.html>.
- [17] NASA, “Earth Fact Sheet.” [Online], January 2010. <http://nssdc.gsfc.nasa.gov/planetary/factsheet/earthfact.html>.

- [18] Jet Propulsion Laboratory, “MSL science corner, REMS.” [Online], January 2010. <http://msl-scicorner.jpl.nasa.gov/Instruments/REMS/>.
- [19] L. H. R. Davey, T. Chamberlain, “Sensor design analysis report TRW report METC-021,” tech. rep., September 1973.
- [20] S. E. Larsen, H. E. Jrgensen, L. Landberg, and J. E. Tillman, “Aspects of the atmospheric surface layers on Mars and Earth,” *Boundary-Layer Meteorology*, vol. 105, pp. 451–470, Dec. 2002.
- [21] J. T. Schofield, J. R. Barnes, D. Crisp, R. M. Haberle, S. Larsen, J. A. Magalhes, J. R. Murphy, A. Seiff, and G. Wilson, “The Mars Pathfinder atmospheric structure investigation/meteorology (ASI/MET) experiment,” *Science*, vol. 278, no. 5344, pp. 1752–1758, 1997.
- [22] A. Seiff, J. E. Tillman, J. R. Murphy, J. T. Schofield, D. Crisp, J. R. Barnes, C. LaBaw, C. Mahoney, J. D. Mihalov, G. R. Wilson, and R. Haberle, “The atmosphere structure and meteorology instrument on the Mars Pathfinder Lander,” *Journal of Geophysical Research: Planets*, vol. 102, no. E2, pp. 4045–4056, 1997.
- [23] F. F. F. C. P. Lognonnè, *Planet Mars Story of Another World*. Praxis, 2008.
- [24] C. R. John Grotzinger, Ashwin Vasavada, *Mars Science Laboratory*. Springer-Verlag New York, 2013. ISBN: 978-1-4614-6338-2.
- [25] E. M. Marc Kaufman, *MARS UP CLOSE: Inside the Curiosity Mission*. August 2014.
- [26] NASA, “Solar System.” [Online], January 2010. <http://solarsystem.nasa.gov/planets/index.cfml>.
- [27] G. L. Vogt, *Landscapes of Mars: A Visual Tour*. Springer-Verlag New York, 2008.
- [28] I. The Gale Group, ed., *UXL Encyclopedia of Science*. Encyclopedia.com, 2002.
- [29] W. M. Haynes, *CRC Handbook of Chemistry and Physics, 93rd Edition*. CRC Press, 2012.
- [30] K. G. Herrmann Schlichting, *Boundary-Layer Theory*. Springer-Verlag Heidelberg New York, 2003.
- [31] The Engineering ToolBox, “Carbon dioxide.” [Online], February 2011. http://www.engineeringtoolbox.com/carbon-dioxide-d_1000.html.

BIBLIOGRAPHY

- [32] L. V. King, "On the convection of heat from small cylinders in a stream of fluid: Determination of the convection constants of small platinum wires, with applications to hot-wire anemometry," *Proceedings of the Royal Society of London A: Mathematical, Physical and Engineering Sciences*, vol. 90, no. 622, pp. 563–570, 1914.
- [33] M. Laghrouche, A. Adane, J. Boussey, S. Ameer, D. Meunier, and S. Tardu, "A miniature silicon hot wire sensor for automatic wind speed measurements," *Renewable Energy*, vol. 30, no. 12, pp. 1881 – 1896, 2005.
- [34] F. Mailly, A. Giani, R. Bonnot, P. Temple-Boyer, F. Pascal-Delanoy, A. Foucaran, and A. Boyer, "Anemometer with hot platinum thin film," *Sensors and Actuators A: Physical*, vol. 94, no. 12, pp. 32 – 38, 2001.
- [35] M. Loomans and A. v. Schijndel, "Simulation and measurement of the stationary and transient characteristics of the hot sphere anemometer," *Building and Environment*, vol. 37, no. 2, pp. 153 – 163, 2002.
- [36] Y. Sun and Y. Zhang, "An overview of room air motion measurement: Technology and application," *HVAC&R Research*, vol. 13, no. 6, pp. 929–950, 2007.
- [37] A. Van Putten and S. Middelhoek, "Integrated silicon anemometer," *Electronics Letters*, vol. 10, pp. 425–426, October 1974.
- [38] A. F. P. van Putten, M. J. A. M. van Putten, and M. H. P. M. van Putten, "Silicon thermal anemometry: developments and applications," *Measurement Science and Technology*, vol. 7, no. 10, p. 1360, 1996.
- [39] K. A. A. Makinwa, *Flow Sensing With Thermal Sigma-Delta Modulators*. PhD thesis, Delft University of Technology, 2004.
- [40] B. van Oudheusden, "Silicon thermal flow sensors," *Sensors and Actuators A: Physical*, vol. 30, no. 1, pp. 5 – 26, 1992.
- [41] B. W. V. Oudheusden, "Silicon thermal flow sensor with a two-dimensional direction sensitivity," *Measurement Science and Technology*, vol. 1, no. 7, p. 565, 1990.
- [42] J. Robadey, O. Paul, and H. Baltes, "Two-dimensional integrated gas flow sensors by CMOS IC technology," *Journal of Micromechanics and Microengineering*, vol. 5, no. 3, p. 243, 1995.
- [43] L. Kowalski, T. Atienza, S. Gorreta, V. Jiménez, M. Domínguez-Pumar, S. Silvestre, and L. Castañer, "Spherical wind sensor for the atmosphere of Mars." submitted to IEEE SENSORS JOURNAL, July 2015.

- [44] H. P. Gunnlaugsson, C. Holstein-Rathlou, J. P. Merrison, S. Knak Jensen, C. F. Lange, S. E. Larsen, M. B. Madsen, P. Nrnberg, H. Bechtold, E. Hald, J. J. Iversen, P. Lange, F. Lykkegaard, F. Rander, M. Lemmon, N. Renno, P. Taylor, and P. Smith, “Telltale wind indicator for the Mars Phoenix lander,” *Journal of Geophysical Research: Planets*, vol. 113, no. E3, pp. n/a–n/a, 2008. E00A04.
- [45] NASA, “Viking Mission to Mars.” [Online], February 2010. <http://nssdc.gsfc.nasa.gov/planetary/viking.html>.
- [46] T. E. Chamberlain, H. L. Cole, R. G. Dutton, G. C. Greene, and J. E. Tillman, “Atmospheric measurements on Mars - the Viking meteorology experiment,” *American Meteorological Society Bulletin*, vol. 57, pp. 1094–1104, Sept. 1976.
- [47] O. Kemppinen, J. E. Tillman, W. Schmidt, and A.-M. Harri, “New analysis software for Viking Lander meteorological data,” *Geoscientific Instrumentation, Methods and Data Systems*, vol. 2, no. 1, pp. 61–69, 2013.
- [48] S. L. Hess, R. M. Henry, C. B. Leovy, J. A. Ryan, and J. E. Tillman, “Meteorological results from the surface of Mars: Viking 1 and 2,” *Journal of Geophysical Research*, vol. 82, no. 28, pp. 4559–4574, 1977.
- [49] J. R. Murphy, C. B. Leovy, and J. E. Tillman, “Observations of Martian surface winds at the Viking Lander 1 Site,” *Journal of Geophysical Research: Solid Earth*, vol. 95, no. B9, pp. 14555–14576, 1990.
- [50] L. N. E. Jane Van Nimmen, Leonard C. Bruno, *NASA Historical Data Book, NASA Launch system, Space Transportation, Human Space and Space Science 1989-1999*, vol. VII. Library of Congress, 2009.
- [51] Mars Science Program Synthesis Group, “Mars Exploration Strategy 2009 - 2020,” tech. rep., NASA, 2003.
- [52] J. Gómez-Elvira and REMS Team, “Environmental monitoring instrument for Mars exploration,” in *Lunar and Planetary Institute Science Conference Abstracts*, vol. 39 of *Lunar and Planetary Inst. Technical Report*, pp. 1647–+, mar 2008.
- [53] NASA, “Next NASA Mars Mission Rescheduled for 2011.” [Online], April 2008. http://www.nasa.gov/mission_pages/mars/news/msl-20081204.html.
- [54] W. L. S. Rob Manning, *Mars Rover Curiosity: An Inside Account from Curiosity’s Chief Engineer*. Smithsonian Books, 2014.

BIBLIOGRAPHY

- [55] Jet Propulsion Laboratory, “Rover Environmental Monitoring Station (REMS).” [Online], January 2010. <http://mars.jpl.nasa.gov/msl/mission/instruments/enviro sensors/rem s/>.
- [56] J. G.-E. L. Vázquez, “The Rover Environmental Monitoring Station (REMS) of the Mars Science Laboratory (MSL,NASA/JPL 2009),” in *Second workshop on Mars atmosphere modelling and observations*, (Granada, Spain), p. 721, LMD, IAA, AOPP, CNES, ESA, 02 2006. held February 27 - March 3, 2006.
- [57] NASA, “REMS In-Situ instrumentation.” [Online], January 2010. <http://mars.nasa.gov/msl/mission/instruments/enviro sensors/>.
- [58] J. Gómez-Elvira, L. Castañer, A. Lepinette, J. Moreno, J. Polko, E. S. and J. Torres, M. P. Zorzano, and REMS Team, “REMS, an instrument for Mars Science Laboratory Rover,” *40th Lunar and Planetary Science Conference (2009)*, vol. 40, p. 1540, March 2009.
- [59] J. Gómez-Elvira and REMS Team, “Environmental monitoring station for Mars Science Laboratory,” *LPI Contributions*, vol. 1447, pp. 9052–+, November 2008.
- [60] A. Groenland, “Degradation processes of platinum thin films on a silicon nitride surface,” June 2006.
- [61] V. Jiménez, F. Masana, M. Domínguez, and L. Castañer, “Simulation of flow sensors for home appliances,” *Microelectronics Journal*, vol. 29, no. 45, pp. 283 – 289, 1998. Thermal Investigations of {ICs} and Microstructures {II}.
- [62] L. Castañer, V. Jiménez, M. Domínguez-Pumar, F. Masana, and A. Rodríguez, “A conduction-convection design for liquid flow sensing,” *Sensors and Actuators A: Physical*, vol. 66, no. 13, pp. 131 – 137, 1998.
- [63] M. Domínguez-Pumar, M, F. Masana, V. Jiménez, S. Bermejo, J. Amirola, J. Ballester, N. Fueyo, and L. Castañer, “Low-cost thermal Sigma-Delta air flow sensor,” *Sensors Journal, IEEE*, vol. 2, pp. 453–462, Oct 2002.
- [64] M. Domínguez, J. Ricart, A. Moreno, X. Contestí, and S. Garriga, “Low cost PCB thermal Sigma-Delta air flowmeter with improved thermal isolation,” *Sensors and Actuators A: Physical*, vol. 121, no. 2, pp. 388 – 394, 2005.
- [65] B. van Oudheusden, “Effect of operating conditions on the dynamic response of thermal sensors with and without analog feedback,” *Sensors and Actuators A: Physical*, vol. 58, no. 2, pp. 129 – 135, 1997.

- [66] Z. FISK and G. WEBB, “5 - electrical resistivity of metals,” in *Electronic Structure and Properties* (F. Y. FRADIN, ed.), vol. 21 of *Treatise on Materials Science & Technology*, pp. 297 – 349, Elsevier, 1981.
- [67] D. Dimitrov, A. Zahariev, J. Georgiev, G. Kolev, J. Petrinski, and T. Ivanov, “Thin film platinum resistance thermometers: calibration and mathematical description of $t(r)$ function,” *Cryogenics*, vol. 34, no. 6, pp. 487 – 489, 1994.
- [68] “Chapter 6 - thin films on silicon,” in *Handbook of Silicon Based {MEMS} Materials and Technologies (Second Edition)* (M. Tilli, T. Mootooka, V.-M. Airaksinen, S. Franssila, M. Paulasto-Krckel, and V. Lindroos, eds.), *Micro and Nano Technologies*, pp. 124 – 205, Boston: William Andrew Publishing, second edition ed., 2015.
- [69] J. Foerster and R. Wolffenbuttel, “High-temperature accurate thermal sensing using integrated platinum resistors on silicon,” in *Instrumentation and Measurement Technology Conference, 1995. IMTC/95. Proceedings. Integrating Intelligent Instrumentation and Control., IEEE*, pp. 538–, April 1995.
- [70] Y. A. Cengel, *Heat Transfer: A Practical Approach*. McGraw-Hill, November 2003.
- [71] J. Merrison, H. Bechtold, H. Gunnlaugsson, A. Jensen, K. Kinch, P. Nornberg, and K. Rasmussen, “An environmental simulation wind tunnel for studying aeolian transport on mars,” *Planetary and Space Science*, vol. 56, no. 34, pp. 426 – 437, 2008.
- [72] C. Wilson, A. Camilletti, S. Calcutt, and P. Ligrani, “A wind tunnel for the calibration of Mars wind sensors,” *Planetary and Space Science*, vol. 56, no. 11, pp. 1532 – 1541, 2008.
- [73] Centro de Astrobiología (CAB), “Linear wind tunnel.” [Online]. <https://cab.inta-csic.es/remes/facilities/linear-wind-tunnel/>.
- [74] J. Merrison, H. Gunnlaugsson, J. Jensen, K. Kinch, P. Nrnberg, and K. Rasmussen, “A miniature laser anemometer for measurement of wind speed and dust suspension on Mars,” *Planetary and Space Science*, vol. 52, no. 13, pp. 1177 – 1186, 2004.
- [75] B. M. A. C. Churchill SW, “Equation for forced convection from gases and liquids to a circular cylinder in crossflow,” *ASME. J. Heat Transfer.*, vol. 99, pp. 300–306, May 1977.
- [76] A. S. L. Theodore L. Bergman, Frank P. Incropera, *Fundamentals of Heat and Mass Transfer*. John Wiley & Sons, 2002.

BIBLIOGRAPHY

- [77] D. C. Collis and M. J. Williams, “Two-dimensional convection from heated wires at low Reynolds numbers,” *Journal of Fluid Mechanics*, vol. 6, pp. 357–384, 10 1959.
- [78] L. J. C. Baldwin L. V., Sandborn V. A., “Heat transfer from transverse and yawed cylinders in continuum, slip, and free molecule air flows.,” *ASME. Journal Heat Transfer.*, vol. 82, no. 2, pp. 77–86, 1960.
- [79] S. KASSAR, “Anemometria Marciana, anemometro termico,” Master’s thesis, Universitat Politècnica de Catalunya, Escola Tècnica Superior de Enginyeria de Telecomunicació de Barcelona, Department of Electronics, 2009.
- [80] J. P. Arroyo, “Dielectric characterization for hot film anemometry in METNET Mars mission,” Master’s thesis, Universitat Politècnica de Catalunya, Escola Tècnica Superior de Enginyeria de Telecomunicació de Barcelona, Department of Electronics, 2010.
- [81] M. Benzoni, “Wind sensor and electronic interface circuitry for space applications,” Master’s thesis, UNIVERSITÀ DEGLI STUDI DI BRESCIA FACOLTÀ DI INGEGNERIA, 2010.
- [82] Finnish Meteorological Institute (FMI), “MetNet.” [Online], April 2013. <http://metnet.fmi.fi>.
- [83] M. Díaz-Michelena, “Small magnetic sensors for space applications,” *Sensors*, vol. 9, no. 4, p. 2271, 2009.
- [84] L. V. M-P Zorzano and S. Jiménez., “Retrieval of ultraviolet spectral irradiance from filtered photodiode measurements,” *Inverse Problems*, vol. 25, p. 115023, November 2009.
- [85] F. Cortés, A. González, A. Llopis, A. J. de Castro, J. Meléndez, and F. López, “Optimization of the dust sensor in the Mars MetNet mission; extension to in situ CO₂ concentration and surface temperature measurements by infrared multispectral sensing,” *Proc. SPIE*, vol. 8550, pp. 855018–855018–15, 2012.
- [86] B. van Oudheusden and A. van Herwaarden, “High-sensitivity 2-d flow sensor with an etched thermal isolation structure,” *Sensors and Actuators A: Physical*, vol. 22, no. 1, pp. 425 – 430, 1990.
- [87] K. A. Makinwa and J. H. Huijsing, “A smart wind sensor using thermal sigma-delta modulation techniques,” *Sensors and Actuators A: Physical*, vol. 9798, pp. 15 – 20, 2002. Selected papers from Eurosenors {XV}.

- [88] A. S. Cubukcu, E. Zernickel, U. Buerklin, and G. A. Urban, "A 2d thermal flow sensor with sub-mw power consumption," *Sensors and Actuators A: Physical*, vol. 163, no. 2, pp. 449 – 456, 2010.
- [89] S. Sherif and R. Pletcher, "A normal sensor hot-wire/film probe method for the analysis of three-dimensional flows," *Flow Measurement and Instrumentation*, vol. 5, no. 3, pp. 150 – 154, 1994.
- [90] D. M. Riggin, E. Kudeki, and M. Sarango, "Tropospheric and stratospheric momentum flux measurements from radar wind data collected at Jicamarca," *Journal of Atmospheric and Solar-Terrestrial Physics*, vol. 66, no. 34, pp. 277 – 283, 2004.
- [91] Z.-G. Feng and E. E. Michaelides, "A numerical study on the transient heat transfer from a sphere at high Reynolds and Peclet numbers," *International Journal of Heat and Mass Transfer*, vol. 43, no. 2, pp. 219 – 229, 2000.
- [92] S. Dhole, R. Chhabra, and V. Eswaran, "A numerical study on the forced convection heat transfer from an isothermal and isoflux sphere in the steady symmetric flow regime," *International Journal of Heat and Mass Transfer*, vol. 49, no. 56, pp. 984 – 994, 2006.
- [93] S. Whitaker, "Forced convection heat transfer correlations for flow in pipes, past flat plates, single cylinders, single spheres, and for flow in packed beds and tube bundles," *AIChE Journal*, vol. 18, pp. 361 – 371, March 1972.
- [94] K. A. A. N. M. Sadikin, N. A. Mohd Yunus, "Numerical study of flow past a solid sphere at moderate Reynolds number," *Applied Mechanics and Materials*, vol. 660, pp. 674–678, October 2014.
- [95] R. T. W. Sabuga, "Effect of roughness on the emissivity of the precious metals silver, gold, palladium, platinum, rhodium, and iridium," *High Temperatures-High Pressures*, vol. 33(3), pp. 261–269, 2001.
- [96] A.-M. Harri, W. Schmidt, H. Guerrero, and L. Vázquez, "Future plans for MetNet lander Mars missions," in *EGU General Assembly Conference Abstracts*, vol. 14, p. 8224, 2012.

Appendix A

Metodo para la medida de la velocidad del aire y de su dirección en dos dimensiones para aplicaciones aeroespaciales

Spanish patent number P200700259. Presentation: 25.01.2007. Request form: 19.07.2010. Concession: 30.05.2011. Publication: 09.06.2011.

Manuel Domínguez-Pumar,
Lukasz Kowalski,
Vicente Jiménez Serres,
Alberto Moreno,
Luis Castañer Muñoz,
Jordi Ricart Campos.



**MINISTERIO
DE INDUSTRIA, ENERGÍA
Y TURISMO**



Oficina Española
de Patentes y Marcas



OFICINA ESPAÑOLA DE
PATENTES Y MARCAS

ESPAÑA



① Número de publicación: **2 342 953**

② Número de solicitud: 200700259

⑤ Int. Cl.:
G01F 1/69 (2006.01)

G01P 5/12 (2006.01)

G01W 1/17 (2006.01)

⑫

PATENTE DE INVENCION

B1

② Fecha de presentación: **25.01.2007**

④ Fecha de publicación de la solicitud: **19.07.2010**

Fecha de la concesión: **30.05.2011**

④ Fecha de anuncio de la concesión: **09.06.2011**

④ Fecha de publicación del folleto de la patente:
09.06.2011

⑦ Titular/es: **Universitat Politècnica de Catalunya
c/ Jordi Girona, 31
08034 Barcelona, ES**

⑦ Inventor/es: **Domínguez Pumar, Manuel;
Kowalski, Lukasz;
Jiménez Serres, Vicente;
Moreno, Alberto;
Castañer Muñoz, Luis y
Ricart Campos, Jordi**

⑦ Agente: **No consta**

⑤ Título: **Método para la medida de la velocidad del aire y de su dirección en dos dimensiones para aplicaciones aeroespaciales y de baja presión.**

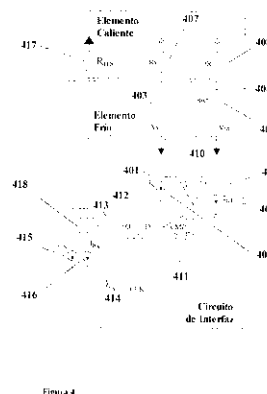
⑤ Resumen:

Método para la medida de la velocidad del aire y de su dirección en dos dimensiones para aplicaciones aeroespaciales y de baja presión.

Método para la medida de la velocidad y dirección del viento en dos dimensiones, basado en anemometría térmica, para trabajar en aplicaciones aeroespaciales en la superficie de otros planetas.

El método descrito utiliza dos invenciones para eliminar la dependencia de la medida con la temperatura del viento: utiliza de tres resistencias dependientes de la temperatura en el elemento caliente y una estructura matricial de elementos calientes con un único elemento de referencia. La estructura matricial tiene simetría de rotación lo que permite la obtención de la medida mediante combinaciones diferenciales de las señales de los elementos calientes.

El segundo problema es la precisión de la medida en atmósfera enrarecida como resultado del pequeño valor del camino libre medio de las moléculas. El método descrito reduce ese problema mediante el aislamiento térmico optimizado entre los elementos calientes entre sí, y entre éstos y el sustrato y el elemento de referencia.



ES 2 342 953 B1

Aviso: Se puede realizar consulta prevista por el art. 37.3.8 LP.

Venta de fascículos: Oficina Española de Patentes y Marcas, Pº de la Castellana, 75 – 28071 Madrid

ES 2 342 953 B1

DESCRIPCIÓN

Método para la medida de la velocidad del aire y de su dirección en dos dimensiones para aplicaciones aeroespaciales y de baja presión.

5 **Sector técnico**

Tecnología electrónica (sensores de viento), tecnología espacial, instrumentación de laboratorio.

10 **Estado de la técnica**

La medida de la velocidad del viento se viene haciendo tradicionalmente usando varios procedimientos, como por ejemplo cazoletas giratorias, diferencia de presión, propagación de ultrasonidos, desplazamiento iónico (Ion drift), efecto doppler usando láser (LDA) y siendo el mas popular el principio de anemometría térmica que es en el que se centra esta invención.

Los anemómetros convencionales utilizan un elemento que se calienta deliberadamente de forma que se establece una diferencia de temperatura entre él y el entorno que lo rodea. Se establece así un equilibrio térmico mediante conducción y convección térmicas. Cuando el aire o gas que rodea al sensor se mueve, la convección térmica aumenta y el elemento caliente se enfría reduciéndose la diferencia de temperatura entre el elemento caliente y su entorno. Esta reducción está relacionada con la velocidad del viento a través de los números de Reynolds y de Prandtl, existiendo numerosas correlaciones empíricas para ellos en función de la geometría del sensor propiamente dicho y la geometría de la interacción del sensor con el ambiente, que se encuentran recogidas en los libros de texto.

El elemento caliente debe estar en íntimo contacto con el fluido, la mayoría de invenciones anteriores a ésta aportan diferentes modificaciones de montaje del elemento caliente en el paso del flujo de gas (US 6,968,283), aire o líquido (US 6,971,274) para hacerlo sumergible. Las tecnologías avanzadas de microelectrónica y de micromecanizado también se han usado para obtener sensores anemométricos sobre soportes elevados (US 6,923,054).

El circuito mas utilizado hasta ahora para el anemómetro consiste en un puente resistivo de cuatro ramas, en una de las cuales se coloca una resistencia cuyo valor depende de la temperatura. Cuando el puente está en equilibrio, es decir cuando el valor de la resistencia del elemento sensor es igual que el valor de las otras tres resistencias, la potencia que se hace circular por elemento sensor es nula. Por el contrario cuando la velocidad del viento hace que se establezca una diferencia de temperatura en el elemento caliente respecto al ambiente, el puente se desequilibra y se aplica una potencia hasta que se restablece el equilibrio. Este procedimiento tradicional es un procedimiento analógico cuya precisión y sensibilidad depende del ruido de la medida y además es de respuesta lenta por tratarse de un método a potencia constante. Se conoce que una modificación del método consistente en utilizar una estrategia diferente basada en "diferencia de temperatura constante" es decir que se aplica la potencia necesaria hasta que se establece una cierta diferencia de temperatura es mas rápida que la estrategia anterior.

En el pasado se ha usado el método de anemometría térmica de forma muy extendida, incorporando modificaciones en el numero de amplificadores del circuito mas tradicionalmente usado (US 7,013,725), así como haciendo el resultado independiente del valor de la fuente de alimentación (US 7,072,776) o usando redundancia en la medida en combinación con una medida de diferencia de presión (US 6,945,123).

Los anemómetros convencionales se basan en un hilo fino de platino o tungsteno, colocado entre dos soportes que proporcionan adecuado contacto eléctrico. Asimismo se han usado en lugar de hilos finos, películas delgadas depositadas en un sustrato adecuado. La configuración clásica incluye al hilo o película delgada de platino o tungsteno en una de las ramas del puente de medida.

Estos anemómetros convencionales sufren de varios inconvenientes. El primero de ellos es que por tratarse de un principio de medida basado en el equilibrio térmico, el valor de la temperatura del fluido influye sobre el resultado de la medida de la velocidad del flujo. Si bien invenciones mas recientes han intentado reducir esta dependencia usando técnicas de separación de sensor y sustrato bien sea mediante micromecanizado de volumen, eliminando silicio, o bien sea mediante micromecanizado de superficie que al liberar las estructuras quedan separadas del sustrato, esta dependencia no ha sido suficientemente cancelada hasta el presente. Este hecho tiene que ver, en parte, con el uso de resistencias de calefacción realizadas mediante polisilicio o aleaciones de Níquel y Cromo cuyos coeficientes de temperatura son muy diferentes del coeficiente de temperatura del elemento sensor ya sea de platino o de tungsteno. La dependencia excesiva con la temperatura es un inconveniente más importante cuando se trata de aplicaciones aeroespaciales en las que los cambios de temperatura son muy grandes y muy rápidos, lo que puede inducir a grandes errores en la medida.

El segundo problema que tienen estos sensores convencionales para su utilización aeroespacial es su fragilidad, así como la posibilidad de desajuste en las fases de prueba, ensayo y lanzamiento.

Para la medida de la dirección del viento en un plano, los anemómetros convencionales han utilizado dos elementos calientes ortogonales entre si y un elemento que resuelve el cuadrante. Este principio ha sido utilizado por ejemplo en la medida de la dirección del viento en la superficie de Marte por la misión Viking. También se han utilizado elementos

ES 2 342 953 B1

calefactores y termopilas coplanares dispuestos en los cuatro lados de un cuadrado para medir el ángulo de ataque del viento a la estructura con el inconveniente del acoplo térmico por el propio sustrato y la pérdida de sensibilidad.

Resumen de la invención

5 La presente invención proporciona, entre otras cosas, un sensor de velocidad y dirección de viento en un plano, incluyendo cuatro elementos independientes, sin excluir un número distinto, denominados calientes, y dispuestos de manera que su perímetro total forma un cuadrado, sin excluir otras formas geométricas y un elemento de referencia denominado "frío". Cada elemento caliente incluye tres resistencias del mismo material resistivo sensible a la temperatura, depositadas por un método adecuado en el mismo sustrato. Una de cada tres resistencias de cada elemento caliente es una resistencia calefactora que permite subir la temperatura de todo el sustrato, la segunda resistencia es una resistencia sensora de temperatura y la tercera es una resistencia que permite al circuito adecuado establecer y fijar una diferencia de temperatura consigna entre el elemento caliente y el ambiente.

15 El sustrato puede ser de diferentes materiales, siempre que sean buenos conductores térmicos como el silicio sin excluir otros. El material con el que se forman las resistencias es el mismo para las tres de cada mismo elemento caliente y es un material cuya resistividad es una función de la temperatura como por ejemplo el platino sin excluir otros. Esta parte de la invención es la que permite cancelar la dependencia de la conductancia térmica de convección con la temperatura del medio.

20 El elemento de referencia o "frío" puede ser idéntico a los elementos calientes, aunque no necesariamente puesto que tanto la resistencia calefactora como la resistencia de consigna no son necesarias para su funcionamiento.

25 Los elementos calientes están adecuadamente aislados térmicamente y eléctricamente entre sí y respecto a una base que puede ser un PCB, sin excluir otro tipo de base, mediante soportes de la forma y sección adecuados para reducir el acoplo térmico por convección así como las pérdidas por conducción térmica. Esta reducción viene acompañada de una estrategia de medida consistente en la medida de diferencias, dos a dos, de las conductancias térmicas de los cuatro elementos calientes, con lo que se consigue eliminar la dependencia con la temperatura del medio producida por los acoplos térmicos de los elementos calientes al sustrato. Simultáneamente el hecho de que en un entorno aeroespacial en el que la densidad del medio es baja, la cancelación de términos de pérdidas térmicas comunes a los elementos calientes, permite mejorar la sensibilidad del sensor así como su precisión respecto a los anemómetros convencionales.

30 A diferencia de los anemómetros convencionales, el método descrito en esta invención incluye un circuito de adquisición de datos basado en un circuito realimentado sigma delta electrotérmico, con la ventaja de que la salida es digital directamente y que el rango de medida puede ser ajustado dentro del rango dinámico de la salida digital.

Descripción detallada de la invención

40 La presente invención proporciona entre otras cosas, un sensor de velocidad y dirección del viento en dos dimensiones incluyendo entre otras cosas, cuatro elementos, sin excluir un número diferente, que se calientan a una temperatura por encima del ambiente, incluyendo cada uno de ellos una primera resistencia calefactora, una sensora de temperatura formado por una segunda resistencia y una tercera resistencia para fijar la diferencia de temperatura consigna entre el elemento caliente y el ambiente. Cada elemento caliente esta formado por un sustrato buen conductor térmico preferentemente silicio sin excluir otros sustratos, en el que se han depositado y grabado con la tecnología y el procedimiento adecuados, la película de material resistivo conformando las tres resistencias. El material resistivo con el que se forman las tres resistencias es un material cuya resistividad es dependiente de la temperatura, como puede ser el platino o el tungsteno sin excluir otros materiales. Las resistencias de los elementos calientes están formadas del mismo material sensible a la temperatura, Las resistencias están aisladas eléctricamente del sustrato mediante un procedimiento adecuado y están en contacto térmico entre sí y con el sustrato. La invención incluye también un elemento denominado elemento de referencia o elemento frío de las mismas dimensiones que los otros elementos y que incluye un sensor de temperatura formado por una resistencia. El elemento de referencia puede ser, aunque no tiene porque ser necesariamente, idéntico a los elementos calientes para facilitar la fabricación, pero del elemento de referencia solamente se usa el sensor de temperatura.

55 Los elementos calientes y el elemento de referencia se colocan encima de un elemento de soporte, que puede ser un circuito impreso sin excluir otro tipo de soporte, de forma que los cinco elementos estén separados del soporte una distancia suficiente para que haya un mejor aislamiento térmico de los elementos calientes y del de referencia respecto al soporte. Para las aplicaciones aeroespaciales, en las que la densidad del ambiente es baja, el aislamiento térmico se ve favorecido por este hecho. La presente invención incluye un aislamiento térmico que se consigue mediante una estructura micromecanizada que proporciona una separación entre los elementos calientes y el soporte y además proporciona la sujeción necesaria usando un procedimiento adecuado que puede ser un adhesivo sin excluir otros procedimientos.

60 La presente invención incluye un circuito de conversión que, para cada uno de los elementos calientes, consiste en un puente formado por dos fuentes de corriente una en cada una de dos de las ramas, la resistencia sensora en la tercera rama y la resistencia consigna en serie con la resistencia del elemento de referencia en la cuarta rama. La salida del puente se conduce a un amplificador cuya salida se compara con una tensión de referencia y el resultado se envía a la entrada de dato de un biestable. La salida del biestable controla un interruptor que cambia el valor de la

ES 2 342 953 B1

- corriente que se hace circular por la resistencia calefactora. Este circuito de conversión tiene una parte que se denomina convertidor sigma -delta térmico y que esta compuesto por el comparador, el biestable y un filtro paso bajo que actúa en el dominio térmico debido a las constantes de tiempo térmicas. La resistencia del elemento de referencia es común a los circuitos de los elementos calientes. El resultado de la medida, para cada elemento caliente es el flujo de bits que sale del biestable, cuyo valor acumulado en una ventana temporal dividido por la diferencia de temperatura consigna entre el elemento caliente y el ambiente proporciona el valor de la conductancia térmica entre el elemento caliente y el ambiente. El resultado de la salida de los circuitos de los elementos calientes proporciona, el valor de las conductancias térmicas.
- 10 La invención incluye también la estrategia de proceso de los datos para la obtención de la magnitud y la dirección del viento y consiste en el cálculo de las diferencias de los valores de las conductancias térmicas de los elementos calientes dos a dos de manera que obtienen dos componentes ortogonales, sin excluir componentes en otras direcciones y de ellas se deducen los valores de la intensidad y dirección del viento.
- 15 En referencia a las figuras, Fig. 1 representa un esquema del elemento caliente en el que encima del sustrato 1 preferentemente de silicio sin excluir otros sustratos conductores térmicos, se deposita o crece por un procedimiento adecuado, un material aislante eléctricamente 2 preferentemente óxido de silicio mediante la oxidación térmica del silicio, sin excluir otros procedimientos de crecimiento o deposito. Encima del material aislante se deposita o crece un material, cuya resistividad es sensible a la temperatura preferentemente de platino sin excluir otros materiales, en forma de película delgada y posteriormente se graba o delinea siguiendo un procedimiento fotolitográfico, sin excluir otros procedimientos, de forma que quedan en la superficie del material aislante unas pistas en forma de U, sin excluir otras formas, de manera que quedan configuradas tres resistencias de valores distintos. 3 es la resistencia calefactora, 4 es la resistencia sensora y 5 es la resistencia consigna.
- 20
- 25 El espesor del sustrato es preferentemente el mismo grosor de la oblea de silicio, sin excluir otros espesores. La dimensión del elemento caliente es preferentemente un cuadrado del orden de un milímetro de lado sin excluir otras dimensiones mayores o menores para poder ajustar el valor de la máxima frecuencia de respuesta del sensor que es dependiente de la masa del elemento.
- 30 Las dimensiones de las resistencias son de unas centésimas a décimas de milímetro sin excluir otras dimensiones mayores o menores para poder ajustar el valor de las resistencias eléctrica a los valores mas adecuados para el sensor.
- La Fig 2 representa el elemento de referencia o elemento frío, que es básicamente de las mismas dimensiones y forma, así como esta fabricado usando el mismo procedimiento del elemento caliente. 1 es el sustrato preferentemente de silicio sin excluir otros sustratos conductores térmicos, se deposita o crece por un procedimiento adecuado, un material aislante eléctricamente 2 preferentemente óxido de silicio mediante la oxidación térmica del silicio, sin excluir otros procedimientos de crecimiento o deposito. Encima del material aislante se deposita o crece un material, cuya resistividad es sensible a la temperatura preferentemente de platino sin excluir otros materiales, en forma de película delgada y posteriormente se graba o delinea siguiendo un procedimiento fotolitográfico, sin excluir otros procedimientos, de forma que quedan en la superficie del material aislante unas pistas en forma de U, sin excluir otras formas, de manera que queda configurada la resistencia sensora 4.
- 35
- 40
- La Fig 3 representa la disposición de los elementos calientes 31, 32, 33 y 34 en el caso de ser cuatro y del elemento de referencia 35 cada uno de ellos encima del soporte 36 que los separa del soporte 37 una cierta distancia preferentemente del mismo orden de magnitud que el espesor del sustrato de silicio, sin excluir distancias mayores o menores para poder reducir las pérdidas por acoplo térmico con el sustrato.
- 45
- La Fig 4 es un diagrama esquemático del circuito utilizado por el sensor de viento. En la figura se muestra que el circuito de esta invención está formado, por un puente de cuatro ramas formado por la rama 401 en la que se conecta una fuente de corriente de valor I_x 405, una rama 402 en la que se conecta una fuente de corriente de valor I_{ref} 406, una rama 403 en la que se conecta la resistencia sensora R_x 407, una rama 404 en la que se conecta la resistencia consigna ΔR , 408 en serie con la resistencia del elemento de referencia Ref., 409. Entre los nodos comunes a las ramas 401 y 403 y a las ramas 402 y 404 se conectan los terminales de entrada de un amplificador 410 cuya salida se conecta a la entrada de un comparador 411. La salida del comparador 411 se conecta a la entrada de un biestable tipo D 412 a cuya salida 413 se conecta la salida del circuito 414 y por, otro lado se conecta el control de un interruptor SW 418 que conecta o desconecta una fuente de corriente I_{hx} 416 a la resistencia calefactora RHX 417. Finalmente la fuente de corriente I_{mx} 415 está siempre conectada a la resistencia calefactora 417 cerrándose de esta forma el lazo.
- 50
- 55
- La invención aquí descrita incluye un número de circuitos idéntico al de la Fig 4 uno por cada elemento caliente y por lo tanto suministra salidas digitales, cada una de ellas proporcional a la conductancia térmica entre cada elemento caliente y el ambiente. Esta conductancia térmica de convección es independiente de la temperatura por el hecho de que las tres resistencias de cada uno de los elementos calientes tienen el mismo coeficiente de temperatura al ser resistencias fabricadas con el mismo material, en efecto el cálculo del circuito de la Fig 4 da el siguiente resultado:
- 60
- 65

ES 2 342 953 B1

$$G_{TH} = \frac{\bar{P}}{\Delta T_0} = \frac{\alpha R_{REF0} \{I_{min}^2 + (I_{max}^2 - I_{min}^2) \lambda\} R_{RX0}}{\Delta R_0}$$

5

Donde GTH es el valor de la conductancia térmica definida como el valor medio de la potencia suministrada a la resistencia calefactora dividido por el valor de la diferencia de temperatura consigna entre el elemento caliente y el ambiente, α es el coeficiente de temperatura de la resistividad del material usado para fabricar las resistencias, R_{ref0} es el valor de la resistencia de referencia extrapolado a temperatura 0K, I_{min} es el valor I_{mx} de la figura 4 I_{max} es igual a $I_{mx} + I_{hx}$ de la figura 4 λ es el numero de "unos" de la salida del biestable en una ventana de tiempo dividido por el numero de ciclos de reloj de esa ventana temporal, R_{RX0} es el valor de la resistencia calefactora extrapolada a 0° y ΔR_0 es el valor de la resistencia consigna extrapolado a 0°.

15

Sin embargo el equilibrio térmico en el circuito se tiene que completar con las contribuciones debidas a la convección natural, a la convección forzada de los soportes y a la conducción térmica que se establece entre los elementos calientes y el resto de la estructura compuesta por el sustrato, los soportes aislantes y el resto de la estructura que da soporte al sensor. La presente invención incluye un método de cálculo de la velocidad y dirección del viento basado en el cálculo de diferencias de conductancias térmicas, según se describe en la Fig 5. En la Fig 5 se representan esquemáticamente un ejemplo con cuatro elementos calientes A, B, C, D. La invención descrita calcula las conductancias térmicas resultantes de la realización de dos operaciones algebraicas: (A+D)-(C+B) que da lugar a la variable Y, y (D+C)-(A+B) que da lugar a la variable X. La realización de estas operaciones algebraicas supone eliminar en gran medida todos aquellos términos de pérdidas de calor que sean iguales en los cuatro dados. Esto incluye prácticamente todas las pérdidas por conducción puesto que en todos los elementos calientes la diferencia de temperatura entre el elemento caliente y el soporte es la misma.

20

25

La intensidad del viento se calcula a partir de $\sqrt{X^2 + Y^2}$ y el ángulo de incidencia del viento se calcula a partir de $\tan^{-1}\left(\frac{Y}{X}\right)$, de esta forma se consigue cancelar en gran medida la dependencia de la medida con la temperatura del viento.

30

35

40

45

50

55

60

65

ES 2 342 953 B1

REIVINDICACIONES

1. Un sensor anemométrico de velocidad y dirección del viento que comprende:
- 5 Cuatro elementos iguales formados por un volumen de material conductor térmico recubierto de un material aislante eléctrico,
- Cada uno de los elementos antedichos comprendiendo tres resistencias situadas encima del material aislante
- 10 Una de las tres resistencias antedichas siendo una resistencia calefactora proporcionando calor al elemento
- Una de las tres resistencias antedichas siendo un sensor de temperatura
- 15 Una de las tres resistencias antedichas siendo una resistencia sensible a la temperatura.
- Cada una de las resistencias antedichas formadas del mismo material
- El material antedicho tiene su resistividad dependiente de la temperatura.
- 20 Un elemento de la misma forma y materiales que los elementos antedichos comprendiendo una resistencia del mismo material que las resistencias de los antedichos elementos
- La resistencia del quinto elemento antedicho siendo una resistencia sensora de la temperatura.
- 25 Los cinco elementos situados coplanarmente.
2. El sensor de viento de la reivindicación 1 donde cada uno de los cinco elementos antedichos, sin excluir un número diferente, se encuentran separados del soporte mediante unos elementos micromecanizados hechos de material aislante térmico que proporciona además soporte mecánico.
3. El sensor de viento de la reivindicación 1 donde los cuatro elementos iguales se encuentran a una distancia menor que la distancia que hay entre ellos y el quinto elemento.
- 35 4. El sensor de viento de la reivindicación 1 donde las conexiones eléctricas de las resistencias de los cinco elementos se realizan mediante la soldadura de hilos al sustrato.
5. El sensor de viento de la reivindicación 1 comprendiendo además un circuito idéntico para cada uno de los cuatro elementos antedichos incluyendo
- 40 a. Dos fuentes de corriente ubicadas en las dos primeras ramas de un puente de cuatro ramas
- b. Donde la resistencia sensora está conectada a la tercera rama del puente
- 45 c. Donde la resistencia consigna y la resistencia del quinto elemento están situadas en la cuarta rama del puente
- d. Dos fuentes de corriente suministrando potencia a las resistencias calefactoras
- 50 e. Un interruptor conmutando una de las dos fuentes de corriente que suministran potencia a las resistencias calefactores
- f. Un amplificador conectado a la salida del puente
- 55 g. Un comparador
- h. Un biestable.
- 60 6. El sensor de viento de la reivindicación 1 comprendiendo un método de cálculo de la intensidad y dirección del viento incluyendo
- a. El cálculo de dos magnitudes diferenciales de las cuatro salidas de los cuatro circuitos antedichos
- 65 b. Una de las dos magnitudes es la suma de las salidas de los dos elementos más cercanos a la entrada del viento con ángulo cero menos la suma de las salidas de los dos elementos más alejados de la entrada del viento

ES 2 342 953 B1

- c. La segunda de las magnitudes antedichas es la suma de las salidas de los dos elementos paralelos a la entrada del viento con ángulo cero y situados a la izquierda menos la suma de las salidas de los otros dos elementos
 - 5 d. La intensidad del viento se calcula mediante la raíz cuadrada de la suma de los cuadrados de las dos magnitudes antedichas
 - e. La dirección del viento se calcula mediante el cálculo del arcotangente del cociente de las dos magnitudes antedichas.
- 10
- 15
- 20
- 25
- 30
- 35
- 40
- 45
- 50
- 55
- 60
- 65

ES 2 342 953 B1

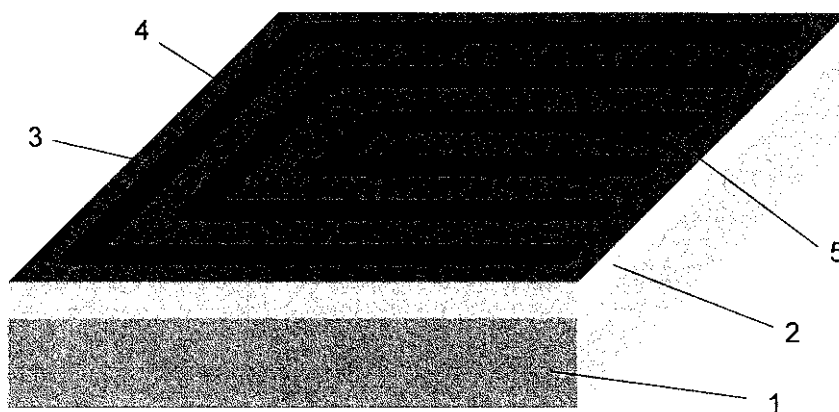


Figura 1

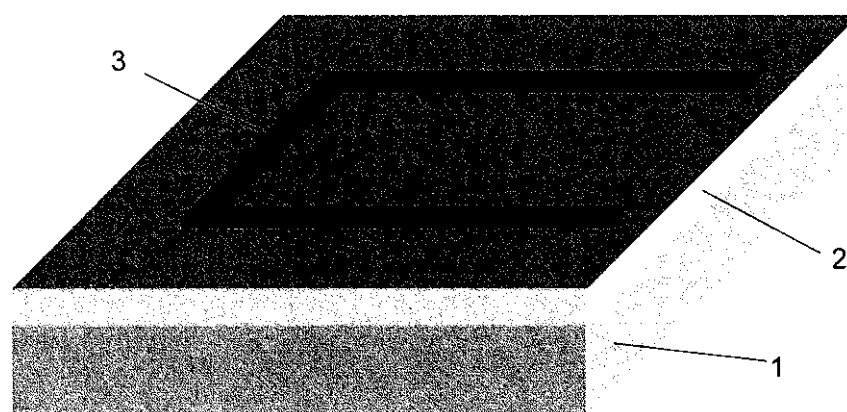


Figura 2

ES 2 342 953 B1

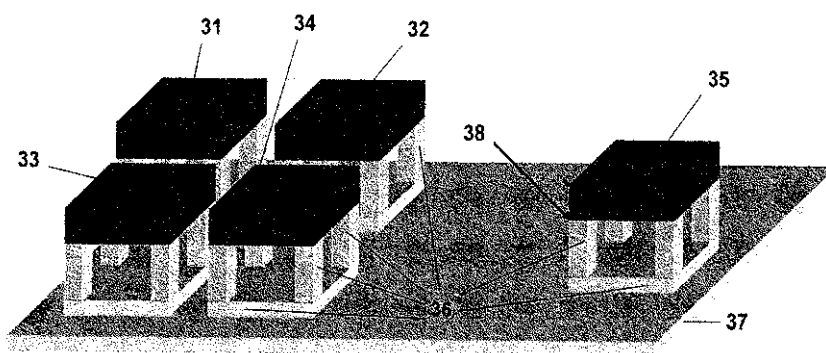


Figura 3

ES 2 342 953 B1

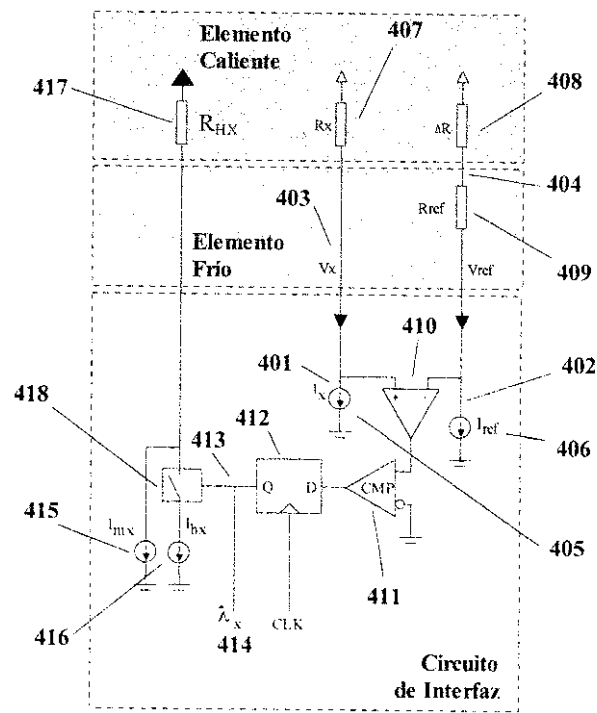


Figura 4

ES 2 342 953 B1

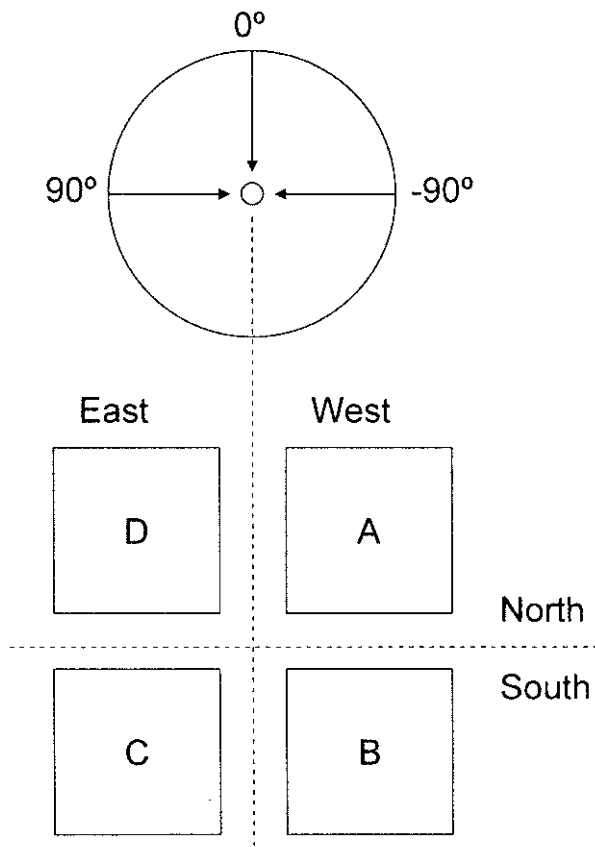


Figura 5

Appendix A



OFICINA ESPAÑOLA DE
PATENTES Y MARCAS
ESPAÑA

- ① ES 2 342 953
- ② N° de solicitud: 200700259
- ③ Fecha de presentación de la solicitud: 25.01.2007
- ④ Fecha de prioridad:

INFORME SOBRE EL ESTADO DE LA TÉCNICA

⑤ Int. Cl.: Ver hoja adicional

DOCUMENTOS RELEVANTES

Categoría	⑥ Documentos citados	Reivindicaciones afectadas
A	DOMINGUEZ M. et al. "Low cost PCB thermal sigma-delta air flowmeter with improved thermal isolation". Sensors and Actuators A: Physical, Vol. 121, pag. 388-394. 30-06-2005. Apartados 1 y 2.	1-6
A	MAKINWA K. et al. "A smart wind sensor using thermal sigma-delta modulation techniques". Sensors and actuators A: Physical, Vol. 97-98, pag. 15-20. 01-04-2002. Todo el documento.	1-6
A	VAN OUDHEUSDEN B. W. et al. "An electronic wind meter based on a silicon flow sensor". Sensors and actuators A: Physical, Vol. 22, Pag. 420-424. 01-06-1989. Apartado 2.	1-6

Categoría de los documentos citados

X: de particular relevancia
Y: de particular relevancia combinado con otro/s de la misma categoría
A: refleja el estado de la técnica

O: referido a divulgación no escrita
P: publicado entre la fecha de prioridad y la de presentación de la solicitud
E: documento anterior, pero publicado después de la fecha de presentación de la solicitud

El presente informe ha sido realizado

para todas las reivindicaciones para las reivindicaciones nº:

Fecha de realización del informe 05.07.2010	Examinador J. Cotillas Castellano	Página 1/2
---	---	---------------

INFORME DEL ESTADO DE LA TÉCNICA

Nº de solicitud: 200700259

CLASIFICACIÓN DEL OBJETO DE LA SOLICITUD

G01F 1/69 (2006.01)

G01P 5/12 (2006.01)

G01W 1/17 (2006.01)

Appendix B

A hot film anemometer for the Martian atmosphere

Journal Planetary and Space Science

February 2008, Volume 56, Pages 1169-1179, DOI:10.1016/j.pss.2008.02.013

Manuel Domínguez-Pumar,

Vicente Jiménez Serres,

Jordi Ricart Campos,

Lukasz Kowalski,

Josefina Torres,

Sara Navarro,

Julio Romeral,

Luis Castañer Muñoz.



ATTENTION !

Pages 186 to 198 of the thesis, containing the text, are available
at the editor's web

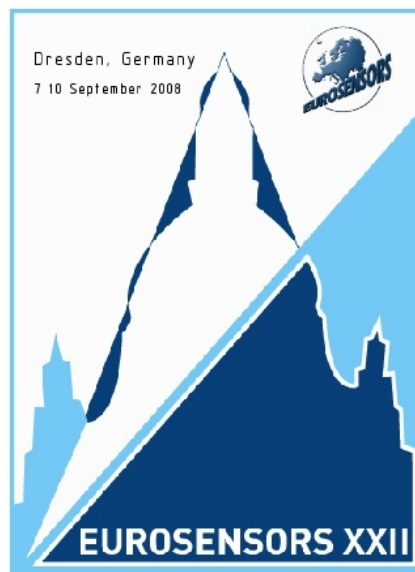
<http://www.sciencedirect.com/science/article/pii/S003206330800072X>

Appendix C

Applications of hot film anemometry to space missions

EUROSENSORS XXIII conference proceedings and opening plenary session
Dresden (Germany), 7-10 September 2008, ISBN 987-3-00-025217-4

Vicente Jiménez Serres,
Manuel Domínguez-Pumar,
Jordi Ricart Campos,
Lukasz Kowalski,
Sara Navarro,
Josefina Torres,
Julio Romeral,
Jonathan Merrison,
Luis Castañer Muñoz.



Appendix D

Sensitivity analysis of the chip for REMS wind sensor

Poster for the 7th Spanish Conference on Electron Devices,
Santiago de Compostela (Spain) 11-13 February 2009,
* Best Poster Award.

Lukasz Kowalski,
Jordi Ricart Campos,
Vicente Jiménez Serres,
Manuel Domínguez-Pumar,
Luis Castañer Muñoz.





7th Spanish Conference on Electron Devices
Santiago de Compostela, Spain. Feb 11-13, 2009



PREMIO AL MEJOR PÓSTER

BEST POSTER AWARD

Lukasz Kowalski

ha obtenido el premio al mejor póster presentado
como estudiante por el trabajo titulado

has won the award to the best student poster with the work entitled

Sensitivity analysis of the chip for REMS wind sensor

en la

in the

7^a Conferencia de Dispositivos Electrónicos

2009 Spanish Conference on Electron Devices

celebrada en el Museo do Pobo Galego,
held at the Museo do Pobo Galego,

Santiago de Compostela,
Santiago de Compostela,

los días 11, 12 y 13 de Febrero de 2009.

on February 11, 12 and 13, 2009.




Antonio García Loureiro

Coordinador del comité del CDE 2009
Chair of the CDE 2009 Committee




www.cde-conf.org - info@cde-conf.org





Sensitivity analysis of the chip for REMS wind sensor

L. Kowalski, J. Ricart, V. Jiménez, M. Domínguez*, L. Castañer*, * Member IEEE
 Universitat Politècnica de Catalunya (UPC), Jordi Girona 1-3, Barcelona 08034, Spain
 Micro and Nano Technologies research group (MNT)


Lukasz Kowalski
 (+34) 93 401-67-66
 Lukasz@eel.upc.edu



1. Introduction

Mars is the first neighbourhood planet with Earth. Even though its boundary layer differs from the Earth-like, Martian boundary layer is deeper, much more strongly forced and provoking dynamical processes with relatively significance of radiation and thermal fluxes. For full and comprehensive understanding of processes, which governing this important component of the Martian climate system, modeling and observation studies together with in-situ measurements in the lower boundary layer are necessary. Therefore in 2011 JPL launches MSL rover equipped with REMS wind sensor.

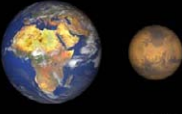
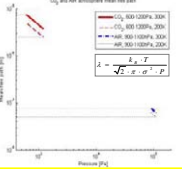


2. Martian climate

Mars and Earth interestingly have the same land surface. Beside this fact Mars volume size is about 7.5 hall times smaller than Earth. But what really makes both planets differs from each other are their atmosphere layer describing parameters (climate):

- Martian atmosphere is composed in: 95% of carbon dioxide, 2.7% of nitrogen, 1.5% of argon, only 0.13% of oxygen and other gasses.
- Ambient pressure on Mars is very rarefied, just 600Pa, that is about 180 times less than the one on our planet, typical 1013hPa.
- 87°C is the average temperature for the "Red Planet" and it is about 100°C colder than on Earth.

Very rarefied atmosphere condition provokes the mean free path of carbon dioxide molecules for Martian atmosphere to be around 100 times longer in comparison with Earth air free path.

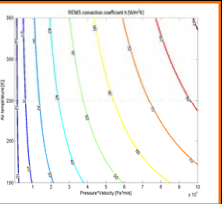
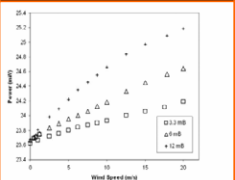
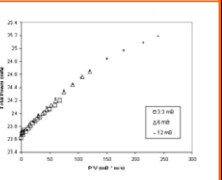
3. Pressure sensitiveness

Dimensionless analysis of how the heat is being exchange with the ambient by the forced convection process show the sensor sensitivity not only to the wind speed and overheat value but also gas pressure:

$$D_{eff} = \frac{D_{conv} - F_{rad} \sqrt{P} \sqrt{T}}{k} \sqrt{\frac{D_{cond}}{k}}$$

C_p - gas heat capacity
 k - thermal conductivity
 μ - absolute viscosity
 T - gas temperature

Experimental results agree with dimensional theory

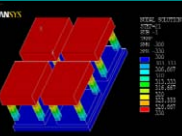
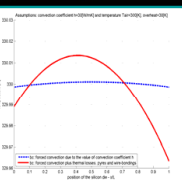
4. Temperature profile

REMS Wind sensor chip is made by silicon which has very high thermal conductivity value 150W/mK. Every die is fixed on pyrex pillars which isolates normally hotter dice from colder surface thanks to its low value thermal conductivity 1.1W/mK. Sigma-Delta closed loop circuits maintain typically working sensor temperature on 30 degrees above ambient temperature.

Supply of thermal heat is delivered to each unit die by the corresponding current, according to the Joule law, floating through Titanium-Platinum resistance path being printed on the surface of the each silicon die. Mathematical study on temperature distribution profile along the every silicon die lead as to equation:

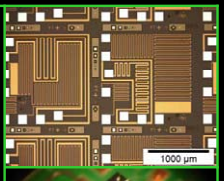



$$\frac{d^2 T}{dx^2} = \frac{h A_{conv} \Delta T}{k A_{cond} \Delta x} + \frac{I^2 dR}{k A_{cond} \Delta x}$$

From the Equation derives conclusion that: Temperature distribution along the silicon die is almost uniform and can be consider as it would be.

6. Conclusions

- Wind sensor is sensitive to the rarefied atmosphere pressure value.
- Wind sensor is sensitive to temperature changes of gas properties of Martian atmosphere.
- Silicon based die has the same temperature along unit element elevated above ambient temperature.
- Wind sensor response is sensitive for the wind speed.
- Heat distribution among array of four hot point element depends on wind angle.
- REMS wind sensor has potential and abilities for Martian flow measurements.

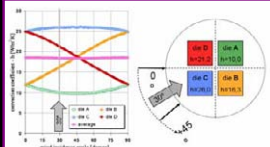
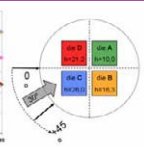
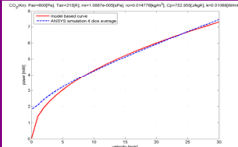
5. Incidence angle and wind velocity estimation

Finite element method simulation were performed for wind speed 10m/s and taking into account that all four hot points array has the same and uniformly distributed temperature. From the simulations and preliminary measurement is found that the average value of coefficient h doesn't change as the horizontal angle changes. The only variation that is noticed happens in reevaluation of h coefficients for hot dice, where these vary accordingly to the direction of the wind. This knowledge opens us a way to use various estimators for horizontal wind incidence angle recognition. For new differential terms:

$$NS = (h_A + h_B) - (h_C + h_D) \quad |N| = f(\Sigma h) \quad |N| = f(\sqrt{NS^2 + EW^2})$$

$$EW = (h_C + h_D) - (h_A + h_B) \quad \phi = f\left(\frac{NS}{EW}\right) \Rightarrow \arctan\left(\frac{NS}{EW}\right)$$

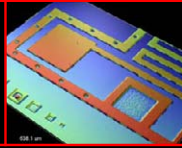
the possible solutions are:

1. REFERENCES

[1] M.Dominguez, V. Jiménez, J.Ricart, L.Kowalski, J. Torres, S. Navarro, J.Romeral and L.Castañer "A hot film anemometer for the Martian atmosphere" Planetary and Space Science, 56, pp. 1169-1179,2008

[2] V. Jiménez, M.Dominguez, J.Ricart, L. Kowalski, S.Navarro, J.Torres, J.Romeral, J.Merrison, L.Castañer, "Applications of hot film anemometry to space missions" Proceedings of Eurosensors XXII, Dresden 7-10 September 2008, pp.1-6

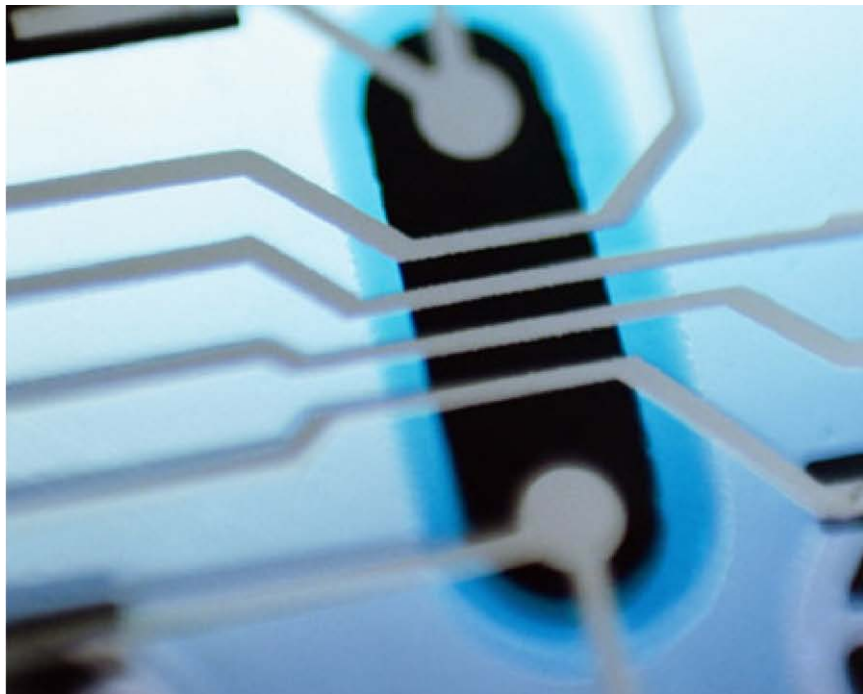


Appendix E

Contribution to advanced hot wire wind sensing

1st Barcelona Forum on Ph.D Research in Electronic Engineering,
Barcelona (Spain), 16 October 2009, ISBN 978-84-7653-398-7.

Ph.D Student: **Lukasz Kowalski**,
Thesis Advisor: Vicente Jiménez Serres.



Contribution to advanced hot wire wind sensing

Author: Lukasz Kowalski Thesis Advisor: Vicente Jiménez Serres

I. Introduction

According to the NASA Mars exploration strategy 2009-2020, issued by Mars Science Program synthesis group in April 2003 Jet Propulsion Laboratory is planning to launch in 2013 Mars Science Laboratory mission. MSL Rover will be equipped with state-of-art tools to look for potential bio-signatures on Mars but also to do acquire information about geology, environmental condition and atmosphere. The government of Spain, working with investigators at the Centro de Astrobiología (CAB) INTA-CSIC, is providing a Rover Environmental Monitoring Station (REMS), which contains among many other whether instruments a hot dice anemometer designed and developed by Technical University of Catalunya. The author role in the project was assist in development and proof that newly design sensor will be able to measure wind velocity and direction in harsh conditions characterizing 'Red Planet'.

II. Mars atmospheric conditions

In situ measurements of atmosphere fluxes on the surface of Mars are difficult because of three things: Mars is a cold planet (average temperature -63°C) with wide spam of diurnal temperature from -125°C to +25°C, has a very rarefied atmosphere of carbon dioxide with typical pressure of 6mBar to 8mBar, which is about 150 times less than on Earth, see Table 1. Both temperature and pressure reveals tendency to the fast changes especially when a storm or even a dust devil occurs.

MARS	parameter	EARTH
591	Solar constant [W/m ²]	1373
3.7	Gravity force [m/s ²]	9.8
CO ₂ =95.3 N ₂ =2.7,Ar=1.6 O ₂ =0.13	Atmosphere composition of planetary air [%]	N ₂ =78.0 O ₂ =21,Ar=0.9 H ₂ =0.01
6.8	Surface pressure [hPa]	1013
0.0015	Surface density [kg/m ³]	1.2
0.01	Kinematic viscosity [m ² /s]	150000
210 (-63°C)	Average temperature [K]	300 (+27°C)
-125 to +25	Temperature variation [°C]	-80 to +50

Table 1. Terrestrial and Martian climate comparison.

III. Wind sensor concept

The concept of wind sensor is based on hot point transducers, where the wind speed is worked out from the forced convection measurement of a hot element. The hot point is made by an array of four equally shaped square silicon dice overheated above ambient temperature respect to a fifth reference die standing alone and away in order to sense ambient temperature as is depicted on the Figure 1.

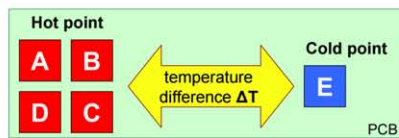


Figure 1. Wind transducer with cold and hot terminals.

The effect of the wind shadowing for the dice, which are on the rear of the complex structure and effective cooling for the dice, which are in the front of the wind blow, are the thermal domain phenomena that create differences in convective power accordingly to the dice position and wind parameters. For a single die, as shown in the Figure 2, convection power (P_{conv}) can be related with the air pressure (P_{air}), wind velocity (V_{air}) and also with the overheat between hot temperature (T_{hot}) and ambient air temperature (T_{air}), as follow:

$$P_{conv} = const \cdot \sqrt{P_{air} \cdot V_{air}} \cdot (T_{hot} - T_{air})$$

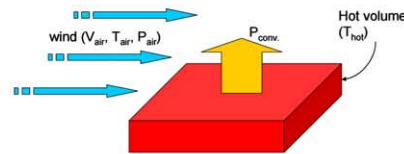


Figure 2. Hot anemometry principle diagram

Novel design of the sensor is precisely explained in [1].

IV. Sensor chip fabrication

The crucial part of the sensor is the silicon chip with printed-on titanium-platinum resistance paths. Silicon chip has a square shape 1,6mm long with a standard thickness of 0.4mm. On an oxidized silicon wafer a Titanium layer (10nm) is deposited previous to the Platinum in order to assure adherence to the SiO₂. Then deposition of Platinum material (70nm), which is linearly dependent of the temperature, is followed. In consequence of these processes every chip has three separated resistances: sensing (8000Ω), deltaR (800Ω), and heating (800Ω), where values of these resistances were measured in reference to the typical ambient temperature (300K), see Figure 3a.

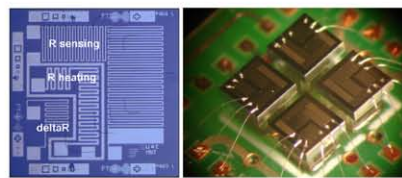


Figure 3. a) Chip mask b) assembled structure

After fabrication, similar chip characteristic have been carefully selected from the batch of dice and assembled in four size group. Then silicon units have been glued to previously shaped Pyrex supports and wire bonded with the external electrical circuits as at Figure 5b. The pyrex structure, which has a shape of inverted table, fulfills two important for the sensor roles: mechanically it supports the suspended silicon die and thermally it isolates the hot chip from the lower temperature surface reducing in the same time thermal losses to the substrate.

V. Operational circuit

In order to keep hot dice overheated a closed loop circuit with sigma-delta counter has been implemented. To control the whole process we have taken advantage of lineal characteristic of platinum material as function of temperature. The higher value resistances, have been used to monitor die temperature whereas specific current pulses were leaded trough other much thicker heating resistance in order to heat silicon die up to a preset temperature which depends on the third resistance, called deltaR. This shame is applied for each hot point die. Detailed diagram for die C shows Figure 4.

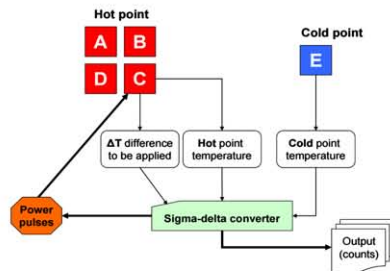


Figure 4. Wind transducer block diagram for die C.

Whenever one of the dice cools down from the expected temperature level sigma-delta converter sends extra power pulses, which are consequently counted (λ) and afterwards translated into the power delivered to each unit. Monitoring temperature condition of each silicon chip and knowing amount of power supplied to every die, the thermal conductances of each die are calculated from:

$$G_{TH} = \frac{\overline{Power}}{\Delta T} = \frac{P_{MIN} + (P_{MAX} - P_{MIN})\lambda}{(T_{hot} - T_{air})}$$

VI. Finite Element Method simulation

Detailed silicon ship analysis recently published in [3] shown uniform temperature distribution along the die unit. According to this fact series of FEM simulation has been performed. Sensor structure has been modeled as it is in original size (Figure 5a), then Martian-like air physical parameters were translated into ANSYS gas parameters used for thermal flow simulation (Figure 5b).

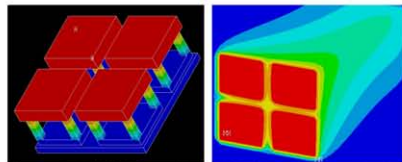


Figure 5. a) ANSYS model b) FEM simulation, 45° wind.

Simulation reveals that average thermal conductance of the group of four dice depends only on the wind velocity independently of the wind incidence angle of attack. Whereas the individual distribution of thermal conductance of each die strongly depends on wind direction. Simulation confirms that units situated in front of the wind head have bigger value of thermal

conductance in comparison to the ones allocated in the rear thermally shadowed from the cooling blow Figure 6.

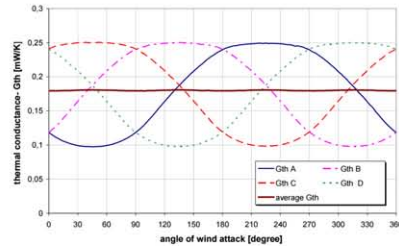


Figure 6. Thermal conductance of each die and average value for CO₂ wind: velocity 20m/s and pressure 600Pa.

VII. Measurements and tests

Vacuum chamber test shows good thermal isolation of chip from the base and at the same time exposes good sensor ability for coupling with rarified Martian atmosphere. One of the measurements in the Aarhus university Marslab wind tunnel [4] shows in agreement to the previous calculation that convection power of the sensor depends on a square of wind velocity (Figure 7).

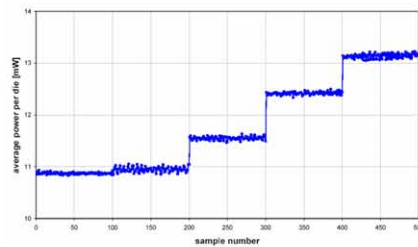


Figure 7. Average die power consumption response for different velocity flows: 0m/s, 0.3 m/s, 4 m/s, 11m/s, 20m/s.

Measurements also show better sensor performance to its predecessor Viking and Pathfinder missions units [2].

VIII. Acknowledgments

This work has been done with the support of the Commissioner for Universities and Research of the Department of Innovation, Universities and Company of the Generalitat de Catalunya and of the European Social Fund (scholarship 2006F100302).

IX. References

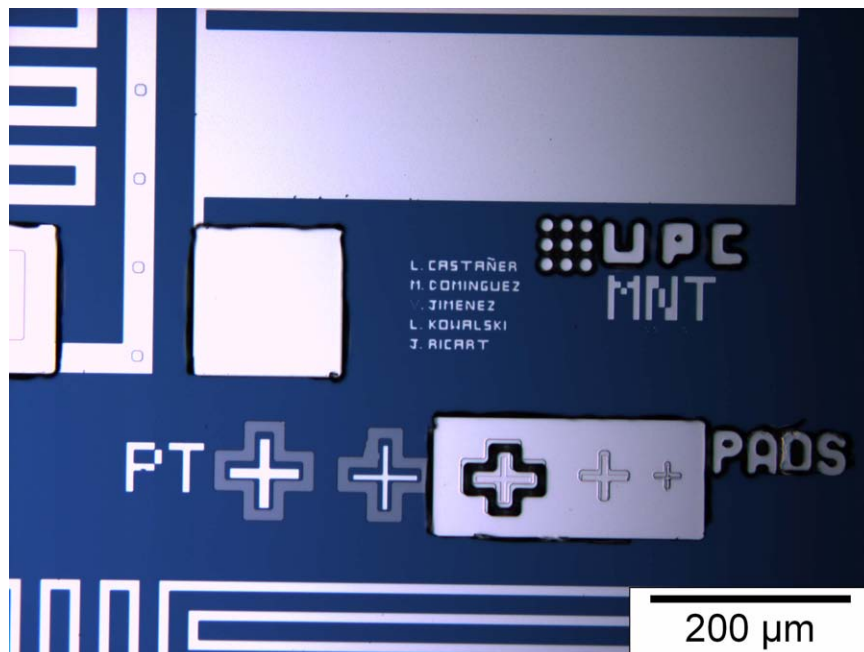
[1] Dominguez M, Jimenez V, Ricart J, Kowalski L, Torres J, Navarro S, Romeral J, Castañer L, "A hot Film anemometer for the Martian atmosphere" Planetary and Space Science, vol. 56, pp. 1169-1179, February 2008
 [2] Jimenez V, Dominguez M, Ricart J, Kowalski L, Navarro S, Torres J, Romeral J, Merrison J, Castañer L. "Applications of hot film anemometry to space missions" in Eurosensors XXII, September 2008, pp. 15-19
 [3] Kowalski L, Ricart J, Jiménez V, Domínguez M, Castañer L, "Sensitivity analysis of the chip for REMS wind sensor", in 7th Spanish Conference on Electron Devices, February 2009, pp. 189-190.
 [4] Marslab webpage: <http://www.marslab.dk>, September 2009.

Appendix F

Chip UPC para la medida del viento en Marte

Technical report submitted for *DURAN FARELL* award, edition 2010.

Luis Castañer Muñoz,
Manuel Domínguez-Pumar,
Vicente Jiménez Serres,
Jordi Ricart Campos,
Lukasz Kowalski.



Chip UPC para la medida del viento en Marte

L. Castañer, M. Domínguez, V. Jimenez, J. Ricart y L. Kowalski

Grupo de Micro y nanotecnología (MNT), Departament d'Enginyeria Electrónica, E.T.S.E. Telecomunicació
Universitat Politècnica de Catalunya, Barcelona, e-mail: castaner@eel.upc.edu

Abstract—Se presenta a la edici3n 2010 del Premi Duran Farell del Consell Social de la Universitat Politècnica de Catalunya el trabajo de investigaci3n desarrollado para la concepci3n diseño y fabricaci3n de un chip que es el componente crucial del sensor de viento para la estaci3n meteorol3gica REMS (<http://msl-scicorner.jpl.nasa.gov/Instruments/REMS/>) que equipa al rover de la misi3n MSL de la NASA MSL (<http://marsprogram.jpl.nasa.gov/msl/>) para la exploraci3n de Marte para 2013 (<http://news.bbc.co.uk/2/hi/science/nature/8509080.stm>)

REMS

I. OBJETIVOS PLANTEADOS

MARTE es el planeta mas cercano a la Tierra y se encuentra en otra fase de su evolucion. Se conoce que su atm3sfera es muy ligera, con presiones atmosféricas entre 500Pa y 1000 Pa, está compuesta en su mayor parte por anhídrido carbónico (95,3%) y concentraciones pequeñas de nitr3geno, arg3n, oxígeno y otros gases. Al estar mas alejado del Sol que la Tierra, su temperatura media es de -63°C oscilando entre 150K y 300K. Se conoce también que el campo magnético es débil y no protege a la superficie de la radiaci3n. La baja densidad de la atm3sfera hace que el camino libre medio de las moléculas sea mas de cien veces mas largo que en la superficie de la Tierra y ademas las fluctuaciones de calor locales pueden producir cambios de temperatura grandes en pocos segundos.

La investigaci3n del planeta Marte tiene un interés científico extraordinario para entender su evolucion, averiguar las propiedades de su campo magnético, de la dinámica atmosférica, los flujos de calor, la radiaci3n solar en el visible, infrarrojo y ultravioleta y eventualmente saber si en ese planeta se han dado actualmente o en el pasado condiciones para soportar vida, tal como se entiende en la Tierra. Desde 1960 en que se lanzó la misi3n Korabl 4 por la antigua USSR, hasta hoy se han lanzado 39 misiones a Marte, 22 de las cuales han sido declaradas fracaso. Ha habido cuatro landers con éxito: Viking (1975), Pathfinder (1997), Mars exploration Spirit and Opportunity (2003) y Phoenix (2008). Las misiones a Marte han experimentado recientemente un gran impulso, al haberse descubierto la presencia de hielo de agua en su superficie, lo que da pie a que las agencias espaciales se planteen la programaci3n de una misi3n tripulada. En ese contexto, el conocimiento de las condiciones de la atm3sfera del planeta tanto en elevaci3n como en superficie adquiere una gran relevancia. En particular, el viento es un gran desconocido todavía porque, a pesar de que se conoce la existencia de tormentas de polvo de dimensiones planetarias, existen muy pocas medidas de esta variable meteorol3gica, prácticamente

la mayoría enviadas por la misi3n Viking en 1976 y otras, mas limitadas, por la misi3n Pathfinder en 1997.

El Proyecto REMS nació cuando la NASA invitó a España a participar en el proyecto MSL (Mars Science Laboratory) aportando una estaci3n meteorol3gica para ubicarla en el mástil del rover que será desplegado en la superficie de Marte. Esta participaci3n tiene el nombre de REMS (Remote Environmental Monitoring Station) . REMS está liderado por el Centro de Astrobiología (CAB), centro mixto entre el CSIC y el INTA, siendo su investigador principal Javier Gómez Elvira, en el que participan EADS-CRISA, el Finnish Meteorological Institute y la Universitat Politècnica de Catalunya (UPC) e incorpora varios sensores: viento, infrarrojo, ultravioleta, presi3n, humedad, temperatura.

Como consecuencia de la experiencia del grupo investigador en el desarrollo de sensores de caudal de aire y agua , el primer Investigador principal del Proyecto REMS, Prof. Luis Vazquez de la UCM, ofreció la participaci3n en el desarrollo de un sensor de viento para REMS.

El objetivo concreto fue la medida de intensidad y direcci3n del viento en la superficie de Marte dentro de las limitaciones de tamaño, peso y consumo de potencia que impone la misi3n. En el proyecto REMS , la integraci3n de la estaci3n meteorol3gica la lidera EADS-CRISA y la fórmula de participaci3n del grupo investigador fue a través de un subcontrato de suministro de los chips que se describen mas abajo para los tres modelos contemplados: el modelo de ingeniería , el modelo de calificaci3n y el modelo de vuelo. Asimismo el trabajo asignado a la UPC consistió en el diseño conceptual y la validaci3n del front-end electrónico en la fase del modelo de ingeniería de manera que pudiera trasladarse a un circuito específico ASIC, responsabilidad de EADS-CRISA.

II. RESULTADOS OBTENIDOS

LA misi3n Viking fue la primera que midió la velocidad y direcci3n del viento en la superficie de Marte usando un anemómetro térmico basado en una película de platino y trabajando en modo de temperatura constante (CTA). Mas de 20 años después, en 1997 el rover de Pathfinder midió direcci3n del viento usando un anemómetro también térmico pero usando el modo de potencia constante (CPA) y también analizando las imágenes tomadas de unas mangas anemométricas tomadas por una cámara. La misi3n Beagle2 llevaba un anemómetro térmico también pero la misi3n fracasó. Finalmente la misi3n Phoenix utilizó una veleta miniatura para observar también el efecto del viento mediante una cámara. Existen otros métodos de medida, a parte del térmico, pero

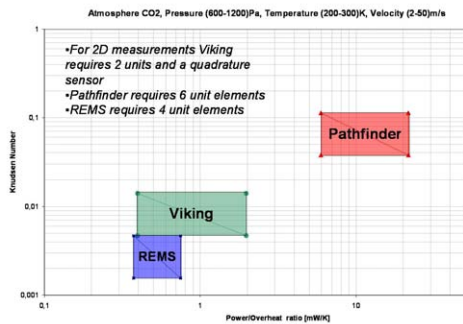


Fig. 1. Espacio de diseño del chip UPC comparado con Viking y Pathfinder. el eje vertical es el número de Knudsen y el horizontal es la figura de mérito Potencia/ sobretemperatura . Cuando mas abajo y a la izquierda, mejor son las condiciones de funcionamiento. Los datos de la Figura han sido extraídos de la publicación:

no son tan adecuados para las misiones espaciales , ya sea porque consumen mas potencia como los de ion-drift o ,porque necesitan de partículas en suspensión como los basados en láser.

La experiencia anterior nos dice que la medida de viento en la superficie de Marte no es un asunto trivial por la baja presión, gran rango de variación de temperatura y la presencia de polvo en ocasión de tormentas. La baja presión es un aspecto que condiciona el diseño del sensor porque el camino libre medio de las moléculas, que también depende de la temperatura, es grande. Por tanto, las dimensiones del dispositivo no pueden ser muy pequeñas en comparación con él para que exista interacción suficiente. Esto se mide mediante el conocido número de Knudsen que es precisamente el cociente entre el camino libre medio y la longitud característica del sensor. Este número, para que se pueda considerar la aproximación de medio continuo, debe ser inferior a 0.01 típicamente. Esto lleva a que la dimensión característica del sensor debe situarse por encima de un milímetro. Simultáneamente, un sensor que se basa en un principio térmico no puede hacerse excesivamente grande porque se precisará una potencia elevada para calentarlo superando los límites energéticos del instrumento. Otro punto muy importante en el diseño del sensor es que, debido a la poca interacción por la baja presión, las pérdidas de calor por conducción hacia los soportes son comparativamente altas y es preciso reducirlas al máximo. Reuniendo ambas restricciones , el grupo investigador ubicó el diseño del sensor del chip UPC en el proyecto REMS en una zona operativa mas favorable que los diseños anteriores de Viking y Pathfinder como se ve en la Figura 1.

El componente crucial en el sensor de viento es el 'chip UPC' que ha sido desarrollado y fabricado íntegramente en el Laboratorio 'Sala Blanca' del grupo de Micro y Nanotecnologías (MNT) del Departament d'Enginyeria Electronica, de la ETSETB de Barcelona de la Universitat Politècnica de

Catalunya.

En nuestro conocimiento, es el primer chip íntegramente diseñado y fabricado en España que equipa una misión científica para la superficie del planeta Marte. El chip UPC lleva grabado en su superficie los nombres de los miembros del equipo investigador y el logo del grupo de investigación.

A. Antecedentes

Este desarrollo se encuadra dentro de las actividades iniciadas por el grupo investigador en el año 1994 cuando, mediante financiación del Programa GAME (Grupo Activador de la Microelectrónica en España), desarrolló un sensor de flujo pensado para la medida de caudal de agua y de gas para el sector del electrodoméstico en colaboración con el Grupo Mondragón Corporación Cooperativa. El concepto desarrollado entonces se basó en el principio de anemometría térmica ampliamente usado hasta entonces para la medida de caudales en el sector aeroespacial, médico y meteorológico. Este principio, bien conocido, consiste en la medida indirecta de la velocidad de un fluido en movimiento a partir de la medida de las pérdidas por convección de un elemento caliente.

La experiencia acumulada en la aplicación al sector del electrodoméstico, permitió al grupo investigador integrarse en el Proyecto REMS en 2006.

El presente chip UPC supone un hito en los dispositivos de medida de viento en una atmósfera rarificada como es la del Planeta Marte. Aunque el principio de funcionamiento sigue siendo la anemometría térmica , este diseño es totalmente nuevo incorporando una serie de propiedades y características que lo hacen adecuado para la medida en condiciones de baja presión (6-12 mbar) y baja temperatura (200K-300K).

B. Descripción del diseño del chip UPC

El dispositivo se compone de un chip de silicio monocristalino de 1.6 mm de lado y 400 micras de espesor en cuya superficie se encuentran grabadas tres resistencias de película delgada de Titanio-Platino de tres valores nominales distintos. Una de éstas resistencias, cuando está excitada por una corriente eléctrica, se usa para calentar, por efecto Joule, el chip. Como consecuencia del elevado valor de la conductividad térmica del silicio, la temperatura es prácticamente homogénea en todo el volumen. La segunda resistencia de platino se utiliza para medir la temperatura y la tercera resistencia se utiliza en el circuito para introducir un desequilibrio controlado en el puente de medida diferencial que impone una diferencia de temperatura constante con el ambiente.

Una peculiaridad importante que se ha utilizado en este diseño consiste en que las tres resistencias son de una película de platino y por consiguiente son fabricadas simultáneamente. El platino sirve tanto como elemento calefactor en la primera resistencia como de elemento sensor en la segunda por que este material tiene una resistividad que depende de forma lineal con la temperatura en un amplio rango. En otros diseños se utiliza la misma resistencia para calentar y para medir , lo

que obliga a multiplexar la funci3n de la resistencia. La opci3n adoptada por el grupo investigador independiza los circuitos de se3al y de potencia y es viable al poder integrarse resistencias del orden del kilo-ohmio en superficies peque3as como las necesarias en este proyecto.

En la Figura 2 se ve una fotograf3a del chip en su superficie frontal donde se ven las tres resistencias y los PAD's de conexi3n al exterior. Asimismo, en la parte inferior derecha se ve el logo del grupo investigador MNT y los nombres de los cinco investigadores. Esta parte est3 ampliada en la Figura 3.

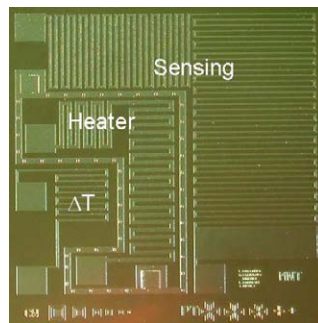


Fig. 2. Fotograf3a de la superficie del chip donde se ven las tres resistencias en forma de serpientes

C. Fabricaci3n

En la Figura 4 se ve una secci3n transversal del chip en donde se ve que sobre un sustrato de silicio se realiza una

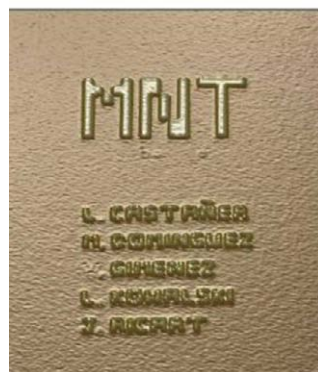


Fig. 3. Ampliaci3n de la fotograf3a de la superficie del chip donde se ven los nombres del equipo investigador

oxidaci3n t3rmica para crecer un 3xido electricamente aislante de unos 200nm de espesor sobre el que se deposita una resina fotosensible que se graba con los dibujos correspondientes a la m3scara de las resistencias y se revela. A continuaci3n se deposita una pel3cula muy fina de titanio cuya misi3n es proporcionar adherencia a la pel3cula de platino que se deposita a continuaci3n. Se procede a disolver la resina de forma que las resistencias quedan grabadas mediante la t3cnica de lift-off. El 3ltimo paso consiste en soldar los terminales el3ctricos. Se han fabricado un total de 1000 de estos dispositivos y

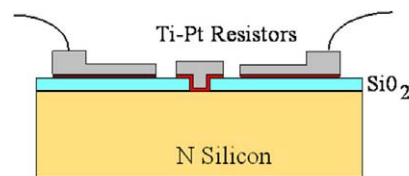


Fig. 4. Esquema de la secci3n transversal

sus caracter3sticas (valor de las tres resistencias) han sido individualmente medidos para proceder al apareamiento de los chips con caracter3sticas mas parecidas. El laboratorio donde se han fabricado se conoce con el nombre de 'Sala Blanca' porque fue la primera que se construy3 en la Universitat Polit3cnica de Catalunya antes de la existencia del Campus Nord. En ese Laboratorio se reunen un conjunto de equipos de fabricaci3n de muestras incluyendo equipos de difusi3n y oxidaci3n t3rmica, fotolitograf3a 3ptica, deposito de materiales por sputtering, plasma y evaporaci3n t3rmica.

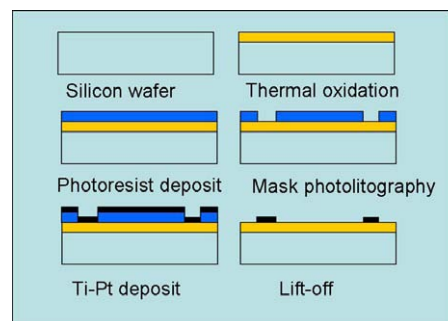


Fig. 5. Esquema de los pasos tecnol3gicos de fabricaci3n

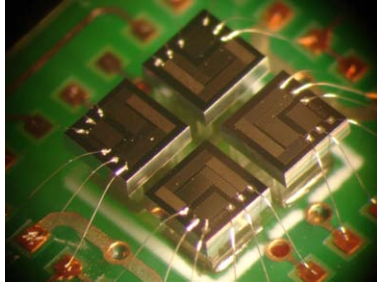


Fig. 6. Disposición coplanar de los cuatro dados

D. El concepto sensor en 2D

El grupo investigador concibió el método y la disposición de este chip para poder realizar una medida de magnitud y dirección del viento en dos dimensiones. En efecto, un chip como el descrito, si estuviera suspendido en el aire, tendría sensibilidad al viento poco directiva porque la convección se produciría aproximadamente igual en todas las direcciones en el mismo plano. Para dotarle de sensibilidad direccional en dos dimensiones es preciso componer un conjunto de al menos tres chips coplanares y en nuestro caso hemos optado por cuatro chips por las ventajas adicionales que presenta desde el punto de vista de la manipulación de las señales detectadas. En efecto, los chips más próximos a la entrada del viento dispararán más potencia que los que están detrás de ellos; de esta forma se dota de sensibilidad 2D al conjunto. Simulaciones desarrolladas usando métodos de elementos finitos corroboraron esta idea y permitieron obtener los datos fundamentales de diseño. En la Figura 6 se aprecia la disposición coplanar de los cuatro chips.

En este diseño hay dos magnitudes que pueden afectar la medida: temperatura del viento y presión atmosférica. Una de las consideraciones más importantes se refiere a cómo conseguir que este anemómetro sea poco dependiente de la temperatura del viento. Al tratarse de un anemómetro térmico, la temperatura ambiente modifica la convección. La forma en que los dispositivos de Viking y Pathfinder abordaron este problema consiste en utilizar una temperatura de los elementos calientes muy superior al ambiente, lo cual repercutiría en el consumo de potencia del sensor más allá de lo tolerable en este diseño para REMS. En nuestro caso el algoritmo de funcionamiento está diseñado de forma que la variable consigna es la diferencia de temperatura entre el elemento caliente y una referencia que consiste en otro dado igual que los demás pero que no se calienta. De esta forma el conjunto de medida en 2D está compuesto por cinco chips iguales, cuatro activos y uno de referencia situado lo más lejos posible de los activos. Similarmente la presión atmosférica varía entre 6 y 10 mbar típicamente. Este cambio de presión modifica la convección al cambiar la densidad del aire. Un análisis detallado de las ecuaciones que regulan la conductividad térmica del punto caliente al aire revela que en realidad la

potencia de convección depende del producto de la presión por la velocidad del aire, de manera que una medida independiente de la presión atmosférica resuelve el problema. Este hecho ha sido también verificado experimentalmente.

E. El circuito de medida

El grupo investigador desarrolló un circuito de medida basado en el circuito de la Figura 7. Es un circuito en puente excitado por dos fuentes de corriente, una para el circuito de referencia y otra para el circuito de medida. El desequilibrio del puente hace conmutar entre dos valores la corriente que circulará por la resistencia calefactora. La señal de salida es directamente el bit-stream de salida del biestable. Esta arquitectura es la de un modulador sigma-delta en el que el filtrado paso-bajo se realiza en el dominio térmico.

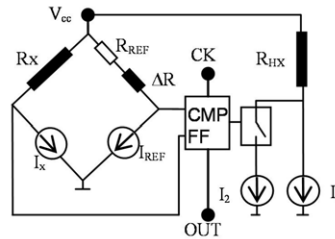


Fig. 7. Esquema del circuito de medida

F. Ensayos y validaciones

Este proyecto ha comprendido muchas fases, y el trabajo del grupo investigador se ha centrado en las fases de diseño construcción y suministro de los chips así como la concepción del circuito de medida y su validación utilizando electrónica discreta antes de dar soporte a las especificaciones de un ASIC que se fabricó posteriormente por EADS-CRISA. Estas validaciones han consistido en varias campañas de medias en el MarsLab de la Universidad de Aarhus en Dinamarca y en la Universidad de Oxford. En estas campañas también participaron miembros de EADS-CRISA, del CAB y de JPL. Las medidas han permitido demostrar una sensibilidad mejor que 0.3m/s en amplitud del viento y mejor que 20° en dirección. Se ha podido comprobar que la sensibilidad a la temperatura del aire es reducida y que mediante la medida de presión ambiente se puede derivar la lectura de velocidad del viento corregido con el valor instantáneo de la presión.

III. RELEVANCIA Y APORTACIONES

Este proyecto presenta varios aspectos relevantes. Desde el punto de vista científico las aportaciones y su relevancia son las siguientes::

- Contribuye al estado del arte de los sensores en ambiente de baja presión y baja temperatura adaptando su tamaño

- y consumo de potencia a los requisitos de ésta y otras misiones espaciales.
- Modifica el concepto habitual de 'hilo caliente' e incluso de 'película fina caliente' dando paso al concepto de volumen isotérmico, nunca usado con anterioridad en el espacio.
- Aplica el método de conversión digital de modulación sigma-delta a un sistema trabajando simultáneamente en el dominio térmico y en el dominio eléctrico. También aplicado por primera vez en este tipo de misiones.
- El concepto de un algoritmo que trabaje en modo de diferencia de temperatura constante (CTDA), es también nuevo y mejora la respuesta estacionaria y dinámica de los modos CTA y CPA anteriormente usados.
- El concepto de sensor bidimensional, basado en cuatro chips colocados en el mismo plano y el algoritmo diferencial de lectura de las componentes longitudinales y transversales, es original de este proyecto y tiene la relevancia de poder cancelar errores comunes en las lecturas individuales y dar sensibilidad angular dentro de las especificaciones. Es un concepto nuevo que no ha sido usado antes.
- El mercado espacial es muy competitivo y la presencia española en el mismo puede verse incrementada.
- Estos proyectos ofrecen a los que trabajan en ellos, un trabajo de calidad, desafiante intelectual y técnicamente.

IV. CONTINUIDAD DEL TRABAJO

Como consecuencia de este desarrollo, el grupo investigador está desarrollando las etapas preliminares de un nuevo sensor de viento para la superficie de Marte también pero esta vez en la misión MetNet (<http://europlanet.fmi.fi/MetNet/index.php>, <http://metnet.fmi.fi/index.php>) y en la parte española correspondiente que es el proyecto MEIGA (www.fdi.ucm.es/profesor/vazquez/meiga/meigaMetNet.html). La misión MEIGA (Mars Environmental Instrumentation for Ground and Atmosphere) es un proyecto del Ministerio de Ciencia e Innovación (AYA2008-06420-C04-01/ESP). La misión forma parte del proyecto MetNet (Meteorological Network) en el que participan personal científico y técnico de Finlandia (Finnish Meteorological Institute (FMI)), que lidera el proyecto, de Rusia (Lavochkin Association (LA) y Russian Space Research Institute (IKI)) y de España (Instituto Nacional de Técnica Aeroespacial (INTA)). El director científico del proyecto es el profesor Luis Vázquez de la Universidad Complutense de Madrid. El objetivo consiste en desplegar 16 estaciones meteorológicas fijas en distintos puntos del planeta que enviarían sus datos a una nave en órbita. El nuevo sensor de viento equiparía a las 16 estaciones. Con anterioridad se lanzará una misión precursora que no llevará sensor de viento pero sí de radiación solar en su lugar.

Desde el punto de vista técnico las aportaciones y su relevancia son las siguientes:

- Primer chip totalmente diseñado y fabricado en España que equipa una misión espacial a Marte.
- Fabricación de mas de 1000 chips y apareamiento de sus características. Es un logro en un medio universitario.
- Sensibilidad de lectura de velocidad de viento de 0.3 m/s
- Rango de lectura de 1m/s a 70 m/s, superior a los rangos de medida de Viking y de Pathfinder
- Sensibilidad de dirección 10° y discriminación de cuadrante. Por ejemplo la misión Viking precisó un sensor adicional de detección de cuadrante.
- Consumo de potencia por chip de 1mW/K muy por debajo de los de Viking y Pathfinder.

Desde el punto de vista económico y social las aportaciones y su relevancia son las siguientes:

- Las misiones espaciales tienen un gran atractivo social, las personas perciben estos proyectos como algo complejo, espectacular que precisa de un conocimiento técnico y científico sofisticado y que muchas veces permite a la humanidad entender mejor el universo. Si bien este proyecto es una parte minúscula del esfuerzo en la exploración espacial, nuestra sociedad lo acaba percibiendo como algo mas cercano (como cuando hay un astronauta español por ejemplo), y que podemos contribuir mas y mejor.
- Este proyecto contribuye a estimular el interés por la ciencia y la tecnología en los mas jóvenes que están en fase de descubrir su vocación y objetivos profesionales.
- Ha tenido una amplia repercusión mediática como consecuencia de los puntos anteriores y porque, además, el chip lleva grabados los nombres de sus inventores que serán, quizá, los primeros nombres de españoles (y de un polaco que forma parte del equipo) que se posarán en Marte.

Es de destacar que este tipo de instrumentos de vuelo han sido frecuentemente desarrollados en laboratorios universitarios: el sensor de viento para Viking fue desarrollado en la Universidad de Washington, el sensor de viento para Beagle2 en la Universidad de Oxford (UK) y el sensor de presión y humedad para REMS y MetNet en el Finnish Meteorological Institute. Esto es posible porque se precisan pocas unidades en general, pero calibradas y verificadas individualmente, con lo que la producción en serie queda descartada. Esto da una ventaja competitiva importante para los grupos que tienen ya experiencia en dispositivos de vuelo en su trayectoria. En el caso del grupo investigador los laboratorios disponibles son flexibles y permiten adaptarse mejor a este tipo de proyectos que un centro de mayor tamaño actuando como centro de servicios.

La visibilidad que ha dado el proyecto REMS también ha dado frutos en otro sensor espacial, concretamente un sensor de posición del sol de alta precisión cuyo desarrollo ha liderado la Universidad de Sevilla y el chip que lleva ha sido fabricado también por el grupo investigador de la UPC. Este sensor equipa el Nanosat 1B del INTA y ha sido lanzado recientemente.

V. PROCEDENCIA DE LOS FONDOS DE FINANCIACIÓN

El proyecto REMS ha sido financiado por el Ministerio de Ciencia e Innovación a través del CDTI, el Plan Nacional de I+D+i y el Ministerio de Defensa a través del Instituto

Nacional de Técnica Aeroespacial. La parte correspondiente al grupo investigador ha procedido del INTA y de un subcontrato entre EADS-CRISA y la UPC.

Además el miembro del equipo investigador Lukasz Kowalski ha sido becado por el Comissionat per a Universitats i Recerca del Departament d'Innovació, Universitats i Empresa de la Generalitat de Catalunya i del Fons Social Europeu, 2006FI00302. .

VI. LISTA DE PUBLICACIONES RELACIONADAS CON LA INVESTIGACIÓN

- M.Dominguez, V.Jimenez, J.Ricart, L.Kowalski, J.Torres, S.Navarro, J.Romeral and L.Castañer ‘ A hot film anemometer for the Martian atmosphere’ **Planetary and Space Science** vol. 56, pp. 1169-1179 (2008) doi:10.1016/j.pss.2008.02.013
- L.Kowalski J.Ricart, V. Jimenez, M.Dominguez and L.Castañer ‘ Thermal modelling of the chip for the REMS wind sensor’ **International Journal of Numerical Modelling** (2009) DOI: 10.1002/jnm.738
- V. Jimenez, M. Dominguez, J. Ricart, L. Kowalski, S.Navarro, J.Torres, J.Romeral, J.Merrison, L.Castañer, ‘ Applications of hot film anemometry to space missions’ **Proceedings of Eurosensors XXII** . Dresden 7-10 September 2008 . pp.1-6, ISBN 978-3-00-025218-1 (Conferencia invitada plenaria L.Castañer)
- L. Kowalski, J. Ricart, V. Jiménez, M. Domínguez, L. Castañer.’ Sensitivity analysis of the chip for REMS wind sensor, Proceedings Spanish Conference on Electron Devices, 2009. (CDE 2009), Santiago de Compostela (Spain) Awards: Best poster presentation primer premio
- Lukasz Kowalski ‘Contribution to advanced hot wire wind sensing’ 1st Barcelona Forum on Ph.D. research in Electronic Engineering, Barcelona(Spain) , October, 2009 ISBN:978-84-7653-398-7

1de Marzo de 2010

AGRADECIMIENTOS

Los autores agradecen al Prof. Luis Vazquez de la UCM por haber involucrado al grupo en el proyecto REMS y por los innumerables apoyos que ha dado a este desarrollo, al Dr. Javier Gómez Elvira del CAB, que es actualmente el IP del proyecto REMS, por el apoyo y confianza que nos ha dado. Agradecemos también la colaboración y participación del grupo del CAB: Josefina Torres, Sara Navarro, Julio Romeral . Nuestro sincero agradecimiento a Jaime Serrano líder del proyecto en EADS-CASA por la intensa colaboración y estímulo. Agradecemos también a Jon Merrison por las facilidades que ha proporcionado para la realización de medidas en Aarhus y a Manuel de la Torre de JPL por su asistencia continua e infatigable. Finalmente el grupo agradece al personal de la sala blanca, Miguel García, Xavier Fermín por su asistencia y al Prof. Ramon Alcubilla , responsable del laboratorio. Este trabajo ha sido posible gracias a la financiación procedente de los fondos mencionados mas arriba.

VII. NOTICIAS DE PRENSA

Aqui reproducimos algunas de las noticias que han salido en la prensa

Un ingeniero gallego presumirá de aterrizaje en Marte en 2010

Manuel Domínguez participa, dentro del equipo de Luis Castañer en la Politecnica de Cataluña, en el diseño del sensor meteorológico integrado en la misión Mars Science Laboratory de la NASA. El minichip que viajará hasta el Planeta Rojo lleva el grabado los nombres de sus creadores

Los pioneros en el espacio

El lanzamiento del minichip para la misión Mars Science Laboratory de la NASA se realizará el próximo 25 de noviembre desde el Centro de Lanzamiento de Cabo Cañaveral, en Florida. El minichip que viajará hasta el Planeta Rojo llevará grabado los nombres de sus creadores: Manuel Domínguez, V. Jiménez, J. Ricart, L. Kowalski, J. Torres, J. Romeral, J. Merrison y L. Castañer.

Un ingeniero gallego presumirá de aterrizaje en Marte en 2010

Manuel Domínguez, ingeniero de la UPC, participará en el diseño del sensor meteorológico que se instalará en la misión Mars Science Laboratory de la NASA. El minichip que viajará hasta el Planeta Rojo llevará grabado los nombres de sus creadores.

Un ingeniero gallego presumirá de aterrizaje en Marte en 2010

Manuel Domínguez, ingeniero de la UPC, participará en el diseño del sensor meteorológico que se instalará en la misión Mars Science Laboratory de la NASA. El minichip que viajará hasta el Planeta Rojo llevará grabado los nombres de sus creadores.

Un ingeniero gallego presumirá de aterrizaje en Marte en 2010

Manuel Domínguez, ingeniero de la UPC, participará en el diseño del sensor meteorológico que se instalará en la misión Mars Science Laboratory de la NASA. El minichip que viajará hasta el Planeta Rojo llevará grabado los nombres de sus creadores.

España crea el primer chip capaz de medir el viento de Marte

EFE ■ MADRID

Un grupo de investigadores de la Universidad Politécnica de Catalunya (UPC) ha diseñado el primer chip que con la pica clave del sensor de viento de la estación meteorológica desarrollada por científicos españoles para el vehículo espacial de la NASA que se lanzará en noviembre de 2009.

El coordinador del grupo de micro y nano tecnología de la UPC, Luis Castañer, explicó que este trabajo se enmarca dentro del proyecto denominado REMS (Estación Remota de Monitorización Ambiental) y agregó que el chip es un dado de silicio que mide 1,5 milímetros de lado.

Castañer señaló que ese chip lleva el nombre de los cinco investigadores que lo han concebido, diseñado y fabricado, totalmente en España en el laboratorio del grupo de investigación.

Este chip es la pieza clave del anemómetro (instrumento que mide la velocidad del viento) que incorpora la estación meteorológica del vehículo espacial rover Mars Science Laboratory (MSL) de la NASA.



Health & Medicine Mind & Brain Plants & Animals Earth & Climate Space & Time Matter & E

Science News

Scientists Design A Chip To Measure The Wind On Mars

ScienceDaily (Oct. 4, 2008) — A team of researchers at the Universitat Politècnica de Catalunya (UPC) has designed the first chip manufactured completely in Spain that will be used to measure the wind on Mars. This chip is the key piece of the anemometer on a weather monitoring station run by Spanish scientists for NASA's Mars Science Laboratory (MSL) rover, whose launch is planned for fall 2009.



Illustration of the Mars Science Laboratory. (Credit: NASA/JPL-Caltech)

The MSL rover, a robotized vehicle, will determine whether Mars is or has been able to support any kind of life. Among the instruments it contains are the Rover Environment Monitoring Station (REMS), which will measure air and ground temperature, atmospheric pressure, ultraviolet radiation and humidity, in addition to the speed and direction of the wind measured by the chip designed by the Spanish engineers. The details on this scientific contribution were recently published in the journal Planetary and Space Science.

Luis Castañer, coordinator of the Micro and Nano Technologies Research Group at the UPC which developed the piece, tells GING that this chip "is more efficient in terms of energy than those previously developed, and silicon technology is being used for the first time for this application in space".

Each silicon chip is 1.5 millimetres thick and includes three temperature-sensitive platinum components: One measures the temperature of the chip, the second heats it to some 25°C above ambient temperature and the third controls the characteristics of the wind sensor. The chip also carries the names of its creators.

Ads by Google Advertise here

Engineering Solutions
Industrial Project Management for critical applications
www.cooperallloys.net

Hannover Messe 2010
Top marketplace for scientific findings and technology transfer!
www.hannovermesse.de

Pharma SalesForce Tools
Interactive tools to present health economic evidence to doctors
basecase.com

medicine intermediat
high quality superior price purchase quickly 86-311-86721449
www.cqjchem.com

Biological Science
Online courses in human and animal anatomy, biochemistry, statistics
www.acsedu.co.uk/Courses/

Related Stories

ENT
MAGAZINE FOR ENTRENDEDY

Article Tools

- Print-friendly
- Email this article
- Comment on the article
- Daily News Email Digest
- News Feeds

Research and General News

(click here for Business News)

- European industry starts EU hydrogen initiative as not ambitious enough
Posted: Oct 15th, 2008
- Futuristic electronics and energy nanotechnologies pave the way for 21st Century applications
Posted: Oct 14th, 2008
- International textile conference will address nanofibers and nanocomposites
Posted: Oct 14th, 2008
- Nanotechnology Research Foundation seeks to advance nano education and research in the U.S.
Posted: Oct 14th, 2008
- New report for piezoelectric energy more nanotesters
Posted: Oct 14th, 2008
- Nanomotor helps tiny robot swim
Posted: Oct 14th, 2008
- Smart textiles: the new fabric
Posted: Oct 14th, 2008
- University of Utah announces the establishment of the Nano Institute of Utah
Posted: Oct 14th, 2008
- Terahertz version of single pixel camera could lead to breakthrough technologies
Posted: Oct 14th, 2008
- IMEC develops innovative architecture for feasible low-cost error correction
Posted: Oct 14th, 2008
- Researchers develop method to extend lifetime of organic solar cells
Posted: Oct 14th, 2008
- Natural nanotechnology probe limits damage to cells and biological tissue
Posted: Oct 14th, 2008
- Measurement of state represents important discovery in search for superconducting hydrogen
Posted: Oct 14th, 2008



A hot film anemometer for the Martian atmosphere

(Nanometer News) A team of researchers at the Universitat Politècnica de Catalunya (UPC) has designed the first chip manufactured completely in Spain that will be used to measure the wind on Mars. This chip is the key piece of the anemometer on a weather monitoring station run by Spanish scientists for NASA's Mars Science Laboratory (MSL) rover, whose launch is planned for fall 2009.

The MSL rover, a robotized vehicle, will determine whether Mars is or has been able to support any kind of life. Among the instruments it contains are the Rover Environment Monitoring Station (REMS), which will measure air and ground temperature, atmospheric pressure, ultraviolet radiation and humidity, in addition to the speed and direction of the wind measured by the chip designed by the Spanish engineers. The details on this scientific contribution were recently published in the journal Planetary and Space Science ("Encapsulation of Semiconducting Polymers in Vault Protein Cages").



Illustration of the Mars Science Laboratory (Image: NASA/JPL-Caltech)

Luis Castañer, coordinator of the Micro and Nano Technologies Research Group at the UPC which developed the piece, tells GING that this chip "is more efficient in terms of energy than those previously developed, and silicon technology is being used for the first time for this application in space".

Each silicon chip is 1.5 millimetres thick and includes three temperature-sensitive platinum components: One measures the temperature of the chip, the second heats it to some 25°C above ambient temperature and the third controls the characteristics of the wind sensor. The chip also carries the names of its creators.

Hot wire anemometry was the principle used by the engineers to measure the wind. Castañer, a founding member of the Royal Spanish Academy of Engineering (RAE), notes that wind had traditionally been measured by a technique in which a wire was heated and then the air cooled it, varying its temperature. This made it possible to establish a relationship with the speed of the air flow. "In the case of the chip, the hot point is not a wire, but instead a piece of silicon heated by a fine film that covers it and acts as the resistance to heat", he says.

The Micro and Nano Technologies Research Group (MNT) has patented a system that makes it possible to calculate the magnitude of the wind and its direction on a plane using four chips on a plate on that same plane, while at the same time taking the ambient temperature as a reference. The temperature is measured by a fifth chip, identical to the other four.

Wind speed can be measured in 2D with this methodology, but the speed in 3D can be deduced by using as many plates as necessary. The REMS weather monitoring station uses 6 wind sensors, with 6 silicon chips each, located on the ends of two booms and separated by an angle of 120°.

The chips were manufactured at the MNT group's Laboratorio de Sale Blanca, which counts on collaboration from the Centro de Astrobiología (CSA), the joint centre of the Instituto Nacional de Técnica Aeroespacial and the Consejo Superior de Investigaciones Científicas; IANIGLA Astrum (the company in charge of the industrial assembly of the station) and the Centro Nacional de Microelectrónica in Barcelona. Some tests were carried out in the wind tunnel at the University of Aachen (Germany).

The first principal researcher of the REMS project was Professor Luis Vázquez from the Complutense University of Madrid. This year, aerospace engineer Javier Gómez Florin from CSA, the current responsible for the Martian weather monitoring station, as well as its principal contractor, took over the station.

The station has already incorporated the MSL rover, and is currently verifying its instruments under the supervision of the Jet Propulsion Laboratory in California (USA) so as to have everything ready in the fall of 2009 when its launch is planned.

The MSL will carry out four types of research. First, it will study the biological potential of the environment, taking inventory of the chemical elements required for life and detecting the presence of organic compounds. It will also classify the geology and geo-chemical makeup of the region, analysing the composition of the planet's surface and interpreting the processes that have formed and modified its rocks. The rover's instruments will also be used to investigate surface radiation and some atmospheric processes—such as those that involve water—that may be relevant in determining if living beings could have existed on the red planet in the past.

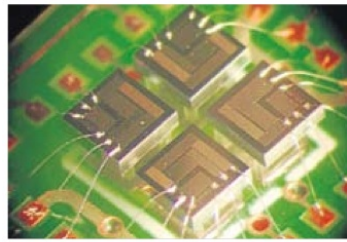


El chip que viajará a Marte. / SINC

Expertos españoles diseñan un chip para estudiar el viento de Marte

MADRID.- El viento de Marte se analizará en el futuro con tecnología española. Un equipo de investigadores de la Universidad Politécnica de Cataluña (UPC) ha diseñado el primer chip fabricado íntegramente en nuestro país destinado a medir el viento del planeta rojo. Ésta es la pieza clave del instrumento que incorpora una estación meteorológica desarrollada por científicos españoles para el vehículo *Mars Science Laboratory (MSL)* de la NASA, cuyo lanzamiento está previsto para el otoño de 2009.

El rover o vehículo robotizado MSL servirá para investigar si el entorno marciano es o ha sido propicio para el desarrollo de algún tipo de vida. Entre los instrumentos que lleva se encuentra la estación meteorológica REMS (*Rover Environment Monitoring Station*), que medirá la velocidad y dirección del viento, con el chip *made in Spain*.



Una imagen del componente electrónico. RICART ET AL

Un chip marciano con firma española

Científicos de la UPC equipan la estación meteorológica del próximo rover a Marte

J. V.
MADRID

Un grupo de la Universidad Politécnica de Catalunya ha diseñado un chip que permitirá medir el viento marciano mediante uno de los instrumentos del *Mars Science Laboratory (MSL)*, el vehículo rodante que la NASA lanzará al planeta rojo el año próximo.

El chip es un cubo de silicio de 1,5 milímetros de arista que incorpora tres elementos de platino sensibles a la temperatura, lo que hará posible determinar la velocidad del aire midiendo el enfriamiento del sistema. El grupo de Micro y Nano Tecnologías de la UPC ha logrado con ello, se-

gún su director, Luis Castañer, un chip "más eficiente" y que "por primera vez utiliza tecnología de silicio para esta aplicación en el espacio".

El chip estará integrado en la estación meteorológica REMS (siglas en inglés de Estación de Monitorización Ambiental del Rover), una aportación española al MSL. El grupo de Castañer ha elaborado el chip para el Centro de Astrobiología (CSIC-INTIA), que dirige el proyecto REMS. Los investigadores, que han grabado sus nombres en el chip, han publicado su desarrollo en la revista *Planetary and Space Science*.

La misión del rover, vehículo de exploración cuyo lanzamiento está previsto para septiembre de 2009, consistirá en examinar la idoneidad del entorno marciano para la existencia de vida, presente o pasada. •

Científicos españoles diseñan un chip para medir el viento de Marte

Efe / MADRID

Un grupo de investigadores de la Universidad Politécnica de Cataluña (UPC) ha diseñado el primer chip que será la pieza clave del sensor de viento de la estación meteorológica desarrollada por científicos españoles para el vehículo espacial de la NASA que se lanzará en noviembre de 2009.

En declaraciones a Efe, el coordinador del Grupo de micro y nano tecnología de la UPC, que ha desarrollado esta pieza, Luis Castañer, explicó que este trabajo se enmarca dentro del proyecto denominado REMS (Estación Remota de Monitorización Ambiental) y ha agregado que el chip es un dado de silicio que mide 1,5 milímetros de lado.

Castañer señaló que ese chip lleva el nombre de los cinco investigadores que lo han concebido, diseñado y fabricado, totalmente en España en el laboratorio del grupo de investigación.

El investigador detalló que este chip es la pieza clave del anemómetro (instrumento que sirve para medir la velocidad del viento) que incorpora la estación meteorológica desarrollada por científicos españoles para el vehículo espacial rover Mars Science Laboratory (MSL) de la NASA.

El proyecto está financiado por el Ministerio de Educación, recordó Castañer, quien declaró que el viento se media con una técnica por "la que se calienta un hilo y cuando sopla el aire la temperatura de ese hilo disminuye, cuanto más aire hay, más se refriera ese hilo caliente".

"Es como se hacía antiguamente en la superficie de Marte, concretamente en dos misiones, en 1975 y 1997", manifestó el también académico de la Real Academia de Ingeniería.

Para poder saber la dirección por la que llega el viento es preciso usar varios hilos calientes en distintas posiciones.

EN ÓRBITA Diseñado un chip para medir el viento de Marte

Es el primero fabricado íntegramente en España y la Politécnica de Catalunya (UPC) es la responsable. El equipo dirigido por el miembro de la Real Academia de Ingeniería (RAI) Luis Castañer, coordinador del Grupo MNT de Micro y Nano



Tecnologías de la UPC, ha desarrollado esta pieza clave del

anemómetro

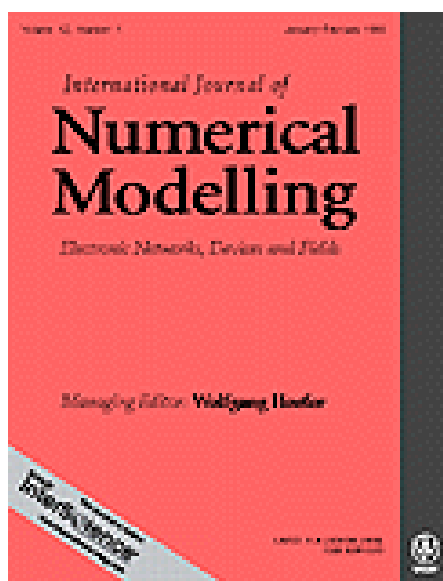
que incorpora una estación meteorológica, desarrollada por científicos españoles, para el vehículo Mars Science Laboratory (MSL) de la NASA, cuyo lanzamiento está previsto para el otoño de 2009. Según Castañer, "este chip es más eficiente en términos energéticos que los desarrollados anteriormente y, por primera vez, se utiliza tecnología de silicio para esta aplicación en el espacio", según ha comunicado el Servicio de Información y Noticias

Appendix G

Thermal modelling of the chip for the REMS wind sensor

International Journal of Numerical Modelling: Electronic Networks, Devices and Fields; Special Issue on the 7th Spanish Conference on Electron Devices, July 2010, Volume 23, Issue 4-5, Pages 340-353, DOI:10.1002/jnm.v23:4/5.

Lukasz Kowalski,
Jordi Ricart Campos,
Vicente Jiménez Serres,
Manuel Domínguez-Pumar,
Luis Castañer Muñoz.



ATTENTION !

Pages 228 to 242 of the thesis, containing the text, are available at the editor's web

<http://onlinelibrary.wiley.com/doi/10.1002/jnm.738/abstract>

Appendix H

Multiphysics simulation of REMS hot-film anemometer under typical Martian atmosphere conditions

Proceeding of the COMSOL 2010 conference,
Paris (France), 17-19 November 2010.

Lukasz Kowalski,
Luis Castañer Muñoz,
Manuel Domínguez-Pumar,
Vicente Jiménez Serres.

ATTENTION !

Pages 244 to 248 of the thesis, unpublished here by copyright, can be found in the copy of the thesis which is preserved in the UPC Archive.



Appendix I

Hypobaric chamber for wind sensor testing in Martian conditions

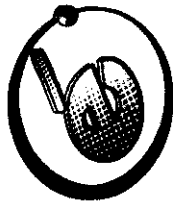
Proceedings and Poster of the 8th Spanish Conference on Electron Devices, Palma de Mallorca (Spain), 8-11 February 2011, DOI:10.1109/SCED.2011.5744212, *Best Poster Award.

Lukasz Kowalski,
Miguel Garcia Molina.



ATTENTION !
Pages 250 to 253 of the thesis, containing the text, are available at
the editor's web

http://ieeexplore.ieee.org/xpls/abs_all.jsp?arnumber=5744212&tag=1



8th Spanish Conference on Electron Devices
Palma de Mallorca, 8-11 February 2011



BEST POSTER AWARD

For the contribution entitled:


Hypobaric chamber for wind sensor testing in Martian conditions

Lukasz Kowalski and Miguel Garcia Molina

Palma de Mallorca, Spain
February 11th, 2011


Eugenio García Moreno
CDE 2011 General Chair

José Millán
CDE Advisory Committee President




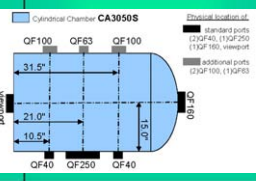

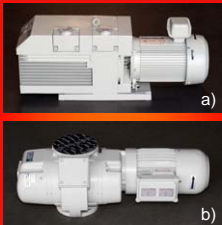
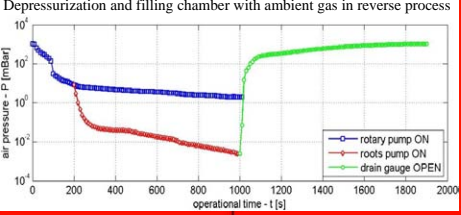
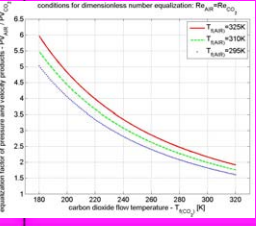

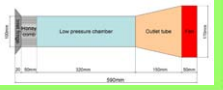

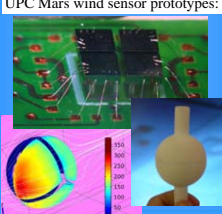
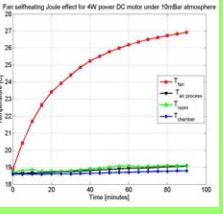
8th Spanish Conference on Electron Devices

Palma de Mallorca, 8-11 February 2011



Hypobaric chamber for wind sensor testing in Martian conditions

Lukasz Kowalski lukasz@eel.upc.edu (+34)9340154585, Miguel Garcia Molina molina@eel.upc.edu (+34)9340154202
 Universitat Politècnica de Catalunya, Departament d'Enginyeria Electrònica, Micro & NanoTechnology Group, Barcelona

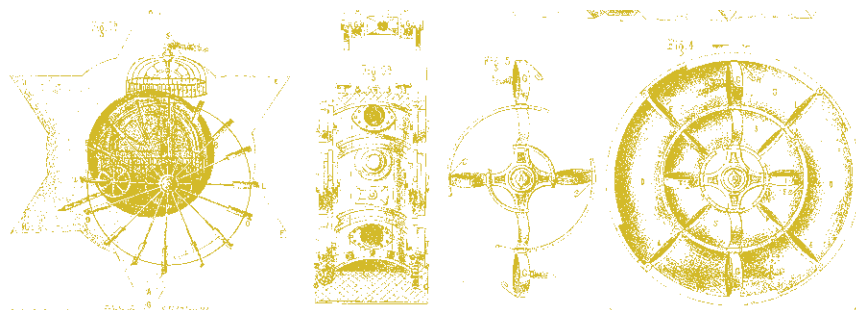
<p>MOTIVATION</p> <p>Space exploration program grows what rises unprecedented challenge for appropriate sensor engineering. For MNT-UPC engineering group it was a motivation to build simpler and more operational wind tunnel chamber to reproduce MARS-like conditions which in future would enable us proof of concept for the novel sensor in development phase.</p>	 <p style="text-align: center;">CA3050S</p>	<p>Easy access and manipulation comfort by the main door entrance</p> 	<p>VACUUM SYSTEM</p> <p>Appropriate exhaust of the 0.6m³ interior volume of the vacuum chamber is provided by connected in chain two stage vacuum system:</p> <ol style="list-style-type: none"> Leybold TRIVAC D65BCS two-stage rotary vane vacuum pump Leybold RUVAC WS-251 roots vacuum pump 															
 <p style="text-align: center;">MarsLab-UPC</p> <p style="text-align: center;">HYPOBARIC CHAMBER</p> <p>Standard horizontal stainless steel vacuum chamber type CA3050S provided by K.J. Lesker has been customized through additional QF port manufacture.</p> <ul style="list-style-type: none"> • QF40 gas entrance and exhaust • QF100 and QF63 electrical feed • QF160 and view-port window • QF250 tapped not yet specified <p>Financial support AYA2010-20847</p>	<p>Earth image by Galileo orbiter, Mars image by Global Surveyor.</p> <table border="1" style="width: 100%; border-collapse: collapse;"> <thead> <tr> <th>Parameter</th> <th>Earth</th> <th>Mars</th> </tr> </thead> <tbody> <tr> <td>Pressure, [Bar]</td> <td>1</td> <td>6-9 · 10⁻³</td> </tr> <tr> <td>Temperature, [K]</td> <td>300</td> <td>210</td> </tr> <tr> <td>Gas composition</td> <td>N₂: 78% O₂: 21%</td> <td>CO₂: 95%</td> </tr> <tr> <td>Gravity, [m/s²]</td> <td>9,80</td> <td>3,71</td> </tr> </tbody> </table>	Parameter	Earth	Mars	Pressure, [Bar]	1	6-9 · 10 ⁻³	Temperature, [K]	300	210	Gas composition	N ₂ : 78% O ₂ : 21%	CO ₂ : 95%	Gravity, [m/s ²]	9,80	3,71	<p>REYNOLDS NUMBER</p> <p>Reynolds number value describes whether flow is laminar with no disruption between the layers and streamlines or turbulent flow characterized by chaotic, stochastic property changes flow lines. Although not as cold as on Mars and not the same atmospheric gas composition but we reproduced the same dimensionless Re parameter.</p>  <p style="text-align: right;">a) b)</p>	 <p>Depressurization and filling chamber with ambient gas in reverse process</p>
Parameter	Earth	Mars																
Pressure, [Bar]	1	6-9 · 10 ⁻³																
Temperature, [K]	300	210																
Gas composition	N ₂ : 78% O ₂ : 21%	CO ₂ : 95%																
Gravity, [m/s ²]	9,80	3,71																
<p>WIND TUNNEL</p> <p>For our specific design we acquired educational mini wind tunnel WTM-1000 with tube shape cross section of diameter 10cm and highly uniform flow-rate. This enable us through the adjustable power supply regulation for setting up desirable wind speed produced by DC fan rotation.</p>	<p>Fundamental equations:</p> $Re = \frac{\rho V L}{\mu} \quad \rho = \frac{MP}{RT}$ $Re = \frac{MPVL}{RT\mu}$ $Re = \frac{M}{T\mu} \cdot PV \cdot \frac{L}{R}$ $\frac{P_{AIR} V_{AIR}}{P_{CO_2} V_{CO_2}} = \frac{M_{CO_2} T_{AIR} \mu_{AIR}}{T_{CO_2} \mu_{CO_2} M_{AIR}}$	<p>conditions for dimensionless number equalization: $Re_{AIR} = Re_{CO_2}$</p>  <p>equalization factor of pressure and velocity products: $P_{AIR} V_{AIR} / P_{CO_2} V_{CO_2}$</p>	<p>CONCLUSIONS</p> <p>Marslab-UPC hypobaric chamber facility has been completed with commonly available commercial elements and refurbished vacuum system pumps. It takes 15 minutes to depressurize interior of the chamber for low pressure Martian conditions. Using smart pressure and velocity product adjustment we achieved the same Reynolds number dimensionless parameter.</p>															
<p>WTM-1000</p>  	<p>Wind tunnel inside vacuum chamber</p> 	<p>REFERENCES</p> <ol style="list-style-type: none"> [1] M. Dominguez, V. Jimenez, J. Ricart, L. Kowalski, J. Torres, S. Navarro, J. Romeral, L. Castaner, A hot film anemometer for the Martian atmosphere, Planetary and Space Science, Volume 56, Issue 8, pp. 1169-1179, June 2008. [2] Robert M. Haberle, David C. Catling, A Micro-Meteorological mission for global network science on Mars: rationale and measurement requirements, Planetary and Space Science, Volume 44, Issue 11, pp 1361-1375, Internetsnet, Nov. 1996. 	<p>UPC Mars wind sensor prototypes:</p> 															
 <p>Fan selfheating Joule effect for 4W power DC motor under 10⁻³bar atmosphere</p>																		

Appendix J

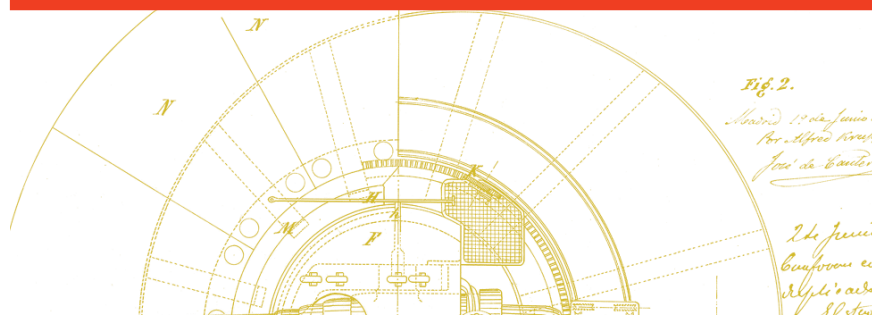
Congratulations & Exhibitions

Antoni Giró Roca, El Rector de UPC,
Barcelona (Spain), 8 May 2012.

Album y Exposición Virtual - Oficina Española de Patentes
200 años de patentes 1811-2011, www.exposicionesvirtuales.oepm.es



200 años
de patentes





UNIVERSITAT POLITÈCNICA
DE CATALUNYA

El Rector

Sr. Luis Castañer Muñoz
Eng. Electrònica
Edifici C4 Despatx: 307
C. Jordi Girona, 1-3
08034 Barcelona

Benvolgut Luis,

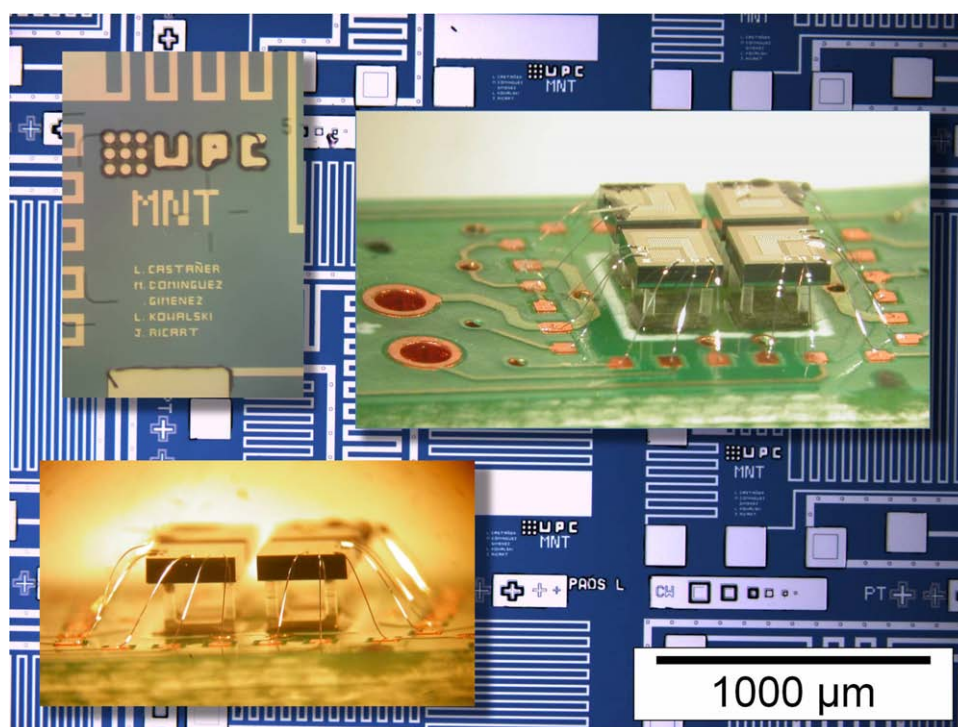
M'omple d'orgull i de satisfacció assabentar-me que la UPC ha arribat a Mart amb el disseny d'un sensor de vent del Curiosity, del qual n'ets responsable. Vull fer-te arribar, doncs, una molt efusiva felicitació per part de l'equip rectoral així com el nostre agraïment per haver contribuït a que la UPC formi part d'aquesta important missió i permetre que la "nostra universitat" trepitgi el planeta vermell.

T'agrairia que facis extensiva aquesta felicitació a la resta d'investigadors responsables: Vicente Jiménez, Manuel Domínguez, Lukasz Kowalski i Jordi Ricart.

Moltes felicitats!

Antoni Giró Roca

Barcelona, 8 de maig de 2012



A finales de Noviembre de 2011 se lanzará, con destino a Marte, el Mars Science Laboratory. Se trata de un vehículo robotizado que forma parte del programa de exploración del planeta rojo llevado a cabo por la NASA, y su misión será determinar las condiciones de habitabilidad en dicho planeta. Entre la instrumentación, el robot cuenta con el REMS (Rover Enviromental Monitoring Station), una completa estación meteorológica desarrollada conjuntamente por diversas instituciones científicas españolas, que monitorizará las condiciones atmosféricas en la superficie de Marte.

Una parte fundamental de dicha estación es un chip electrónico (patente ES 2342953) capaz de medir la velocidad y la dirección del viento, utilizando la técnica conocida como anemometría por punto caliente. Para ello se calienta un elemento mediante una corriente eléctrica, y se mide la potencia que se necesita para mantener la temperatura del elemento independientemente de la velocidad del viento. La medida de esa potencia permite conocer la velocidad del viento en ese instante. Haciendo lo mismo con varios de elementos en diferentes posiciones, es posible determinar también la dirección. El dispositivo consta de cuatro dados iguales fabricados en silicio, cada uno de los cuales contiene tres resistencias de platino: una mide la temperatura del chip, otra lo calienta y la tercera sirve para fijar una diferencia de temperatura consigna entre el elemento caliente y el ambiente. La temperatura del ambiente se mide mediante otra resistencia situada en un quinto dado. Un circuito electrónico transforma las medidas en datos digitales en el formato adecuado.

Appendix K

NASA Group Achievement Award

Charles F. Bolden, 12th NASA Administrator,
Washington, DC (United States), 18 July 2013.

Signs of a Whirlwinds reported by REMS instrument,
Gale Crater (Mars), 25 October 2012.



National Aeronautics and Space Administration

Presents the

Group Achievement Award

to

MSL REMS Instrument Development and Science Team

For exceptional achievement defining the REMS scientific goals and requirements, developing the instrument suite and investigation, and operating REMS successfully on Mars.

Lukasz Kowalski

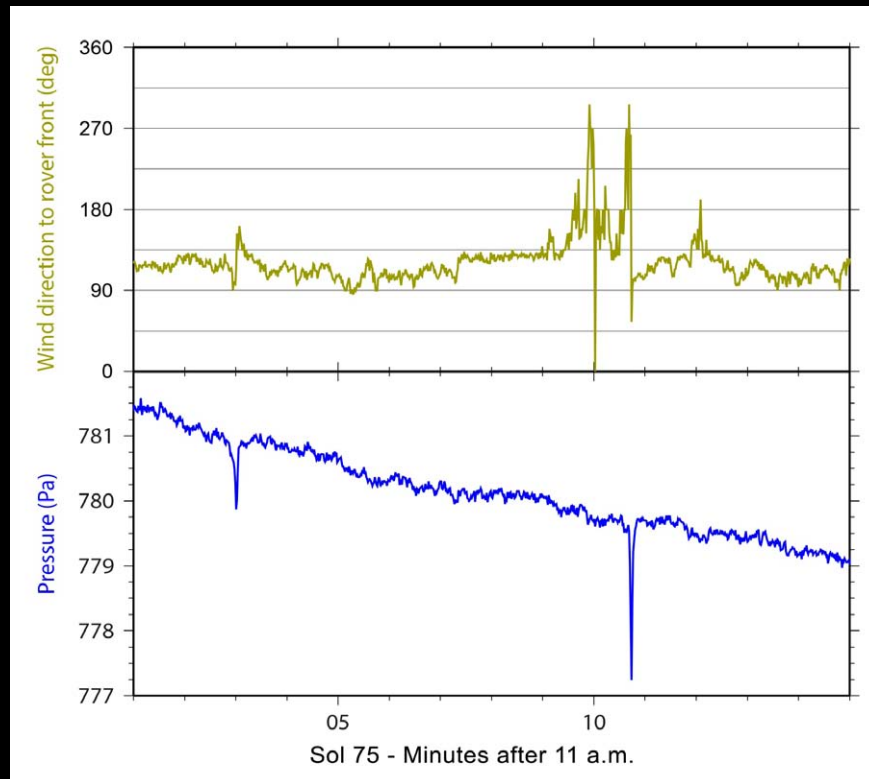


*Signed and Sealed at Washington, DC
this eighteenth day of July
Two Thousand Thirteen*

CR Boldt

Administrator, NASA

Signs of a Whirlwind in Gale Crater



Twenty-one times during the first 12 weeks that NASA's Mars rover Curiosity worked on Mars, the rover's Rover Environmental Monitoring Station (REMS) detected brief dips in air pressure that could be caused by a passing whirlwind. The blue line in this chart shows two examples, both shortly after 11 a.m. local Mars time, when the air pressure dipped on the 75th Martian day, or sol, of the mission (Oct. 25, 2012). In both cases, wind direction monitored by REMS changed within a few seconds of the dip in pressure, as indicated by the green line on the chart. That is additional evidence that the pressure dips were whirlwinds.

A Finnish, Spanish and American team is using REMS, which Spain provided for Curiosity, to watch for signs of dust devils - whirlwinds carrying dust.

In many regions of Mars, dust-devil tracks and shadows have been photographed from orbit, but those visual clues have not been seen at Gale Crater, where Curiosity is working. The evidence from REMS indicates that whirlwinds may be forming in Gale Crater. While Curiosity is watching for them with cameras on some days, researchers are also considering the possibility that these swirling, convective winds do not lift as much dust at Gale as in other parts of Mars.

In this chart, the air-pressure scale is in Pascals. The wind direction scale is an estimate in degrees relative to the front of the rover. On Sol 75, the rover was facing approximately westward, and 90 degrees on this graph indicates winds coming from the north.

Image credit: NASA/JPL-Caltech/ CAB (CSIC-INTA), find this article at:
http://www.nasa.gov/mission_pages/msl/multimedia/pia16476.html



Appendix L

Low pressure spherical thermal anemometer for space mission

Proceedings and Oral presentation of the IEEE SENSORS 2013 conference, Baltimore (United States), 3-6 November 2013.

* Student Best Paper Award - Track 5 (Mechanical, Magnetic, and Physical Sensors)

Lukasz Kowalski,

Vicente Jiménez Serres.

Manuel Domínguez-Pumar,

Sergi Gorreta Marine,

Santiago Silvestre,

Luis Castañer Muñoz.



ATTENTION ;

Pages 266 to 269 of the thesis, containing the text, are available at the editor's web

<http://ieeexplore.ieee.org/stamp/stamp.jsp?tp=&arnumber=6688493>



*2013 IEEE Sensors
Student Best Paper Award – Track 5*

hereby presents the

to

Lukasz Kowalski

for the paper

Low Pressure Spherical Thermal Anemometer for Space Missions



B. Sambandan

Yogesh Gianchandani,

Technical Program Committee Chair



IEEE SENSORS 2013

Low pressure spherical thermal anemometer for space missions (to Mars)

by
 Lukasz Kowalski, Vicente Jiménez,
 Manuel Dominguez-Pumar, Sergi Gorreta,
 Santiago Silvestre and Luis Castañer.

Polytechnic University of Catalonia
 Electronic Engineering Department
 Micro & Nano Technologies Research Group

November 24, 2013 | Baltimore, Maryland, USA | Electronics System Integration

Sensor objectives

Compact, reliable, and efficient Mars anemometer to:

- Measure wind velocity (U_{∞})
- Measure 3D wind angle (θ, ϕ)

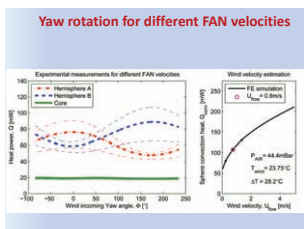
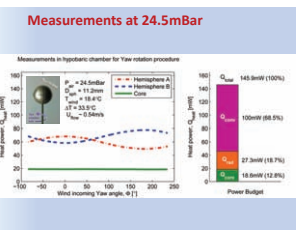
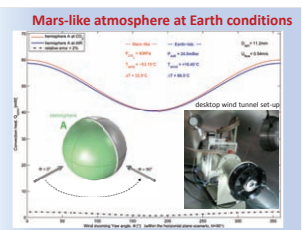
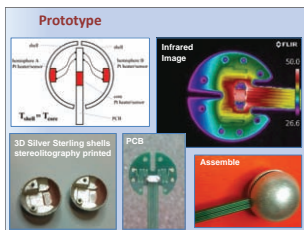
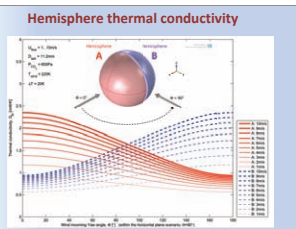
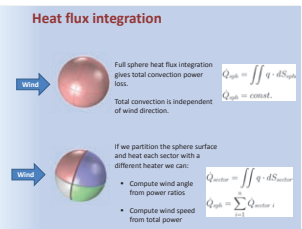
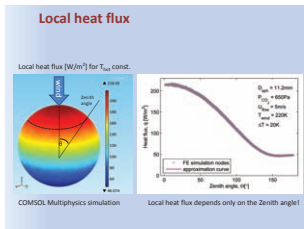
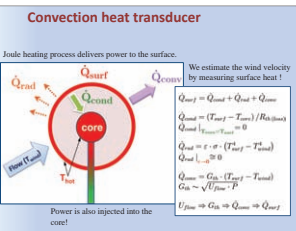
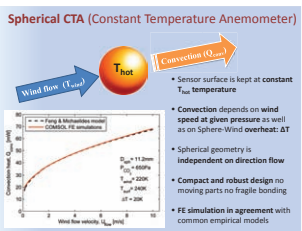
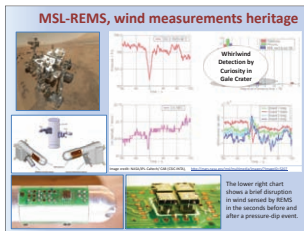
Why?

- atmosphere characterization: polar cap sublimation and deposition, tidal flows, local blows, planetary storms, dust devils, particle charge
- Optimal NO wind condition for soil scooping and drill procedure
- Planetary aerial navigation: Mars balloons and planes
- Manned mission to Mars ...

Mars atmosphere vs. Earth

MARS	Planet	EARTH
	Photos done by the Hubble telescope. Mars diameter is around a half size of the Earth.	
3.7	Gravity, g [m/s²]	9.8
CO ₂ 95.32%, N ₂ 2.7%, Ar 1.9%, O ₂ 0.17%	Atmosphere air element composition [%]	N ₂ 78.08%, O ₂ 20.9%, Ar 0.93%
5.93Pa (5.4mBar)	Surface pressure [Pa]	1013 Pa (1bar)
-0.020	Surface density [kg/m³]	1.2
2-10 (50 dust storms)	Wind speed [m/s]	0-100
210 (43°C)	Average temperature [°C]	300 (27°C)
from -125°C to +20°C	Temperature variation [°C]	from -50°C to +40°C

<http://nssdc.gsfc.nasa.gov/planetary/factsheet/marsfact.html> ... /earthfact.html



Conclusions

Spherical constant temperature anemometer is a great candidate for the Martian atmosphere wind sensor!

- Compact** – external shell protects from environment
- Well behaved** – axis-symmetric and laminar flow behavior
- Efficient** – about 70% of delivered power is valuable

U_{∞} estimation – total convection heat for sphere

Angle discrimination – sectors heat convection ratio

